FINAL REPORT

DOCTORAL THESIS

GEOLOGY, GEOCHRONOLOGY AND ZIRCON GEOCHEMISTRY STUDY OF THE HUMPA LEU EAST PORPHYRY COPPER-GOLD PROSPECT IN HU'U DISTRICT , SUMBAWA ISLAND, INDONESIA

インドネシア、スンバワ島、Hu'u 地域、Humpa Leu East 斑岩銅-金鉱徴地の地質、地質年代、地球化学

Fadlin

B. Eng. in Geology (STTNAS Yogyakarta)

M. Eng. in Economic Geology (UGM Yogyakarta)

Official Supervisor:

Assoc. Prof. Dr. Ryohei Takahashi

Prof. Dr. Andrea Agangi

DOCTORAL PROGRAM

DEPARTEMENT OF GEOSCIENCES, GEOTECHNOLOGY, AND MATERIALS ENGINEERING FOR RESOURCES, GRADUATE SCHOOL OF INTERNATIONAL RESOURCE SCIENCES, AKITA UNIVERSITY, JAPAN

MARCH 2023

THESIS FOREWORD

Ph.D candidate of Akita University
Fadlin (D5620104)

LIST OF CONTENT

LIST OF FIGURES

LIST OF TABLES

APPENDICES

ABSTRACT

The Humpa Leu East (HLE) porphyry Cu-Au prospect is located in Sumbawa Island, within the eastern margin of the Sunda metallogenic belt, Indonesia. There are several world-class porphyry Cu-Au deposits with Miocene-Holocene ages in the belt, such as the Tujuh Bukit, Batu Hijau, Elang, and Onto-Hu'u deposits.

The HLE prospect formed in an active continental margin with a calc-alkaline magma affinity. The prospect is characterized by typical multiphase porphyry intrusions associated with hypogene mineralization. On the basis of the petrographic observation, the porphyry intrusions can be classified into early, intermediate, and late phases, which consists of two types of rocks, *i.e.*, diorite porphyry, and quartz diorite porphyry. The diorite porphyry intrusions are dark grey in color, consisting mainly of plagioclase and alteration minerals of carbonate, quartz, chlorite, anhydrite, albite, and K-feldspar. The quartz diorite porphyry intrusions are grey in color and consist of plagioclase, minor quartz, and alteration minerals of carbonate, quartz, chlorite, anhydrite, albite, and K-feldspar. Hydrothermal alteration associated with the main mineralization in the drill cores can be classified into potassic, chlorite-sericite, and sericite alteration. The potassic alteration includes quartz, magnetite, K-feldspar, calcite, albite, anhydrite, and chlorite. Secondary biotite has not been identified in this alteration, and it might have been replaced by chlorite. The chlorite-sericite alteration includes quartz, chlorite, sericite, calcite, and anhydrite. The sericite alteration includes abundant quartz, sericite, and calcite, and minor chlorite, anhydrite, and gypsum. The mineralization stages of the HLE prospect can be divided into early, intermediate, and late. The early stage is associated with M (magnetite-bornite±chalcopyrite), A (quartz+ magnetite), and AB (quartz+magnetite+chalcopyrite±pyrite) veins. These veins mainly formed in the potassic alteration zone. The intermediate stage is characterized by B veins (quartz+chalcopyrite+pyrite) and C veins (chalcopyrite±pyrite), which mostly occur in the chlorite-sericite and sericite alteration zones. The late stage is mostly associated with D veins (calcite+gypsum+quartz+pyrite±chalcopyrite± sphalerite±galena) that accompany sericite and chlorite alteration halo. Two styles of mineralization have been identified in the HLE prospect, *i.e.*, quartz-sulfide veins, and sulfide dissemination, where the former related with chlorite-sericite alteration are the most dominant copper and gold mineralization. Gold (Au) is mostly contained in chalcopyrite within intermediate stage.

Microscopic observation and laser Raman spectroscopy of fluid inclusions in quartz of

the A, AB, B and D veins were conducted. There are three types of fluid inclusions, *i.e.*, liquid-rich two-phase V+L, monophase vapor (or vapor rich V-L), and multi-phase vapor rich V+L+S inclusions. The laser Raman spectroscopic analysis revealed the presence of CO_2 in the vapor, two-phase (V+L) and multi-phase (V+L+S) fluid inclusions, which was identified by two main peaks at 1,388 and 1,285 cm-1. Calcite in the potassic alteration zone would have been formed by a reaction of Ca-rich plagioclase and CO_2-rich fluids. The CO_2 in the hydrothermal fluids was likely derived from the magma. The microthermometry analysis data shows the trapping temperature of fluid inclusions in early stage (A; AB), intermediate (B), and late stages (D) of quartz veins are 470, 305, and 285 °C. The salinity of early stage (A; AB), intermediate (B), and late stages (D) of quartz veins was average 22, 12.4, and 7.6 wt.% NaCl eq. On the basis of the sulfur isotope analysis data, the $\delta^{34}S$ sulfides and sulfates values are from –3.8 to +3.4 ‰, and +9.9 to +12.4 ‰ which indicate that the sulfur was derived from igneous sources or magmatic fluids.

This study examined trace element compositions of zircon in the porphyry intrusions of the HLE prospect to apply them as a tool to assess magma fertility of copper and gold mineralization. The zircon in the porphyry intrusions is mainly magmatic origin with oscillatory zoning and characterized by a steeply upward REE patterns from La to Lu as well and strongly positive Ce/Ce* and moderately negative Eu/Eu* anomalies. Geochemistry of zircon indicates that the porphyry intrusions of the HLE prospect were a product of magmatism with crystallization temperature at average 780 °C. U-Pb zircon dating on the porphyry intrusions yielded 1.2-1.0 Ma (middle Pleistocene). The presence of magnetite and ilmenite inclusions in zircon indicates that the zircon formed in an oxidized magma. Trace element analysis of zircon indicated Eu/Eu* > 0.4, and Ce/Ce* > 50, and ΔFMQ +2.9±1.9. Ratios of the trace elements, Yb/Dy >0.4 and Lu/Ho >2.0 of zircon indicate fractional crystallization of amphibole in early stage. The presence of amphibole in the porphyry intrusions implies that the magma had high water content, more than ca. 4 wt.%. The Eu/Eu*, Ce/Ce*, Yb/Dy, and Lu/Ho ratios of zircon are applicable fertility assessment of porphyry Cu and Au mineralization for magmas.

CHAPTER 1
INTRODUCTION

1.1 BACKGROUND

Indonesia is located between two continental plates Eurasian and Australian, and between two oceanic plates of the Philippine and Pacific. Tectonic plate interaction, which formed the Indonesian Archipelago, has formed some magmatic arcs, which also become metallogenic belt (Carlile and Mitchell, 1994). Mineral exploration activity has been performed by the government and private companies, from reconnaissance surveys to detailed surveys using various methods and concepts (van Leuwen, 2018). The exploration has discovered many types of gold deposits in the host rock: sedimentary rock, volcanic rock, metamorphic rock, and carbonate rock (van Leuwen, 2018). The exploration for gold deposits in Indonesia increased in technology and geological science.

The exploration of metallic minerals has regularly been carried out along the magmatic belt,such as the Sunda-Banda belt. It has been proven by the presence of large copper and gold mines (van Leuwen, 2018). The Sunda-Banda magmatism belt is one of the corridors where various for gold-copper deposits occur including epithermal, porphyry, skarn, and sediment-hosted types occurred (van Leuwen, 2018). The potential has been proven by the presence of gold-silver and base metal mines, such as Lebong Tandai (Bengkulu, 1896-1941; 1957-1985; 1992), Cikotok Complex (Banten, 1956-2000), Pongkor (West Java, since 1994-present), Batu Hijau (Sumbawa, 1998-present), and the presence of new gold mines such as Cibaliung (Banten, 2010), Waylinggo (Lampung, 2013), Martabe (Tapanuli, 2013), and Tumpangpitu (Banyuwangi, East Java, 2017) (van Leuwen, 2018). The potential of gold mineralization is large in Indonesia, especially the porphyry copper-gold deposits, which is confirmed by the presence of numerous world-class porphyry copper-gold mines in Indonesia, especially at Eastern Sunda Magmatic arc such as Tumpang Pitu (Banyuwangi, the eastern part of Java Island), Batu Hijau (Western part of Sumbawa Island), Dodo-Elang (Western part of Sumbawa Island), and also the newly discovered prospects at Hu'u District (Eastern part of Sumbawa Island) (Maryono et al., 2018).

Most of the world's Cu resources come from porphyry deposits (Sillitoe, 2010). The porphyry deposits mainly occur at the margins of convergent belts, mainly above subduction zones, with fewer occurrences found in post-collisional zones (Sillitoe, 2010).

The formation of porphyry deposits occurs between 1–6 kilometers below the paleosurface in association with intermediate to felsic intrusive rocks (Seedorff et al., 2005). Typically, porphyry deposits are formed by the injection of oxidized magmas saturated with aqueous fluids. Consequently, the magma must be water-rich and oxidized, with most sulfur appearing as sulfate in the magma (Sun et al., 2015). Discovering porphyry deposits is very complex; it involves a significant expense, high risk, and takes a long time. Therefore, an important challenge in mineral exploration is effectively classifying and validating geochemical and geophysical anomalies, especially those hidden beneath young cover sequences (Nevolko, 2021).

1.2 LOCATION AND ACCESS

The research area is a part of PT. Sumbawa Timur Mining (PT. STM) concession, located at Hu'u district , Dompu regency in Sumbawa island, a part of the province of West Nusa Tenggara, Indonesia. The research area is approximately 30 km south of the Dompu regency and 75 km south-west of Bima city (**Fig. 1.1**). The Hu'u prospect lies about 440 km east of the provincial capital of West Nusa Tenggara. There are regular daily flights from Lombok to Bima with approximately 45 minutes and then followed 2 hours by car to the Hu'u.
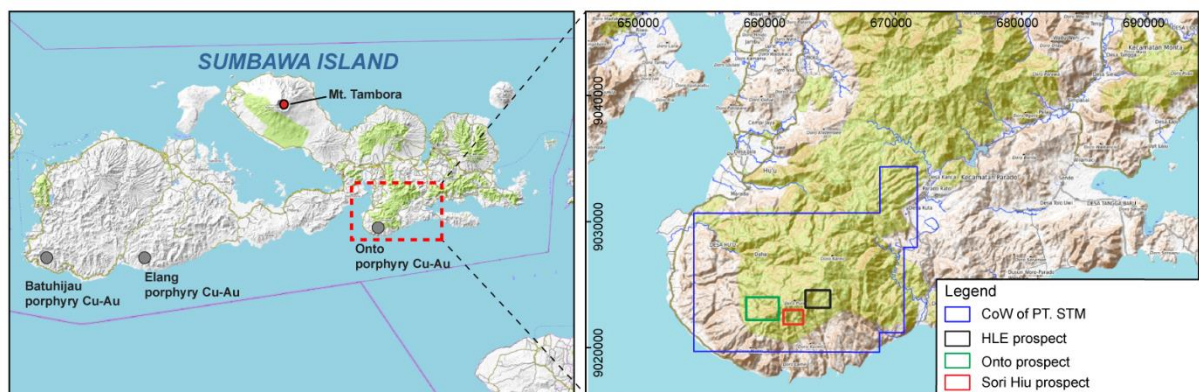
Figure 1. 1 PT. Sumbawa Timur Mining tenement area of Hu'u district , where the HLE prospect is situated.

1.3 OBJECTIVES

This study focuses on the mineralization, alteration, hydrothermal fluids, geochronology, and zircon geochemistry studies of magmatic-hydrothermal activity in the HLE porphyry copper-gold prospect in Hu'u district Sumbawa Island, Indonesia.

The objectives of this study include:

1. To elucidate the geological framework including magma petrogenesis

2. To understand the evolution of hydrothermal fluids
3. To reconstruct the age of the magmatism
4. To understand the zircon geochemistry as a tool of magma fertility assessment.

Those outputs can be used for scientific references in the porphyry Cu-Au mineralization system and the eastern part of the Sunda magmatic arc in Indonesia, particularly related to the deposit's geology and geochronology. Furthermore, the results can also be applied as a guide for porphyry copper-gold exploration in terrain with a similar geological setting.

1.4 PREVIOUS STUDIES

Hu'u District has been researched in ore mineral exploration and geothermal study. Previous research at Hu'u has focused on geological surface mapping by various methods and subsurface with the core drilling method to find the boundaries of lithology **(Table 1.1)**. This research is the development of data from one of the prospects found by PT. Sumbawa Timur Mining (a joint venture with Vale Exploration). In this study, detailed petrologic, whole rocks geochemistry, mineral chemistry, and uranium-lead (U-Pb) dating are presented. In this case, this study is the first study using the U-Pb dating methods as one of the supporting data to explain the timing and episode of the magmatism processes in the research area.

Table 1. 1 A summary of the previous study results about the regional geological mapping, ore mineral exploration, and geothermal study at Hu'u District .

Year	Company/ Institution	Research type	Method	Result	Reference
1978	Nana Ratwan, Aswan Yasin, (Directorate of Geology, P3G, Indonesia)	Regional geological mapping	Surfaces mapping	Regional geological map of Komodo Sheet	(Ratwan dan Yasin, 1978)
1994-1997	Aberfoyle Resources Ltd.	Exploration of precious metals	Regional mapping, soil geochemistry and geophysical survey (ground magnetic survey, IP, CSAMT) and guiding drill)	The anomaly was associated with porphyry-related copper-gold and HSE copper mineralization.	(fade van Leeuwen, 2018)
1997	Adjat Sudradjat, A. Mangga, N. Suwarna (Directorate of Geology, P3G, Indonesia)	Regional geological mapping	Surfaces mapping	Regional geological map of Sumbawa Sheet	(Sudradjat *et al.*, 1998)
1998	Aberfoyle's Western Metal (Sumbawa Timur Mining: JV Antam)	Exploration of precious metals	Review	Anomaly in several places	(fade van Leeuwen, 2018)

2005	Sundhoro et al. (Sub-directorate of Geothermal, ESDM)	Geothermal exploration	Geology, hydrogeochemistry, geophysical survey (magnetic, gravity, geoelectrical)	Geothermal prospect in Lacoha, Sori Rewa, Lapui, Hu'u, Lekey, and Ncangga regions has a temperature between 32.0 - 46.1 ° C with neutral pH (6.5-7.3), and Limea hot spring has a temperature of 80 ° C with acidic pH	(Sundhoro et al., 2005)
2010-2018	Sumbawa Timur Mining (JV Vale & Antam)	Exploration of precious metals	Core drilling in soil anomaly at The HLE prospect, drilling in Wadu Bura-Onto prospect	Found a porphyry deposit of The HLE, Humpa Leu West, Wadu Bura, Onto, Sori Hiu, Joblog, Lere.	(fade van Leeuwen, 2018; Internal report of PT. STM)
2014	Alif Febriansyah, Yoga Aribowo dan Dian Agus Widiarso (internship on PT. Vale Exploration)	Local geological mapping	Surfaces mapping	Argillic and intermediate argillic alterations. Stockwork mineralization with Sulphide minerals such as pyrite and chalcopyrite	(Febriansyah et al., 2014)
2018-now	Sumbawa Timur Mining (JV Vale & Antam)	Exploration of precious metals	Core drilling in Wadu Bura-Onto, Geotech drilling in Wadu Bura - Onto	Preparation of feasibility study (FS) for Wadu Bura-Onto prospect	An internal report of PT. STM

1.5 OWNERSHIP AND EXPLORATION HISTORY

The Hu'u district prospect, including the Onto-Wadu Bura prospect, the HLE prospect, and the Sori Hiu prospect is an owned by Sumbawa Timur Mining company (joint venture with Vale Exploration Indonesia) (PT. STM., 2018). VEI (Vale Exploration Indonesia) has been done with a various detail exploration levels from 2010 to 2017 (PT. STM., 2018). The detail exploration works at the most potential developing area, Wadubura-onto is suspended (PT. STM., 2018). The work started by surface mapping and soil sampling on a grid basis, infill stream sediment sampling, airborne and ground magnetic survey, geochemistry analysis, petrology and petrography analysis, surface structure geology study, rock-forming clay mineral, and rock magnetic content determining (PT. STM., 2018). Various level of drilling such as scout drilling up to resource definition drilling and engineering drilling and investigation purposes such as geotechnical-geothermal-geohydrology drilling, physical rock properties, and discontinuity plane observation on drilling core basis also were conducted (PT. STM., 2018).

Detail geological mapping commenced in 2010 over 8,283 hectares divided into 21 exploration target clusters (PT. STM., 2018). VEI applied the best practice of surface geological mapping procedure on rough terrain areas, which complies with international standard (USGS). All rock samples are applied analytical spectral device (ASD)-magsus and niton assessment for having more confidence in clay mineral content, magnetic figure, and metal content (PT. STM., 2018). Traverse lines were extended until the boundary of the exploration targeting areas is clearly understood and defined (PT. STM., 2018). The completed geology and alteration surface map was interpreted for Hu'u copper property and provides the actual boundary areas where the need to advance exploration works (PT. STM., 2018). Compiling the surface geology–alteration mapping, Cu-Au anomaly of surface geochemistry, and circular high magnetic image data, suggests an advanced exploration with the HLE and Onto cluster (PT. STM., 2018). The detailed geological surface mapping undertaken since 2013 covered approximately 256 Ha. of the HLE cluster when the project ramped up into concept resource definition study. The aim objective is to better understand better advanced argillic alteration associated with porphyry copper mineralization associated with dioritic instrusions (PT. STM., 2018). The work included 5 meters grid outcrop sample collection and soil pulp to produce an ADS-niton and magsus dataset (PT. STM., 2018). By having a clear understanding, outcomes guide the resource definition drilling direction.

The detailed geological surface mapping, undertaken from 2016 to 2017, covers about 1,993 Ha of Wadubura-onto cluster, when the project came into concept reserve definition study (PT. STM., 2018). The aim objectives are to have a better geology understanding of advance argillic alteration is developed in association with porphyry copper mineralization associated with high sulphidation overprinting to have high confidence subsurface and surface structure correlation for geological model generation, to determine the heat source information in association to deal with geothermal consequences in the copper deposit environment (PT. STM., 2018). Drilling Initially, VEI engaged Board Longyear (BLY), multinational drilling VEI to perform resource definition drilling by conducting a diamond bit full coring drilling at Humpa Leu East copper deposit started in January 2011 (PT. STM., 2018). BLY occupied the LF70 machine, which is workable to drill down to 800 meters using NQ barrel size and LF90 machine, drilled down to 1500 meters (PT. STM., 2018). A total of 22 holes or 15,750 meters were finished in May 2012. The two holes are re-drill, which are VHD001 and VHD009, due to wall collapse issues (PT. STM., 2018). Most of the holes intersected the narrow copper-gold

multi phases porphyry-style deposit (PT. STM., 2018). From June 2013 to August 2017, VEI engaged three multinational drilling VEI to perform resource definition and geothermal-geohydrology drilling by applying a diamond bit full coring drilling at Wadubura-Onto copper deposit (PT. STM., 2018). A total of 63 holes or 60,209 meters are finished (PT. STM., 2018). The first stage of exploration drilling, time June 2013 to February 2015, was performed by board Longyear (BLY), occupying the LF70 machine, which is workable to drill down to 800 meters using NQ barrel size LF90 machine, drilled down to 1500 meters (PT. STM., 2018). The first round of exploration drilling about 26 holes, or 26,253 meters is finished (PT. STM., 2018).

1.6 PORPHYRY COPPER DEPOSIT

1.6.1 Definition, grades, and tonnages

Porphyry copper deposits are large and relatively low grade (average 0.4% copper) epigenetic deposits of disseminated and vein type copper and iron sulphide, often associated with gold, molybdenum, and silver (Cooke et al., 2005). They occur within porphyritic subvolcanic calc-alkaline diorite to granodiorite , both in island arcs and on cratonic continental margins (Richards, 2003). Porphyry copper deposits usually develop during several episodes of intrusive activity, hence swarms of dikes and intrusive breccias can be expected (Guilbert and Park, 1999). The alteration effects are visible in both the country and host rocks, a distinctive variation in mineral assemblage occurs within the mineralization (Titley, 1975).
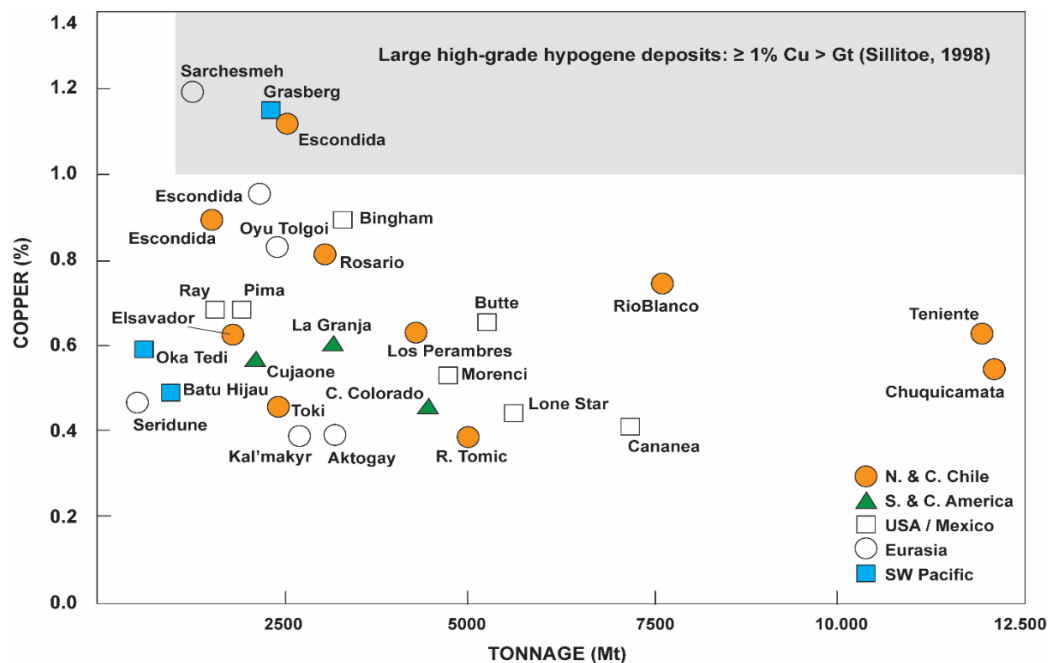
Figure 1. 2 Diagram of copper grade vs. tonnage for the 25 largest porphyry copper deposits showing fields of high-grade, intermediate-grade and low-grade (modified from Cooke et al., 2005).

The arbitrary classification has also been applied to copper porphyries (Sillitoe, 1998): low grade (< 0.5% copper), moderate grade (0.50-0.75% Cu), and high grade (> 0.75% Cu). The 27 largest porphyry copper deposits plotted as a function of resource tonnage vs. copper grades and can be subdivided on the basis of metal grades. The highest grades are found at Sarcheshmeh (Iran), Escondida (Chile) and Grasberg (New Guinea; Cooke et al., 2005; **Fig. 1.2**).

1.6.2 Geotectonic framework

The porphyry copper deposits are commonly associated with convergent plate boundaries and areas of andesitic volcanism (Sillitoe, 1997; Titley, 1975; Sawkins, 1984). Sillitoe (1998) noted that crustal thickening associated with compressive tectonism was synchronous with the formation of giant porphyry copper systems in central and northern Chile, southwest Arizona, Irian Jaya, Batuhijau-Sumbawa and Iran. Most of the porphyry copper deposits form along destructive plate margins, above subduction zones of oceanic crust such as Chuquicamata, Chile and Sarcheshmeh, Iran (Sillitoe, 1998; **Fig. 1.3**).
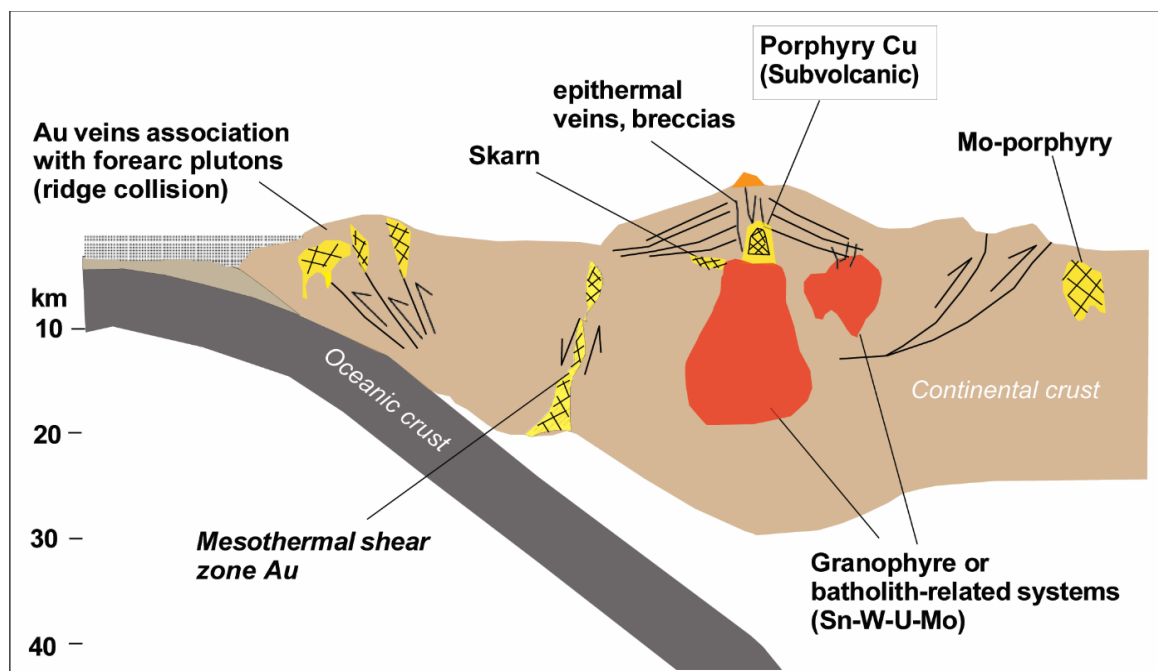
Figure 1. 3 Porphyry copper deposits in the context of plate tectonics (modified from Sillitoe, 1998).

1.6.3 Lithological associations

a. Wall rocks

At many different crustal levels, intrusions related to the porphyry copper-gold deposits are in contact with a variety of wall rocks of different compositions and ages, ranging

7

from Precambrian metamorphic and intrusive rocks, through the Paleozoic-Mesozoic carbonate and clastic-dominated successions to the volcanic rocks of Pleistocene ages (Sillitoe, 2010). The porphyry copper-gold deposits are commonly associated with stocks emplaced at shallow (1-2 km) crustal levels (Sillitoe, 2010) a fact illustrated by widespread preservation of coeval volcanic sequences. The volcanic sequences commonly have andesitic or trachyandesite composition, and in most districts constitute erosional remnants of stratovolcanoes (Sillitoe, 1992; Sillitoe, 2010). In some districts, any coeval volcanic sequences have been eroded entirely, and the stocks are hosted by rocks as disparate as serpentinite at Mamut, gneiss at Skouries and limestone at Ok Tedi and Grasberg. At Ok Tedi, however, the former presence of a stratovolcano is supported by nearby volcanoclastic sedimentary rocks of the Birim formation (Sillitoe, 1992). The compositions of wall rocks strongly control the effects of the hydrothermal processes and perhaps influence the flow of hydrothermal fluids (Sillitoe, 2010). The wall rock composition influences the alteration mineralogy (Sillitoe, 2010).

b. Intrusive rocks

The most common host rocks for porphyry copper deposits are plutonic rocks of granitoid composition, ranging from granite through granodiorite to tonalite and quartz monzodiorite to diorite (Evans, 1993). The series of diorite through monzonite (especially quartz monzonite) to syenite also represents important host rock types. Many authors agree that porphyry copper deposits are normally hosted by I-type granitoids (Babcock, 1995).

1.6.4 Hydrothermal alteration and mineralization

In 1970, Lowell and Guilbert described the San Manuel-Kalamazoo orebody (Arizona) and compared their findings with 27 other porphyry copper deposits (Guilbert and Park, 1999). They are ideally defined as porphyry copper deposits associated with calc-alkaline plutons whose compositions vary from granodiorite to quartz monzonite rocks. Lowell and Guilbert (1977) demonstrated that the distribution of the hydrothermal alteration zones model is the best reference framework for characteristic features of porphyry copper deposits. Generally, the hydrothermal alteration zones usually include orthoclase-biotite (potassic), quartz-sericite-pyrite (phyllic), clay-pyrite (argillic), and chlorite-epidote (propylitic) assemblages (Lowell and Guilbert., 1977). Commonly, the ore minerals include copper and molybdenum sulfides which are found in ore shells within potassic alteration zone **(Fig. 1.4)** (Lowell and Guilbert., 1977)**.** In the following the characteristics of the "classic" alteration types and their associated mineralisation are briefly discussed. Potassic alteration occurs as a result of potassium

metasomatism and may be accompanied by more or less leaching of calcium or sodium from rocks containing original aluminosilicate minerals (Lowell and Guilbert., 1977). Characteristic minerals, which are either introduced or stable as original rock-forming phases include orthoclase, biotite and quartz accompanied by accessory albite, sericite, anhydrite, and apatite (Beane and Titley, 1981). Moreover, the potassic alteration has been divided into the K-feldspar alteration, which is characterized by the appearance of potassium feldspar (as veins or replacement) and the biotite alteration, which is typified by the presence of hydrothermal biotite (White, 1996). The secondary biotite can be distinguished from primary magmatic biotite by its fine-grained, scaly appearance. It typically replaces ferromagnesian minerals such as hornblende or occupies the groundmass of the porphyry stocks (Lowell and Guilbert., 1977). Common opaque minerals in both K-feldspar and biotite alteration zones include magnetite, bornite, digenite-chalcocite, chalcopyrite, and pyrite (Lowell and Guilbert., 1977). Pyrite is mostly minor and antithetic to bornite and magnetite (Lowell and Guilbert., 1977). The potassic alteration commonly occurs in or near the porphyry centers, although a broad aureole of biotite alteration has been observed to pervade igneous wall rocks (Titley, 1975).
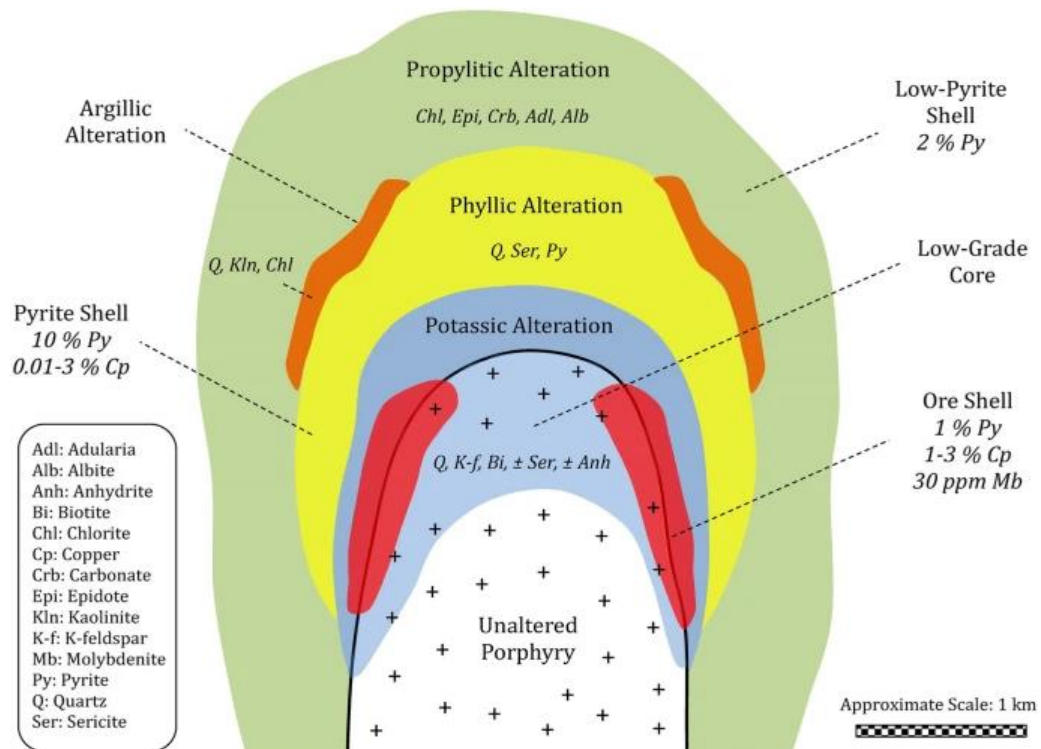
Figure 1. 4 Schematic depiction of a generalized alteration–mineralization zoning pattern for diorite-type porphyry copper systems (modified after Lowell & Guilbert, 1970).

1.6.5 Age relationship

Some of the major porphyry copper-gold deposits are of Tertiary age: Grasberg, Indonesia (3 ± 0.6 Ma by K/Ar on whole rock; MacDonald and Arnold, 1994), Panguna, Papua New Guinea (3.4 ± 0.3 Ma by K/Ar on whole rock; Clark, 1990), Batu Hijau, Indonesia (3.76 ± 0.12 Ma by U-Pb SHRIMP on zircon; Garwin, 2000), Bajo de la Alumbrera, Argentina (7.1 ± 0.03 Ma by Ar/Ar on biotite; Proffett, 2003) and of Quaternary age: Lepanto-Far South East, Philippines (1.4 ± 0.05 Ma by K/Ar on biotite; Arribas et al., 1995), Ok Tedi, Papua New Guinea (1.2 ± 0.2 Ma by K/Ar on whole rock; Rush and Seegers, 1990). However, early Mesozoic deposits are widespread in British Columbia, Canada and even older deposits such as the late Ordovician Goonumbla, NSW Australia (439.2 ± 1.2 Ma by Ar/Ar on sericite; Perkins et al., 1990). Moreover, gold-rich porphyry deposits are also occurred in Archean greenstone belts (Sillitoe, 1992). Therefore, it is concluded that no particular age is characterized by the porphyry copper-gold deposits.

CHAPTER 2
GEOLOGY AND METALOGENIC REVIEW OF EASTERN SUNDA ARC

2.1. SUNDA-BANDA ARC

Generally, the Cenozoic magmatic belt in Indonesia can be divided into six magmatic arcs (Carlile and Mitchell, 1994). The magmatic belt mostly associated with Neogene-aged mineralization, such as Sunda-Banda, Central Kalimantan, Sulawesi-East Mindanao, Halmahera, and the central range Papua (**Fig. 2.1**). Nowadays, the Sunda-Banda magmatic arc is considered a unified magmatic arc, both in the Tertiary magmatic pathway and the present subduction pathway (Katili, 1971; Hamilton, 1979). Research related to magmatism's recent evolution has led to the possibility of segmenting the Sunda-Banda volcanic magmatism and volcanism into several segments (Hall and Sevastjanova, 2012; Hall, 2014). The subduction path in the Sunda-Banda magmatic arc during its evolution can produce magmatism. It may not produce magmatism generally if a back-arc basin is formed, as happened with the Philippine plate (Macpherson and Hall, 1999). That condition has an impact on magmatic activity. In this case, the possibility of the development of magmatism between segments can be very different, and there is a transition period that is quite close between Tertiary and early Quaternary magmatism.
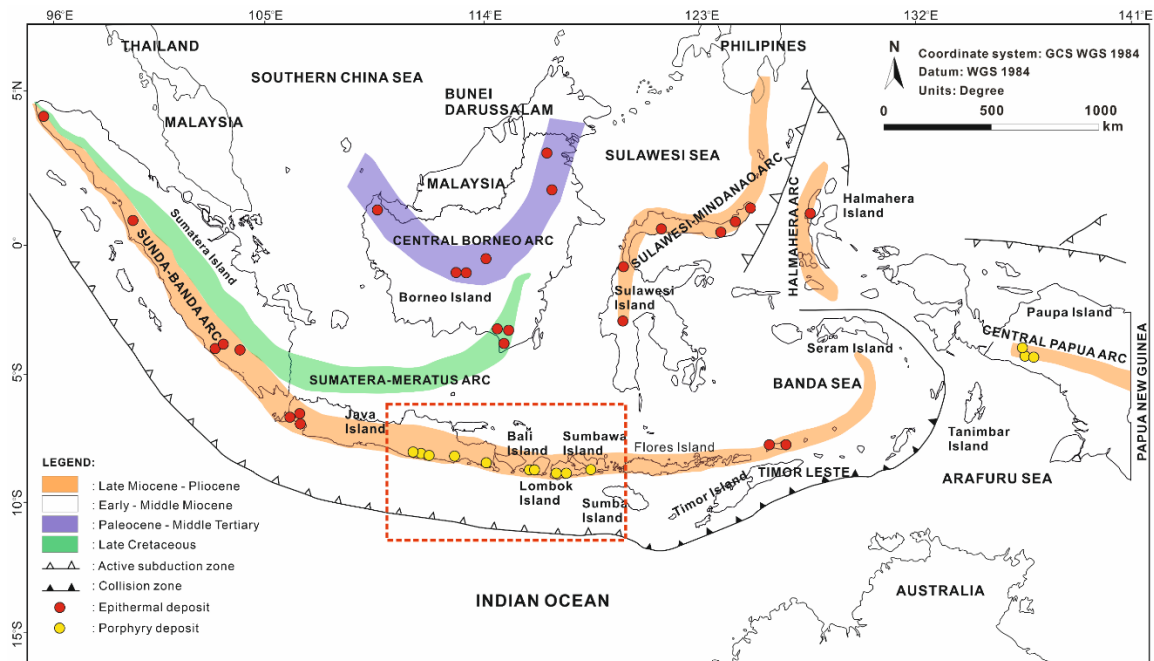
Figure 2. 1 Cenozoic magmatism belt in Indonesian can be divided into the six magmatic arcs (modified from Carlile and Mitchell, 1994). Red box=Eastern Sunda Arc.

The Sunda-Banda magmatic arc results from subduction of three main plates: Eurasian, Indo-Australian, and Pacific. Eastern segmentation such as West Java - East Java was developed from a thick continental plate (Setijadji and Maryono, 2012). The basement rocks from the eastern part of Java were developed by formation as a product from the Australian craton's separation, which later collided with Sunda land, ophiolite fragments, and the accretion complexes Cretaceous volcanic arc (Carlile and Mitchell, 1994). This results in the age of the crust in eastern Java being older and having different characteristics from the western part (Smyth et al., 2008). In Nusa Tenggara, the crustal segmentation formed is much thinner (Maryono et al., 2012). It forms a relatively younger series of magmatism and volcanoes of Plio-Pleistocene age (Maryono et al., 2018).

The Eocene-Holocene Sunda-Banda magmatic belt, reaches 4000 km in length from the northeastern part of Sumatra to Java Island, towards the Banda Islands (**Fig. 2.2**) (Carlile and Mitchell, 1994). This belt is related to the subduction of oceanic crust along Sunda-Banda (Carlile and Mitchell, 1994). The basement rocks in this magmatic arc can be divided into three types, the western part (Sumatra), the middle section (Java), and the eastern part (Banda) (Hamilton, 1979; Katili, 1971). The western part (Sumatra) comprises Eurasian continental rocks that are Mesozoic to late Paleozoic sedimentary rock platforms, which are intruded by Cretaceous granite rocks (Hamilton, 1979; Katili, 1971). The middle section (Java) is composed of Melange and Ophiolites of Cretaceous-Cenozoic age, and the eastern part (Banda) is composed of oceanic crust (Hamilton, 1979; Katili, 1971). Magmatism characteristics in the transition zone (Nusa Tenggara) are probably formed from mantle fusion with water (volatile) (Hamilton, 1979; Katili, 1971). The magmatism originated from dehydration of oceanic crust and mixed with water from sedimentary rock, as established in the Mt. Tambora magmatism system (Hamilton, 1979; Katili, 1971). The location of transition zone between Sunda and Banda is still unknown. The presence of several major north-south trending structures, such as Sumba Fracture (SF), caused a change in subduction patterns after the Java trough and the height of Timor (Audley-Charles, 1975). The Eurasian plate's thickness under Sumatra to Java is around 20-30 km, and about 18 km approaching Bali. The subduction plate includes oceanic crust with ages around 80 Ma to 130 Ma (Plank & Langmuir, 1998; Widiyantoro & van der Hilst, 1996 in Harijoko et al., 2010). Sunda-Banda magmatic belt has a subduction velocity of around 6-7 cm/year (Carlile and Mitchell, 1994; Hall, 2002). The crust characteristics under volcanic arcs in Southeast Asia are still not known with certainty, despite interpretations and

studies of seismic refraction. That is because of volcanic and sedimentary rocks (Smyth et al., 2007). The Eastern part of Java has also been interpreted from the seismic refraction studies for Cretaceous bedrock's existence with character as part of volcanic arcs and ophiolites. However, continental rock's surface outcrops have not been identified yet (Smyth et al., 2007).
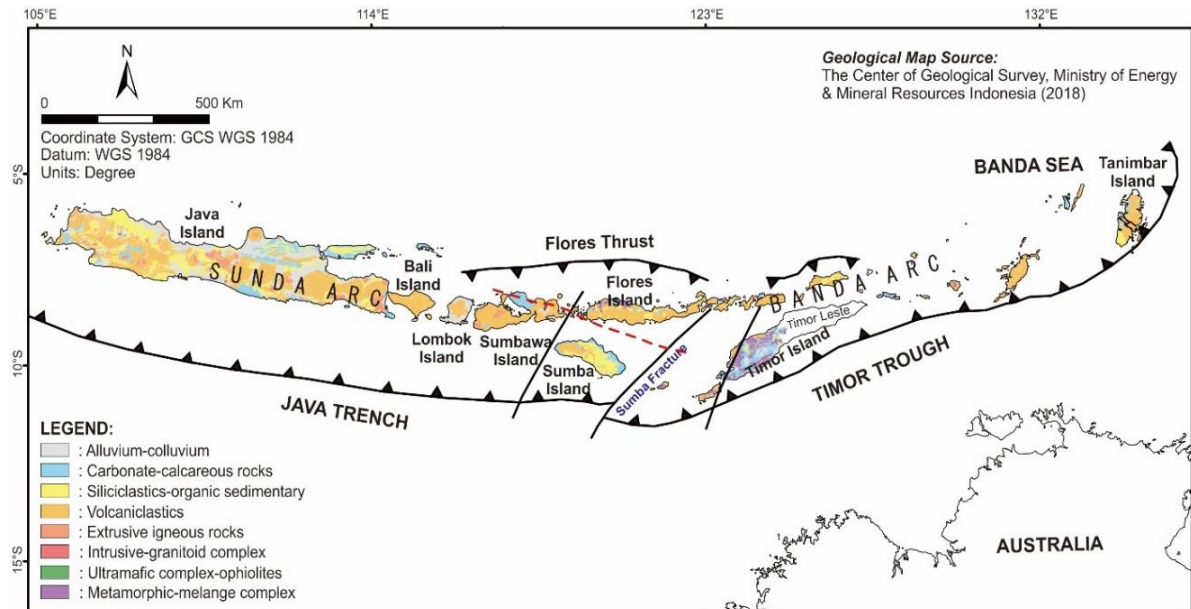
Figure 2. 2 Tectonic map of the Sunda-Banda magmatic belt and Sumba Fracture's presence as a separator between the Java trench as the Sunda and Timor Through as part of Banda (modified from Audley-Charles, 1975). The boundary between Sunda and Banda volcanic arcs is on the islands of Sumbawa and Flores. The red line is *Sumba Fracture 2,* which cuts across the island of Sumbawa (modified from Darman, 2012).

2.2. GEOLOGICAL SETTING OF SUMBAWA ISLAND

The simplified geological map and stratigraphical column of Sumbawa Island have been published by the Indonesian Geological Survey (Suratno, 1994, 1995; Sudradjat et al., 1998) (**Fig. 2.3**). Sumbawa Island has an area of 15.448 km^2 extending east-west for approximately 270 km. Its surface is marked by many volcanoes' mountains, the highest of which is Mt. Tambora (2851m above sea level). Sumbawa Island's morphology and geology are divided into three crustal blocks referred to as western, central, and eastern blocks (Garwin, 2000). They are defined by the Trans-Sumbawa Fault system and northwesterly trending arc-transverse discontinuities (Barberi et al., 1987). The crustal basement of Sumbawa Island consists of the Early-middle Miocene volcanic arc and are related volcaniclastic sequences deposited on oceanic crust, which is adjacent to the margin of the Sunda continental shelf (Barberi et al., 1987). The Indian oceanic floor in southern Sumbawa is Late Jurassic in age. The volcanic crustal thickness ranges from 14-16 km in Batu Hijau's vicinity in the western block to 20-23

km in the Humpa Leu East (Hu'u district and surrounding area) in the central block (Garwin, 2000).

In contrast, the eastern block's crustal thickness is intermediate between the other blocks (Barberi et al., 1987). The greater thickness of the central block is consistent with its downturn concerning Western and eastern blocks (Barberi et al., 1987). The western block's crust thickens to the north, whereas the eastern block's crust thickens to the south (Barberi et al., 1987). It is interpreted that the southern portion of the western block is uplifted and tilted to the north, in the same manner, that the northern portion of the eastern block is uplifted and tilted to the south (Garwin, 2000). In contrast, the down-dropped central and southerly tilted eastern blocks display higher levels of crustal exposure (Garwin, 2000). This hypothesis is supported by the distribution of rock types and the styles of hydrothermal alteration exposed in Sumbawa (Garwin, 2000).
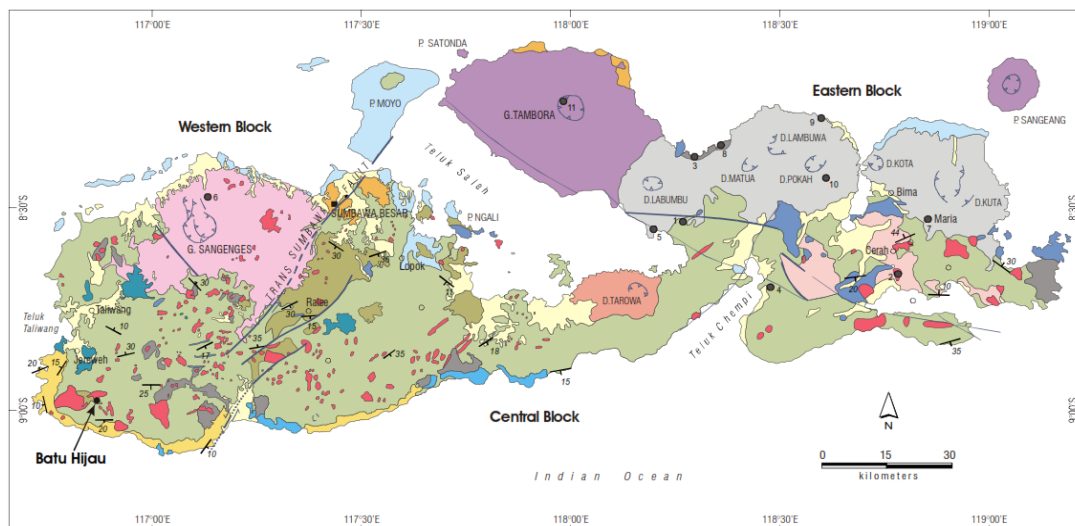
Figure 2. 3 Simplified geological map of Sumbawa Island (modified from Suratno, 1994, 1995; Sudradjat, 1998 and Garwin, 2000).

Sumbawa Island's sedimentary rock units consist of mudstone, sandstone and conglomerate, and coralline- and tuffaceous-limestone. The age of these units ranges from Early Miocene to Holocene (Suratno, 1994; Sudradjat et al., 1998). Four major limestone sequences are recognized based on fossil assemblages and contact relationships underlying volcano-sedimentary and volcanic rocks (Garwin, 2000). The oldest rocks exposed in Sumbawa consist of volcanic sandstone, siltstone, and conglomerate-breccia of basaltic to andesitic composition (Garwin, 2000). This sequence's age is Early to Middle Miocene, constrained based on foraminiferal assemblages in limestone horizons within the sequence

14

(Barberi et al., 1987; Suratno, 1994; Sudradjat et al., 1998). Published geologic maps (Suratno 1994, 1995; Sudradjat et al., 1998) do not indicate this unit's true distribution and locally misidentify it as a sequence of pyroclastic rocks. Plio-Pleistocene volcanic conglomerate-breccia and claystone occupy the coastal regions of western and central Sumbawa and consist of re-sedimented material of contemporaneous and older volcanic centers (Suratno 1994, 1995; Sudradjat et al., 1998). The volcaniclastic sequences lie unconformably upon pre-Pliocene sedimentary, volcanic, and intrusive rocks (Suratno 1994, 1995; Sudradjat et al., 1998).

The oldest limestone sequence exposed in Sumbawa consists of Early Miocene micrite to greenstone, which forms horizons 20-100 m thick throughout the southwestern and southeastern parts of the island (Garwin, 2000). Locally, these horizons are intercalated with volcanic sandstone (Garwin, 2000). The Early Miocene limestone is inferred to have extended east-west and occupied the southern portion of Sumbawa (Garwin, 2000). The Late Miocene to Pliocene limestone forms in the vicinity of Jereweh (up to 100 m thick) and Taliwang in western Sumbawa and the vicinity of Ralee to the east (Garwin, 2000). This unit is sub horizontal to gently dipping, up to 20° towards the south, and lies unconformably upon Middle Miocene and older volcanic and sedimentary rocks (Garwin, 2000). The Pliocene coralline limestone occurs along the southern coastline of western and central Sumbawa. Holocene coral reefs form in portions of the northern coastline and several low-relief islands (e.g., Moyo Island) (Garwin, 2000). The reefs are flat-lying and lie unconformably upon Pliocene and older sedimentary and volcanic rocks (Suratno 1994, 1995; Sudradjat et al., 1998). The limestone dips' variation in western and central Sumbawa's southern coastline indicates an uplift in the Pleistocene (Garwin, 2000).

The two major calc-alkaline volcanic sequences of the Neogene to Early Pleistocene age are recognized in the Sumbawa Island region (Fig. 2.2) (Garwin, 2000). The sequences mostly consist of an Early to Middle Miocene volcanic and volcano-sedimentary succession that includes a large volcaniclastic component (Garwin, 2000). Suratno (1994, 1995) noted the volcanic sequences predominantly as andesitic. Dacitic to rhyolitic compositions, however, occur in the vicinity of Jereweh, Lopok, and Cerah (Suratno 1994, 1995). The andesitic volcanic sequence metamorphosed to lower greenschist facies and commonly contains chlorite, mica, calcite, and epidote (Suratno 1994, 1995). Unit thickness exceeds 1500 m with dips ranging from sub horizontal to moderate. In eastern Sumbawa, the andesitic

volanic sequence is overlain by Middle Miocene dacitic pyroclastic and volcano-sedimentary rocks (Suratno, 1995). The sequences commonly dip less than 20°, but locally the dip up to 45° with thickness exceeding 500 m (Garwin, 2000). The Quaternary volcanoes occupy the northern portion of the island (Garwin, 2000). The volcanoes' alkalinity increases with time; calc-alkaline compositions characterize the Pleistocene volcanoes of northern- northeastern Sumbawa and shoshonitic affinities Sangenges and the historically active Tambora and Sangeang Api (Foden and Varne, 1980; Barberi et al., 1987). The Pleistocene volcanoes are typified by eruptive product of nepheline and leucite-normative leucitite, trachy-basalt, trachy-andesites, and andesite (Foden and Varne, 1980; Barberi et al., 1987), whereas the active volcanoes consist predominantly of nepheline-normative trachy-basalt to trachy-andesite (Foden and Varne, 1980). The radiometric K/Ar ages for lavas of the Quaternary volcanoes range from 1.71 ± 0.05 Ma for Sangenges to 0.043 ± 0.02 Ma for the Tambora base caldera wall (Barberi et al., 1987). In the active Sangeng Api, all whole rocks and minerals are characterized by ^{226}Ra excess. Modeling of the ^{226}Ra–^{230}Th–Ba data suggests that the magmatic evolution beneath the arc volcano occurs on time scales 2000 years (Turner et al., 2003).

Various types of intrusions have also been identified in Sumbawa Island (Garwin, 2000, 2002). They indicate a compositionsl ranging from mafic to felsic. The mapped intrusions in the western block and the western part of the central block are more abundant than those in the eastern block of Sumbawa and the eastern part of the central block, south of Saleh Bay (Garwin, 2000). The affinity of intrusions is calc-alkaline with compositions ranging from diorite or basaltic andesite through quartz diorite and tonalite to granodiorite (Garwin, 2000, 2002). Hypabyssal dacite intrusions intruded the andesitic and dacitic volcanic sequences of eastern Sumbawa. Cross-cutting field relationships and the radiometric determination indicate the intrusions are Middle Miocene to Pliocene in age (Garwin, 2000).

2.3. MINERALIZATION OF SUNDA ARC

In Sunda magmatic arcs, especially in Java and Nusa Tenggara, precious metal mineralization is associated with volcanic centers related to the subduction of Oligocene-Miocene and some to Pleistocene (**Fig. 2.3**) (Carlile and Mitchell, 1994). These types of deposits include the porphyry copper-gold, high-low sulphidation of epithermal, gold-silver-barite-base metal, skarn, and sediment-hosted (Carlile and Mitchell, 1994). The porphyry

deposits type in the Sunda magmatic arc is generally associated with lithocap, epithermal type, and Skarn deposits (Hammarstrom et al., 2010).
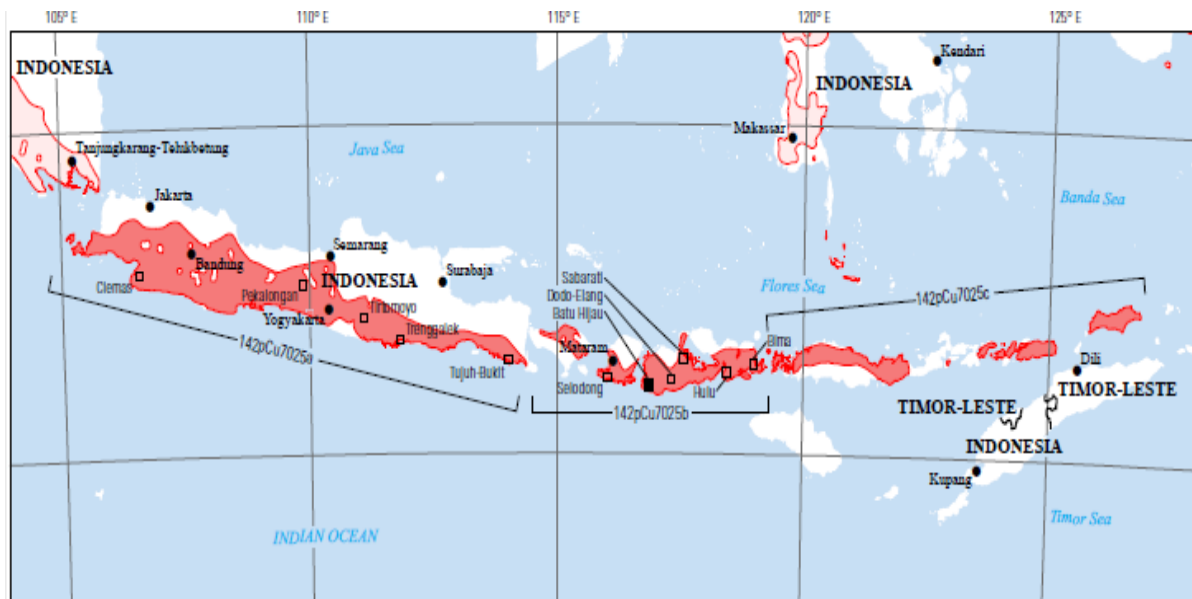
Figure 2. 4 Distribution of gold-copper mineralized deposits in Indonesia in the middle-eastern Sunda magmatism belt (Hammarstrom et al., 2010)

Porphyry deposits in the Sunda-Banda magmatic arc formed at the Eocene-Pliocene. This deposit is associated with porphyry intrusions, such as andesite, dacite, and tonalite (Hammarstrom et al., 2013; Maryono et al., 2018). Calc alkaline magmatism activity has been decreased in the early Miocene and followed by erosion and extensive formation of sedimentation. The presence of mineralization in the Sunda-Banda belt is generally associated with the magmatism of the tectonic of island arc volcanic (Carlile and Mitchell, 1994; Setijadji et al., 2006; Setijadji and Maryono, 2012; Maryono et al., 2018). However, the transition zone between the Sunda arc and Banda arc is on Sumbawa and Flores islands, although its tectonic setting whether it is an island arc or a continental arc is still debated, particularly in the eastern part,. Hamilton (1979) and Katili (1975) suggested that arcs are linked with the continental arcs. Many publications support that statement, including Reubi et al. (2002), Gertisser & Keller (2003), Elburg et al. (2004), Gardner et al. (2013), and Fadlin et al. (2018; 2021). In Sunda magmatic arcs, especially in Java - Nusa Tenggara, the presence of valuable metal mineralization is associated with volcanic centers related to subduction of Oligocene - Miocene such as Selogiri, Trenggalek, and Salakan and some associations with Pliocene-Pleistocene intrusions such as Tumpangpitu, Batuhijau, Elang and Hu'u (**Fig. 2.4**). The porphyry types in

the Sunda magmatic arc are mostly associated with lithocaps, epithermal types, and some form Skarn deposits (Hammarstrom et al., 2013).
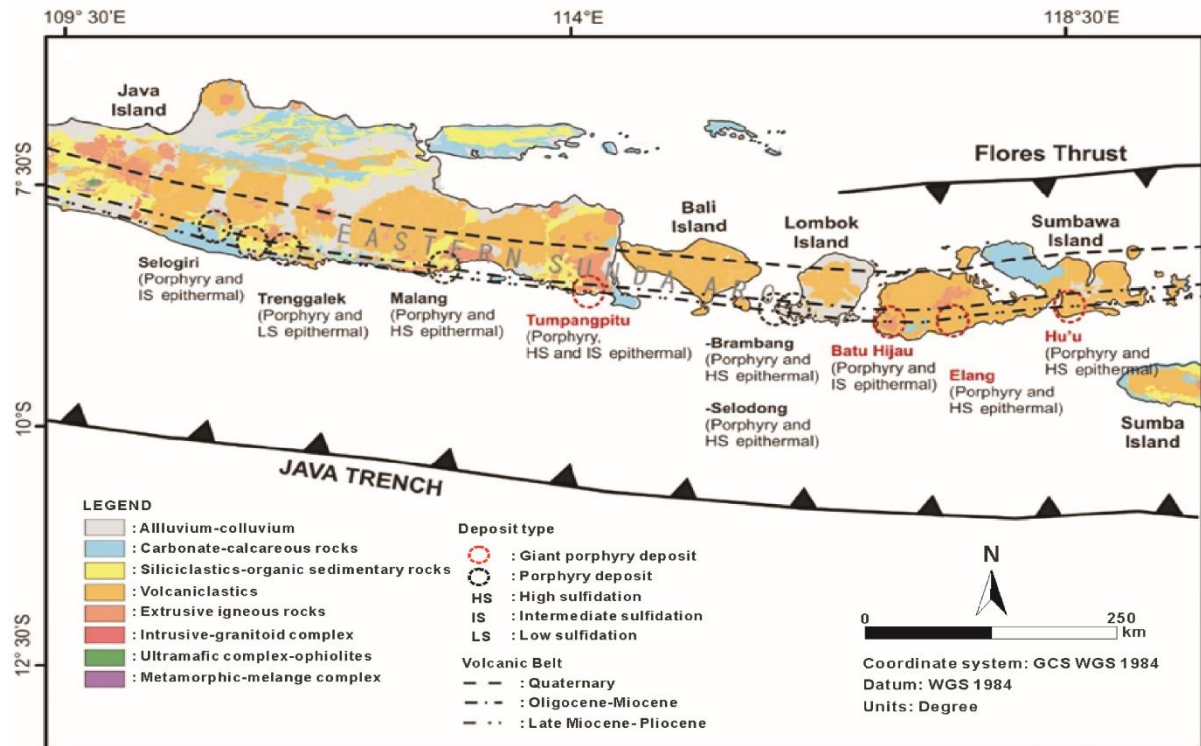
Figure 2. 5 Distribution map of porphyry deposits and their associations in the eastern Sunda belt (modified from Maryono et al., 2018).

The existence of mineralization ages of epithermal deposits in Indonesia are not always younger than porphyry and sometimes not only found in volcanic centers (Setijadji and Maryono, 2012). The presence of gold-copper mineralization in Java, ages, from Miocene to Pliocene-Pleistocene. Initial intrusion (batholit) mineralization are around 5-10 million years ago. A considerable tonnage (300 tons Au and >5 million tons Cu) formed < 5 million years ago. In Batu Hijau, Grasberg, and Tujuh Bukit (Garwin, 2002; Idrus et al., 2009; Maryono et al., 2012; Harrison et al., 2018), the last intrusion carrying mineralization in the Sunda-Banda magmatic arc seems very short in age which is around 30 Ma-860 thousand years (Maryono et al., 2012).

2.4. CHARACTERISTICS OF PORPHYRY SYSTEM IN THE EASTERN SUNDA ARC

In Indonesia, porphyry occurs in Miocene-Pliocene igneous rock with of different type. For example, Grasberg in Papua has a batholith dimension approaching 2 km, with the causative intrusions in the form of quartz-tonalitic diorites (5-3 million years) with the diameter <1.2 km

or <0.62 km^2 (Maryono et al., 2018). The type and size of intrusive rocks are also strongly influenced by erosional levels in each region. In Grasberg (Papua) and Tangse (Aceh) regions, it is seen that volcanic rocks are difficult to find; on the contrary, many intrusions are found, together with sedimentary rocks or old metasediments (Maryono et al., 2018). The Sunda belt shows mineralization occupying district s with predominantly volcanic lithology (volcanic, pyroclastic, diatreme), which are also associated with large dioritic bodies and local causative intrusions or even below the surface (Maryono et al., 2018). In some places, such as in the Trenggalek and Merubetiri regions Miocene-age coral limestone, indicates that volcanism occurred as an archipelago with some distal parts emplaced inseawater. Further to the east, as in Lombok, Sumbawa, limestone is only seen locally near the sea, indicating a more dominant volcanism in land.

The basement of porphyry deposits in the Eastern Sunda arc is dominated by Miocene volcaniclastics, composed of lava and pyroclastic deposits. In other places, they are interrupted by skarn activity, such as in Batuhijau (Idrus et al., 2009). In the Java island sector, there are turbiditic sedimentary rocks, such as in Tujuh bukit (Tumpangpitu), which likely below the surface with Middle Miocene age (20.67 - 16.68 million years) and partly broken through the causative intrusion around 5 meter in thickness (Harrison et al., 2018). In the eastern region, the presence of basement has not been found. That indicates a difference in the crust beneath the surface. The Selogiri area contains metamorphic rocks on the surface while further to the east Merubetiri metamorphic outcrops have not yet been found (Sutarto, 2016). In this case, there may be differences in basement characters between the islands of Java and Nusa Tenggara. In the eastern Sunda arc, porphyry deposits are related to the Miocene igneous and volcanic rock complex. They are hosted in middle Miocene (Selogiri, Trenggalek) and Pliocene (Batu Hijau, Elang, Tumpangpitu) igneous rocks (Maryono et al., 2018).

2.4.1. Causative intrusion

Porphyry Cu systems are formed primarily on the magmatic arc belt (including back-arc), leading to the spectrum of regional-scale stress formation regimes or apparent to extensional from oblique-slip to contractional positions. In extensional settings, bimodal magmatism is usually formed, namely basalt-rhyolite, directly related to porphyry (Sillitoe and Hedenquist, 2003). Tectonics play an important role in forming porphyry systems, such as the presence of faults and intersections between faults that affect the size and geometry of the Cu porphyry system (Sillitoe and Hedenquist, 2003). An active intra-arc fault system is controlled

the formation of Cu porphyry (Sillitoe, 2010). Several investigations on this matter have been carried out outside Indonesia, such as porphyry in Archibarca and Calama-El Toro in Chile (Richards, 2009), Lachlan in New South Walen (Gaetani and Grove, 1998), as well as New Guinea (Corbett and Leach, 1998). The structur controlled may affect the basement rocks and facilitate magma of a specific size in the Porphyry Cu system.

Porphyry systems and their associations generally form clusters that reach a 5-30 km diameter, depending on the magmatism and volcano system (Sillitoe and Bonham, 1984). The size of the system can also be seen from the influence of the presence of a cupola from a batholith or intrusion body, which then affects the distance between deposits which usually reaches 100-1000 m (Sillitoe, 2010), which can also cause surface alteration systems or commonly called footprints that vary in extent.

Porphyry deposits in Eastern Sunda develop in association with tholeiite and calc-alkaline magmatism, which is generally formed in subduction zone to form island arcs or transitions (Setijadji and Maryono, 2012). Porphyris in Indonesia are more likely to form Copper (Cu) deposits, followed by Au with Cu (wt%) : Au (ppm) = 1, meaning about 1% Cu and 1 ppm Au in its porous ore. The Cu / Au ratio values in porphyry deposits in Indonesia are as follows: Batu Hijau (1.26), Selogiri (0.3), Tujuh Bukit (1), Tapadaa (7.9), Tombulato (1.02), Mamut (0.96), Kapentian (1.32) , and Grasberg (0.94). In Batu Hijau, the tonalitic series is formed very quickly in about 90-160 thousand years, from 3.76 ± 0.12 million to 3.67 ± 0.10 million (Garwin, 2002). Idrus et al. (2009) mention that mineralogy in intermediate and young tonalites is very similar, characterized by the presence of phenocrysts of hornblende, plagioclase, quartz, biotite, magnet, and ilmenite. The phenocrysts are between the base with medium-coarse-sized textures. Plagioclase is the main phenocryst of 3-4 mm in size, followed by quartz bipyramids of 2-6 mm. The main mafic mineral present is a coarse-sized hornblende, which is locally rimmed by biotite. Intrusive rocks are carrying mineralization such as tonalite usually form in the bodies of equigranular - sub porphyritic diorite batholith mainly composed of labradorite - andesine plagioclase (reaching 70%) measuring 1-3 mm and quartz (5-15%) measuring 1 mm, and mafic minerals in the form of hornblende> pyroxene (Idrus et al., 2009). The batholith body's size varies between prospects, depending on the removal and stripping mechanism before the porphyry process occurs. Batholith rock age generally has a difference of 2-3 million years, to the causative intrusion, as in Tujuh Bukit aged 5.81 ± 0.20 - 5.18 ± 0.27 Ma (Harrison et al., 2018) or in Batu Hijau aged 5.9-3.7 Ma (Garwin, 2002; Imai and Ohno,

2005). In general, the porphyris in Indonesia are Miocene-Pleistocene. For example, the ages of volcanism in Batu Hijau yield 15-6.9 Ma, while the causative intrusions related to the Cu-Au Porphyry mineralization formed at 3.7 Ma (Garwin, 2002).

2.4.2. Diatreme breccia

Diatreme breccias are associated with all porphyry deposits in the eastern Sunda arc, as a post intrusion process (Maryono et al., 2018), developing into high sulfidation epithermal deposits Tumpangpitu or as alteration, feeders to form lithocaps such as Batuhijau, Elang, and Hu'u. In other cases, the diatreme formation serves as the beginning of the mineralization as control of meteoric water and sulfidation processes (Wilkinson, 2018). The eastern Sunda's porphyry deposits are always associated with the diatreme and phreatomagmatic breccia. However, it still leaves questions about genetics and the relative time of its formation.

Many terms are used to describe diatreme, maar, and related deposits, as well as with kimberlite (White and Ross, 2011). However, concerning porphyry deposits, are mostly related to the diatreme-maar volcano eruption terminology formed as part of the volcanism process. Diatremes can form pipes or diatreme structures that mean all removal of the original rocks in the root zone, diatreme fill and post-eruptive deposits (Geshi et al., 2011; White and Ross, 2011). Diatreme can also be phreatomagmatic, formed by an explosion caused by contact with surface water (aquifer) and magma (feeder), which follows a weak zone and is usually formed after the caldera as happened in the Suoana Crater part of the Kuwanodaira Caldera, Japan (Geshi et al., 2011). Phreatomagmatic breccias are generally formed after mineralization which is proven from the position and fragmentation of breccias that are seen cutting through mineralized intrusion bodies such as those found in Elang, Rinti, Batu Hijau, Selodong, Brambang, Tumpangpitu, Binglis, Trenggalek, and Selogiri (Maryono et al. 2018). The size of diatremes varies from 0.15 km^2 in the Brambang area to 6.8 km2 in the Tumpangpitu area, which generally forms an inverted cone. The age of diatreme breccia is estimated to be younger than the intrusion of about 2.7 Ma in Tumpangpitu (Harrison et al., 2018). The diatreme of Elang Deposit formed around 2.1 Ma (Maryono et al., 2018). The diatreme breccia which associated with the porphyry deposit are generally has advanced argillic alteration formed at the under high temperature and low pH conditions (**Fig. 2.6**) (Maryono et al., 2018).
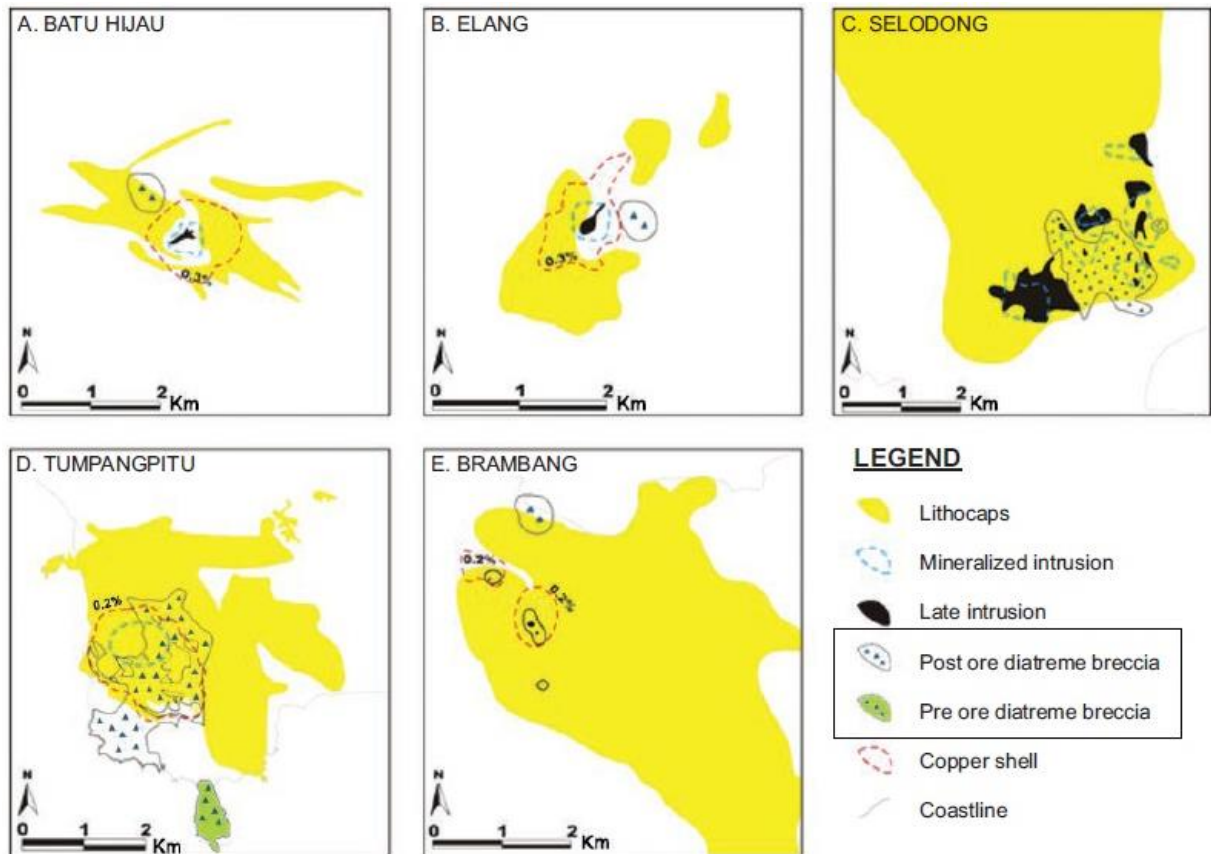
Figure 2. 6 Comparison of Lithocap area and diatreme breccia position in porphyry deposits in Eastern Sunda (Maryono et al., 2018).

2.4.3. Porphyry alteration and mineralization

The porphyry mineralization system is affected by a hydrothermal magmatic system that is characterized by the mineralization-carrying intrusion, fluid exsolutions from cooling magma, followed by progressive mixing of meteoric water (**Fig. 2.7**) (Corbett and Leach, 1998). It is difficult to determine a generalized model of hydrothermal alteration in the porphyry systems because each prospect has different characters. However, it can be summed up into two main stages, namely: prograde and retrograde (Corbett and Leach, 1998). The prograde stage is associated with the placement and cooling of the melt at shallow depths (< 2 km), with heat originating from a large magma apophysis and magmatic fluid and metal exsolutions from the top of the porphyry stock (Corbett and Leach, 1998). At this stage, potassic and propylitic alterations are formed, followed by the development of advanced quartz and argillic veins if there is contact with the surface (Corbett, 2009). The retrograde stage affects the minerals when cooling intrusion towards extension out of the main stock body, and the surrounding rock forms a metal depositional environment (Corbett and Leach, 1998). Most porphyry systems are

formed in this environment, namely at 250-350 ° C (Skinner, 1997; Corbett and Leach, 1998; Naumov et al., 2017).
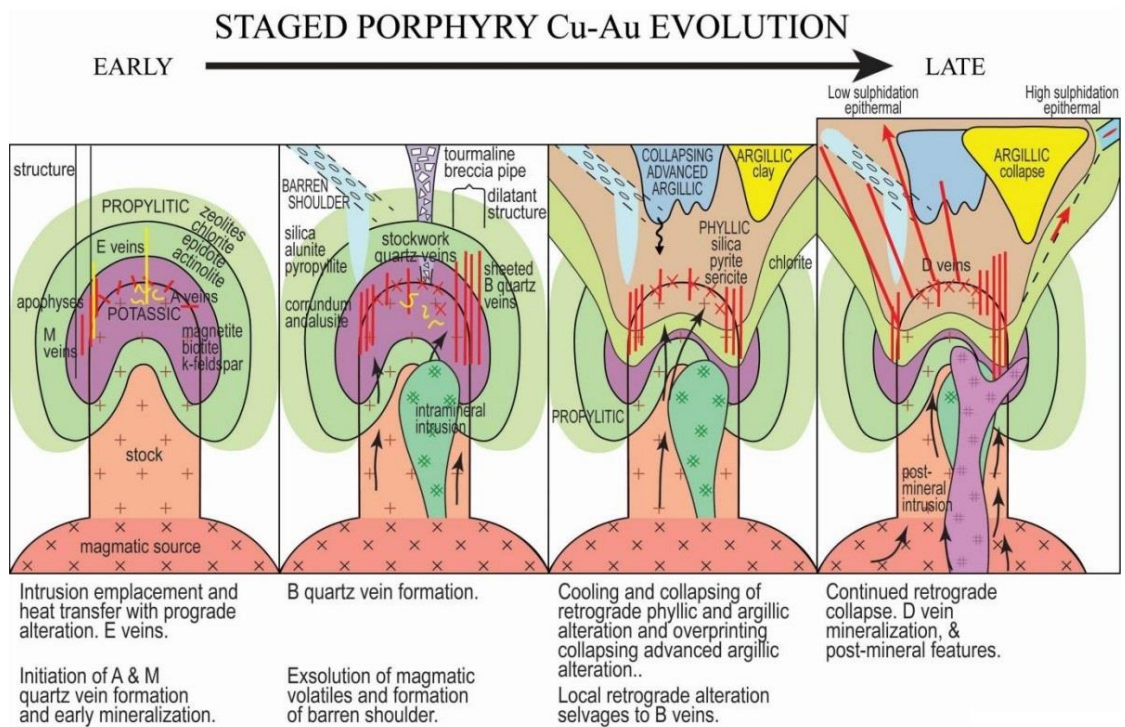
Figure 2. 7 Evolution of hydrothermal alteration in the initial (prograde) phase and the late phase meets the epithermal system (Corbett and Leach, 1998).

Hydrothermal alteration in porphyries is inseparable from quartz vein/veinlet formation at each stage, followed by the mineralization (Corbett and Leach, 1998). The hydrothermal alteration process develops from prograde to retrograde, also commonly called the early, transitional, final, and very late stages (Corbett and Leach, 1998). A good example is Batu Hijau, where the alteration sequence can be seen both spatially and mineralogically defined (Idrus, et al., 2009). Some of the hydrothermal alterations in the porphyry system in Indonesia are associated with the presence of skarn alteration even though they are small in size (Batu Hijau: Idrus, et al., 2009) or in very large size and form separate ore deposits such as in Grasberg, Papua (Pollard and Taylor, 2002; Sevirajati et al., 2017). The hydrothermal alteration area of the porphyry system (prograde) is highly dependent on the size of the existing intrusion, such as Tumpangpitu (1,200 m wide; > 400m deep, Batu Hijau (600 m wide; 800 m deep), and Selogiri (300 m wide; 450 m deep).

Porphyry deposits in Indonesia generally still occupy the surface level, and are associated with volcanic rocks, such as tuffs and trachytic rocks in Grasberg (Sevirajati et al., 2017), which probably originated from a Maar volcano (MacDonald & Arnold, 1994). In other

23

areas, the porphyry body is still visible below the surface with the upper part in the form of pyroclastic rocks or diatreme, such as Tumpangpitu Pitu (Harrison, R., 2012; Hellman, P., 2011) and Batu Hijau (Idrus et al., 2009). The general condition of porphyries in Indonesia are related to the shallow system. Other types of economic mineralization associated, such as high sulfidation epithermal (Tumpangpitu, Harrison, 2012; Hellman 2011) and epithermal intermediate sulfidation (Selogiri, Sutarto, et al., 2015). In general, porphyry type mineralization in Indonesia is near the surface (Sillitoe,2010). The Eastern Sunda porphyry geological model has been developed by Maryono et al. (2018), which states that porphyry mineralization develops on tonalitic intrusion rocks which are small (<1km), multiphase, and gather as intrusion complexes (small, multiphase, nested tonalite intrusive complexes). Generally, 3 phases of tonalitic intrusion are formed, followed by potassic and propylitic alterations and formed mica-sericite alterations near the surface, as well as advanced argillic and argillic alterations at the surface, which make up the lithocap (Maryono et al., 2018). The presence of diatreme breccias indicates that there is a productive porphyry system in an area (Maryono et al., 2018).

CHAPTER 3
METHODOLOGY

3.1. STAGES OF STUDY

In general, this study was conducted in three stages, including desk study, fieldwork, and laboratory work. The desk study mainly covers literature review. Fieldwork include out crops investigations, core logging, and rock sampling. Laboratory work includes petrography, ore microscopy, whole rock geochemical analyses, mineral analyses, sulfur isotopes, fluid inclusions, U-Pb dating and zircon trace element analysis. All of the data and information were processed, evaluated, calculated, and interpreted to fulfill the study's objectives.

3.1.1 Desk study

The literature reviews include previous works on regional geology, volcanism and magmatism, and the study area's geology and mineralization. The regional geology and tectonics of Hu'u district , Sumbawa Island, and its surroundings were studied to understand the geological background. Literature review also included aspects of petrology, mineralogy, hydrothermal ore deposits, whole rock geochemistry, mineral chemistry, sulfur isotopes, fluid inclusions, geochronology, and their significance to understanding the characteristics of porphyry Cu-Au prospect in the research area.

3.1.2 Fieldwork

The fieldwork activity was aimed at identifying alteration and mineralization characteristics in the research area. The priority of this fieldwork was to further investigate the occurrence of potassic alteration which has been observed during drilling activities in the HLE prospect area. The HLE prospect area has challenging access due to remoteness of the area, therefore we must use helicopter to reach the target mapping area.

3.1.3 Laboratory works

There are several methods that I used to reach the research objectives, which include petrography (silicates and ore mineral identification), whole-rock geochemical analysis (X-Ray Fluorescence Spectrometry (XRF), and Inductively Coupled-Mass Spectrometry (ICP-MS)), mineral chemistry analysis (Scanning Electron Microscope (SEM) and Electron Probe Micro Analysis (EPMA)), Raman spectroscopy, sulfur isotope analysis. These analyses were carried out at the laboratory of Economic Geology, Department of Earth Resource Science, Graduate School of International Resource Sciences, Akita University, Japan. In addition, zircon

geochemistry and geochronological study (U-Pb dating) was conducted at the University of Johannesburg, South Africa.

1. Petrography

For optical microscopy, I used 30 µm polished thin sections and polished epoxy-mounted rock chips (here referred to as polish sections), in order to determine the mineral assemblage of rock and vein samples using a Nikon ECLIPSE LV100N POL. The transparent to translucent minerals were observed using transmitted light polarization microscopy. Polished sections were used for the opaque mineral observation using reflected light polarization microscopy. Petrographic analysis was used for classifying the type of rocks, veins, and texture of minerals for more advanced analyses, e.g., SEM-EDS/CL, Raman spectroscopy, EPMA, LA-ICP-MS.

a. Thin section or polished thin section

Sections of rock and vein samples were cut and ground until they were 0.03 mm thick. After that, the thin section sample was polished with diamond polishes of 3 m and 1 m. A total of 60 selected rock samples from the different alteration zones was prepared as thin sections.

b. Polished section

Samples rich in sulfide minerals were prepared for reflected light microscopy observations. To facilitate mounting the samples into SEM and EPMA specimen holders, approximately 1 cm thick polish sections were made. Additionally, the polish section samples were polished by 3 µm and 1 µm diamond paste until the sulfide minerals could be observed. A total of 23 selected rock and vein samples from the different stages and alteration zones was prepared and observed.

2. Whole-rock geochemistry

Geochemistry analysis was performed using two methods: X-ray fluorescence (XRF) and Inductively Coupled Plasma-Mass Spectrometry (ICP-MS). A total of 37 selected rock samples from the different stage and alteration zones was analysed.Before these analyses, LOI measurements were made, where 1.5 g of pulverized sample was put into a crucible and dried inside a DX 400 Drying oven at 110 °C for 12 hours. Then, the weight of the sample was measured (H_2O-data). After that, the sample was heated at temperature of 900 °C for four hours using an Electric Furnace 1500-Plus. After drying in the furnace machine, the weight of the sample was measured again (H_2O^+data). The loss on ignition (LOI) value was calculated using this formula [(H_2O^+)/initial sample weight] * 100%.

26

a. XRF analysis was conducted with a Rigaku machine to determine the concentration of major oxides and several trace elements (V, Zr, Ni, and Zn). All of the rock samples from HLE prospect were prepared as pressed powder pellets because they contain sulfide minerals (>1 wt.% sulfur). First, I prepared approximately 10 g of powdered sample and poured it into the sample ring. Next, the sample was pressed using a press for about one minute. Pressed pellets were stored inside a desiccator to keep samples dry.

b. The ICP-MS method was used to analyze the trace element (including metals Ag, Cu, Sb, etc.) concentrations, using an Agilent 7500 Series ICP-MS machine. First, 0.1 g of sample powder was prepared with the sample standard (JA-2). In this research, two sample preparations were carried out, [1] HNO_3 dilution for trace elements and metals (except Au) and [2] Aqua regia dilution for Au. The sample treatment used in this research was 10,000 times dilution, and 2,000 times dilution were divided into two dilution processes. The first dilution process was performed by adding 4 mL of $HClO_4$, HNO_3, and HF to dissolve rock powder. Then, this solution was diluted 1000 times by adding distilled water. The second dilution was performed by adding 8.5 mL of distilled water and 0.5 mL HNO_3 to 1 mL of 1000 times-diluted sample. The dilution procedure for aqua regia dilution is the same process as HNO_3 dilution, by replacing HNO_3 with aqua regia in each stage.

3. SEM-EDS/CL ANALYSIS

Scanning Electron Microscope with Energy Disperse Spectroscopy (SEM-EDS) analysis was used for qualitative mineral identification of polished samples using an Oxford Instrument JEOL JSM-6610 SEM-EDS. This study used this method to clarify the causative intrusions mineral assemblage, including rock-forming minerals, alteration, and ore minerals. Furthermore, CL (Cathodoluminescence) with Gatan MONO CL4 detector was used to understand the zircon internal textures. The samples were C-coated.

4. EPMA

The Electron Probe Micro Analyzer (EPMA) analysis can use polished samples to quantify the mineral compositions of individual minerals. A JEOL-JXA 8230 electron probe micro analyzer was used for this analysis. A total of 8 selected polished and thin section samples were selected to analysed.

5. Sulfur isotope analysis

This method was conducted using a DELTA V advantage (IRMS), Thermo Fisher Scientific. Approximately 20 mg of sulfide and sulfate minerals was picked and diluted. Sulfide

minerals samples was dissolved by adding 20 mL HNO_3 and 2mL bromine and heated up on a hot plate for one day. Later, 10 mL HCl and 90 mL of distilled water was added to the solution.

Filtration was conducted, to eliminate any precipitation at the bottom of the beaker. After that, cation exchange procedure was performed by passing the sample solution through the cation exchange column to separate S from the other elements. Afterward, 10% $BaCl_2$ was added to the sample solution until it reached about 300 mL. Sulfate minerals were diluted in 20 mL HNO_3. After one-night heating on the hot plate $BaSO_4$ was formed. This $BaSO_4$ was filtered using 0.25μm filter paper. After one night drying of filter paper, about 4-5 mg precipitated $BaSO_4$ and 5-6 times V_3O_5 sample weight was added into atin capsule. A total of 22 selected sulfide and sulfate minerals were analysed.

6. Fluid inclusion analysis

Microthermometry analyses of the fluid inclusions from 4 doubly polished thin sections representative of the different alteration stages were performed to record the temperature of homogenization and determine the salinity of fluids. Microthermometry was conducted using a LINKAM THM 600 heating-freezing stage and LINKAM THM 600 (high temperature) heating equipped. The heating rate of employed to observe the phase change was 0.1–5 °C/min.

7. Laser Raman spectroscopy

Raman analysis of fluid inclusions in quartz veins was performed to identify the fluid compositionusing a Renishaw inVia Raman microscope . Background subtraction was performed in the Wire 4.0 software. Invisible D2 and D3 bands were manually processed using the gaussian method in the Peakfit 4.2 . This analysis was focused on vapor to detect the occurrence of CO_2. Four selected fluid inclusion samples which represent the stage of mineralization and alteration zones.

8. U-Pb dating and zircon geochemistry

The U-Pb isotope compositions of zircon was analysed by LA-ICP-MS. Between 15 and 70 grains of zircon were analyzed per sample. The samples collected from all causative intrusions (diorite porphyries) are representative of multiple intrusion phases (early, intermediate, and late) at the HLE prospect. Approximately 2 kg of diorite porphyry from three borehole samples (VHD006/500-502, VHD009A/250-252, and VHD001R/600-602) were crushed and milled to < 300 μm. Zircon grains were then separated using conventional techniques: panning, magnetic separation, and heavy liquid separation (using sodium polytungstate) before handpicking under a binocular microscope. The zircons were mounted in

epoxy resin and polished to expose their interiors. Cathodoluminescence (CL) and backscatter images were taken to examine zircon morphology and internal textures using a JEOL JSM-6610 SEM with Gatan Mono CL4 CL detector at the Department of Earth Resource Science, Akita University, Japan. Furthermore, transmitted light microscope images were taken to observe the inclusion's mineral compositions. All these images were used to select areas with no cracks and inclusions for laser ablation analyses. The zircon U–Pb dating, and zircon trace element analysis was conducted at the Laboratory of Geochronology, University of Johannesburg, South Africa. The weighted mean age was calculated using Isoplot/Ex_ver4.15 (Ludwig, 2003).

3.2. DATA ANALYSIS

The result of laboratory analysis from rock samples that have been taken can be a number, images, or graphics **(Table 3.1)**. Numerical data processing was performed on individual and/or group samples using simple statistics such as scatter plots, schematic plots, histograms, smoothing, and residual plots. Furthermore, to interpret the data, it can be done by observing the population and the number of samples, the median or mean of the data, and the covariance and the variation of the data. At the end, the data were processed and evaluated to be a final data according to our proposed. The flowchart of the analytical method carried out in this study is illustrated in **Figure 3.1**

Table 3. 1. The methodology, type, and result of an analysis

No	Method of analysis	Sample type	Preparation type	Result of data analysis			
				Type	Figure	Value	Chart
1	Petrography and ore microscopy	Fresh/least altered rock	PTS	Silicate mineral in % volume, texture, and ore mineral			
2	Whole-rock geochemistry (XRF and ICP-MS)	Fresh/least altered rock	RP	Major element and trace element			
3	EPMA	Silica and ore mineral	PTS/PS	Mineral chemistry in % vol.			
4	SEM-EDS/CL	Silica and ore mineral	PTS/PS	Mineral chemistry in % Vol, internal and external texture mineral			
	Microthermometry	Fluid inclusion	DP	Phases, Temperature, and Salinity			

5	Raman Spectroscopy	Fluid inclusion	PTS	Mineral band			
6	Sulfur isotope	Sulfide and Sulfate mineral	SG				
7	U-Pb dating and zircon geochemistry (LA-ICP-MS)	Zircon mineral	SG	Age of magmatism, trace element (ppm)			
Description:							
Preparation type				**Sample type**			
PTS (Polish Thin Section)				RP (Rock Powder)			
PS (Polish section)				SG (Selective grain)			
DP(Double Polish)							

3.3. ORGANIZATION OF THE THESIS

The thesis structure was organized into seven chapters. **Chapter 1** focuses on the outlines of this study: background, major objectives of the research project, a previous study of the research area, location and access of the research area, ownership of the prospect area, and include the exploration history. **Chapter 2** provides a background to the geology, magmatism, and tectonic setting of the eastern part of Sunda Magmatic Arc, particularly Sumbawa island, and the regional setting of host rocks of the Hu'u prospect also is given. **Chapter 3** describes desk study, fieldwork, methodology, and thesis organization**.** A description of the lithology, alteration, and mineralization characteristics of the Hu'u district will be given in Chapter 4. This chapter also describes the geological framework, alteration, mineralization, and the petrogenesis. **This chapter** addresses the study of whole-rock geochemistry of igneous rocks, including major element geochemistry, trace element geochemistry, and REE-immobile element geochemistry characteristics, which provides an insight into a magmatic characteristic of the Humpa Leu East prospect. **Chapter 5** will describe the fluid inclusion, Raman spectroscopy, and sulfur isotope, chlorite, and quartz chemistry for understand the temperature formation and fluid hydrothermal evolution. Finally, a geochronology study of the HLE prospect and magma fertility assessment will be explained in **Chapter 7**.
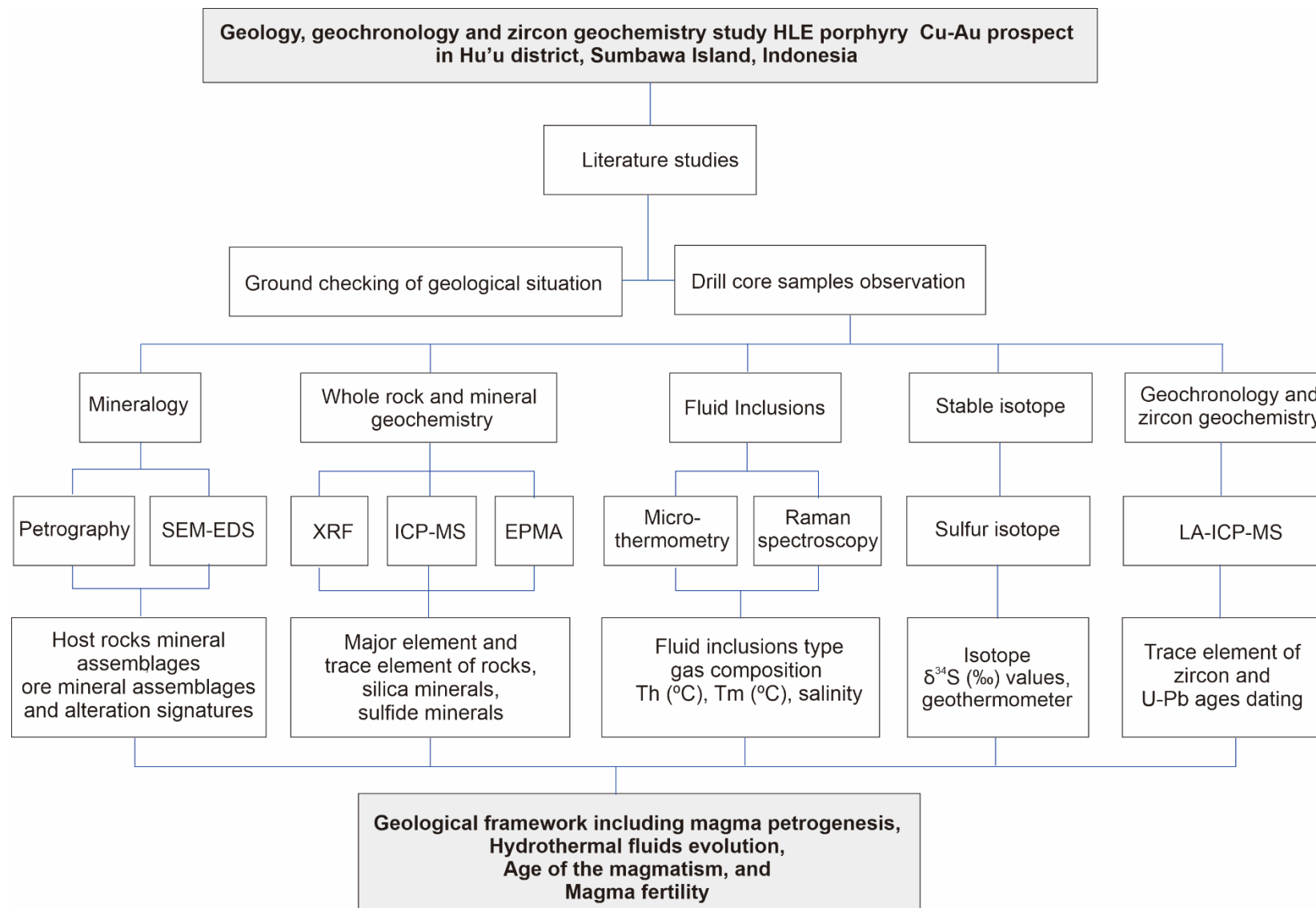
Figure 3. 1 The flowchart of the analytical method carried out in this study

CHAPTER 4

GEOLOGY, ALTERATION, AND MINERALIZATION OF HLE Cu-Au PROSPECT

4.1 INTRODUCTION

The geology of the Hu'u district includes the eruptive products of Puma and Wawosigi volcanos (Sundhoro et al., 2005), and is surrounded by lowlands and coastal plains. The maximum elevation in the Hu'u district is about 1020 meters above sea level. Generally, the rocks of Hu'u district consist of andesite lava and breccias with inserts of sandy tuff, tuff, and tuffaceous sandstone (Ratman & Yasin, 1978; Sudrajat et al. 1998). The age of the Puma lava has been determined by fission track as Upper Miocene (5.8 ± 0.2 Ma; Sundhoro et al., 2005). Based on the geological mapping (PT. Sumbawa Timur Mining, 2018) and Landsat imagery, the Hu'u district can be grouped into eleven lithology units **(Figure 4.1).**
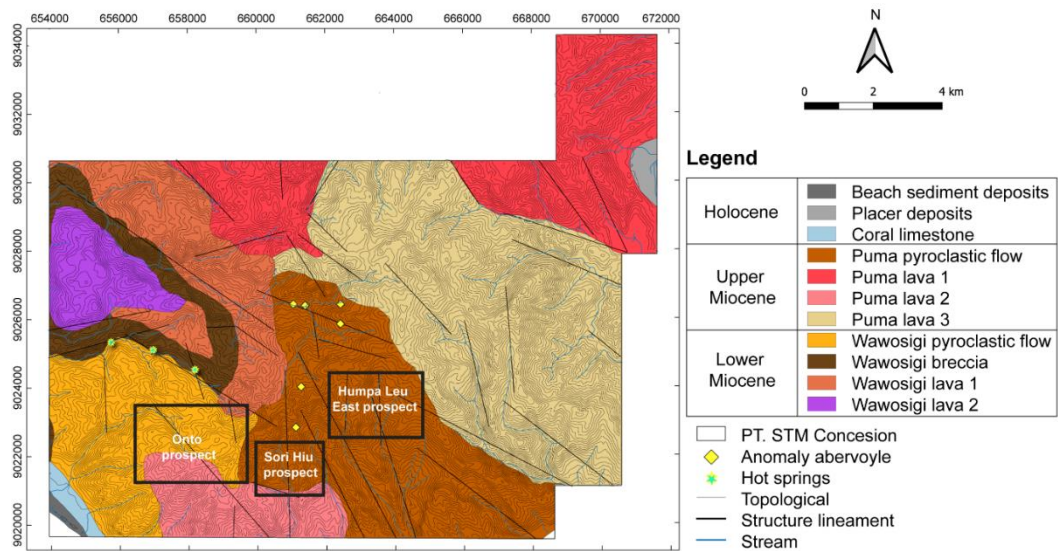
Figure 4. 1 Geology map of Hu'u District (*modified from* Sundhoro et al., 2005).

The presence of a hydrothermal system is proven by the argillic and advanced argillic alterations, which extend for 48 kilometers square (Maryono et al., 2018). Surface alteration in volcanic rocks such as tuff, andesite (Febriansyah et al., 2014), and diatreme breccias (Maryono et al., 2018) commonly occurs at Puma volcano. The hydrothermal alteration in the research area is related to late Miocene-Pleistocene dioritic magmatism, which can be divided into three phases: early phase, intermediate phase, and late phase. All phases carry mineralization (Maryono et al., 2018). The porphyry copper-gold mineralization at Hu'u district is proven by the presence of veins **(Table 3.1)** (Maryono et al., 2018)**.** The hydrothermal system is currently still active on the east and south sides of the Hu'u district, which is proven by the manifestation

of hot spring water with a temperature of about 32.0 - 46.1 °C and a neutral pH (6.5-7.3). In the Limea region, there is also a hot spring manifestation with a temperature of about 80 °C and acidic pH (2.1-2.7) (Sundhoro et al., 2005). The Hu'u district has both of porphyry Cu-Au and geothermal energy potential, which can have an economic value like the Lihir deposit, Papua New Guinea (Van Leeuwen, 2018).

Lithologically, the HLE porphyry Cu-Au prospect consists of volcanic rocks such as andesitic tuffs, crystalline tuffs, volcanic breccias, subvolcanic intrusions, diorite, and andesite lava (PT. STM 2018). The presence of spotted diorite porphyry is controlled by the reverse faults (PT. STM, 2018) (**Fig. 4.2**). Five hydrothermal alteration types are present at the surface: potassic, propylitic, advanced argillic, intermediate argillic and argillic (PT. STM, 2018) (**Fig. 4.2**). The distributions of the potassic alterations are spotted, which is focused on the center of the prospect area, and the distribution of this alteration varies from 50 to 250 meters (PT. STM 2018). Meanwhile, propylitic alteration is most widely spread in the northeast and also distributed in the eastern and western parts of the prospect area (**Fig. 4.2**) (PT. STM 2018). This alteration has an approximately 1 km in distribution. Advanced and intermediate argillic alterations are only scattered in the middle and bordered by potassic and propylitic alterations. Alteration has probably been controlled by a south-north fault (PT. STM 2018). The argillic alteration was found throughout the prospect area, spreading approximately 2 km (**Fig. 4.2**). Chlorite-sericite and sericite alteration was not found at the surface (PT. STM 2018). Diatreme breccias are also distributed in the HLE prospect over an area of approximately 500 m with a southwest-northeast orientation (PT. STM 2018). Diatreme breccia in the HLE prospect formed post intrusion, which is proven by the presence of intrusive rock as fragments in breccia (PT. STM 2018). The HLE porphyry copper-gold mineralization is a typical porphyry copper deposit with hypogene mineralization linked with a multiphase diorite porphyry stock that has been differentiated into early, intermineral, and late mineral phases (Sillitoe, 2012). The early porphyries average 0.5 % Cu and 0.5 gr/tones Au (Sillitoe, 2012). The inter-mineral porphyries have a significantly lower grade, averaging 0.2-0.3 percent Cu and 0.2-0.5 gr/tones Au; however, the eastern side of the stock has a much higher gold content, averaging 0.3 % Cu and 1 gr/tones Au (Sillitoe, 2012). The late mineral stages are virtually barren, with only 0.1 % Cu and 0.01-0.05 gr/tones of gold (Sillitoe, 2012).
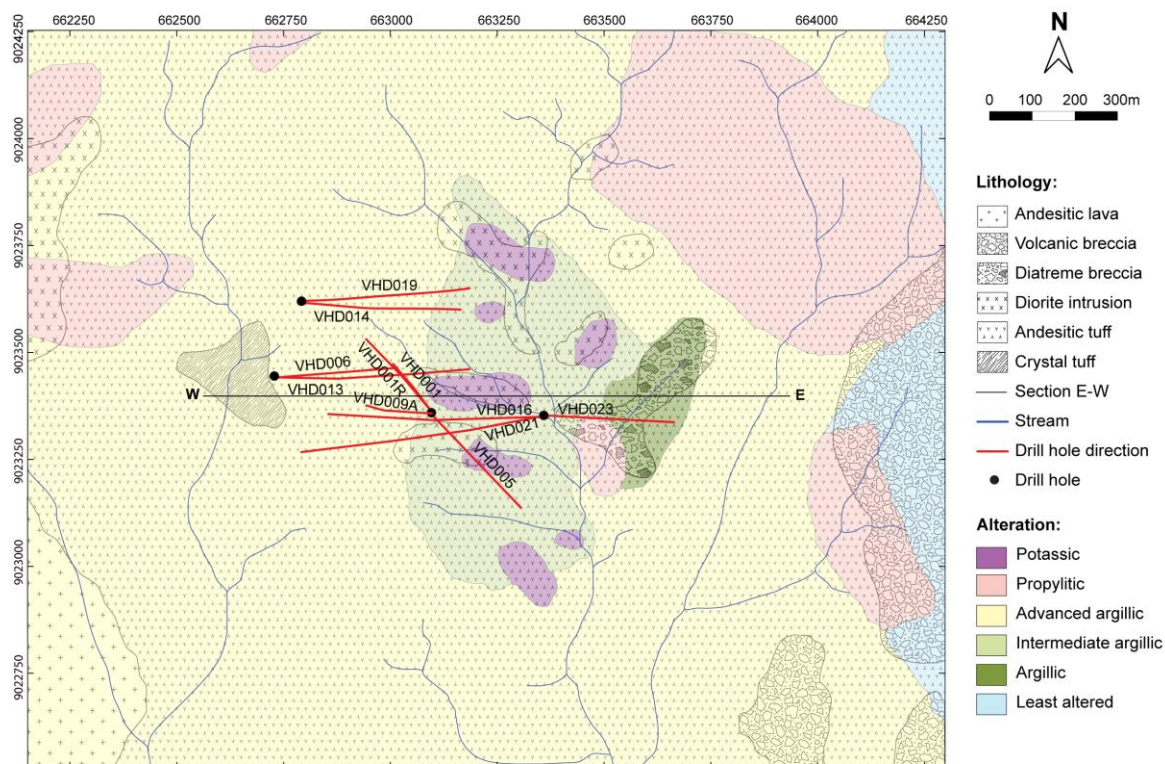
Figure 4. 2 Geological map of the research area (modified from PT. Sumbawa Timur Mining, 2018).

4.2 RESULTS

4.2.1 Petrography observation of causative intrusions

Forty samples of intrusive rocks from five drill holes were studied. According to petrographic observation, the multiphase intrusion consists of two types of intrusive rock: quartz diorite and diorite porphyry (**Fig. 4.3**). The quartz diorite porphyry intrusions are part of the early-intermediate intrusive phases and are related to the main mineralization. They have a grey color with a porphyritic texture, and consist of plagioclase, minor quartz, and secondary minerals such as calcite, secondary quartz, chlorite, anhydrite, albite, and K-feldspar. The quartz diorite porphyry intrusions contain less than 65% of phenocrysts, mainly consisting of subhedral plagioclase (labradorite-andesine), and plagioclase or mafic minerals replaced by secondary quartz and chlorite. The groundmass of quartz diorite porphyry intrusions is microcrystalline and consists mainly of plagioclase with lesser primary quartz. Several samples of the late phase intrusion have dark grey-grey color with porphyritic texture, consisting of dominant plagioclase and alteration minerals, such as calcite, secondary quartz, chlorite, anhydrite, albite, and K-feldspar. No primary quartz and mafic minerals are found. This

34

intrusion contains up to 75% of phenocrysts, consisting mainly of subhedral plagioclase (labradorite with minor andesine). The rock can be categorized as diorite.
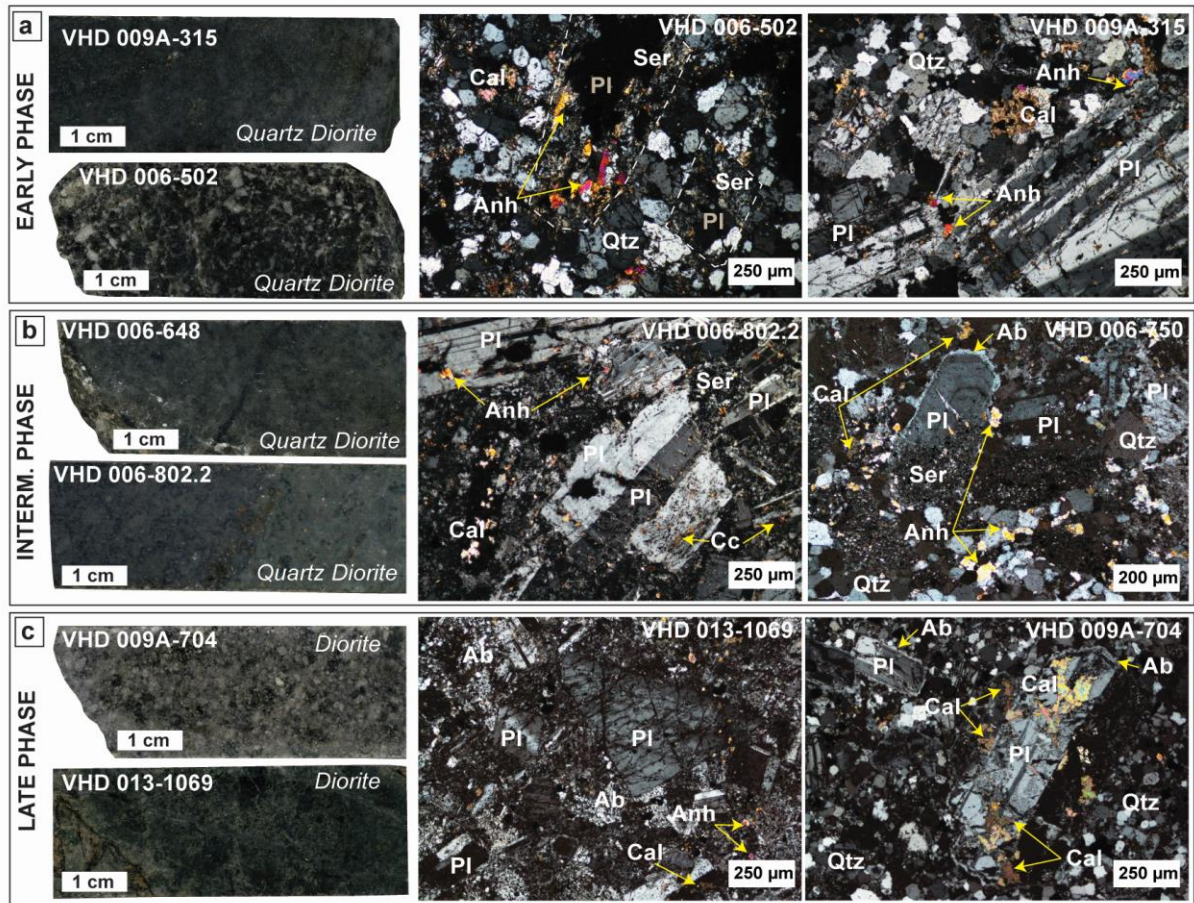
Figure 4. 3 Representative macro- and microphotographs of various intrusion phases at the Humpa Leu East porphyry Cu-Au prospect. *Abbreviations:* Qtz= quartz, Cal= calcite, Chl= chlorite, Ser= sericite, Anh= anhydrite , pl= plagioclase, Ab=albite. and Kfs= K-feldspar.

A detailed petrographic study of hydrothermal alteration associated with the main mineralization in the drill cores VHD001, VHD001R, VHD006, VHD009A, and VHD013 was also conducted. At least three types of hydrothermal alteration can be observed: potassic (Qtz-Mt-Kfs-Cal-Ab-Anh), chlorite-sericite (Qtz-Chl-Ser-Cal-Anh), and sericite (Qtz-Ser-Chl-Cal-Anh) alteration. The potassic alteration was observed in drill hole VHD009A at a depth of >550 m, and is composed of secondary quartz, K-feldspar, calcite, anhydrite, and chlorite (**Fig. 4.4-a, b & c**). Alteration biotite has not been identified in this zone, and it may have been converted to chlorite. Common opaque minerals in the potassic alteration zone include magnetite, chalcopyrite, bornite, chalcocite-covellite, and minor pyrite.
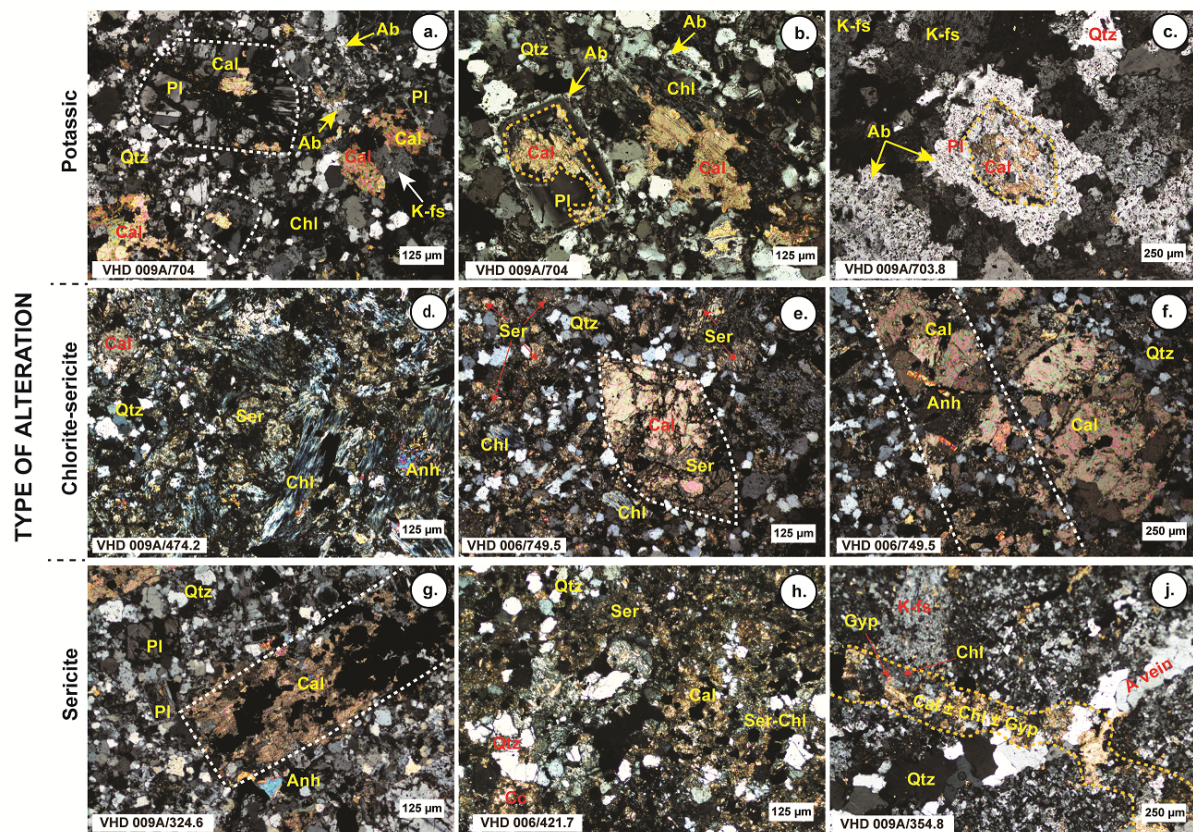
Figure 4.4 Representative microphotographs of various altered intrusion phases at the Humpa Leu East porphyry Cu-Au prospect. (**a, b, c**) Calcite as a partial replacement of plagioclase in the potassic zone. (**d, e, f**) Calcite as replacement of plagioclase matrix, fracture filling, and full replacement of mafic minerals (hornblende) in the chlorite-sericite zone. (**g, h, i**) Calcite replacement of plagioclase matrix, full replacement of mafic minerals (hornblende), and a calcite vein in the sericite zone. The calcite vein is cutting the remnant K-feldspar. *Abbreviations:* Qtz= quartz, Cal= calcite, Chl= chlorite, Ser= sericite, Anh= anhydrite , pl= plagioclase, Ab= albite, and Kfs= K-feldspar.

The chlorite-sericite and sericite alteration zones are poorly represented at the surface within the prospect. The only significant area of pervasive chlorite-sericite and sericite alteration is associated with the early to intermediate diorite phase in the drillcore VHD001, VHD 001R, and VHD 009A within the range of 400-550 m depth, overprinting a previous potassic alteration. The chlorite-sericite alteration is mostly present at a 350-550 m depth, and it was observed in drill holes VHD001, VHD001R, and VHD009A. This alteration includes quartz, chlorite, sericite, calcite, and anhydrite (**Fig. 4.4-d, e & f**). The most common opaque minerals in this zone are chalcopyrite and pyrite, although minor remnant magnetite is still present in places. In general, the sericite alteration is present at a < 400 m depth, and it was observed in drill holes VHD001, VHD001R, and VHD009A. The abundance of quartz, sericite, and calcite are typical of this alteration zone (**Fig. 4.4-g, h & i**). However, alteration minerals such as chlorite, anhydrite, and gypsum are also present. Chalcopyrite and pyrite are the most

common sulfide minerals in the sericite alteration zone, while sphalerite-galena were also found in a very small amount.

4.2.2 Whole-rock geochemistry of causative intrusions

The results of major and trace element analyses of twenty-five samples of intrusive rocks which have been normalized are shown in **Table 4.1.** The samples have LOI (loss on ignition) values of 0.52 – 8.57 wt.%. In this study, only samples with the LOI < 3% are used. The intrusive rocks have 49.77-76.26 wt.% SiO_2, 0.25-0.98 wt.% TiO_2, 12.9-20.78 wt.% Al_2O_3, 2.87-13.68 wt.% Fe_2O_3(t), 0.04-4.65 wt.% Na_2O, and 0.21-2.85 wt.% K_2O. Copper (Cu) and gold (Au) contents are 41.6 – 11,860 ppm and 0.1 - 4.2 ppm, respectively (**Table 4.1**). The high field strength elements are relatively low. The Th averages 2.23 ppm with a range of 0.73-8.41 ppm, Nb averages 1.99 ppm with a large range of 0.51–16.79 ppm, Ta averages 0.59 ppm with a range of 0.07-2.47 ppm, Hf averages 0.23 ppm with a range of 0.07-0.96 ppm and Zr averages 65.30 ppm with a range of 33.4-88.9 ppm (**Table 4.1**). The large ion lithophile elements are relatively high. Ba ranges from 125.3 to 974.9 ppm (average of 440.99 ppm), Sr ranges from 155.3 to 532.3 ppm (average of 333.99 ppm), and Rb ranges from 4.66 to 80.11 ppm (average of 28.28 ppm) (**Table 4.1**). Based on the ternary rock classification diagram using the Zr/Ti vs. Nb/Y diagram (after Pearce, 1996), the samples plot in the field of basalt to basalt-andesit (gabbro to diorite) (**Fig. 4.5-a**). Furthermore, the Al_2O_3 vs. Ti (%) diagram (Yan et al., 2016) shows a similar result, where the samples plotted on display mafic-intermediate rocks (**Fig. 4.5-b**). In this case, discriminant diagram from Pearce (1996) based on the Zr/Ti vs. Nb/Y and diagram from (Yan et al., 2016) using the Al_2O_3 vs. Ti (%) shows a consistency in results. Primitive mantle-normalized diagram (after Sun and McDonough, 1989) shows the distribution of element has a similar pattern with the geochemical signature of a subduction system which is showing the depletion of high field strength elements (HFSE) and enrichment of the large ion lithophile elements (LILE) (**Fig. 4.6**).

The wall rocks (andesite lava) have 55.9-63.95 wt.% SiO_2, 0.45-0.52 wt.% TiO_2, 17.9-20.0 wt.% Al_2O_3, 4.72-6.65 wt.% Fe_2O_3(t), 0.00-0.16 wt.% Na_2O, and 0.21-2.5 wt.% K_2O. (Table 1). The overall copper and gold contents are 343-3206 ppm and 0.07-0.4 ppm, respectively (Table 1). The high field strength elements are relatively low, *i.e.*, 1.2-1.78 ppm Th (av. 1.42 ppm), 1.80–2.26 ppm Nb (av. 2.03 ppm), 0.79-1.90 ppm Ta (av. 1.38 ppm), 0.09-0.2 ppm Hf (av. 0.15ppm), and 47.2-82.1 ppm Zr (av. 66.3 ppm) (Table 1). The large ion

lithophile elements (LILE) are relatively high, *i.e.*, 227.8-2272 ppm Ba (av. 983.5 ppm), 155.3-383 ppm Sr (av. 236.7 ppm), and 5.59-65.8 ppm Rb (av. 26.6 ppm) (Table 1).
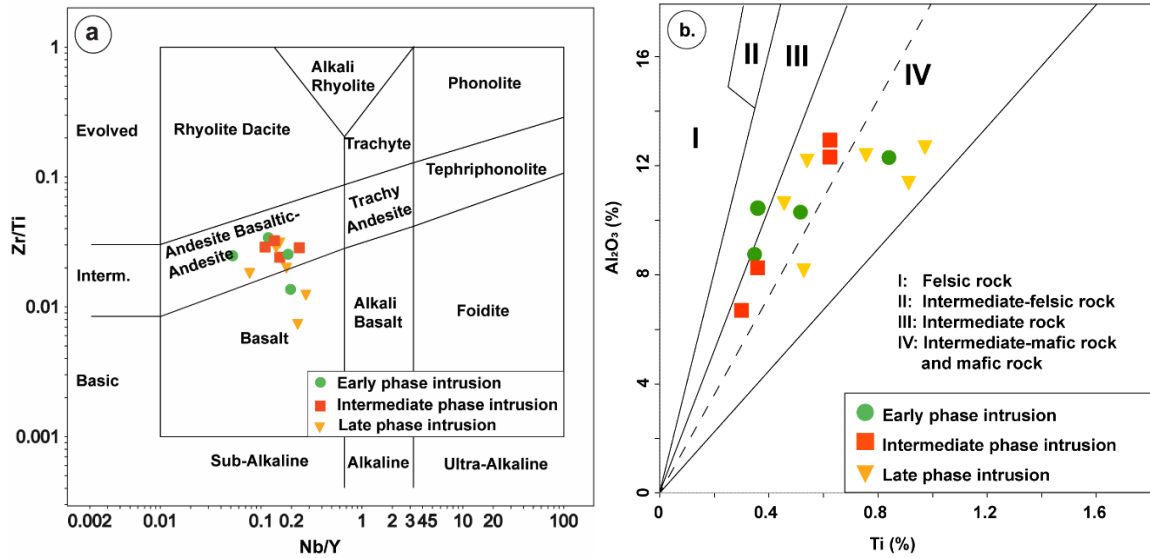
Figure 4.5 (**a**)Classification diagram of volcanic rocks (after Pearce, 1996) using immobile trace elements (Zr/Ti versus Nb/Y) of causative intrusions. (**b**) Classification diagram of igneous rock based on Al_2O_3 vs. Ti (%) of causative intrusions after (Yan et al., 2016).
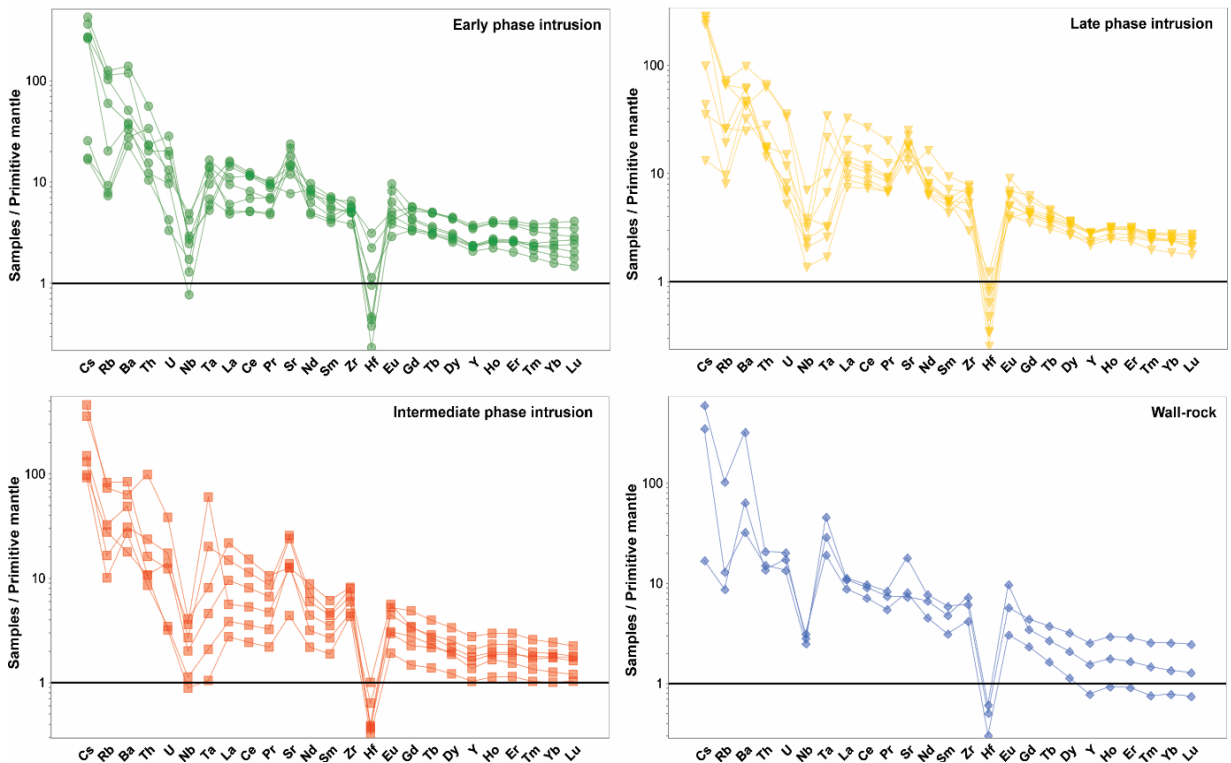
Figure 4. 6 Spidegram of trace elements normalized of causative intrusions to the primitive mantle (after Sun and McDonough, 1989)

Magma affinity diagram based on trace element Zr vs. Y and Th/Yb vs. Zr/Y (Ross & Bedard, 2009) indicate transitional to calc-alkaline compositions (**Fig. 4.7-a,b**). The Th/Yb vs. Nb/Yb diagram (Pearce, 2014) shows that samples mostly plot in the continental arc field, and a few samples in the oceanic arc field (**Fig. 4.7-c**).
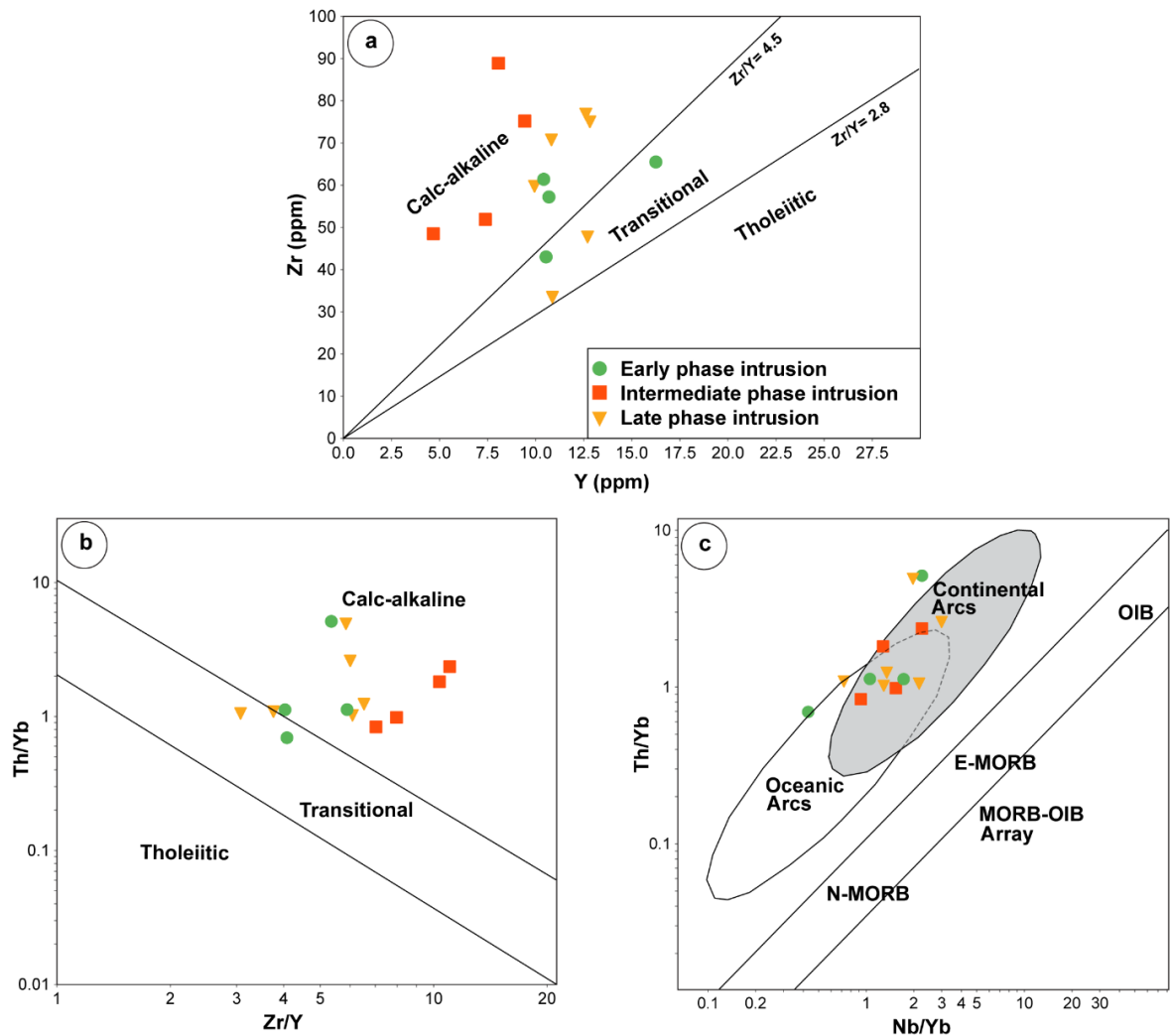
Figure 4. 7 (**a**; **b**) Zirconium vs. Y and Th/Yb vs. Zr/Y diagrams for magma affinity (after Ross & Bedard, 2009). (**c**) A tectonic discrimination diagram based on Th/Yb and Nb/Yb (after Pearce, 2008). (c) Magmatic contamination by Subducted Sedimentary Input Diagram (after Hawkesworth et al., 1997; after He et al., 2008). These classification diagrams are based on whole-rock geochemistry data of causative intrusions.

Table 4. 1 Whole-rock geochemical results of major, trace and rare earth elements for all phases of diorite and quartz diorite porphyry at the Humpa Leu East porphyry Cu-Au prospect.

Sample	VHD 001-459	VHD 001-421.7	VHD 001-445.7	VHD 001-450.5	VHD 001R-715.4	VHD 001R-517	VHD 001R-661.3	VHD 001R-539.8	VHD 001R-503.8
Intrusion Phase	Early phase	Early phase	Early phase	Early phase	Late phase	Late phase	Late phase	Late phase	Intermediate phase
SiO_2 (wt.%)	49.8	56.6	57.6	61.7	60.0	55.4	53.6	58.5	54.2
TiO_2	0.98	0.45	0.70	0.64	0.52	0.68	0.81	0.63	0.68
Al_2O_3	20.8	17.2	15.4	13.4	17.2	17.9	15.9	15.5	17.0
$Fe_2O_3(t)$	10.6	6.81	7.98	3.66	4.99	8.91	11.82	9.76	7.15
MnO	0.09	0.09	0.08	0.08	0.12	0.15	0.17	0.16	0.20
MgO	3.96	4.54	4.78	3.94	3.47	3.20	4.98	3.62	4.82
CaO	3.66	6.25	4.57	6.39	5.37	5.64	5.56	3.98	5.62
Na_2O	0.00	1.96	0.81	0.69	2.23	0.00	2.17	0.53	0.15
K_2O	2.52	0.75	2.85	2.66	1.38	1.92	0.58	2.01	1.96
P_2O_5	0.10	0.11	0.15	0.13	0.14	0.10	0.22	0.26	0.15
LOI	5.97	3.34	2.94	3.34	3.65	3.37	2.61	2.98	5.25
Total	98.5	98.2	97.9	96.6	99.0	97.2	98.4	98.0	97.2
Mn (ppm)	723	658	619	606	906	1,125	1,268	1,252	1,577
Cu	4,446	4,452	6,687	3,103	41.5	4,537	4,223	3,051	3,911
Au	0.10	0.28	0.31	0.20	0.07	0.13	0.38	0.18	0.14
Zn	415	156	383	154	118.	485.	280	492	267
Ga	41.4	31.8	68.0	56.4	43.5	32.8	30.8	55.1	44
Mo	27.5	15.1	15.6	15.0	12.9	14.9	4.73	10.8	11.1
Ag	0.84	1.48	2.00	0.79	0.89	0.45	0.85	0.76	0.61
Sb	0.21	0.20	0.42	0.18	1.19	0.16	0.13	0.24	0.22
Rb	65.4	12.9	80.1	72.1	42.0	43.4	16.6	46.5	46.7
Sr	162	309	252	379	398	228	377	283	266
Zr	55.9	63.2	57.2	55.6	84.3	88.2	59.7	75.0	91.8

Nb	1.76	0.92	2.09	1.96	1.48	5.06	2.76	2.29	2.92
Cs	2.87	2.13	3.36	2.13	2.07	1.91	2.26	2.25	3.63
Ba	357	257	975	834	425.	297	174	689	442
Hf	0.14	0.07	0.14	0.12	0.11	0.15	0.08	0.11	0.12
Ta	0.24	0.58	0.22	0.39	0.11	0.41	0.13	0.28	0.33
Pb	20.1	25.0	15.6	11.6	10.2	14.7	15.9	19.3	59.1
Th	1.98	1.04	4.77	1.73	1.50	5.36	2.39	5.68	8.41
U	0.60	0.20	0.39	0.42	0.32	0.75	0.25	0.71	0.81
La	10.6	6.52	9.82	11.1	8.81	22.4	10.1	14.1	15.0
Ce	21.0	14.4	20.3	22.0	19.5	47.6	21.4	29.9	27.0
Pr	2.59	1.88	2.44	2.66	2.52	5.58	2.58	3.45	2.92
Nd	11.5	8.50	10.7	11.2	11.1	22.3	11.0	14.3	12.0
Sm	3.05	2.04	2.39	2.54	2.59	4.18	2.47	3.19	2.73
Eu	1.61	0.78	1.07	1.38	1.10	1.17	0.86	1.53	0.88
Gd	3.41	2.15	2.52	2.61	2.76	3.74	2.46	3.34	2.92
Tb	0.55	0.33	0.37	0.39	0.44	0.50	0.37	0.49	0.43
Dy	3.23	1.88	2.18	2.27	2.62	2.69	2.05	2.70	2.48
Ho	0.65	0.37	0.43	0.45	0.53	0.53	0.41	0.52	0.49
Er	1.81	0.98	1.22	1.28	1.55	1.52	1.13	1.43	1.43
Tm	0.24	0.13	0.16	0.17	0.20	0.19	0.15	0.19	0.19
Yb	1.50	0.78	0.93	1.10	1.31	1.21	0.92	1.16	1.20
Lu	0.21	0.11	0.13	0.15	0.19	0.16	0.13	0.16	0.17
Y	15.7	9.44	10.7	10.8	13.1	12.8	9.94	12.8	12.6
V	295	125	177	118	107	122	206	164	158

Table 1 (cont.)

Sample	VHD 006-400.2	VHD 006-240.6	VHD 006-749.5	VHD 006-723	VHD 006-802.3	VHD 009A-354.8	VHD 009A-324.6	VHD 009A-669.6	VHD 009A-703.2
Intrusion Phase	Wall-rock (andesite)	Wall-rock (andesite)	Intermediate phase	Intermediate phase	Intermediate phase	Early phase	Early phase	Late phase	Late phase
SiO_2 (wt.%)	55.9	60.1	60.8	62.3	61.2	61.8	64.5	65.8	63.7
TiO_2	0.49	0.52	0.48	0.52	0.52	0.29	0.43	0.38	0.44
Al_2O_3	18.0	20.0	16.9	15.4	16.2	11.0	12.9	13.3	10.2
$Fe_2O_3(t)$	5.68	6.65	6.71	2.44	4.31	9.77	7.07	6.35	13.7
MnO	0.16	0.06	0.13	0.06	0.15	0.33	0.20	0.13	0.10
MgO	5.55	2.85	3.59	2.52	3.97	2.91	2.09	2.99	2.72
CaO	6.63	2.77	2.81	6.62	6.15	6.10	5.33	3.91	3.60
Na_2O	2.28	0.00	0.05	4.38	3.44	3.30	3.89	3.48	3.43
K_2O	0.35	2.47	2.31	1.04	0.31	0.47	0.44	0.74	0.36
P_2O_5	0.11	0.15	0.15	0.08	0.08	0.19	0.06	0.12	0.11
LOI	4.14	3.49	4.25	1.44	2.31	2.56	1.21	2.10	0.72
Total	99.3	99.0	98.1	96.9	98.6	98.7	98.1	99.3	99.1
Mn (ppm)	1,161	483	945	348	1,087	2,649	993	1,020	775
Cu	1,061	343	3,104	2,194	433	11,860	4,791	2,004	3,165
Au	0.09	0.07	0.11	0.13	0.13	4.24	0.13	0.21	0.58
Zn	547	819	188	114	226	582	460	131	151
Ga	30.5	180	50.8	32.7	30.3	24.3	29.3	36.8	30.0
Mo	3.23	141	14.1	76.1	7.16	8.93	11.6	5.02	2.85
Ag	0.36	0.14	13.2	0.55	0.20	3.35	0.74	0.42	0.69
Sb	0.14	0.45	13.9	1.11	0.45	1.51	0.34	0.42	0.66
Rb	8.31	65.8	52.7	20.7	10.5	4.66	38.0	12.3	5.13
Sr	383	155	267	508	543	310	299	385	323
Zr	69.7	82.1	66.6	75.2	88.9	43.0	65.5	70.7	47.7

Nb	1.80	2.04	2.58	1.44	1.93	0.55	3.01	1.65	0.98
Cs	2.80	4.77	2.83	1.19	1.04	0.13	2.06	0.79	0.35
Ba	228	2,272	589	343	216	159	267	328	226
Hf	0.16	0.19	0.12	0.11	0.31	0.35	0.97	0.20	0.25
Ta	1.90	1.20	2.47	0.19	0.83	0.28	0.68	0.89	0.07
Pb	17.1	11.0	28.3	21.5	30.8	62.1	24.6	10.5	8.02
Th	1.30	1.78	1.38	0.92	2.02	0.89	1.96	1.51	1.47
U	0.29	0.43	0.26	0.29	0.37	0.09	0.28	0.11	0.14
La	7.80	7.53	3.88	6.55	10.26	3.33	7.61	6.86	5.13
Ce	17.4	16.3	9.48	14.4	20.3	9.18	20.5	15.5	13.0
Pr	2.32	2.07	1.31	1.84	2.39	1.38	2.82	1.96	1.87
Nd	10.5	9.12	6.02	8.11	9.79	6.78	13.1	8.58	9.09
Sm	2.64	2.14	1.56	1.95	2.08	1.89	3.17	1.93	2.44
Eu	0.97	1.65	0.52	0.75	0.95	0.49	0.86	0.69	0.65
Gd	2.64	2.08	1.66	2.01	2.06	2.01	3.34	2.11	2.63
Tb	0.41	0.29	0.25	0.31	0.29	0.34	0.53	0.33	0.42
Dy	2.38	1.56	1.38	1.87	1.60	2.07	3.18	1.99	2.50
Ho	0.49	0.29	0.27	0.38	0.32	0.44	0.65	0.41	0.51
Er	1.39	0.80	0.74	1.11	0.94	1.26	1.88	1.24	1.44
Tm	0.19	0.11	0.10	0.15	0.12	0.18	0.26	0.18	0.21
Yb	1.26	0.67	0.62	0.93	0.86	1.28	1.74	1.23	1.35
Lu	0.18	0.10	0.09	0.13	0.12	0.20	0.26	0.18	0.20
Y	11.6	7.12	6.23	9.43	8.06	10.5	16.3	10.8	12.7
V	89.5	99.9	68.5	74.6	132	130	63.2	93.4	203

4.2.3 Ore microscopy and vein paragenesis

The subdivision of mineralization stages of the HLE prospect by Sillitoe (2012) on the internal report of PT. STM has been adopted in this paper and also confirmed by the presence of mineral assemblages from ore microscopy analysis in this study. The mineralization stages of HLE porphyry Cu-Au prospect including early, intermediate, and late stage (**Table 4.2**).

4.2.3.1 Early-stage

Early-stage mineralization is associated with the M, A, and AB veins. The terminology of M veins is adopted after Gustafson & Hunt (1975), Gustafson & Quiroga (1995), Corbet (2008), and Sillitoe (2010). Magnetite is the main vein-filling mineral in these veins (>95%), and some parts are accompanied by minor chalcopyrite and bornite (**Fig. 4.8-A5 & 4.8-B**). Generally, the veins are 10 to 30 millimeters wide and occur as single vein, stockwork, and sheeted texture (**Fig. 4.8-A5 & 4.8-B**). The A-type veins are the most common veins in the early stage and are formed mainly in the potassic alteration zone accompanied by magnetite and minor chalcopyrite-bornite-chalcocite, with minor calcite and chlorite minerals, and locally rutile and sericite. The veins are 20 to >100 millimeters thick. These veins are composed of quartz ± magnetite and are surrounded by a K-feldspar halo (**Fig. 4.8-A5,4.8-A6, & 4.8-C**). The A and M veins are mostly recognized in the deeper intrusions and mostly lack sulfide minerals. The AB veins, nomenclature after Sutarto (2015); Klimentyeva (2020) consist mainly of quartz + magnetite + sulfides such as chalcopyrite and minor pyrite, have a width of 10 to >100 millimeters (**Fig. 4.8-A3 & 4.8-D**). The central confluence of sulfides forms the AB veins in the A veins, resulting in chalcopyrite being concentrated at the center of these veins. These veins mostly occur in the potassic zone or at the transition with the chlorite-sericite zone. These veins represent the first sulphidation stage in the HLE porphyry Cu-Au prospect. Some samples show disseminated chalcopyrite, covellite, and chalcocite intergrown with bornite, accompanied by magnetite (**Fig. 4.8-I**).

4.2.3.2 Intermediate stage

This stage is related to the B and C veins/veinlets (nomenclature after Gustafson & Hunt, 1975; Gustafson & Quiroga, 1995; Corbet, 2008; Sillitoe, 2010). The B veins are composed mainly of quartz, chalcopyrite, and pyrite, which formed within the chlorite-sericite alteration zone, and remnants of magnetite are still found. The B veins are typically irregular 10 to >200 micrometers wide and generally cut type-A veins (**Fig. 4.8-A2 & 4.8-E**). The C veins are mainly composed of sulfide minerals which are chalcopyrite (> 98 %) with rare pyrite and

sphalerite (< 2%). Generally, the veins are >300 micrometers wide (**Fig. 4.8-A4 & 4.8-F**). The C veins are associated with the chlorite-sericite and sericite alteration zone. These stages are also indicated by the presence of disseminated chalcopyrite intergrown with pyrite, accompanied by a remnant of magnetite, which is some part turning into hematite (**Fig. 4.8-J**).

4.2.3.3 Late-stage

The D vein type is the most common vein in this stage (nomenclature after Gustafson & Hunt, 1975; Gustafson & Quiroga, 1995; Corbet, 2008; Sillitoe, 2010). This vein type consists of quartz, sulfides, and calcite with distinct sericite alteration remnants and has a thickness of 500-1000 microns. Pyrite is the main vein filling sulfide with sericite and chlorite halo. Mostly D veins (quartz-calcite-gypsum-sulfide veins) are associated with sericite and inner propylitic alteration zone. Pyrite is the most common sulfide mineral found in these veins, with rare sphalerite and galena (**Fig. 4.8-A1, 4.8-A5 & 4.8-G**), and a minor amount of chalcopyrite. These veins generally represent the latest stage vein in the porphyry Cu-Au environment or possibly the transitions from porphyry to the epithermal environment. Disseminated chalcopyrite, a partial replacement by the sphalerite and galena (**Fig. 4.8-H**), is interpreted to be late-stage mineralization formed at a relatively low-temperature environment.

Table 4. 2 Summary of mineralization stage of the HLE prospect.

Mineralization stage	Vein type	Mineral assemblage	Vein halo	Alteration	Fluid inclusions
Early stage	M vein *A vein* *AB vein*	Mt ± Bn ± Ccp Qtz + Mt Qtz + Mt + Ccp ± Py	No halo Kfs - halo No halo	Potassic Potassic Potassic	Monophase vapor; multiphase vapor rich; two-phase
Intermediate stage	B vein C vein	Qtz + Ccp + Py Ccp ± Py	No halo No halo	Chlorite-sericite Chlorite-sericite, Sericite	Liquid-rich two-phase
Late stage	D vein	Cal + Gyp + Qtz + Py ± Ccp ± Sph ± Gn	Chl - halo, Ser - halo	Inner propylitic, sericite	Liquid-rich two-phase
Post-mineralization	Barren vein	Cal + Gyp+ Barite	No halo	Sericite	

Abbreviations: *Mt= Magnetite, Bn= Bornite , Ccp= Chalcopyrite, Py= Pyrite, Ccp= Chalcocite, Sph= Sphalerite (Sph), Gn= Galena, Qtz= Quartz, Cal= Calcite, Chl= Chlorite, Ser=Sericite, Gyp=Gypsum, Bar=Barite, and Kfs=K-feldspar.*
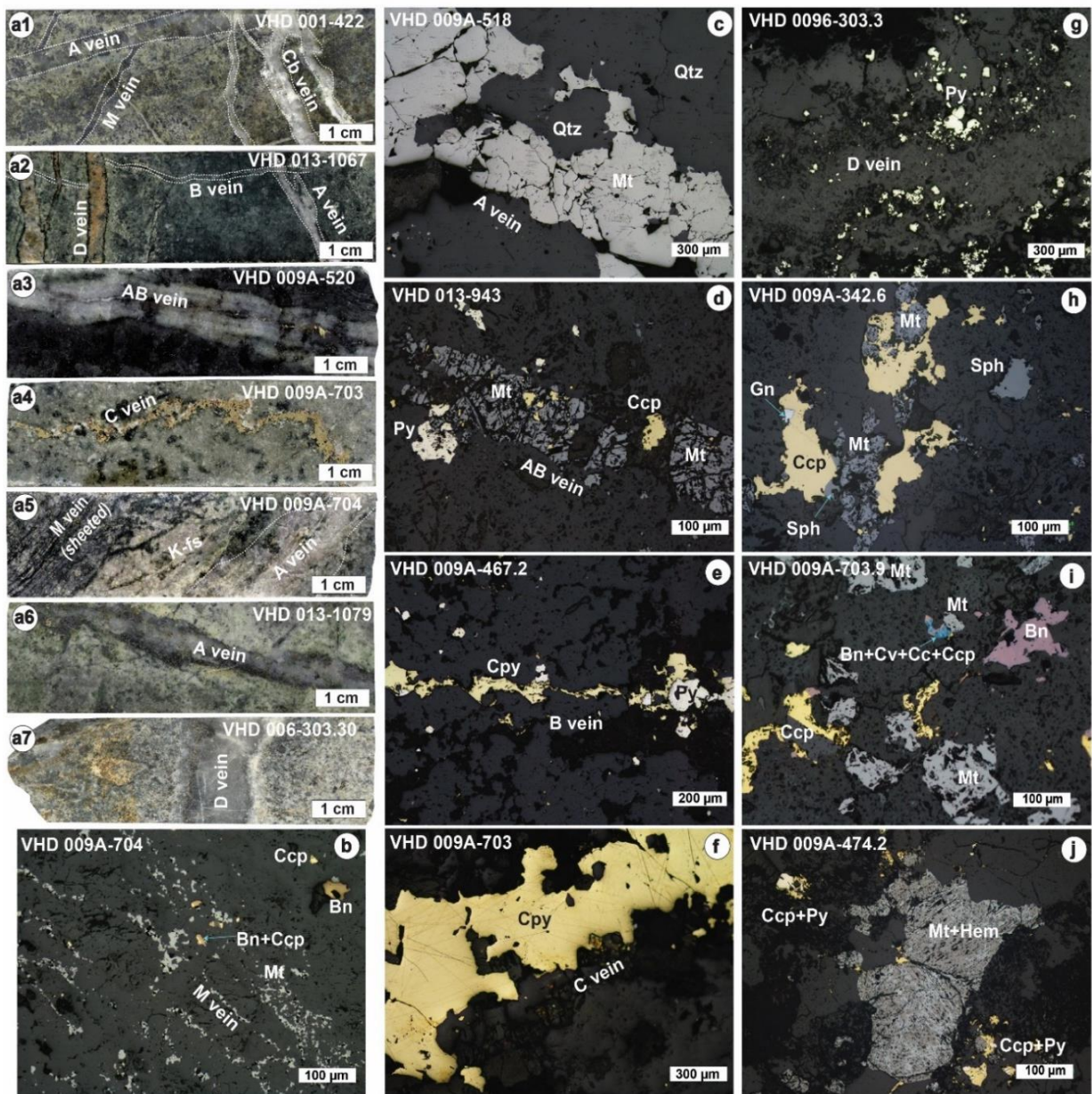
Figure 4. 8 Photos and photomicrographs of representative ores in the Humpa Leu East porphyry Cu-Au prospect; (**a1**) M vein is cut by A vein, while the A vein is cut by a calcite vein of the post mineralization stage; (**a2**) B vein is cut by a D vein, while A vein is cut by a B vein; (**a3**) AB vein shows a center line of chalcopyrite-magnetite with minor pyrite; (**a4**) C vein of chalcopyrite; (**a5**) M vein; (**a6**) A vein consisting of quartz and magnetite; (**a7**) D vein consisting of calcite and gypsum with sericite halo; (**b, c, d**) photomicrographs of M, A, and AB veins in the early-stage; (**e, f**) B and C veins in the intermediate stage; (**g**) D vein in the late-stage, where pyrite is the most common sulfide mineral; (**h, i, j**) disseminated ore minerals. *Abbreviations:* Mt=Magnetite, Bn=Bornite, Ccp=Chalcopyrite, Py=Pyrite, Cc=Chalcocite, Sph=Sphalerite, Gn=Galena, and Qt z=Quartz.

4.2.4 Geochemistry of sulfide minerals

The distribution of trace element Se, As, Ni, Au, Cu, Co, Zn, Sb, Ag, and Pb of pyrite, chalcopyrite, and bornite from each stage were analyzed.

4.2.4.1 Pyrite

Forty five pyrite crystals in early stage A-B veins , nineteen pyrite in intermediate stage B veins, and thirty three pyrite from late stage D vein were analyzed by EPMA. The EPMA shows relatively abundance of Se, As, and Co, moderate of Cu, Ni, and Zn, and Ag, Pb, and Sb were below detection (**Appendix 2**; **Fig. 4.9**). The As and Cu is more abundant in early than intermediate and late mineralization stage, while the Se and Co are more abundant in intermediate than early or late mineralization stage. In addition, Ni and Zn values are similar in all mineralization stages.

AB vein (VHD 009A-518)   B vein (VHD 009A-520)   D vein (VHD 013-1069)
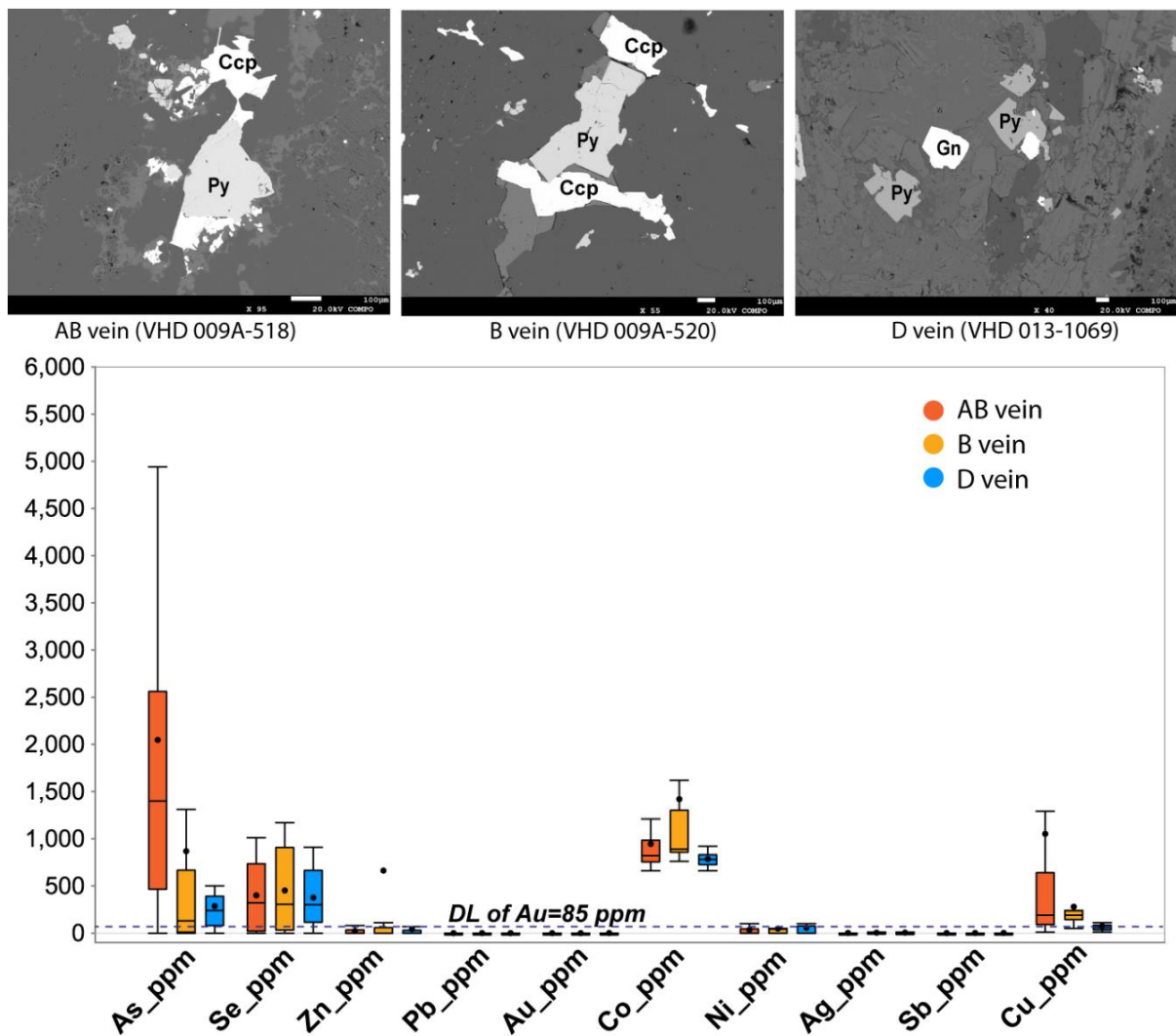
Figure 4. 9 Box plot diagram of pyrite concentration

4.2.4.2 Chalcopyrite

The trace element concentration of chalcopyrite was analyzed from ninety-six points; sixteen points in B vein, forty points from AB vein and forty points from C vein. The Zn, Co, Pb, and As are the most abundant trace elements in chalcopyrite, while Ag and Cd are less

abundant (Appendix 3; **Fig. 4.10**). Gold was only detected from chalcopyrite in a B vein and some spots in an AB vein (Fig.), even though some values are under detection limit (DL 80 ppm). Zinc in AB and B veins is more abundant than in the C vein. Furthermore, Pb is more abundant in B veins than AB veins and C, while Co has similar contents in AB, B, and C veins.

AB vein (VHD 009A-518)   B vein (VHD 009A-520)   C vein (VHD 009A-713)
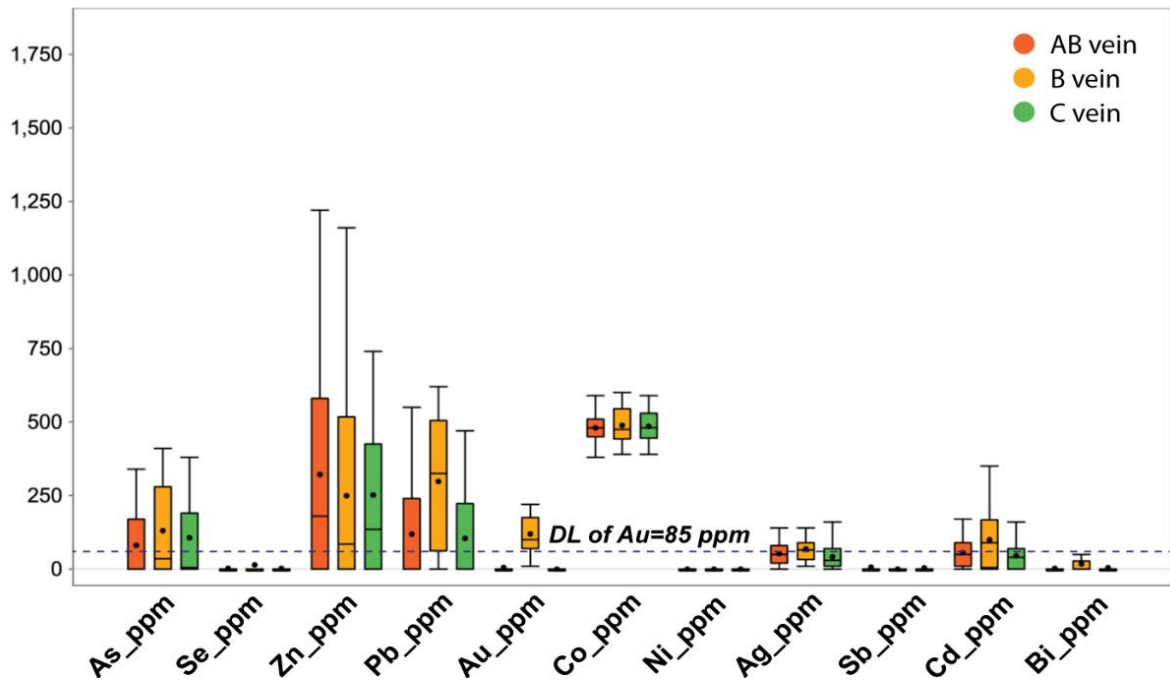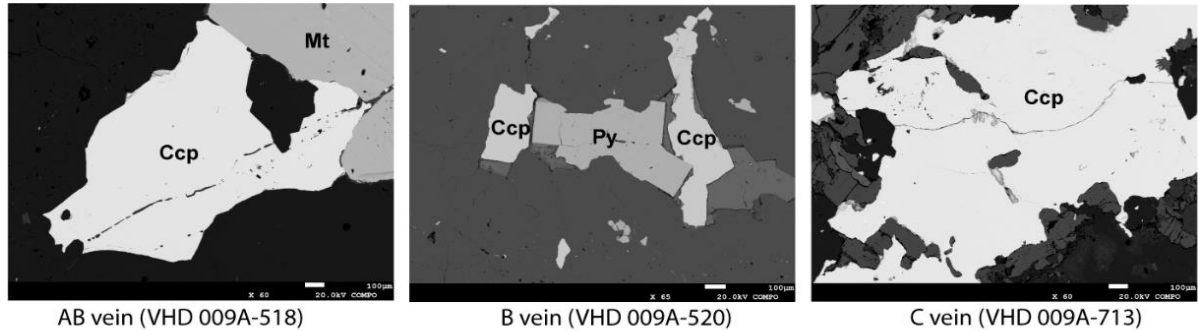
Figure 4. 10 Box plot diagram of chalcopyrite concentration

4.2.4.3 Bornite

The eighty-eighth spots of bornite were analyzed, showing that Zn, Pb, and Ag are more abundant than As, Au, Co, Cd, and Bi, but Ni and Sb are under detection limit (**Appendix 4; Fig. 4.11**). The Zn and Pb have wide ranges of concentration as first quartile and third quartile value), Ag and Co have a narrow range of concentration in bornite. Interestingly, some bornite has zero concentration of Au, As, Cd, and Bi, but in some cases contain of those elements.
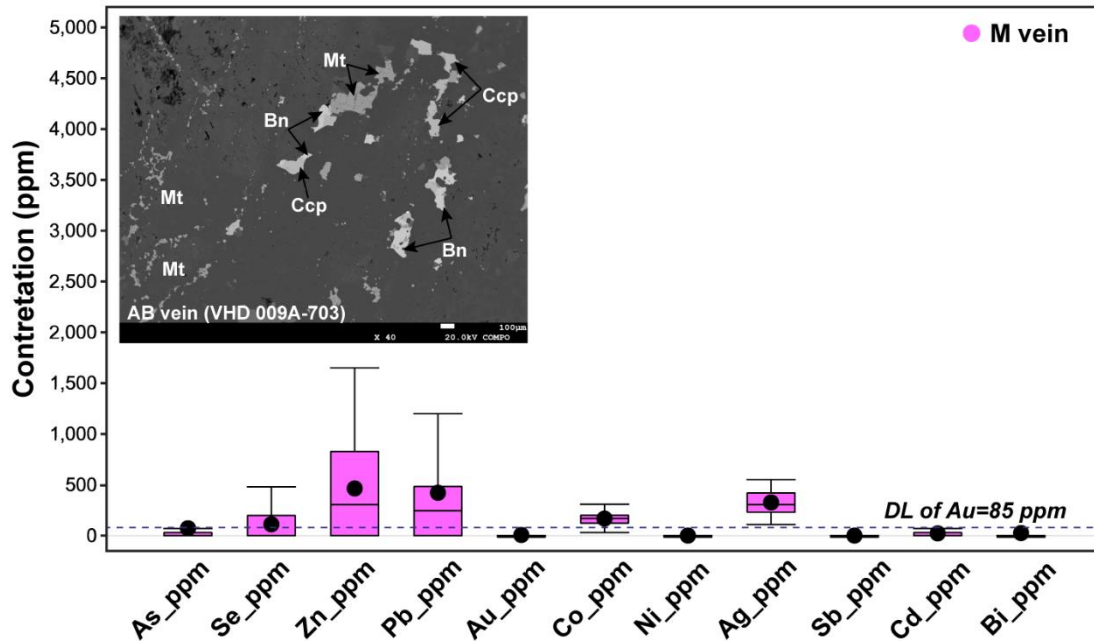
Figure 4. 11 Box plot diagram of bornite concentration

4.3 DISCUSSION

4.3.1 Geochemical signature of porphyry intrusions

The chemical compositions of all the phases of diorite and quartz diorite porphyry in the HLE prospect indicate calc-alkaline affinity (Fig. 4.7a, b).The primitive mantle-normalized trace element compositions of the porphyry intrusions plotted on a spider diagram (*cf.* Sun & McDonough, 1989) show slight enrichment compared to the composition of primitive mantle (**Fig. 4.6**). The spider diagram indicates the enrichment of Sr and Ba, while Rb shows a depletion. The enrichment of Sr is due to the abundance of Sr element in plagioclase as well as calcite alteration, while the enrichment of Ba related to the presence of barite (**Table 4.1, 4.2**). Furthermore, the depletion of Rb content in the porphyry intrusions compared to the mantle value is probably due to the disappearance of biotite during hydrothermal alteration. The spider diagram shows that the porphyry intrusions have positive anomalies of high field strength elements (HFSE) such as Ta and Zr compared to the mantle values, however Nb show negative anomalies. The diagram shows that Th is slightly more enriched than U compared to the mantle values, implying that the porphyry intrusions are arc-type igneous rocks (e.g., Taylor & McLennan, 1995). The REE concentrations of the porphyry intrusions were slightly changed through the hydrothermal alteration, particularly LREE and HREE, *i.e.*, enrichment of LREE over HREE as it is indicated by La/Yb = 2.60−11.99. The total REE contents are 19.0−89.2

ppm, and those have variable Eu anomalies. Furthermore, twenty-five samples of the porphyry intrusive rocks show both positive and negative anomalies of Eu, where the Eu/Eu* ranges from 0.84 to 1.30 (Fig. 4.6). On the other hand, the andesite lava of the wall rock shows only positive of Eu anomaly (Fig. 4.6). The positive Eu anomaly in some altered samples of hydrothermal deposits has been reported in previous studies (e.g. Palacios et al., 1986; Idrus et al., 2009b; Torres et al., 2010) as well as in hydrothermal fluids from mid-ocean ridges (e.g. Klinkhammer et al., 1994; Cole et al., 2014). They interpreted that the partition of Eu^{2+} is dominated by chemical substitution of Ca^{2+} and Sr^{2+} in plagioclase during hydrothermal processes. A remarkably positive anomaly of Eu in Ca-bearing hydrothermal minerals such as epidote is also recognized (Palacios et al., 1986; Torres et al., 2010). On the basis of the above statements, the positive anomalies of Eu in the porphyry intrusions of the HLE prospect were caused by substitution from Ca^{2+} during hydrothermal alteration processes, where the Eu^{2+} is probably concentrated in other Ca-bearing hydrothermal minerals such as calcite and anhydrite (Fig. 4.4).

The tectonic setting of Sunda arc is still debated whether it is island arc or continental arc. Several previous studies proposed that porphyry Cu-Au deposits in the eastern Sunda arc such as Batu Hijau (Sumbawa Island) and Tumpangpitu (eastern Java) exhibit island arc setting characteristics, (Groove et al., 2002; Maryono et al., 2018). However, the chemical compositions of least altered samples of the porphyry intrusions of the HLE prospect fall into the fields of continental arc and, to a lesser extent, oceanic arc (Fig. 4.7c). The relatively high Th/Yb and Nb/Yb values of these samples suggest the presence of evolved continental crust components in the magmas, as it is typical in a continental arc. We consider that the origin magma of the porphyry intrusive in the HLE prospect was a product of the subduction process of the Indian-Australian oceanic plate beneath the southeastern margin of the Eurasian continental plate (Sundaland) (e.g. Hamilton,1979; Katili, 1989). The presence of active continental margin (continental arc) along the Sunda magmatic arc was recently proposed in several studies (e.g. Reubi et al., 2002; Gertisser & Keller, 2003; Gardner et al., 2013; Fadlin et al., 2018; and Fadlin et al., 2021). In addition, the whole-rock geochemistry data of intrusive rocks from the HLE prospect, *i.e.,* Th/Ce ≥ 0.1 (Hawkesworth et al.,1997; He et al., 2008) and Zr/Y > 3 (Pearce, 1983) suggest sediment cycling input and continental crust signature, respectively (Fig. 4.12). The cutoff at Th/Ce=0.1 is the lower limit for modern arcs with an input from sediment melting. Zr/Y > 3 is a signature of a constituent of continental crust (Pearce, 1983).
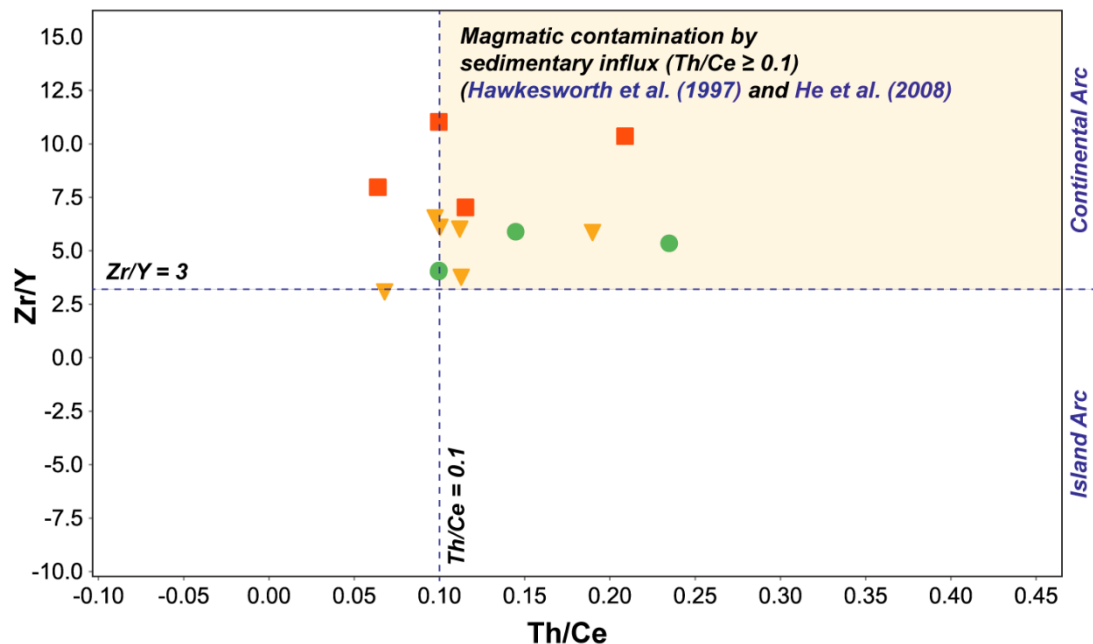
Figure 4. 12 Magmatic contamination by Subducted Sedimentary Input Diagram (after Hawkesworth et al., 1997; after He et al., 2008).

4.3.2 Copper-gold mineralization style

In the porphyry systems of the Sunda magmatic arc, the potassic alteration is generally characterized by secondary biotite formed from mafic minerals, such as hornblende, primary biotite, and pyroxene (Maryono et al., 2018; Sutarto et al., 2015). For, example, in the Batu Hijau deposit (western part of Sumbawa Island) the potassic alteration is characterize by disseminated biotite and early veinlets composed of magnetite-biotite-quartz (A-type) veins (Idrus et al., 2009). In the Selogiri Porphyry deposit, the potassic alteration associated with microdiorite is characterized by magnetite-quartz-biotite ± K-Feldspar (Sutarto et al., 2015). By comparison with these porphyry deposits in the eastern Sunda arc, the potassic alteration in the HLE prospect has some differences, including the presence of abundant M and A veins and secondary K-feldspar with abundant calcite accompanied by anhydrite and chlorite (**Table 4.2; Fig. 4.4**). No secondary biotite is found in the study area, as it may have turned into chlorite. The occurrence of significant calcite-rich alteration at HLE is unusual in porphyry systems. Furthermore, calcite is also observed in the chlorite-sericite and sericite zones (**Fig. 4.4**). Precipitation of calcite in the porphyry system cannot be separated from the supply of CO_2 from hydrothermal fluids and the availability of sufficient Ca in the system, which can derive from Ca-bearing minerals, such as plagioclase and mafic minerals (hornblende). In this case I

suggest that the calcite in the potassic zone is probably formed by the reaction of Ca-rich plagioclase and CO_2-rich bearing hydrothermal fluids.

Ore mineralization style of the HLE porphyry Cu-Au copper-gold prospect in the Hu'u district is mainly associated with sulfide minerals such as chalcopyrite [$CuFeS_2$], bornite [Cu_5FeS_4], chalcocite [Cu_2S], covellite [CuS], pyrite [FeS_2], with rare galena [PbS], and sphalerite [ZnS] (Fig 4.8). In this case, the HLE porphyry Cu-Au prospect shows that the occurrence of chalcopyrite and bornite with minor chalcocite and covellite is intimately related to the potassic zone. The upper zone extending to the chlorite-sericite zone is mostly associated with chalcopyrite and pyrite, while the sericite zone is typified by the presence of pyrite and minor chalcopyrite.

Two styles of mineralization are found in HLE porphyry Cu-Au: quartz-sulfide veins and disseminated sulfides. The quartz-sulfide veins are the most common mineralization style contributing to metals precipitations in this study area. The early mineralization stage (Stage 1), marked by A, M, and AB veins, is generally slightly mineralized with low sulfide content (**Fig. 4.8-b; c; d**). This could be due to the high temperature at which the veins formed, which is not suitable for sulfide minerals precipitation. This condition is also observed at Selogiri porphyry prospect, central Java (Sutarto et al., 2015). Sparse bornite-chalcopyrite coexisting with magnetite in the M and A veins is evidence that Cu precipitation has begun in the early stage of mineralization (**Fig. 4.8-b; c; d**). The intermediate stage is the main mineralization event, which is characterized by abundant sulfide-bearing B and C veins (**Fig. 4.8-e; f**). The pyritic D veins are a typical late stage of the quartz-sulfide vein (stage 3) which mostly contains less sulfide. Disseminated sulfide mineralization also contributes to the metal budget in the prospect. Chalcopyrite, bornite, pyrite, chalcocite, and covellite are the dominant sulfide constituents observed in this mineralization style (**Fig. 4.8-h; i**). In relation to alteration zone, the main Cu mineralization at the HLE prospect is spatially and temporally related to the chlorite-sericite and sericite alteration zones within the diorite quartz porphyries (**Fig. 4.10**). All three phases of causative porphyry intrusion are mineralized, but the main mineralization is intensely associated with the early-intermediate phases. Whole-rock geochemical data supported by petrographic observations indicate that the abundance of copper-gold-bearing sulfides decreases from the early to the late intrusion phases (**Table 4.1; Appendix 1; Table 4.2; Fig 4.8**). The diminishing in mineralization from early to late intrusion phases is also observed in other porphyry copper deposits worldwide, particularly along the eastern Sunda

arc such as Batu Hijau (Garwin, 2002; Idrus et al., 2009), Tumpangpitu (Harrison et al., 2018), and Selogiri (Sutarto et al., 2015). On the other hand, copper-gold content increases from the potassic to the chlorite-sericite, and sericite altered rocks (**Table 4.1; Appendix 1**). The latest observation is uncommon in porphyry Cu-Au systems, where higher copper-gold grade is spatially and genetically related to the potassic alteration zone. In addition, the mineralization in HLE is comparable to the Onto porphyry prospect, in which only about 8% of metal content is associated with the potassic zone, and most of the metal enrichment occurs in the high sulfidation zone (Burrows et al., 2020). Based on EPMA of sulfide minerals such as pyrite, chalcopyrite and bornite, the occurrence of gold (Au) is mostly related with chalcopyrite within intermediate stage.
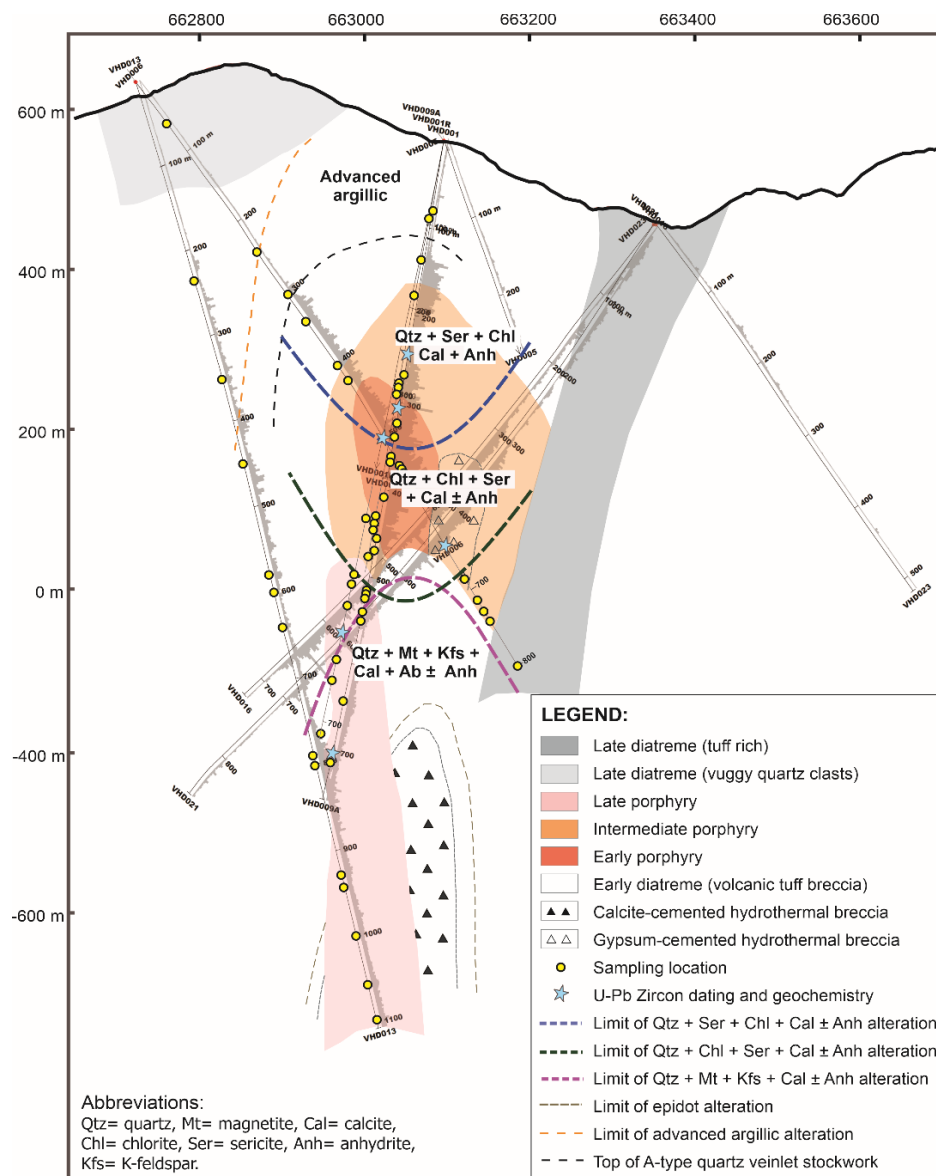
Figure 4. 13 Temporal and spatial geological model of the HLE prospect (modified from Sillitoe, 2012)

4.4   CONCLUSIONS

1. The causative intrusions in the HLE porphyry Cu-Au prospect mainly consist of quartz diorite and diorite porphyry with calc-alkaline magma affinity, which formed in an active continental margin.

2. Th/Ce $\geq$ 0.1 and Zr/Y > 3 in the whole-rock geochemistry data of intrusive rocks in the HLE prospect suggest signatures of input of sediment cycle and continental crust.

3. Two styles of mineralization are found in the HLE porphyry Cu-Au prospect including quartz-sulfide veins and disseminated sulfides.

4. Chalcopyrite is the major copper-bearing sulfide in the HLE prospect and is principally associated with the main stage of mineralization and related to the chlorite-sericite and sericite alteration zone, rather than the early stages of mineralization (potassic alteration).

5. The occurrence of gold is mostly related with chalcopyrite within intermediate stage.

CHAPTER 5
HYDROTHERMAL FLUID EVOLUTION OF HUMPA LEU EAST PORPHYRY Cu-Au PROSPECT

5.1 INTRODUCTION

Some differences may exist between upper and lower portions of the porphyry Cu deposits (Sillitoe, 2010). In porphyry Cu systems, hydrothermal fluid will depart from points of partial-rock buffering and subsequently cool in contact with already partially altered rock (Heinrich, 2004). Overprinting of alteration and mineralization in this deposit type is common (Sillitoe, 2010), and changing fluid conditions, particularly temperature, are recorded by the cross-cutting veins and associated wall-rock alteration. The formation of hydrothermal minerals, particularly white mica, generally is initiated as a halo along the sulfide ± quartz veins and becomes more pervasive as a result of overlapping alteration halos (Sillitoe, 2010). The evolution of ore-forming fluid, including the formation temperature of hydrothermal assemblage, can be inferred based on fluid inclusion (Roedder, 1979; Bakker and Diamond, 2006; Shepherd, 1981; Bakker, 2001; Fall et al., 2011), sulfur isotope (Ohmoto and Rye, 1979; Rye, 2005; Hedenquist et al., 2017), as well as mineral geothermometry such as chlorite (Cathelineau and Nieva, 1985; Cathelineau, 1988; Jowett, 1991) and quartz (Wark and Watson, 2006; Ferry & Watson, 2007; Thomas et al., 2010).

The inclusion of fluids in rocks can reveal a great deal about the geofluids that were involved in their petrogenesis. Temperature, pressure, density, salinity, and composition of fluids can be determined from such inclusions (Roedder, 1979; Bakker and Diamond, 2006) (Roedder, 1979; Bakker and Diamond, 2006). Fluid inclusions occur in different patterns, such as those found isolated in a host crystal trapped during initial crystallization or in trails along former microfractures or grain boundaries (Randive et al., 2014). Studying the abundance, orientation, and chemistry of fluid inclusions provides the history of formation and alteration over time, contributing to both fundamental processes in geology and the exploration of mineral deposits (Randive et al., 2014). The trapped fluids may be liquid, vapor, or supercritical fluid, and the composition of the trapped fluid may include essentially pure water, brines of various salinity, gas or gas-bearing liquids, and silicate, sulfide, or calcite melts, among others (Roedder, 1984; Shepherd et al., 1985).

Sulfur isotope studies of sulfide-sulfate minerals are especially useful for unraveling the geochemical history of geological systems. All sulfide-sulfate minerals can yield sulfur isotope data. The equilibrium partitioning of sulfur isotope between sulfide and sulfate is a function of temperature (e.g., pyrite-anhydrite; sphalerite-aqueous sulfate (Ohmoto and Rye, 1979); and alunite-pyrite (Hedenquist et al., 2017). Studies can also use as a tracer to fingerprint various sources of sulfur, and to identify physical and chemical processes such as evaporation of water, mixing of waters, and reduction of sulfate to sulfide (Rye, 2005).

Chlorite geothermometry has been popularized by Cathelineau since 1985. Cathelineau and Nieva (1985) found a positive correlation between Al^{IV} and temperature and suggested that Al^{IV} could be used as a geothermometer. Based on new chlorite analyses and fluid inclusion data from Los Azufres, Cathelineau (1988) derived the following relationship between temperature (T^{O}C) and Al^{IV}. Cathelineau (1988) suggested that the equation has the potential to be used as a chlorite geothermometer of general applicability in diagenetic, hydrothermal, and metamorphic settings because the value of Al^{IV} appears to be independent of rock lithology. Furthermore, Jowett (1991) suggested a similar type of correction, derived from an isothermal Fe/(Fe+Mg) normalization based on Salton Sea and Los Azufres chlorite compositions. Jowett (1991) claimed that this Fe-Mg-modified geothermometer is applicable to a variety of systems in the range ~150 to ~325 for chlorites with Fe/(Fe +Mg) values < 0.6.

Quartz is a common mineral in siliceous igneous rocks, including volcanic rhyolite and plutonic granites. In addition, it is common in metamorphic rocks at all grades of metamorphism and is the chief constituent of sand. Sedimentary rocks also contain it since it is highly resistant to chemical weathering. The TitaniQ method to revealing the temperature from quartz geochemistry has been used for ignous rocks and hydrothermal (Wark and Watson, 2006; Lowers et al. 2007; Ferry & Watson, 2007; Thomas et al., 2010), as well asmetamorphic rocks (Spear & Wark 2009; Peterman & Grove 2010). The method also provides an opportunity to analyze different quartz zones (Holness & Sawyer 2008).

This chapter will describe the fluids composition, formation temperature, hydrothermal fluid evolution of the alteration based on microthermometry, isotope sulfur, chlorite, and quartz geothermometer. Furthermore, this chapter also will report for the first time the presence of CO_2-rich hydrothermal fluid.

5.2 RESULTS

5.2.1 Petrography of fluid inclusions

The investigation of fluid inclusions in this study was mostly focused on the early stage (A/AB veins) quartz which is characterize of Qtz-Mt-Kfs-Cal-Ab-Anh (potassic), intermediate stage (B veins) Qtz-Chl-Ser-Cal-Anh (chlorite-sericite) and the late stage (D veins) Qtz- Ser-Chl-Cal-Anh (sericite). Petrography was focused on fluid inclusions hosted in quartz of the A, AB, B and D vein types (see **Fig 4.8**; **Table 4.2**) obtained from drill cores VHD 009A/474,2 VHD 009A/520, and VHD 013/1069. A detail morphology of fluid inclusion can be seen in **Figure 5.1**. The classification and terminology for the fluid inclusion types follow those of Roedder (1971). Based on phase ratios observed at room temperature, the fluid inclusions in quartz veins are categorized into monophase vapor-rich "V" (V=100%), multiphase-vapor rich "S+V±L" (S<50%), and liquid-rich two-phase "L+V" (L>50%) inclusions (**Table 5.1**).

Monophase vapor-rich "V" (V=100%), are typically 10-50 µm in length and 20-30 µm in width with spheroidal, discoidal/oval to long-oval (cylindrical) in shape, and no daughter minerals are present. This type is present in all stages of a veins (A, AB, B, and D), but monophase vapor-rich inclusions are relatively more abundant in early to transition stages (A, AB, and B veins). However, monophase vapor-rich inclusions are closely related to the early stage potassic alteration. Multiphase-vapor rich "S+V±L" (S<50%) are typically 10-25 µm in mean dimension, equidimensional to slightly elongate. Furthermore, liquid-rich two-phase "L+V" (L>50%) are typically up to 20 µm in length and 5-20 µm in mean dimension, with a spheroidal, tubular, equant to irregular in shape, no daughter minerals are found. This type is present in all stages of veins (A, AB, B, and D), but the liquid-rich type is more abundant in the late stage (D veins) than the other two inclusion types.

Daughter minerals include hematite, halite, sylvite, and other opaque phases, occur in multiphase-vapor rich inclusions S+V±L. The hematite daughter mineral typically shows orange-deep red internal reflection color, translucent and sometimes opaque with various sizes (3-20 µm). Halite and sylvite show similarities in properties, being translucent, cubic, and non-birefringent, although halite has a higher relief than the sylvite (**Table 5.2**; **Fig 5.1**).
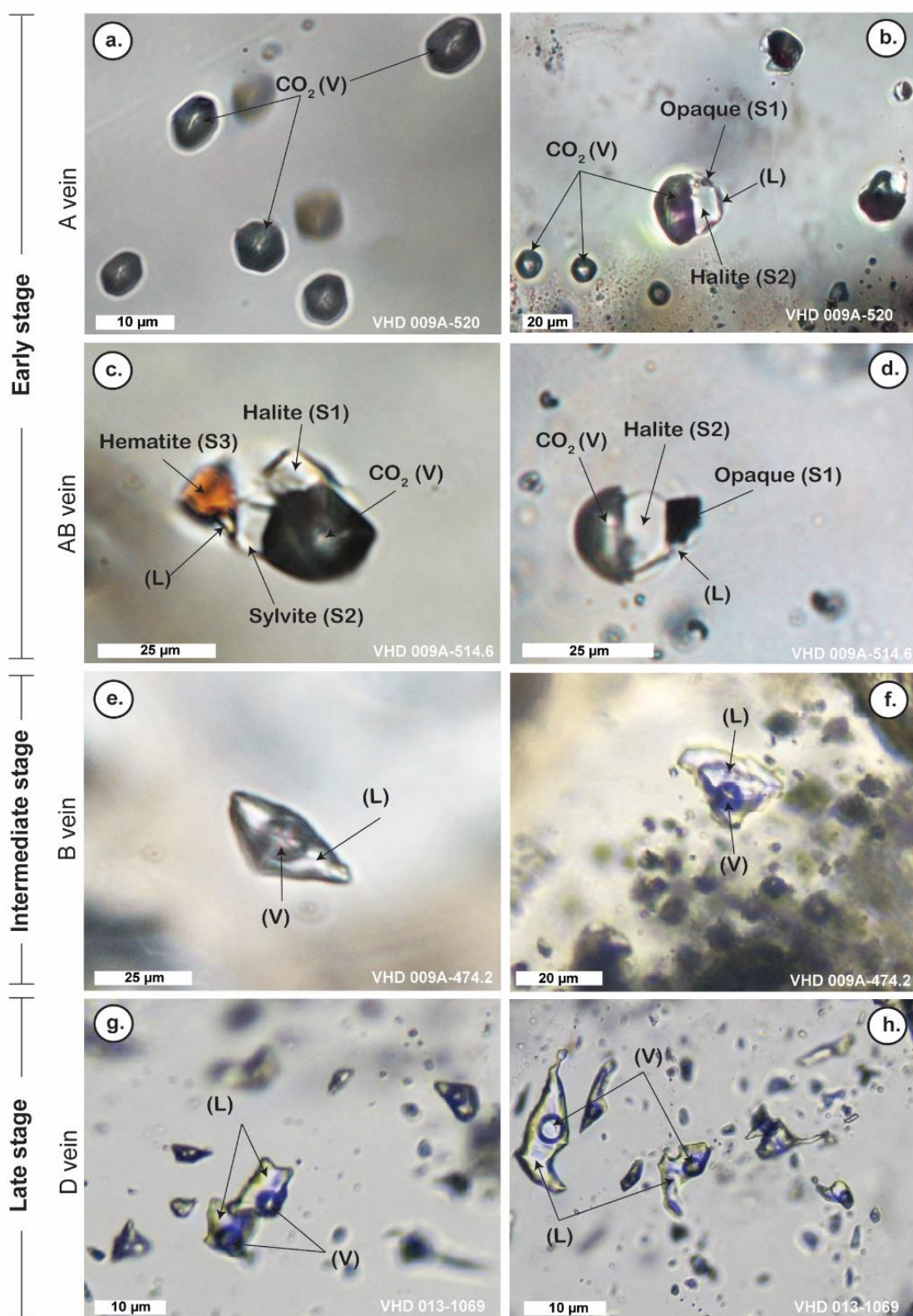
Figure 5. 1 Photomicrographs of fluid inclusions in A; AB veins (early stage) and B veins (intermediate stage) and D veins (late stage) in the HLE porphyry Cu-Au prospect. **a**: Monophase vapor-rich "V" (V=100 %). **b, c, d**: Multiphase-solid "V+S±L" (S<50 %). **e, f, g, h**: Liquid-rich two-phase "L+V" (L>50 %) after Sheperd (1985). *Abbreviations:* V=Vapor, L= Liquid, S= Solid.

57

Table 5. 1 Classification of fluid inclusions hosted in quartz veins/veinlets within the HLE porphyry Cu-Au prospect in Hu'u district , Sumbawa Island, Indonesia (after Roedder, 1971).
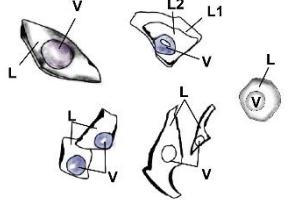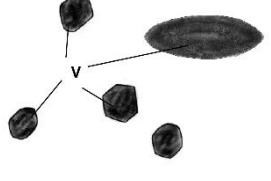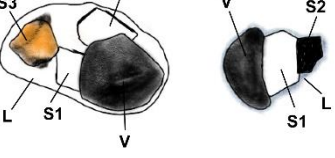
Physical state	Composition	Typical examples
Liquid-rich biphase	Liquid-rich "L+V", typically up to 20 µm in length and 5-20 µm in mean dimension; (< 50 vol. % vapor), no daughter minerals are found, spheroidal, tubular, equant to irregular shape	
Monophase vapor	Vapor-rich "V" (V=100%), spheroidal, discoidal/oval to long oval (cylindrical) shape, typically, 10-50 µm in length and 20-30 µm in width; no daughter minerals are present.	
Multiphase vapor rich	Vapor-rich, "S+V±L" (S<50%), equidimensional to slightly elongate, typically 10-25 µm in mean dimension; abundant of daughter minerals, which include halite, sylvite, hematite, and other opaque.	

Table 5. 2 Physical and optical properties of daughter minerals in fluid inclusions.

Daughter minerals	Physical and optical properties
Halite	Translucent, cubic, non-birefringent, high relief
Sylvite	Translucent, cubic, non-birefringent, low relief
Hematite	Opaque to translucent, platy hexagonal, orange-deep red
sulphide (?)	Opaque, octahedral

5.2.2. Microthermometry

The microthermometry study of fluid inclusions is done using a heating and cooling stage, a device that allows increasing or decreasing temperature over a wide range, between –200°C and +1500°C approximately (Randive et al., 2014). This stage is placed on a microscope, so that the phase changes occurring, as well as the temperature at which these changes take place can be observed. As a normal working protocol, the fluid inclusions are cooled to the lowest temperature that the stage can achieve and subsequently, the phase changes taking place are observed while the temperature rises towards room temperature again (Randive et al., 2014). This temperature is characteristic of each system and, therefore, helps to associate the

composition of the fluid inclusion with a chemical system (Shepherd, 1981; Bakker, 2001; Fall et al., 2011).

The vapor-rich multiphase fluid inclusions (V+S+L) in the A veins related to the potassic alteration have homogenization temperatures of 1004−1247 °C (mode: 1209 °C) and salinities of 41.7−52.1 wt.% NaCl eq. (mode: 45 wt.% NaCl eq.), (**Table 5.3**; **Fig. 5.5**). Two-phase (V+L) fluid inclusions in the A veins, which were probably trapped at the same time to the vapor-rich multiphase fluid inclusions, showed homogenization temperatures of 378−503 °C (mode: 460) with salinities of 18.5−22.9 wt. % NaCl eq. (mode: 22 wt.% NaCl eq.). Two-phase (L+V) fluid inclusions in the B veins associated with the chlorite-sericite alteration have homogenization temperatures of 236−324 °C (mode: 270 °C) and salinities of 10.7−14.4 wt. % NaCl eq. (mode: 12.4 wt.% NaCl eq.), indicating a non-boiling state of fluids (**Table 5.3**; **Fig. 5.5**). The two-phase (L+V) fluid inclusions in the D veins associated with the sericite alteration have homogenization temperatures of 230-270 °C (mode: 250 °C) and salinities of 5.6−9.4 wt.% NaCl eq. (mode: 7.6 wt.% NaCl eq.), indicating a non-boiling state of fluids (**Table 5.3**; **Fig. 5.5**). The fluid inclusions in the A-veins in the early stage would have been mainly magmatic fluids, while the decrease of temperatures of the fluids for the B and D veins in the intermediate, and late stages, respectively, was probably due to mixing of meteoric water (e.g. Shepherd et al., 1985).

Table 5. 3 Summarized of microthermometry data measurement in early, intermediate, and late stage veins.

Alteration type	Vein Stage	Fluid inclusion Type	Statistical parameter	Th temp. (°C)	Tm temp. (°C)	Halite dissolve temp. (°C)	Salinity (Wt. % NaCl equiv.)
Sericite	Late (D vein)	Biphase (L+V), n=30	Mode	250	−4.6	nd	7.6
			Minimum	229	−6.2	nd	5.6
			Maximum	294	−3.4	nd	9.4
Chlorite-sericite	Inter. (B vein)	Biphase (L+V), n=12	Mode	270	−9.4	nd	12.4
			Minimum	236	−12.8	nd	10.7
			Maximum	324	−7.6	nd	14.4
Potassic	Early (A vein)	Biphase (L+V), n=8	Mode	470	−13.0	nd	22.0
			Minimum	378	−14.1	nd	18.5
			Maximum	503	−11.4	nd	22.9
		Multiphase (V+S+L), n=29	Mode	1209	nd	377	45.0
			Minimum	1004	nd	313	39.2
			Maximum	1247	nd	441	52.1

Abbreviations: Th= homogenization temperature, Tm= melting temperature, and n.d.= not determined
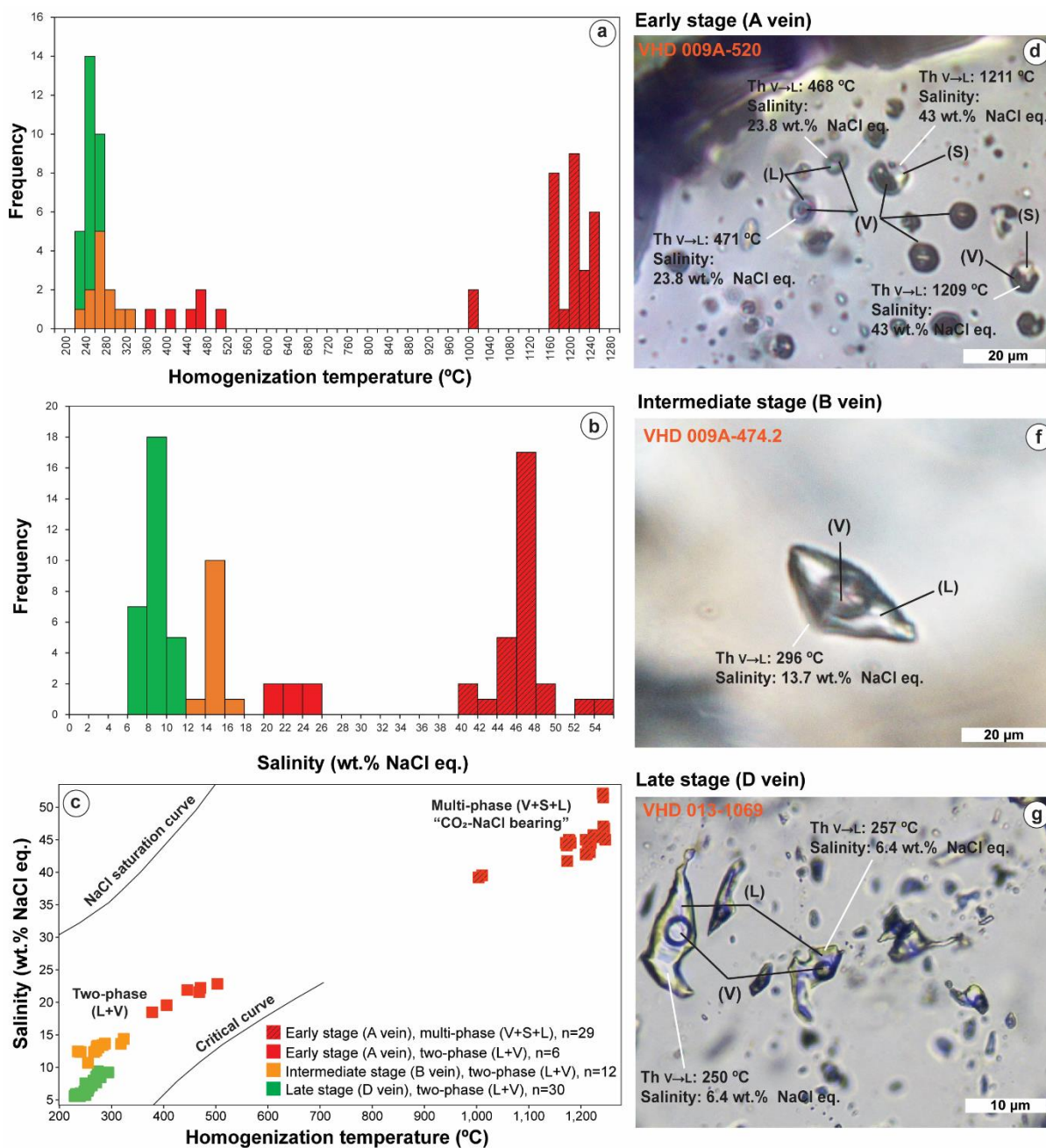
Figure 5. 2 Frequency plots of homogenization temperature (ºC) and salinity (wt.% NaCl eq.) related to the early (A vein), intermediate (B vein) and late stage (D vein). (**c**) Correlative plots for homogenization temperature (Th) vs. Salinity (wt. % NaCl eq.) of fluid inclusion related to the early (potassic), intermediate (chlorite-sericite) and late stage (sericite). (**d, e, f**). Photomicrograph of fluid inclusions phase within early, intermediate, and late stage. Abbreviations: V=Vapor, L= Liquid, S= Solid.

5.2.3 Raman Spectroscopy

The Raman spectroscopy indicated the presence of CO_2 in vapor (monophase) inclusions. The vapor phase in biphase (V+L) and multiphase (V+L+S) fluid inclusions includes CO_2 (**Fig. 5.6**). In Raman spectra CO_2 can be identified by the presence of two main peaks at 1,388 and

60

1,285 cm^{-1} (Frezzotti, 2012; Hurai et al., 2015). The formula of Yamamoto & Kagi (2006): -00111808*($\triangle$ -100)^8+0.04498451*($\triangle$ -100)^7-0.7727143*($\triangle$ -100)^6 + 7.4128146 *($\triangle$ -100)^5-43.468301*($\triangle$ -100)^4+159.54433*($\triangle$ -100)^3-357.7651*($\triangle$ -100)^2+ 48.2404 *($\triangle$ -100) -240.461, was used to calculate the density of the vapor phase. The density of CO_2 in the monophase vapor-rich is about 0.124 g/cm^3 and can be categorized into low density.
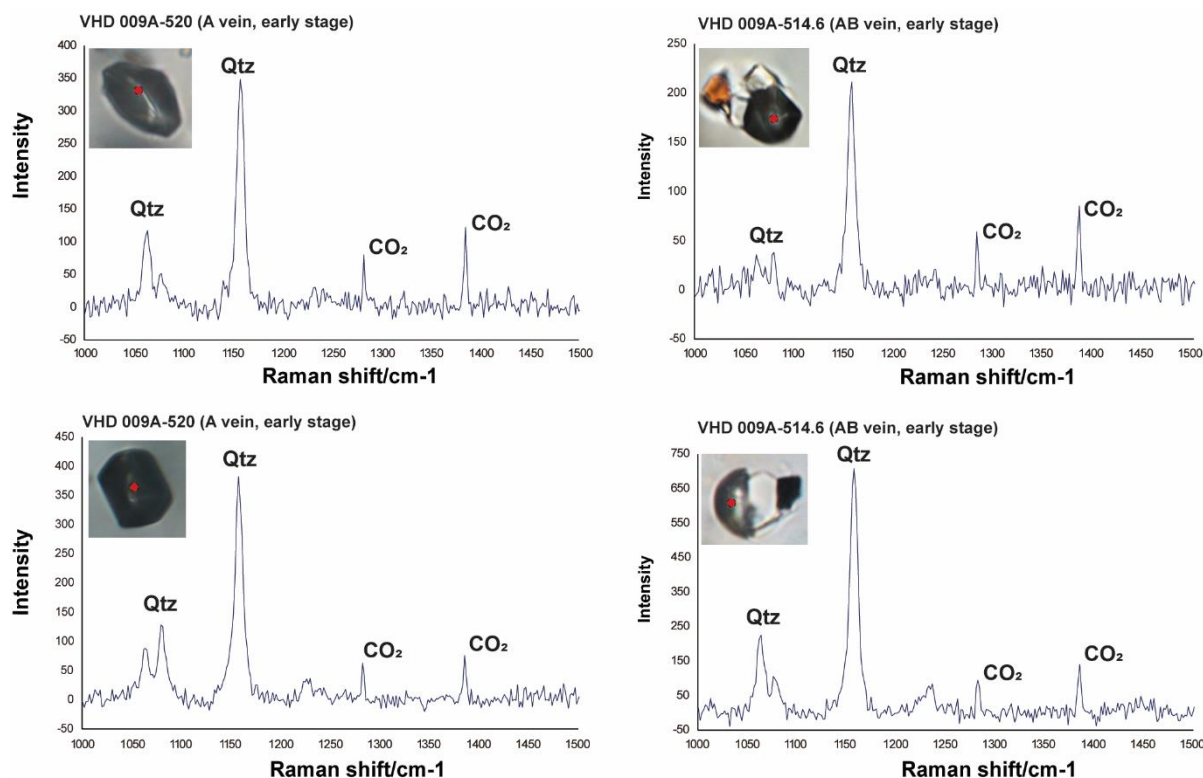
Figure 5. 3 Profiles of laser Raman spectroscopy for fluid inclusions which is focused on early stage. Vapor inclusion showing the CO_2 peaks (1388 and 1285 cm^{-1}) with CO_2 density of about 0.124 g/cm^3.

5.2.4 Chlorite composition

On the basis of the petrography analysis, chlorite in the HLE prospect is pale green in plane polarized light, very weak pleochroism (brown, deep green, gray), usually with anomalous deep berlin blue interference colors, and low-moderate relief. The crystal size of chlorite varies widely from 10 µm to larger than 1 mm present as a vein and disseminated. Disseminated grains of chlorite mostly replace plagioclase phenocrysts and mafic minerals. In general, chlorite minerals are distributed in almost all alteration zones including potassic, chlorite-sericite, and sericite alteration zones (**Fig. 5.7**).

Petrographically, there are two main genetic types of chlorite in the HLE porphyry prospect ,which are chlorite produced by alteration of plagioclase/mafic minerals (**Fig. 5.7-b-**

d) and chlorite precipitated from Fe and Mg-rich hydrothermal fluids , as veins or cracks between minerals (**Fig. 5.7-a-c**). The presence of chlorite minerals within potassic alteration is probably as a low-temperture overprinting of initial biotite.
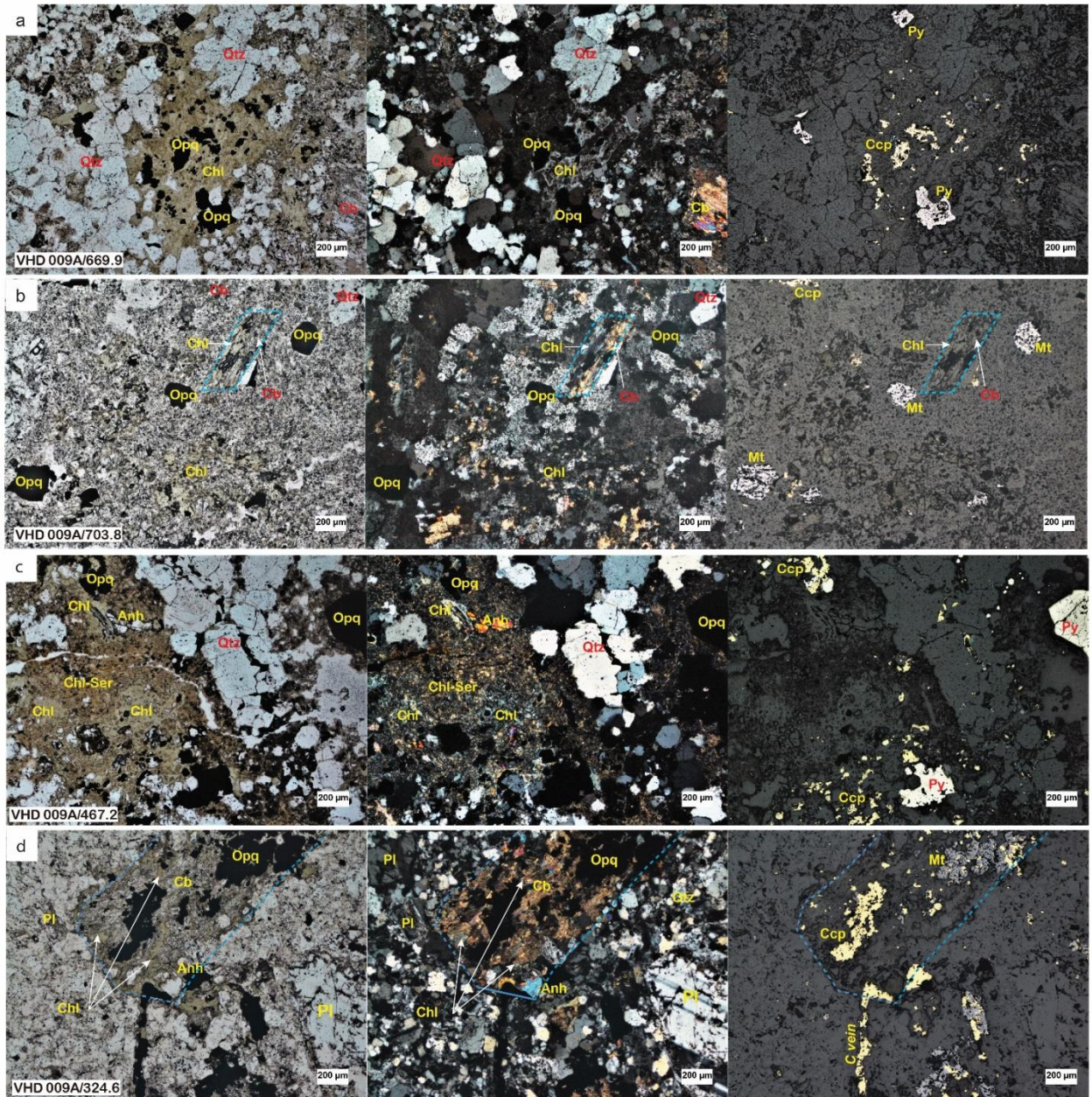
Figure 5. 4 Chlorite petrography samples which representative of the potassic, chlorite-sericite and sericite zone.

Chlorite geochemistry results in potassic, chlorite-sericite and sericite zone alteration are listed on **Appendix 5.** A comparison of the elements in the three alteration types shows significant differences between FeO, MgO, and MnO (**Appendix 5; Table 5.3; Figure 5.8**). The potassic alteration has lower Fe and Mn but higher Mg than chlorite-sericite and sericite alteration. The composition of Mg in chlorite-sericite alteration has a lower value than in

potassic and sericite alteration. However, in sericite alteration, the Fe concentration is higher than in potassic and chlorite-sericite alteration. Furthermore, chlorite geothermometry was calculated based on the element Al^{IV} using the formula from Jowett (1991), where chlorite chemistry showed no significant temperature difference in the three alterations. In addition, most of the chlorite minerals are classified as Clinochlore (Mg-chlorite) Wang et al., 2018 (**Fig. 5.9**).

Table 5. 4 Summary of EPMA analysis result of chlorite minerals in potassic, chlorite-sericite and sericite alteration

Pot (n=42)	SiO2	TiO2	Al2O3	FeO	MnO	MgO	CaO	Na2O	K2O	CuO	CoO	ZnO	T (°C)
Max	29.4	0.11	19.0	21.8	0.82	22.1	0.36	0.12	0.10	0.51	0.05	0.22	305
Min	26.9	0.00	16.3	17.7	0.46	17.8	0.10	0.00	0.01	0.00	0.01	0.05	264
Avg	28.2	0.03	17.5	19.6	0.67	20.0	0.23	0.02	0.03	0.07	0.03	0.11	283
Chl-Ser (n=106)	SiO2	TiO2	Al2O3	FeO	MnO	MgO	CaO	Na2O	K2O	CuO	CoO	ZnO	T (°C)
Max	32.0	0.65	20.6	33.1	2.88	19.1	0.49	0.43	0.97	0.12	0.08	0.45	384
Min	24.3	0.00	14.4	12.0	0.34	10.0	0.06	0.00	0.01	0.00	0.01	0.10	185
Avg	27.3	0.04	18.1	20.7	1.37	15.8	0.18	0.03	0.16	0.03	0.04	0.24	277
Ser (n=40)	SiO2	TiO2	Al2O3	FeO	MnO	MgO	CaO	Na2O	K2O	CuO	CoO	ZnO	T (°C)
Max	29.1	0.10	18.3	24.2	2.57	19.7	0.32	0.07	0.06	0.39	0.06	0.51	301
Min	26.7	0.00	16.2	21.1	1.05	15.7	0.16	0.01	0.01	0.00	0.02	0.20	263
Avg	27.7	0.03	17.1	22.3	1.76	17.4	0.23	0.03	0.03	0.08	0.04	0.30	285
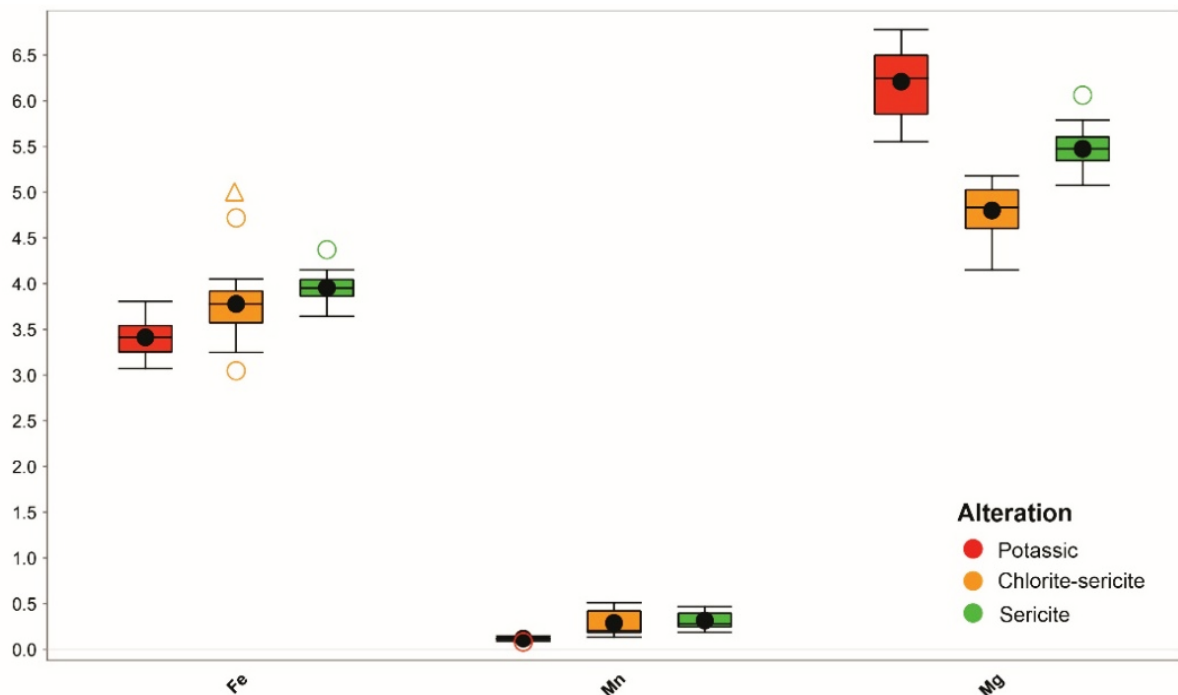
Figure 5. 5 Distribution of trace element of Fe, Mn, and Mg in potassic, chlorite-sericite, and sericite alterations
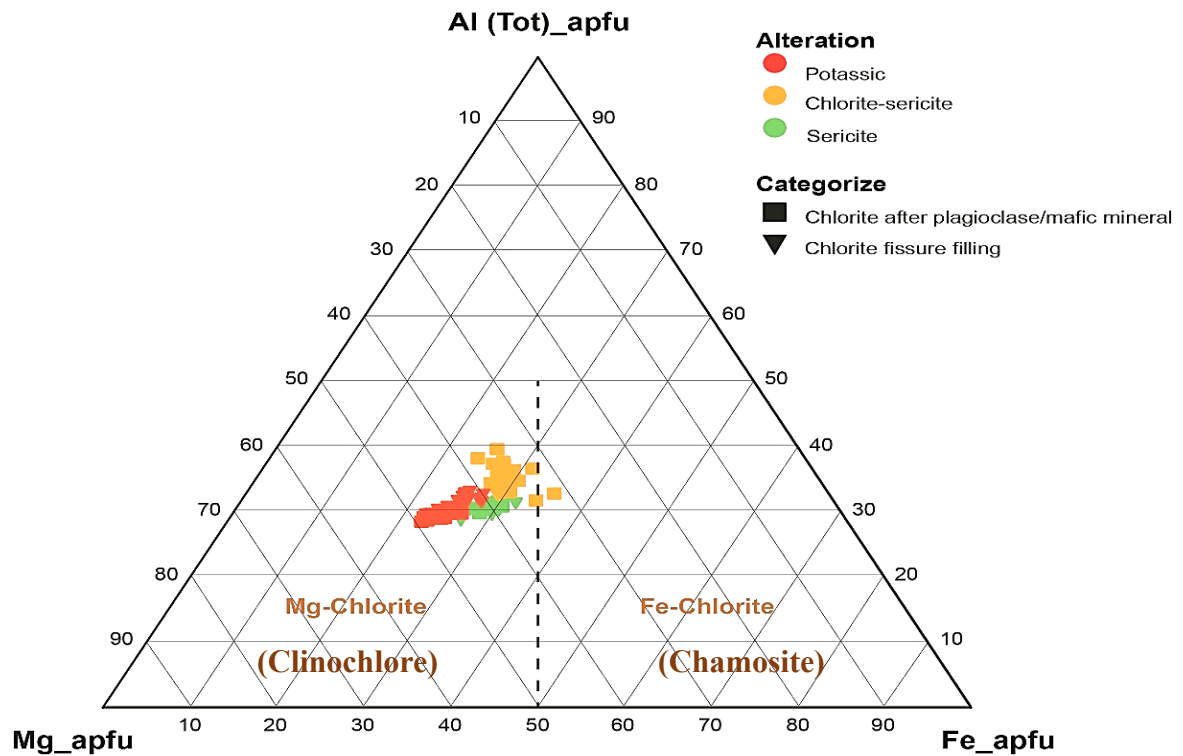
Figure 5. 6 Chlorite classification using cations of Si, Mg and Fe after Wang et al.,2018.

5.2.5 Trace element composition of quartz

The trace element within quartz in A-AB veins, related to potassic alteration has Al ranges from below detection limit to 1762 ppm (avg. 80 ppm), Na below detection limit to 2511 ppm (avg. 115 ppm), K ranges below detection limit to 548 ppm (avg. 40 ppm), Ti range from 36 to 312 ppm (avg. 139 ppm), Fe ranges below detection limit to 443 ppm (avg.74 ppm), Mn ranges below detection limit to 54 ppm (avg. 3 ppm), (**Appendix 6**). Quartz in B veins has Al from below detection limit to 720 ppm (avg. 160 ppm), Na below detection limit to 1025 ppm (avg. 229 ppm), K ranges below detection limit to 274 ppm (avg. 58 ppm), Ti range from 60 to 234 ppm (avg. 112 ppm), Fe ranges below detection limit to 194 ppm (avg.74 ppm), Mn ranges below detection limit to 23 ppm (avg. 4 ppm), (**Appendix 6**). Quartz in potassic alteration which is related with A-AB vein such as Al ranges from below detection limit to 1921 ppm (avg. 575 ppm), Na below detection limit to 2737 ppm (avg. 820 ppm), K ranges below detection limit to 58 ppm (avg. 12 ppm), Ti ranges below detection limit to 312 ppm (avg. 15 ppm), Fe ranges

below detection limit to 443 ppm (avg.94 ppm), Mn ranges below detection limit to 31 ppm (avg. 7 ppm), (**Appendix 6**).

The variation of the element composition of the three alteration types is clearly visible in the **Appendix 6**, **Table 5.4** and **Figure 5.12.** Quartz veins associated with potassic alteration have lower Fe and Mn than the quartz vein in chlorite-sericite and sericite alteration. Mg content in chlorite-sericite alteration is significantly different from potassic and sericite alteration, where the Mg concentration in chlorite-sericite alteration is lower than in potassic and sericite alteration.

Quartz crystallization temperatures were calculated by the Ti-in-quartz method (Wark and Watson, 2006). The geothermometer can be applied even in the absence of rutile, if the activity of Ti can be estimated. For rutile-present conditions, $\alpha TiO_2 = 1$ and it will provide a minimum temperature of equilibration (Wark and Watson, 2006); if rutile is absent, $0 < \alpha TiO_2 < 1$ or $\alpha TiO_2 = 0.7$ (Ferry & Watson, 2007). If rutile is absent, the temperature can be estimated based on the equation: $T (^oC) = -3765 / [(\log X_{qtz/Ti} / \acute{a}TiO_2) - (5.69)] - 273$, and if rutile absent: $T (^oC) = -3765 / [(\log X_{qtz/Ti}) - 5.69)] - 273$. Generally, vein quartz in the HLE prospect shows anhedral texture with a suture contact as a response to pressure.

Quartz geothermometry estimates in potassic alteration range from 632 to 905 ^oC (avg. 782 ^oC), chlorite-sericite ranges from 653 to 810 ^oC (avg. 713 ^oC), and sericite alteration ranges from 470 to 738 ^oC (avg. 529 ^oC) (**Table 5.4**). The temperature of a potassic alteration is slightly higher than the chlorite-sericite alteration, while the temperature of sericite is lower than potassic and chlorite sericite alteration.

Table 5. 5 Summary of EPMA analysis result of quartz minerals related to early stage (A-AB vein), intermediate stage (B vein) and late stage (D vein)

Vein A-AB (n=80)	Si (ppm)	Al (ppm)	Na (ppm)	K (ppm)	Ti (ppm)	Fe (ppm)	Mn (ppm)	T ^oC
Max	476517	1762	2511	548	312	443	54	905
Min	455413	0	0	0	36	0	0	638
Avg	468721	80	115	40	139	74	3	782
Vein B (n=19)	Si (ppm)	Al (ppm)	Na (ppm)	K (ppm)	Ti (ppm)	Fe (ppm)	Mn (ppm)	T ^oC
Max	472722	720	1025	274	234	194	23	810
Min	461817	0	0	0	60	0	0	653
Avg	468561	160	229	58	112	74	4	713
Vein D (n=11)	Si (ppm)	Al (ppm)	Na (ppm)	K (ppm)	Ti (ppm)	Fe (ppm)	Mn (ppm)	T ^oC

	Max	471591	1921	2737	58	132	443	31	738
	Min	467253	0	0	0	0	0	0	470
	Avg	469866	575	820	12	15	94	7	529
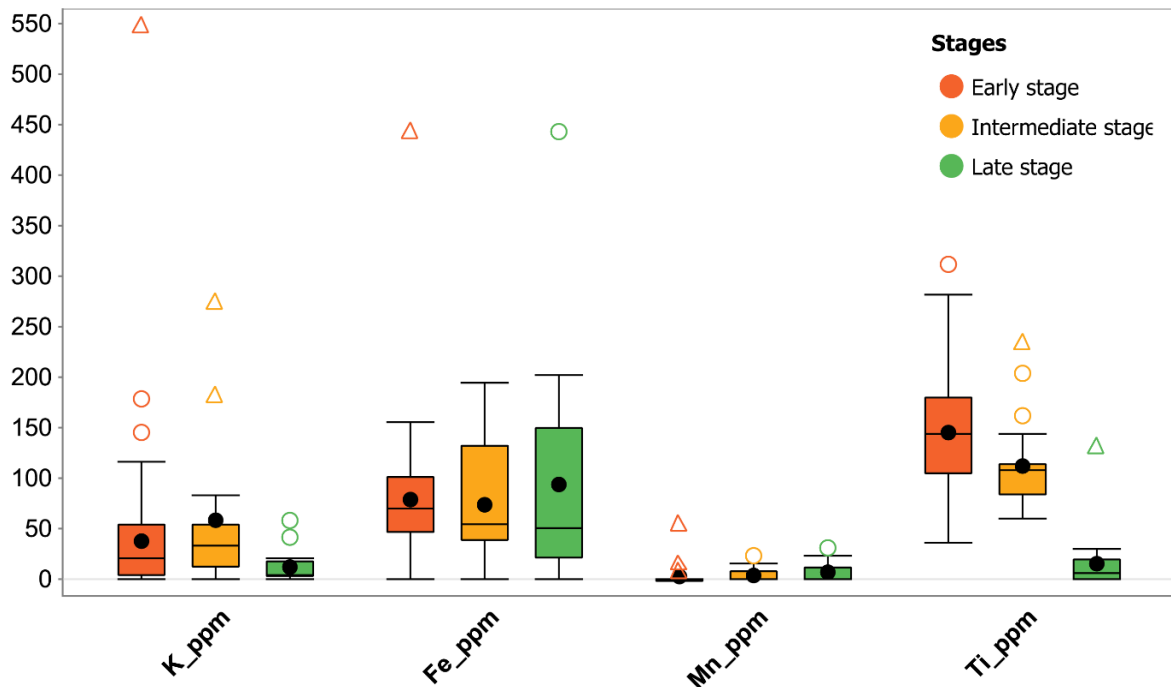
Figure 5. 7 Distribution of trace element of K, Fe, Mn, and Ti of quartz minerals in early, intermediate, and late stage of quartz vein

5.2.6 Sulfur isotopes

Sixteen samples of sulfide and sulfide minerals were analyzed by sulfur isotope at the Economic Geology laboratory at Akita University. The formula of temperature estimates from $\delta^{34}S$ (‰) of pyrite-anhydrite pair has been adopted from the equation after (Ohmoto and Lasaga, 1982; Ohmoto and Rye, 1979): $T\ (^OC) = [(6.063 \times 10^6)/(\Delta-0,56)]^{1/2}$. Sulfides analyzed consists of chalcopyrite and pyrite, while sulfate mineral consists of barite, anhydrite, and gypsum. The sulfur isotope results of sulfide and sulfate mineral samples from the HLE prospect are shown in **Figure 5.13** and **Table 5.5**. The $\delta^{34}S_{sulfides}$ across alteration types show a wide range values between -3.8 to $+3.4$ ‰, while the $\delta^{34}S_{sulfates}$ values are between $+9.9$ and $+12.4$ ‰ (**Fig. 5.13**). The $\delta^{34}S_{sulfides}$ of potassic alteration, consist of chalcopyrite, range from -2.1 to $+0.9$ ‰. However, $\delta^{34}S_{sulfides}$ of chalcopyrite and pyrite from the chlorite-sericite alteration have a wider range from -3.8 to $+3.4$ ‰. The $\delta^{34}S_{sulfides}$ of sericite alteration, consist of pyrite and chalcopyrite, ranging from -2.9 to -0.5 ‰. There is no significant difference for

δ^{34}S sulfate values across chlorite-sericite and sericite alteration. The delta (Δ) value in between coexisting sulfate and sulfide could be used to estimate isotopic temperature following equation by Seal (2006). As shown in **Table 5.5**, the $\Delta\delta^{34}$S$_{sulfates-pyrite}$ in chlorite-sericite alteration is 13.6 ‰ (n=1), while the $\Delta\delta^{34}$S$_{sulfates-pyrite}$ in sericite alteration range from ~13.0 to ~14.0 ‰ (n=3).
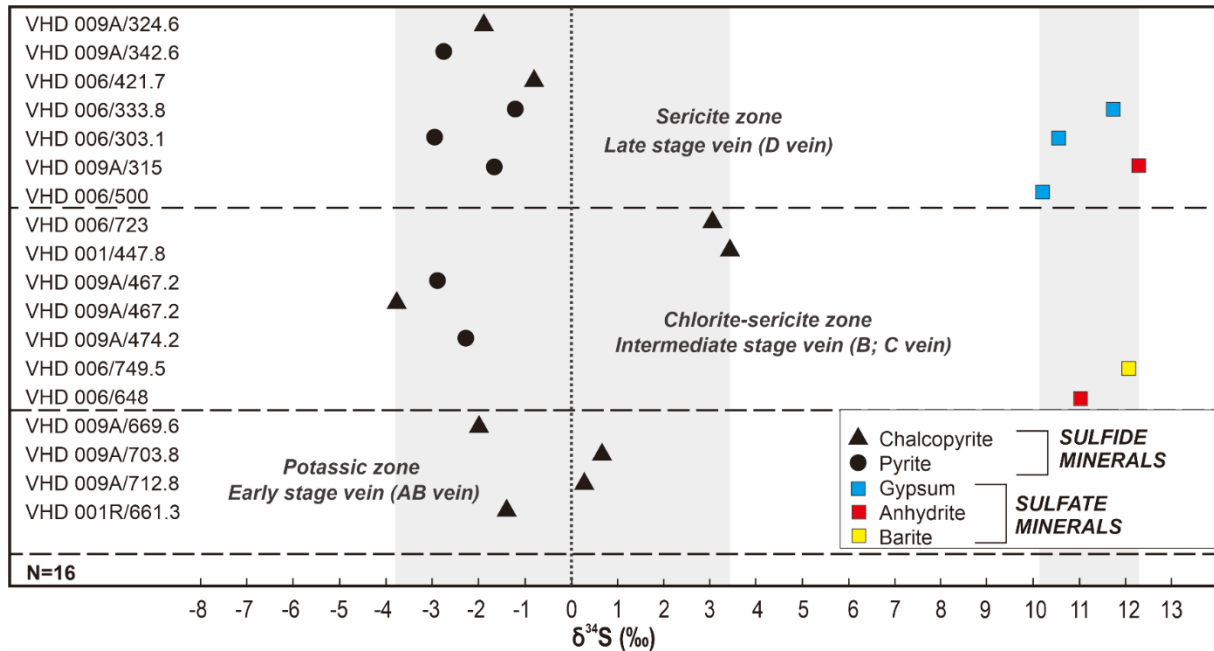
Figure 5. 8 The isotopic Range of sulfur isotopic ratios δ^{34}S (‰) of sulfide and sulfate minerals from the different zone of the alteration of the HLE porphyry Cu-Au prospect.

Table 5. 6 The isotopic δ^{34}S (‰) values of sulfide and sulfate minerals from causative intrusive in the drill cores of the HLE porphyry Cu-Au prospect.

| No | Sample ID | Alteration/vein type | Mineral | δ^{34}S (‰) | | | | | Δ_{Anh-Py} | T (°C) |
				Ccp	Py	Anh	Gyp	Ba		
1	009A/324.6	Ser (D vein)	Ccp	-1.84	-2.80					
2	006/421.7	Ser (D vein)	Ccp	-0.54						
3	006/333.8	Ser (D vein)	Py		-1.58		11.8		13.4	414
4	006/303.1	Ser (D vein)	Py		-2.94		10.5		13.4	413
5	009A/315	Ser (D vein)	Py		-1.72	12.38			14.1	396
6	006/500	Ser (D vein)	Gyp				10.23			
7	006/723	Chl-ser (C vein)	Ccp	3.14						
8	001/447.8	Chl-ser (C vein)	Ccp	3.40						
9	009A/467.2	Chl-ser (C vein)	Py	-3.79	-2.94					
10	009A/474.2	Chl-ser (B vein)	Py		-2.33					
11	006/749.5	Chl-ser (B vein)	Ba					12		
12	006/648	Chl-ser (Bvein)	Py		-2.35	11.24			13.6	409
13	009A/669.6	Pot (AB vein)	Ccp	-2.05						
14	009A/703.8	Pot (AB vein)	Ccp	0.70						
15	009A/712.8	Pot (AB vein)	Ccp	0.37						

16	001R/661.3	Pot (AB vein)	Ccp	-1.14						

The sulfur isotopic values $\delta^{34}S$ (‰) in the HLE prospect have similarities to several types of porphyry deposits worldwide, such as Ajo, Sierrita and Twin Bluffs, Ariz (Rye, 2005). The isotopic $\delta^{34}S$ (‰) values indicate that the sulfur was derived from igneous sources, either as magmatic fluids or by the dissolution of igneous sulfides.

5.3 DISCUSSION

5.3.1 Formation temperature of the Humpa Leu porphyry Cu-Au prospect.

In this chapter I will compare the formation temperature results from the fluid inclusion microthermometry and data of chlorite, quartz, and isotope sulfur geothermomety. According to microthermometry data, showing the extremely high homogenization temperatures of the vapor-rich multiphase fluid inclusions (V+S+L) in the A veins related to the potassic alteration close to 1000 °C suggest the fluid boiling and entrapment of vapor in the fluid inclusions, and these are not the trapping temperature. Halite would have been present in the saturated hydrothermal fluids and some of those were accidentally trapped in the vapor-rich multiphase fluid inclusions. The homogenization temperatures of the vapor-rich multiphase fluid inclusions (V+S+L) in the A veins of the HLE prospect shows similarity with the multi-sloid incluisons of potassic in porphyry deposit of Grasberg (West Papua), which is range from 823 to 1300 °C (Mernagh and Mavrogenes, 2019; Mernagh et al., 2020).

The boiling temperature of 470 °C and salinity of 22 wt.% NaCl eq. of the fluid inclusion data for the A veins indicate a pressure of about 40 MPa (*cf.* Bodnar & Vityk, 1994; Bodnar, 2003), suggesting 1.5 km depth under the lithostatic condition with density of 2.7 g/cm^3. The modes of homogenization temperatures of fluid inclusions of the B and D veins, 270 °C and 250 °C can be converted to trapping temperatures of 305 °C and 285 °C, respectively, on the basis of the pressure correction with 40 MPa (*cf.* Potter, 1977). These indicate that the temperature of hydrothermal fluids gradually decreased from 470 °C, 305 °C, to 285 °C from the early, intermediate, and late stages, respectively.

The chlorite geothermometry using the formula from Jowett (1991) shows that all alteration types, including potassic, chlorite-sericite and sericite formed at approximate temperature between 263–301 °C (**Table 5.3**). The average temperature is about 285 °C. There is a very significant difference between the formation temperature of the potassic alteration based on microthermometry and chlorite geothermometer. Chlorite in potassic alteration may

be the result of over-printing by the intermediate/late stage fluids occurring at lower temperature. Therefore, the chlorite geothermometer related potassic alteration cannot be used to determine formation temperature. The different calculation methods for compositional geothermometers are reviewed in Caritat and Hutcheon (1993). According to the results of this comparative study, no single chlorite geothermometer performs satisfactorily under all natural conditions (different temperatures, coexisting assemblages, Fe/(Fe+Mg), fO2, etc.). Therefore, these authors suggest that chlorite geothermometry should be used cautiously along with other paleotemperature estimation methods. Regarding to quartz geothermometer, temperatures were estimated using the Ti-in-zircon thermometer from the equations of Wark & Watson (2006); Ferry & Watson (2007) whose calibration assumes crystallization under rutile and quartz-saturated conditions (aTiO2 = 1; aSiO2 = 1) at 10 kbar. According to the temperature calculation results, generally, the formation temperature of quartz mineral related potassic alteration ranges from 782 to 905 ^{O}C (avg. 638 ^{O}C). Formation temperature of chlorite-sericite alteration ranges from 713 to 810 ^{O}C (avg. 653 ^{O}C), while sericite alteration ranges from 529 to 738 ^{O}C (avg. 470 ^{O}C) (**Table 5.4**). The formation temperature of quartz mineral related potassic alteration is probably accurate because it is still consistent to microthermometry, where the temperature ranges is similar. In contrast, formation temperature of quartz related chlorite-sericite and sericite alteration temperature showing an overestimated comparing to the microthermometry fluid inclusion result. This is probably due to the quartz vein within the chlorite-sericite and sericite alteration zones that contain significant amounts of rutile. In most igneous systems, rutile is not part of the equilibrium mineral assemblage, and may form as a hydrothermal mineral. Thus, temperatures for quartz crystallization could not be calculated without first determining TiO$_2$ activity after Wark & Watson (2006).

The calculation of the formation temperature in the HLE prospect using sulfur isotope geothermometry only focused on chlorite-sericite and sericite zones, due to the availability of sulfide-sulfate pairs using the equation by Ohmoto and Lasaga (1982), Ohmoto and Rye(1979). The formation temperature of chlorite-sericite zone is 409 ^{O}C, while the sericite zone ranges from 396 to 414 ^{O}C (**Table 5.5**). Similar to the quartz geothermometer, the calculation of the formation temperature chlorite-sericite and sericite zone slightly overestimated compared to the microthermometry analysis. therefore, in terms of formation temperature estimated in this study I prefer to use the results from microthermometry of fluid inclusions.

5.3.2 CO₂-rich fluids related to the formation of calcite-rich potassic alteration and sulfide precipitation.

In the porphyry systems of the Sunda magmatic arc, the potassic alteration is generally characterized by biotite, formed from mafic minerals such as hornblende, primary biotite, and pyroxene Maryono et al. (2018); Sutarto et al. (2015). For example, in the Batu Hijau deposit, the potassic alteration is characterized by disseminated secondary biotite and the development of early veinlets composed of magnetite-biotite-quartz and the presence of A-type veins Idrus et al. (2009). In the Selogiri Porphyry deposit, the potassic alteration associated with microdiorite, which is characterized by magnetite-quartz-biotite ± K-Feldspar Sutarto et al. (2015).

Comparing to the other porphyry deposits such as Batu Hijau and Selogiri in the eastern Sunda arc, the potassic alteration in the HLE prospect has some differences including the presence of abundant M and A veins and secondary K-feldspar with abundant calcite accompanied by anhydrite and chlorite (see **Fig. 4.4** in the previous chapter). Secondary biotite was not found in the HLE prospect as it would have been totally replaced by chlorite. The occurrence of significant calcite-rich alteration at the HLE prospect is a rare case in porphyry systems, particularly compared to those along the eastern Sunda arc. Calcite is also present in the chlorite-sericite and sericite alteration zones. The occurrence of significant calcite-rich alteration at the HLE is unusual in porphyry systems, particularly those that occur along the eastern Sunda arc. Furthermore, calcite-rich alteration is also observed in the chlorite-sericite and sericite zones (**Fig. 4.4**). However, the presence of calcite in a potassic alteration zone has not been well reported in those publications. We revealed the presence of CO₂ gas in fluid inclusions for the HLE prospect using the laser Raman analysis (**Fig. 5.6**). Since there is no signature of late-stage calcite overprinting, the CO₂-rich bearing fluids of the HLE prospect were likely formed during the potassic alteration. The hydrothermal fluids with homogenization temperature of 460 ℃ and salinity of 22 wt.% NaCl eq. in the early stage were related to the calcite-rich potassic alteration, and this relationship is similar to that in other porphyry copper deposits in the Sunda magmatic arc except for the presence of calcite (e.g., Batu Hijau; Imai and Ohno (2005) and Selogiri; Imai et al. (2007).

The formation of calcite was likely caused by the reaction of CO₂-rich fluids and Ca-rich minerals (plagioclase and hornblende) in the HLE prospect. The CO₂-bearing fluids in porphyry deposits were documented in Bingham (Redmond et al., 2004), El Teniente (Klemm et al.,

2007), Butte (Rusk & Reed 2008), Meiduk porphyry (Asadi et al., 2013), and Zhunuo (Dai et al., 2021). These studies suggested that the CO_2-bearing fluids associated with deep magmatic sources. These deposits formed with different tectonic settings, *i.e.*, Bingham, El Teniente, and Butte formed in active continental margins where an oceanic plate subducts beneath a continent (Redmond et al., 2004; Klemm et al., 2007; Rusk & Reed 2008), while Zhuonuo formed in a post-collision extensional setting (Dai et al., 2021), and Meiduk formed in a continental-collision setting (Asadi et al., 2013).

Solubility of CO_2 in hydrothermal fluids is higher in conditions of higher temperature and lower salinity, and vice versa (Takenouchi & Kennedy, 1965), and we observed the evidence of fluid boiling for the fluid inclusions in the A-veins of the HLE prospect. Thus, we consider that 1) relatively large amount of CO_2 was present in early hydrothermal fluids in the HLE prospect, 2) CO_2 was degassed from the high salinity fluids during the boiling, 3) the degassing process concentrated CO_2 vapor in the hydrothermal fluids, and 4) CO_2-bearing hydrothermal fluids formed the calcite-rich potassic alteration zone.

Accidentally trapped solid phases such as hematite and sulfides were observed in the fluid inclusions of the A and AB veins, in addition to the daughter minerals of halite and sylvite. There is a report about the presence of chalcopyrite in fluid inclusions of A veins of the Batu Hijau deposit (Ryan et al., 2001). The presence of Cu-sulfides in fluid inclusions would be a signature of fertile hydrothermal fluids, *i.e.*, the fluids have a potential to transport copper. We observed the occurrences of CO_2-bearing fluid inclusions in the early stages (A and AB veins) and the intermediate stages (B veins) of the HLE prospect, which are associated with the Cu-sulfide mineralization as well as the calcite-rich potassic alteration. The calcite-rich potassic alteration and the presence of CO_2 gas in the fluid inclusions of the A, AB and B veins related to the main copper mineralization stage in the HLE prospect are new findings for the porphyry Cu-Au systems in Indonesia.

The CO_2-rich fluids can be derived from (1) magma, (2) decarbonation reactions of wall rock, and (3) dissolution of CO_2 and from the crustal hydrothermal system (Lowenstern, 2001). Arc magmas receive the most CO_2 from recycling subducted oceanic crust and its overlying sediment blanket (Lowenstern, 2001). Since the regional stratigraphy, geological mapping, and drill cores investigation show no occurrence of authigenic carbonate in the wall rocks of the HLE prospect (PT. STM, 2018), the sources of CO_2 rich fluids in the HLE prospect were probably derived from magma. The CO_2-rich magma was likely formed by the recycling

subducted oceanic crust and its overlying sediment blanket during subduction process. It is also suggested by Th/Ce $\geq$ 0.1 of the bulk compositions of the porphyry intrusions in the HLE prospect (Fig. 15), indicating sediment cycling during subduction (Hawkesworth et al., 1997; He et al., 2008). Since not many studies about compositions of fluid inclusions in the porphyry deposits in the world have not been conducted, it is worth to check the presence of CO_2 and other volatiles in fluid inclusions using laser Raman analysis as well as quantitative fluid inclusion gas composition analysis (e.g. Blamey, 2012; Takahashi et al., 2017; Manalo et al., 2020) for the porphyry deposits with calcite-rich alteration zones.

5.4 CONCLUSIONS

1. The trapping temperature of fluid inclusions in early stage (A; AB), intermediate (B), and late stages (D) of quartz veins are 470, 305, and 285 °C.

2. The salinity of early stage (A; AB), intermediate (B), and late stages (D) of quartz veins was average 22, 12.4, and 7.6 wt.% NaCl eq.

3. Fluid inclusion petrography and laser Raman spectroscopy revealed the presence of CO_2 gas in vapor inclusions as well as two-phase (V+L) and multiphase (V+L+S) fluid inclusions in the quartz veins.

4. The potassic alteration including a significant amount of calcite was formed by a reaction of Ca from plagioclase and CO_2-bearing hydrothermal fluids.

5. The CO_2 was probably derived from magmas related to the recycling subducted oceanic crust and its overlying sediment blanket, suggested by ratio of Th/Ce $\geq$ 0.1.

CHAPTER 6
MAGMA FERTILITY

6.1 INTRODUCTION

The Humpa Leu East (HLE) porphyry Cu-Au prospect is located in Sumbawa Island, Indonesia's eastern Sunda metallogenic belt (see **Fig. 2.4** in the previous chapter). This belt hosts many world-class porphyry Cu-Au deposits formed at 5.7-0.5 Ma (Pliocene-Holocene), including Tujuh Bukit, Batu Hijau, Elang, and Onto-Hu'u (Maryono et al., 2018). The eastern Sunda metallogenic belt is currently still under construction. It is difficult to find mineralization cropping out at the surface (van Leuwen, 2018), and young volcanic products mostly cover the mineralization. Advanced geochemical techniques and technology are urgently needed to reduce challenges, costs, and time in exploration. Therefore, this study uses trace elements of zircon ($ZrSiO_4$) to understand the magma's oxidation state and water content as a tool for fertility assessment. Furthermore, the trace element of zircon has been widely used to determine magma fertility in various deposits and metallogenic belts worldwide (Shu et al., 2019). As an accessory mineral, zircon is commonly found in igneous rocks and is highly resistant to weathering or hydrothermal alteration (Shu et al., 2019). Moreover, zircon persists in surficial sediments for many kilometers beyond the porphyry centers' geochemical footprint, which can provide clues to magma fertility. Therefore, the zircon is considered a highly suitable indicator mineral for estimating oxidation state and to identify the evidence of amphibole fractionation which reveal to water content conditions (Bao et al., 2018). Ce and Eu anomaly in zircon has been used in several deposits for revealing the magma's oxidation conditions $\log(fO_2)$ in the circum-Pacific (e.g., Ballard et al. 2002; Trail et al., 2012; Dilles et al. 2015; Shen et al. 2015; Lu et al. 2016; Hattori, 2018; Shu et al.,2019). Ce and Eu are the only REEs usually found in two oxidation states in magmas, in contrast to other REEs whose oxidation state is only +3. Ce occurs as Ce^{4+} (0.97 Å) and Ce^{3+} (1.14 Å), and Eu occurs as Eu^{3+} (1.07 Å) and Eu^{2+} (1.25 Å). Due to similarity in ion radii, Zr^{4+} (0.84 Å) can more easily be replaced by Ce^{4+} (0.97 Å) and Eu^{3+} (1.07 Å). Thus, Ce and Eu anomalies of REE patterns in zircon can be used to estimate the magmatic oxidation state (Ballard et al., 2002; Trail et al., 2012; Dilles et al., 2015; Shen et al., 2015; Lu et al., 2016; Hattori, 2018; Shu et al., 2019). Magmas with high oxygen fugacity can extract more Cu from the source rocks during melting (Sun et al., 2015; Hattori, 2018). Recently, Shu et al. (2019) tried to relate the Ce and Eu anomaly to the tonnage of Mo in several

porphyry deposits in China. They suggested that deposits containing > 0.3 Mt Mo have Ce/Ce* > 100, Ce/Nd > 10, and Eu/Eu* > 0.3, while those containing less or equal to 0.3 Mt Mo have Ce/Ce* < 100, Ce/Nd < 10, and Eu/Eu* < 0.3. Furthermore, Nevolko et al. (2021) combine whole-rock geochemistry with zircon analyses in assessing the magma oxidation state. They suggested that the value of whole-rock trace element ratio of Sr/Y >65, 10,000*(Eu/Eu*)/Y >850 and zircon trace element of the Eu/Eu* > 0.4, Ce/Ce* >750 and Yb/Dy ratios >4 are related with highly oxidized magma.

A high-magma water content (H_2O) is also an essential factor in the formation of porphyry Cu-Au deposits (Richards, 2011; 2015; Richards et al., 2012; Chiaradia & Caricchi, 2017; Nevolko et al., 2021). In porphyry copper deposits, water is one of the essential ingredients, along with copper ligands (e.g., Cl^- and HS^-), which combine with copper to form ore minerals (Richards, 2011; Seward et al., 2014; Chiaradia & Caricchi, 2017). Porphyry copper deposits are controlled by the amount of water available to form a deposit since Cu ligands and S have finite solubilities in water (Chiaradia & Caricchi, 2017). The high amount of water in the magma allows magma to reach fluid saturation earlier (Richards et al., 2012) and causes more Au to be drawn from the melt into volatile aqueous phases (Li & Audetat, 2013). High water content in magma is conducive to the migration and enrichment of metal elements, which are very important for mineralization. Strong magmatic fluid activity (high water content) can promote the fractionation of Y and Ho; therefore, zircon crystallized from magma with high water content has a high Y/Ho ratio (Zheng et al., 2021). Nevolko et al. (2021) suggested the values of Yb/Dy >4 and Eu/Eu* >0.4 as a potential monitor of magma fertility . These values reflect the early fractional crystallization of amphibole and imply a high intrinsic water content in magma (>4 wt.%) necessary for amphibole crystallization (Richards et al., 2012; Lu et al., 2016).

Plagioclase composition can also be a tool to determine a fertile porphyry system by reflecting water content of the magma. Determination of magma water content is essential for understanding the evolution of magmas and the formation of magmatic-hydrothermal ore deposits (Fiedrich et al.,2018). Furthermore, water and other volatile components in the melt are initially concentrated and enriched to form a free volatile phase, which can lead to magmatic-hydrothermal ore deposits, such as porphyry mineralization (Heindrich and Candela, 2014). Williamson et al., 2016 found a relationship between excess Al and porphyry

mineralization. They suggested that plagioclase from fertile systems is distinct in containing 'excess' Al (Williamson et al., 2016).

6.2 RESULTS

6.2.1 U-Pb zircon dating

The LA-ICP-MS U-Pb zircon dating of forty–three grains from three samples of causative intrusion are listed in **Appendix 12**. The phase of intrusion refers to the abundance of Cu-Au mineralization, where the high content of Cu-Au mineralization is considered as early phase, small-moderate content of Cu-Au mineralization is an intermediate stage, and the last/late phase should be infertile (Sillitoe, 2012). The $^{206}Pb/^{238}U$ ages of 8 analytical spots from sample VHD006/500-502, which represents an early intrusion phase, range from 1.00 ± 0.12 Ma to 1.54 ± 0.12 Ma, with weighted mean age of 1.27 ± 0.17 Ma (2σ, MSWD= 4.8, N= 8). Sample VHD009A/250-252 (intermediate phase) yielded $^{206}Pb/^{238}U$ ages of 20 spots ranging from 0.96 ± 0.19 Ma to 1.41 ± 0.52 Ma, which gives a weighted mean age of 1.10 ± 0.50 Ma (2σ, MSWD= 1.6, N= 20) (Fig. 9). Furthermore, fifteen analytical spots from the late phase intrusion sample (VHD001R/600-602) yielded $^{206}Pb/^{238}U$ ages ranging from 0.90 ± 0.07 Ma to 1.51 ± 0.28 Ma, which gives a weighted mean age of 1.20 ± 0.09 Ma (2σ, MSWD= 2.8, N= 15) (**Fig. 6.1**). These ages are considered to represent the crystallization age of the magmatic zircons.
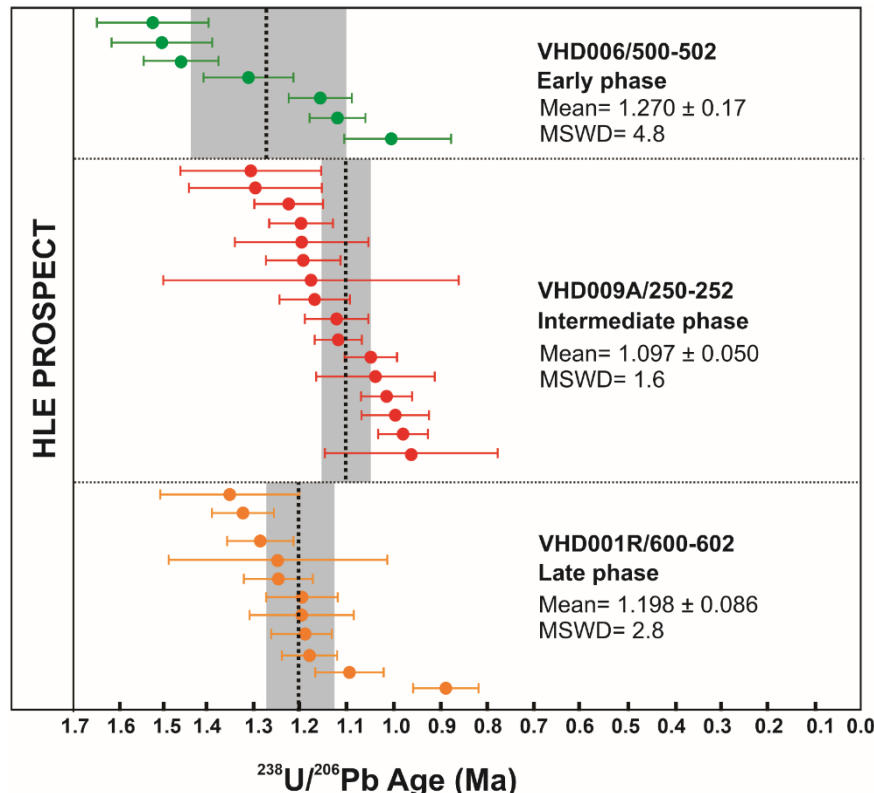
Figure 6. 1 Weighted mean ages of the causative intrusions of the early, intermediate, and late phases of the HLE porphyry Cu-Au prospect.

6.2.2 Zircon geochemistry

6.2.2.1 Morphology and internal texture

Transmitted light microscope images show that zircon grains from the diorite porphyry of the HLE prospect have variations in the external morphology. All grains range between 50 and 300 µm in size, and most have a transparent to gray color **(Fig. 6.2)**. The morphology of zircon grains varies within a single rock sample from prismatic, non-prismatic euhedral-subhedral elliptical, and non-prismatic rounded. The zircon crystal typologies are classified according to the relative development of the {100} vs. {110} prismatic forms and the {211} vs. {101} pyramidal forms based on the "Pupin diagram" (Pupin, 1980), which shows that the HLE zircon crystals are classified as S10, P2, S12, S13, S16, and S17 (**Fig. 6.2**).
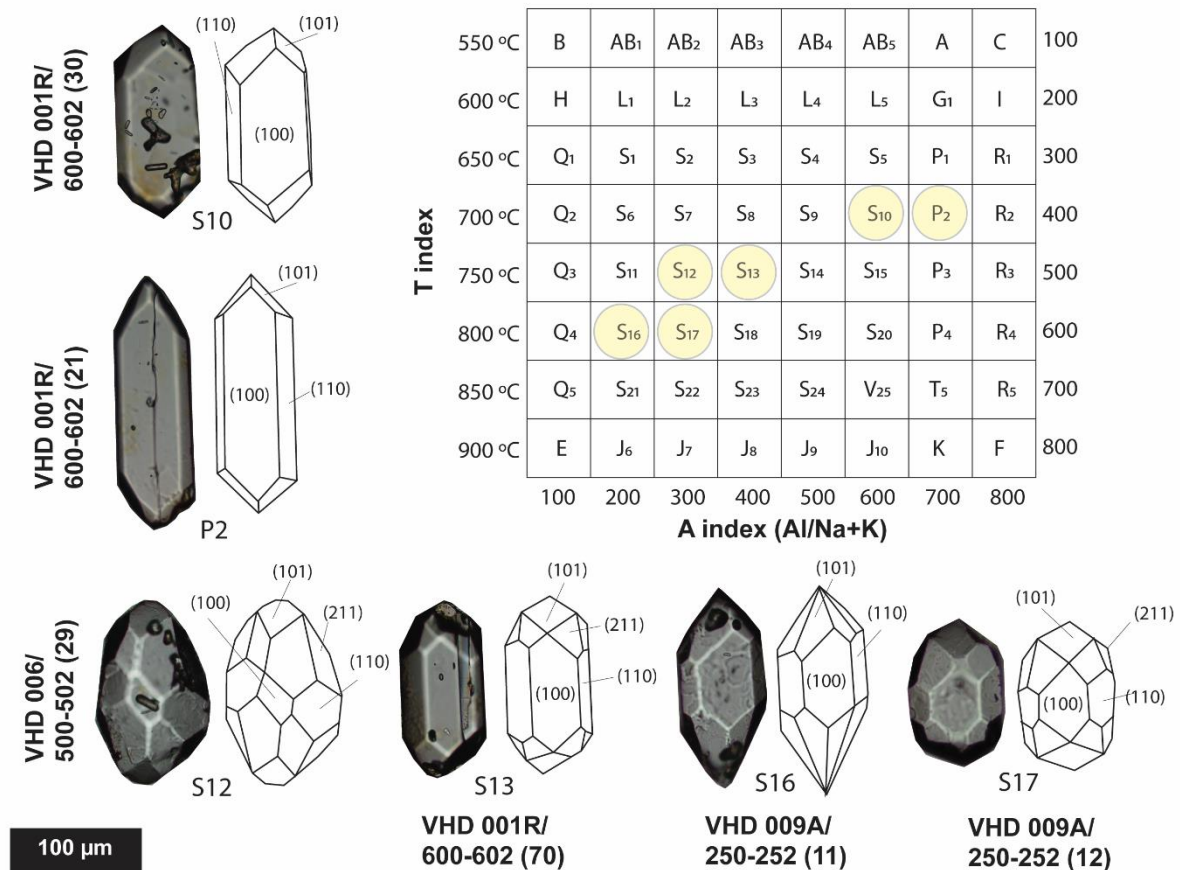
Figure 6. 2 A proposed typological classification of zircons (after Pupin, 1980). Index A represents the Al/(NA+K) ratio (100-800) which controls the development of zircon pyramids, while temperature influences the development of zircon prisms. The HLE zircon typology includes S10, P2, S12, S13, S16, and S17 (yellow box).

Several zircon grains have mineral and melt inclusions, and a few grains have bubble inclusions (**Fig. 6.3**). Based on SEM-EDS analysis, the mineral inclusions consist of apatite, magnetite-ilmenite with lamellae texture, the size varying from 5 µm to 30 µm. Melt inclusions

occur in every grain of zircon, with 30-100 µm in size (**Fig. 6.3-B**). Potassium feldspar, quartz, glass, and Fe-oxide are also present and occur together with the melt inclusions, 3 to 15 µm in size (**Fig. 6.3-B**). Cathodoluminescence (CL) imaging is used to describe the internal structure of zircon grains. Primary magmatic oscillatory zoning (growth zoning) is the most common type of zoning that shows a dark and bright banding texture (**Fig. 6.3-A**). In cathodoluminescence (CL) and scanning electron microscopy (BSE), the HLE zircon shows dominantly oscillatory zoning with thin bands, and some grains show weak zoning in the outer core, typical of magmatic zircon (Martins et al., 2014). A few grains show continuous thin bands zoning from the core to the rim (**Fig. 6.3-A**). Obscure zoning is also present and is sometimes more likely to develop into a rounded shape than normal magmatic zircon (**Fig. 6.3-A**). A thin band zoning is common and occurs around a larger core, and some zircons also show weak magmatic zoning in the core, followed by thin bands zoning in the outer rim (**Fig. 6.3-A**). Furthermore, several grains show a sector zoning in images (**Fig. 6.3-A**) which a different brightness on different facets. There are several causes of crystal sector zoning, including differences in "crystallization force," the relative growth rates of different faces, the ratio of crystal growth rate to element diffusion near the surface of the crystal lattice, and differences in cation adsorption on the face surface (Watson, 1996; Levashova et al., 2021).
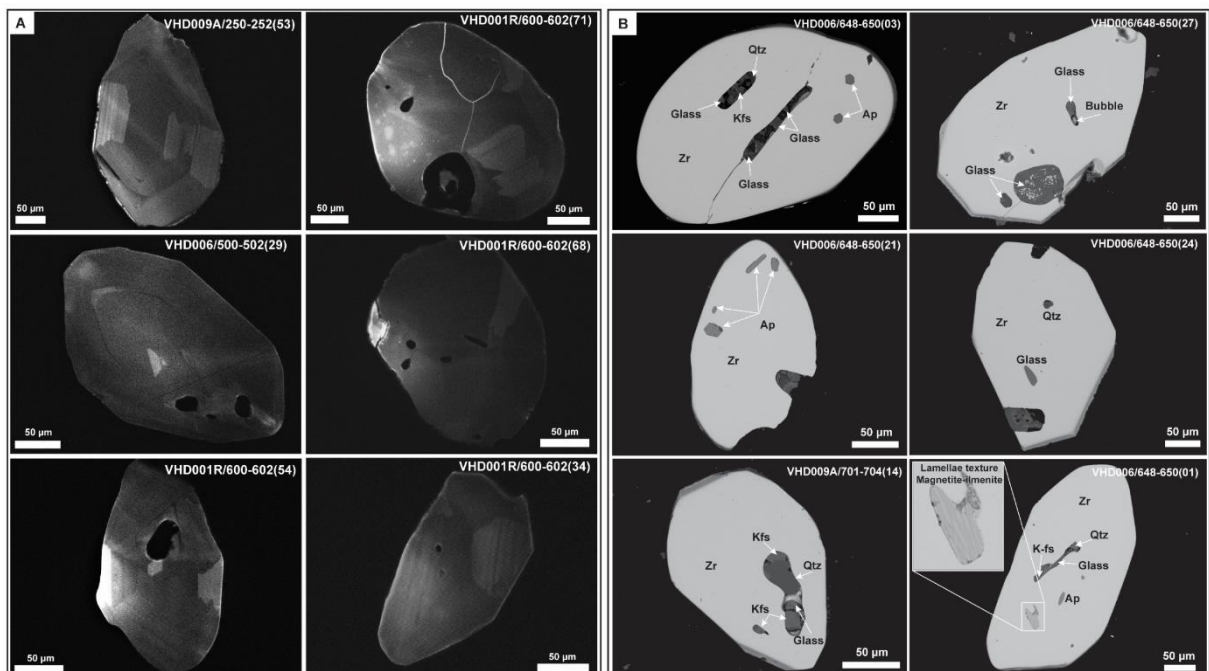
Figure 6. 3 Representative CL-Images (**A**) and BSE images of zircon (**B**) by SEM analysis. Abbreviation: *Zr= Zircon, Ap= Apatite, Qtz= Quartz, K-fs= Potassium feldspar.*

6.2.2.2 Trace element concentrations

The measured zircon trace element concentrations and calculated values, including Ce/Ce*, Ce/Nd, Eu/Eu*, Ti-in-zircon crystallization temperatures, and magma oxygen fugacities (fO_2 values and ΔFMQ values) of HLE zircon are listed in **Appendix 11**. To exclude potential contamination from mineral and melt/fluid inclusions, the analyses have been filtered based on REE concentrations and ratios. LREE enrichment can be associated with secondary alteration or with hydrothermal zircons (Zhong et al., 2018); a ratio of (Sm/La)N < 10 and (dCe) < 10 can be used as a discriminant between magmatic and hydrothermal zircon (Hoskin, 2005).

Sixty-one zircon trace elements analyses were determined from all intrusion phases (early, intermediate, and late). The zircon shows Ti content ranging from 5.51 to 24.58 ppm (Av. 8.81 ppm). Our study found that the HLE zircons have slightly low Hf contents from 9,143 to 12,617 ppm (av. 9,777 ppm) than a general mafic-intermediate igneous rock which is mostly 32,000 – 37,000 (Grimes et al., 2015). Ta content from 0.31 to 0.66 ppm (Av. 0.46 ppm), Nb from 1.69 to 2.78 ppm (Av. 2.13 ppm), Pb from 0.02 to 1.02 ppm (Av. 0.11 ppm). The HLE zircon shows a low concentration of Th ranging from 13.61 to 55.21 ppm (Av. 30.06 ppm) and U from 31.19 to 132.88 ppm (Av. 60.71 ppm). Furthermore, the total REE (∑REE) content in zircon grains varies from 316.2 to 1412.6 ppm (Av. 647.4 ppm) **(Appendix 11)**. Zircons from all the analyzed samples have identical chondrite-normalized REE patterns characterized by HREE enrichments and LREE depletions. Zircons in this study can clearly be classified into two distinct groups based on normalized to chondrite (Sun and McDonough 1989) **(Fig. 6.4)**. Typically, HLE zircons show magmatic zircon patterns characterized by weak negative Eu anomalies, positive Ce anomalies, and a more significant (Sm/La)N ratio (Hoskin and Schaltegger, 2003; Hoskin, 2005Nevolko et al., 2021). A few zircons have enriched LREE patterns, with low dCe, (Sm/La)N content, and high content of La and Pr. However, still have an original trend of magmatic zircon. Thus, types are interpreted as a contaminated by apatite inclusions (VHD001R/600-602; 71, 68, and 34) **(Fig. 6.4)**. These grains from the HLE zircon grains display higher content of Ca and P than the zircon without apatite contamination **(Fig. 6.4)**. These results can be used to avoid a false assessment of the fertility study of magmas by ignoring zircons which has a contamination result.

The HLE zircon has a wide range of Ce/Ce*, which is between 21.2 and 119.1 (Av. 54.8), Ce/Nd ratios between 2.7 and 14.4 (Av. 6.1), and Eu/Eu* from 0.36 to 0.61 (Av. 0.49). In addition, the fO_2 values are calculated from -7.5 to -16.0 (Av. -11.54) with ΔFMQ 0.02 to +6.67

(Av. +2.89), corresponding to crystallization temperatures from 738 to 898 °C (Av. 779 °C). These results were calculated by Geo-fO$_2$ software of Li et al. (2019) based on the Ti-in-zircon thermometer after Ferry & Watson (2007) (**Appendix 11**).
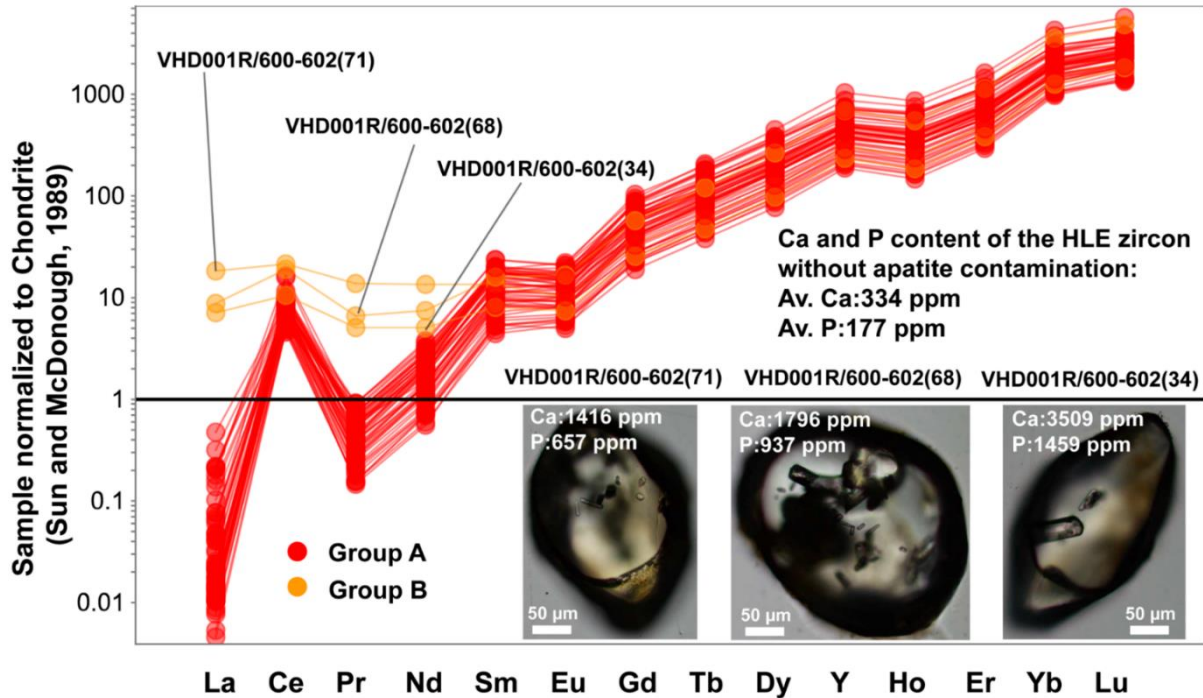
Figure 6. 4 Chondrite normalized REE patterns (Sun and McDonough 1989).

6.2.3 Plagioclase geochemistry

Plagioclase is a dominant phenocryst (~80 % of all phenocrysts, estimated visually in thin sections) in every phase of intrusion. Plagioclase phenocrysts are colorless in plane polarized light, 100 μm to >1 mm in size. Some phenocrysts show a deformation twin microfracture and mostly have oscillatory zoning (see **Fig. 4.3** in the chapter 4). The plagioclase phenocryst classification (after Deer et al., 2013) shows that the plagioclase related to the early phase of intrusion is mostly labradorite, while plagioclase phenocryst associated with intermediate and late phases of intrusion has a wider compositional ranges from labradorite to andesine. EPMA elemental mapping of plagioclase shows that the plagioclase phenocryst has a high concentration of Al, Si, Ca, and Na. However,K, Fe, Mg and Mn show a random distribution (**Fig. 6.5**). Furthermore, the EPMA elemental mapping of plagioclase shows concentric zoning of Al, Si, Ca, and Na (**Fig. 6.5**). In addition, a super high concentration of Si and Ca in EPMA elemental data related to the quartz and calcite mineral which is equilibrium with plagioclase.

The results of EPMA analysis of the plagioclase phenocrysts from several samples, which represent the three types of intrusion phases, show similarity in chemical composition (**Table**

6.1). The SiO$_2$ content of the plagioclase phenocrysts in all phases of intrusion varies between 50.8 wt.% to 56.4 wt.%, the Al$_2$O$_3$ contents range from 25.5 to 29.4 wt.%, and the content of FeO is less than 0.23 wt.%. Generally, plagioclase phenocrysts in all phases of intrusion samples have a low content of TiO$_2$ (<0.01 wt.%) and K$_2$O (< 0.74 wt.%). The concentration of CaO ranges from 8.56 to 13.2 wt.%, and Na$_2$O from 3.72 to 6.25 wt.% (**Table 6.1; Appendix 7**).
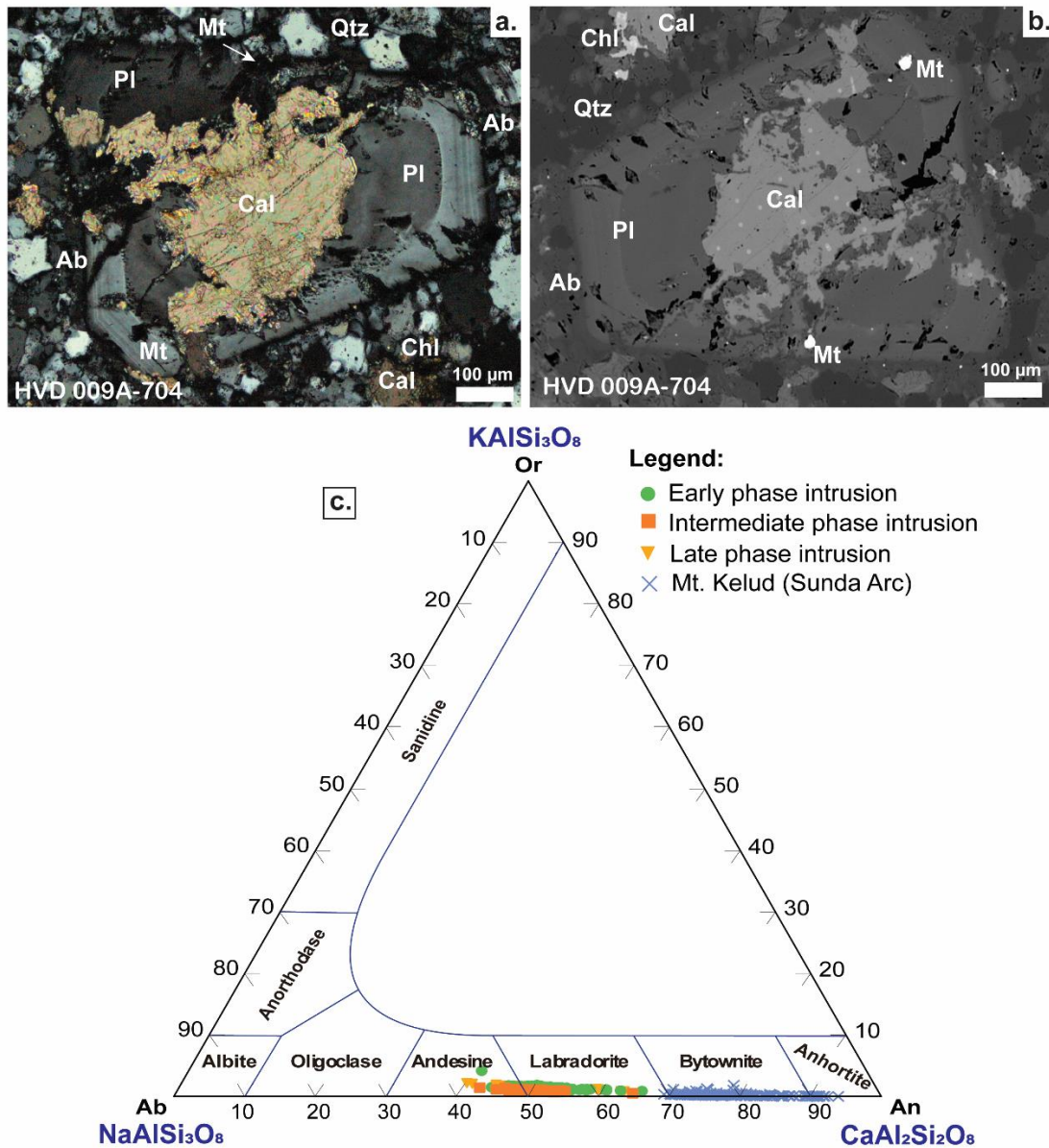
Figure 6. 5 (**a; b**) Petrography and backscattered electron image (BSE) of plagioclase phenocryst, (**c**) Plagioclase phenocryst classification (after Deer et al., 2013). and (**d**) Negative correlation Sr and Ca elements of plagioclase phenocryst in every phase of intrusion.

80
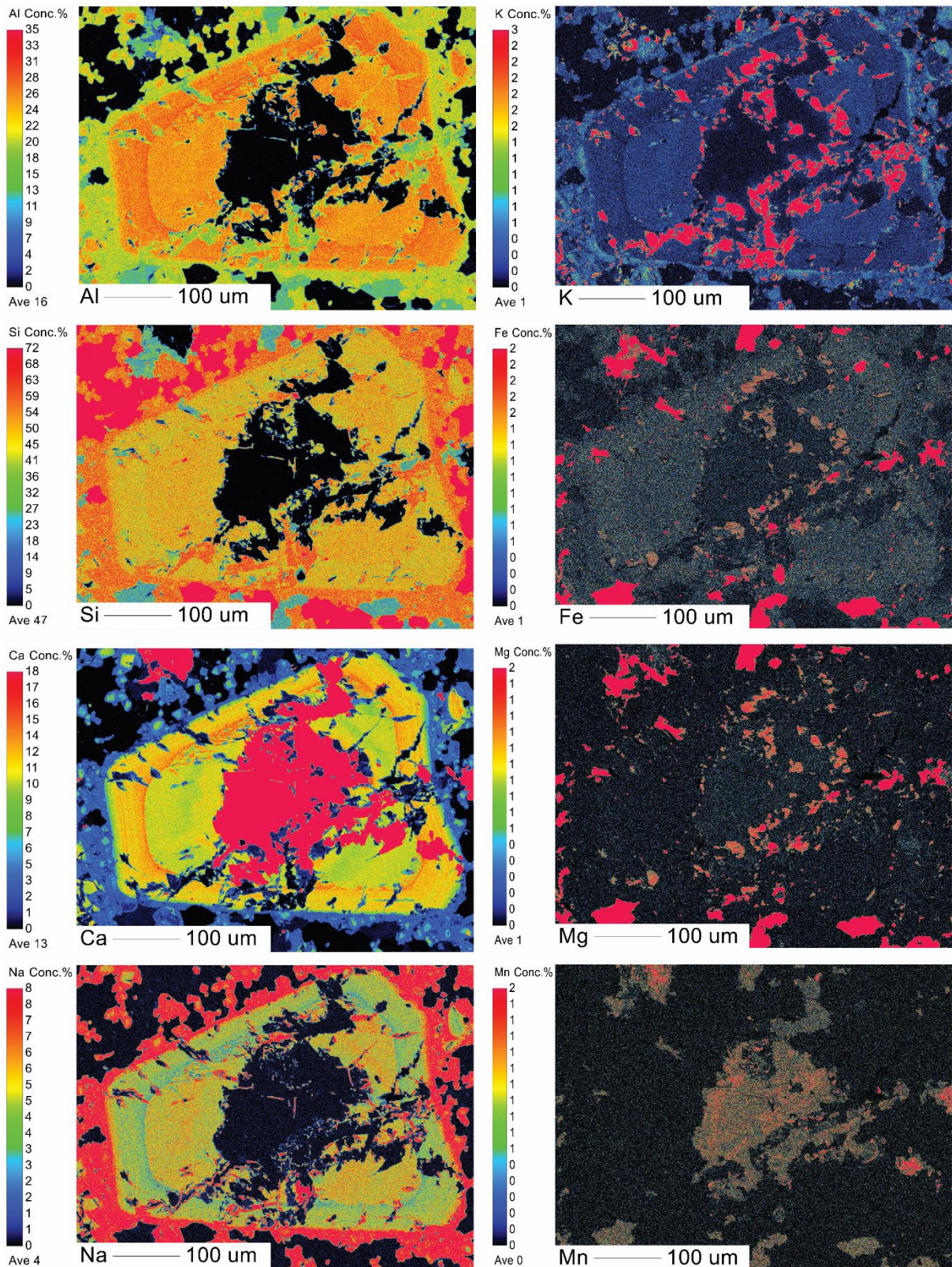
Figure 6. 6 EPMA elemental maps of plagioclase phenocryst showing concentric zoning of Al, Si, Ca and Na

Table 6. 1 Representative mineral chemistry data of plagioclase in diorite and quartz diorite porphyry based on EPMA analysis.

Sample	VHD 009A-416	VHD 009A-416	VHD 009A-416	VHD 009A-416	VHD 009A-416	VHD 009A-416	VHD 009A-416
	Early phase	Early phase	Early phase	Early phase	Early phase	Early phase	Early phase
SiO_2 (wt.%)	54.6	53.2	54.2	54.1	53.8	53.0	54.1
TiO_2	0.00	0.00	0.00	0.00	0.00	0.00	0.00
Al_2O_3	27.5	28.5	27.9	27.6	27.8	28.6	27.8
FeO	0.13	0.14	0.14	0.13	0.12	0.10	0.13
MnO	0.01	0.01	0.00	0.00	0.00	0.00	0.00
MgO	0.01	0.01	0.01	0.00	0.01	0.00	0.01
CaO	10.2	11.6	10.8	10.5	10.6	11.4	10.4
Na_2O	5.60	4.76	5.17	5.47	5.41	4.97	5.40
K_2O	0.24	0.19	0.22	0.24	0.23	0.17	0.21
SrO	0.51	0.54	0.59	0.58	0.58	0.58	0.60
Total	98.8	99.0	99.0	98.7	98.6	99.0	98.8
Si (apfu)	2.50	2.44	2.48	2.49	2.47	2.43	2.48
Al	1.49	1.54	1.51	1.50	1.51	1.55	1.50
Ti	0.00	0.00	0.00	0.000	0.00	0.00	0.00
Fe	0.01	0.01	0.01	0.01	0.01	0.004	0.01
Mn	0.00	0.00	0.00	0.00	0.00	0.00	0.00
Mg	0.00	0.001	0.001	0.00	0.00	0.00	0.00
Ca	0.50	0.57	0.53	0.52	0.52	0.56	0.51
Na	0.50	0.42	0.46	0.49	0.48	0.44	0.48
K	0.014	0.011	0.013	0.012	0.013	0.010	0.012
Sr	0.01	0.01	0.01	0.01	0.01	0.01	0.01
An (mol. %)	49.4	56.7	52.8	50.8	51.3	55.5	51.1
Ab	49.1	42.2	45.9	47.9	47.4	43.6	47.7
Or	1.41	1.09	1.27	1.36	1.31	0.97	1.20

Table 3 (cont.)

Sample	VHD 006-723	VHD 006-723	VHD 006-723	VHD 006-723	VHD 006-723	VHD 006-723	VHD 006-723
Intrusion phase	Intermediate porphyry	Intermediate porphyry	Intermediate porphyry	Intermediate porphyry	Intermediate porphyry	Intermediate porphyry	Intermediate porphyry
SiO_2 (wt.%)	55.3	54.9	55.6	54.7	55.1	55.2	54.8
TiO_2	0.00	0.00	0.01	0.00	0.00	0.00	0.00
Al_2O_3	27.6	26.9	26.6	27.6	27.1	27.1	27.2
FeO	0.13	0.10	0.08	0.13	0.11	0.12	0.11
MnO	0.01	0.00	0.00	0.00	0.00	0.00	0.00
MgO	0.00	0.01	0.00	0.00	0.04	0.00	0.00
CaO	9.89	9.10	8.68	9.95	10.3	10.4	10.5
Na_2O	5.73	6.04	6.36	5.50	5.31	5.32	5.22
K_2O	0.14	0.21	0.25	0.19	0.20	0.170	0.16
SrO	0.61	0.66	0.66	0.68	0.62	0.65	0.58
Total	99.4	98.0	98.3	98.8	98.8	99.0	98.6
Si (apfu)	2.51	2.53	2.55	2.50	2.52	2.52	2.51
Al	1.48	1.46	1.44	1.49	1.46	1.46	1.47
Ti	0.00	0.00	0.00	0.00	0.00	0.00	0.00
Fe	0.004	0.003	0.003	0.003	0.003	0.003	0.003
Mn	0.00	0.00	0.00	0.00	0.00	0.00	0.00
Mg	0.00	0.00	0.00	0.00	0.00	0.00	0.00
Ca	0.48	0.44	0.43	0.49	0.51	0.51	0.51
Na	0.51	0.540	0.57	0.49	0.47	0.47	0.46
K	0.02	0.02	0.02	0.02	0.02	0.02	0.02
Sr	0.01	0.01	0.01	0.01	0.01	0.01	0.01
An (mol. %)	48.4	44.9	42.4	49.4	51.2	51.5	52.1
Ab	50.7	53.9	56.2	49.1	47.6	47.5	47.0
Or	0.81	1.21	1.45	1.15	1.16	1.00	0.93

Table 3 (cont.)

Sample	VHD 009A-703.8	VHD 009A-703.8	VHD 009A-703.8	VHD 009A-703.8	VHD 009A-703.8	VHD 009A-703.8	VHD 009A-703.8
Intrusion phase	Late phase	Late phase	Late phase	Late phase	Late phase	Late phase	Late phase
SiO_2 (wt.%)	56.2	55.0	54.3	54.6	54.9	54.6	54.8
TiO_2	0.00	0.0	0.0	0.0	0.0	0.0	0.0
Al_2O_3	25.6	26.8	27.5	26.9	27.2	27.0	27.2
FeO	0.10	0.09	0.09	0.07	0.07	0.08	0.08
MnO	0.01	0.00	0.00	0.00	0.00	0.00	0.00
MgO	0.01	0.00	0.05	0.00	0.00	0.00	0.00
CaO	8.47	9.67	10.4	9.89	10.1	9.98	10.3
Na_2O	6.63	5.97	5.53	5.76	5.78	5.74	5.46
K_2O	0.39	0.29	0.26	0.27	0.26	0.29	0.30
SrO	0.67	0.65	0.62	0.63	0.66	0.61	0.62
Total	98.0	98.4	98.7	98.1	99.0	98.3	98.8
Si (apfu)	2.59	2.53	2.49	2.52	2.51	2.52	2.51
Al	1.39	1.45	1.49	1.46	1.47	1.47	1.47
Ti	0.00	0.00	0.00	0.00	0.00	0.00	0.00
Fe	0.01	0.004	0.003	0.01	0.004	0.01	0.004
Mn	0.00	0.00	0.00	0.00	0.00	0.00	0.00
Mg	0.00	0.001	0.00	0.00	0.003	0.00	0.00
Ca	0.41	0.48	0.51	0.49	0.49	0.49	0.51
Na	0.59	0.53	0.49	0.52	0.51	0.51	0.49
K	0.01	0.01	0.02	0.01	0.01	0.01	0.01
Sr	0.01	0.01	0.01	0.01	0.01	0.01	0.01
An (mol. %)	40.2	46.4	50.3	47.9	48.3	48.2	50.2
Ab	57.6	52.0	48.2	50.5	50.2	50.1	48.1
Or	2.23	1.64	1.49	1.55	1.50	1.68	1.71

Abbreviations: apfu= atoms per formula unit, An= anorthite, Ab= albite, and Or= orthoclase

84

6.3 DISCUSSION

6.3.1 Petrogenesis and age of magmatism

In recent years, the trace elements of zircon, such as Ti, Hf, Th, U, Nb, Ta, Y, and REEs content in magmatic zircon, has been widely used to interpret the provenance of zircon and distinguish the tectonomagmatic environments (Grimes et al., 2007; Grimes et al., 2015; Sheikh et al., 2020; Wang et al.,2021 and Ngoniri et al., 2021). The zircon geochemistry method has expanded rapidly. Therefore, it can be applied to complex magmatic environments. Most of the zircons from the HLE prospect have a slightly high Hf/Th and low Nb/Hf ratio, which is a clue that these zircons are associated with the arc-related/orogenic setting as a result of subduction magma systems in the continental crust (Sheikh et al., 2020) (**Fig. 6.7-D; E**). The discrimination diagram for continental vs. Mid Oceanic Ridge (MOR) zircon using Ti vs. Yb concentrations (Sheikh et al., 2020) shows that zircon from the continental crust system has a lower Ti content than zircon from MOR. HLE zircon shows a low Ti concentration, < 12 ppm, and slightly high Yb, ranging from >200 to <650 ppm. It can be categorized as a product from a continental environment. Furthermore, the relationship between Ti vs. Yb shows a positive correlation and follows a trend expected from the fractionation of amphibole (**Fig. 6.7-F**). Grimes et al. (2007) suggested that zircon from MOR settings contains slightly depleted amounts of Hf, Yb, and Y, compared to zircon from arc magmas (and the continental crust). The HLE zircon is similar to arc magmas and the continental crust. Zircon from the HLE prospect has the U/Yb ratio between > 0.1 and ≤ 0.3, which corresponds to a continental environment (Grimes et al., 2015) (**Fig. 6.7-A; B; C**). Zircons originating from mantle magmas exhibit negative Hf vs. Th and Y vs. U correlations, contrary to zircons from the crust that display positive correlations (Ngoniri et al., 2021). Furthermore, the temperature formation of zircon was calculated based on the titanium in the zircon thermometer (Ferry & Watson, 2007), which yielded an average temperature of 780 ^{O}C (**Appendix 11**).

The tectonic setting of the Sunda arc, particularly in the eastern part is still controversial, whether it is an island arc or a continental arc. Some researchers have suggested that porphyry Cu-Au deposits in the eastern Sunda arc, such as Tumpangpitu (eastern Java), Batu Hijau, Elang, and Hu'u district (Sumbawa Island), are associated with island arcs, e.g., Carlile & Mitchell (1994); Groove et al. (2002); Setijadji et al. (2006); Setijadji & Maryono (2012); Maryono et al. (2018). Despite these statements, Hamilton (1979) and Katili (1975) suggested that deposits are linked with the continental arc. Many publications support that statement,

including Reubi et al. (2002), Gertisser & Keller (2003), Elburg et al. (2004), Gardner et al. (2013), and Fadlin et al. (2018; 2021). However, the zircon geochemistry results suggest that the causative intrusion in the HLE porphyry Cu-Au prospect is a product of subduction in the continental system/active continental margin, where the Indian plate (oceanic crust) beneath to the Sunda plate (continental crust).
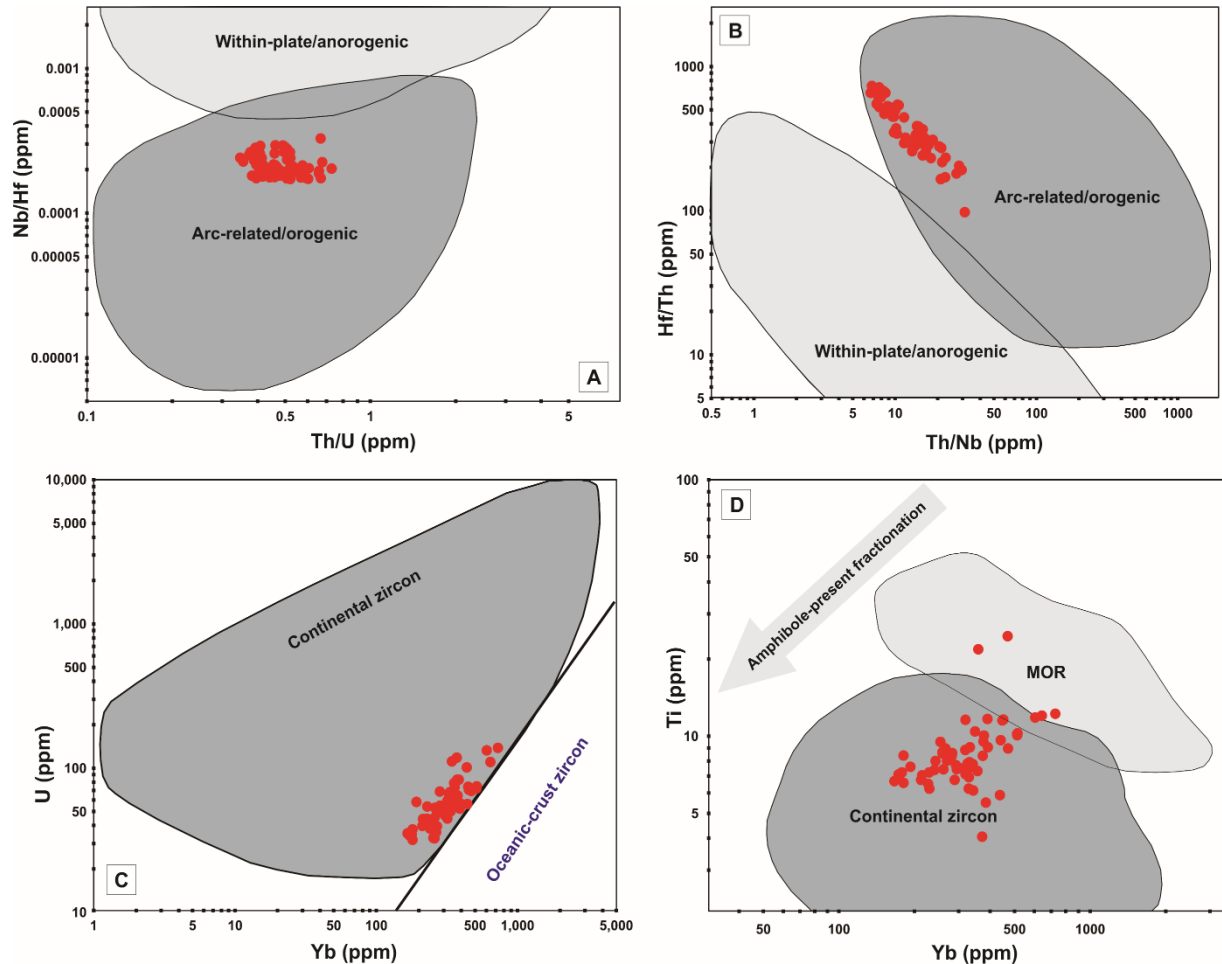
Figure 6. 7 Zircon discrimination for within-plate vs. Arc-related using Nb/Hf vs. Th/U and Hf/Th vs. Th/Nb (in ppm) (Sheikh et al., 2020) (**A, B**). A binary diagram of U vs. Yb for a tectono-magmatic source of igneous zircon (Grimes et al., 2007; Grimes et al., 2015) (**C**). Zircon discrimination for Continental vs. MOR diagram using Ti vs. Yb (Sheikh et al., 2020) (**D**)

Age dating of U-Pb has been done on three samples of intrusions which represent early, intermediate, and late phases, where the high Cu-Au mineralization content is considered an early phase, small-moderate Cu-Au mineralization is an intermediate stage, and the late phase should be very low content of Cu-Au or barren (Sillitoe, 2012). The VHD006/500-502 yield $^{206}Pb/^{238}U$ 1.27 ± 0.17 Ma, VHD009A/250-252 yield $^{206}Pb/^{238}U$ 1.10 ± 0.50 Ma, and VHD001R/600-602 yield $^{206}Pb/^{238}U$ 1.20 ± 0.09 Ma respectively, indicating emplacement during the late Holocene. However, the U-Pb zircon dating shows that the age of the

intermediate and the late phase overlaps, considering the error, which is from 0.50 to 0.17 Ma. The clustering and population U-Pb zircon data from VHD006/500-502, VHD009A/250-252, and VHD001R/600-602 show the causative intrusion ages HLE porphyry Cu-Au prospect range from 1.2 to 1.0 Ma. Furthermore, the metallogenic province of the eastern Sunda arc, especially Sumbawa Island, has limited records of late quarter arc-related magmatism. These are one of the youngest magmatic zircons that have been documented so far besides the Onto porphyry Cu-Au prospect, which is 0.5 - 0.8 Ma (Holocene) (Burrows et al., 2020). The most common causative intrusion ages of porphyry Cu-Au in the eastern Sunda arc (Sumbawa Island) range from 3.5 to 2.1 Ma (Maryono et al., 2018) and have been interpreted as products of the Island arc system (e.g., Setijadji et al., 2006; Setijadji & Maryono, 2012; Maryono et al., 2018). Regarding the data compilation of U-Pb zircon dating of the causative intrusion in HLE prospect with several porphyry Cu-Au along the eastern Sunda arc (Sumbawa Island) modified from Maryono et al., 2018 (**Fig. 11**) show a decrease in ages of the causative intrusions from west to the east. In addition, this information will provide new opportunities for mineral deposit exploration along the eastern Sunda arc to discover porphyry Cu-Au prospects associated Holocene-Pleistocene intrusions.
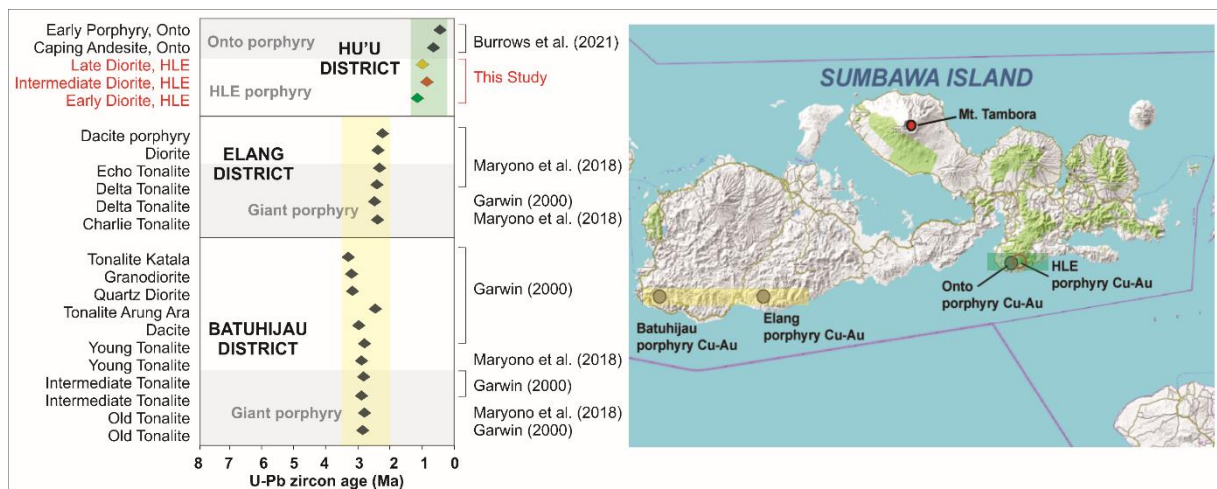
Figure 6. 8 U-Pb zircon age of the causative intrusions in several porphyry Cu-Au in Sumbawa Island, modified from Maryono et al. (2018).

6.3.2 Magma fertility assessment

In this discussion, we compare the HLE zircon with zircon from several locations, in both rocks associated with mineralization (fertile samples) and not associated with mineralization (infertile samples),. Zircon geochemistry data of fertile samples (e.g., Batu Hijau, Dexing, Sar Cheshmeh, Sungun, Tampakan) and infertile samples of zircon geochemistry (e.g., Bishop tuff,

Kadona, Yellowstone, Lucerne pluton, Bandelier) are taken from Lu et al., 2016, while infertile zircon geochemistry of Toba is taken from Smythe and Brenan, 2016. The infertile samples are most enriched in heavy rare earth elements (HREE) and medium rare earth elements (MREE) than the fertile samples. Furthermore, the infertile samples also show a significantly negative Eu anomaly compared to the fertile ones (**Fig. 6.9**). A significant negative Eu anomaly in the fertile samples is evidence of early plagioclase fractionation. In another case, the depletion of HREE and MREE is probably related to the early amphibole fractionation, where the amphibole prefers to carry HREE and MREE rather than LREE.
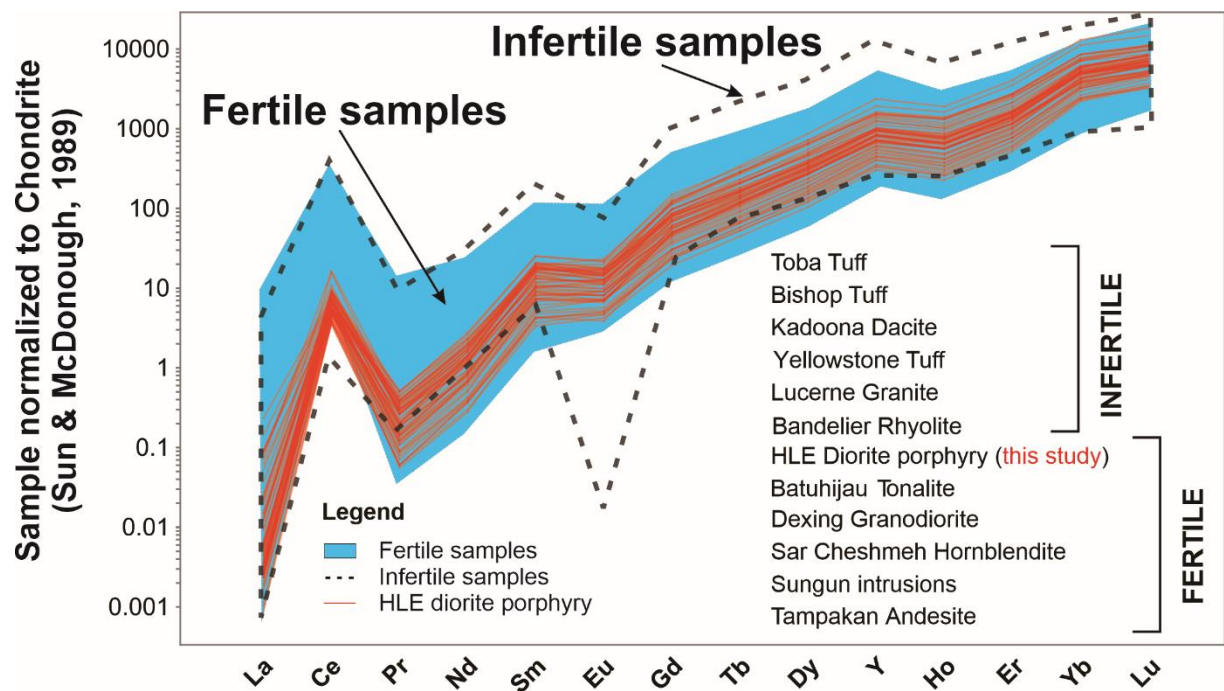
Figure 6. 9 Comparison of REE normalized to chondrite diagram Sun and McDonough (1989) both fertile and infertile zircon samples. The infertile samples show a significant negative Eu anomaly compared to the fertile ones. Zircon geochemistry data of fertile samples (e.g., Batu Hijau, Dexing, Sar Cheshmeh, Sungun, Tampakan) and infertile samples (e.g., Bishop tuff, Kadona, Yellowstone, Lucerne pluton, bandelier) are taken from Lu et al. (2016), while infertile zircon geochemistry of Toba is taken from Smythe and Brenan (2016).

Several studies have used Ce/Ce* and Eu/Eu* in zircon as an indication of the ore-forming ability of magmas associated with skarns and porphyry deposits, e.g., Ballard et al., 2002; Richards et al. (2012); Shen et al. (2015); Dilles et al. (2015); Lee et al. (2017); Hattori, (2018); Shu et al. (2019) and Ngoniri et al. (2021). Previous researchers, e.g., Ballard et al. (2002); Richards et al. (2012); Trail et al. (2012); Shen et al. (2015); Dilles et al. (2015); Lee et al. (2017); Hattori (2018); Shu et al. (2019) and Nevolko et al. (2021) suggested that the zircon in oxidized magmas should have a Ce anomaly (Ce/Ce*) and negative Eu anomaly.

A discrimination of infertile vs. fertile samples by Ngoniri et al. (2021) [Semi-logarithmic Plots: log Ce/Ce* vs. Eu/Eu*] (**Fig. 6.10-A**) clearly shows that Ce/Ce* and Eu/Eu* can discriminate between fertile and infertile samples. Fertile samples mostly have high Eu/Eu* and Ce/Ce* values (> 0.4 and > 50), indicating more oxidized magma. While infertile samples generally show Eu/Eu* value < 0.4, Ce/Ce* shows a wide range, from 4.38 – 1105, corresponding to the low – high oxidizing condition. The high Ce anomalies of infertile zircons samples such as Bishop tuff, Kadona dacite, and Bandelier rhyolite are probably caused by contamination of mineral inclusions which will give a false result (Zhong et al., 2018).

The trace elements diagram of zircon Eu/Eu* vs. Yb/Dy (Nevolko et al., 2021) shows that the zircon from fertile samples includes the HLE porphyry Cu-Au prospect generally have Eu/Eu* > 0.4 [(Eu/Eu*= EuN/(SmN*GdN)$^{0.5}$]. By contrast, zircons from the infertile samples mostly show a low Eu/Eu* (< 0.4) **(Appendix 11)**. Low Eu/Eu* ratio in zircon grains from the infertile samples may be due to the early crystallization of plagioclase (**Fig. 6.9**), which removes Eu from the melt. Plagioclase preferentially incorporates Eu, producing low Eu/Eu* in the remaining melt and zircon grains. Early plagioclase crystallized and preferentially removed Eu^{2+} from the melt to cause low Eu/Eu* ratios in zircon grains (Shen et al., 2015). The Eu/Eu* of the HLE zircon is > 0.4, indicating high oxidizing magma conditions, while Eu/Eu* < 0.4 is less oxidized. Lu et al. (2016) and Nevolko et al. (2021). The ratio of Yb/Dy versus Eu/Eu* can determine the magmatic water content. Fertile samples of zircons, including the HLE porphyry Cu-Au prospect, have a relatively high Yb/Dy > 5 ratio corresponding to the amphibole fractionation. Furthermore, the Eu/Eu* vs. Yb/Dy diagram (**Fig. 6.10-B**) shows a gradual change in zircon Yb/Dy vs. Eu/Eu* ratios from infertile to fertile sampless suggesting an increase in water content within fertile magmas. Consequently, the ratio of Yb/Dy > 5 can be a potential indicator of magma fertility concerning magma water content. However, the infertile samples shows a low ratio of Yb/Dy < 5, which shows indications of plagioclase fractionation (**Fig. 6.10-B**). In addition, we proposed a new trace element ratio of zircon to understand the water content of the magma, which are Lu/Ho ratios. Generally, zircon trace elements of fertile samples include the HLE porphyry Cu-Au prospect shows a high ratio of Lu/Ho, and Yb/Ho, which corresponds to the high-water content. However, the trace element of infertile samples' mostly shows a low ratio of Lu/Ho corresponding to the low-water content (**Appendix 11**).

A high-water content in magma promotes the fractionation of MREE (e.g., Ho, Dy) by stabilizing amphibole (Zheng et al., 2021). Amphibole preferentially hosts MREE over HREE

(Davidson et al., 2007), which increases HREE values (e.g., Lu, Yb). In evolved hydrous melts, high water contents (>3 wt.%) induce amphibole fractionation and suppress plagioclase separation, which results in Eu/Eu* values nearing unity at deep crustal levels (Richards et al., 2012; Lu et al., 2016; Nevolko et al., 2021). Fertile samples, including the HLE porphyry Cu-Au prospect, show evidence for early amphibole fractional crystallization, but not for plagioclase. Therefore, we suggested that the ratio of Lu/Ho >2.0 (**Fig. 6.10-C**) is also applicable for magma fertility assessment.

Oxygen fugacity (fO_2) is a significant geological parameter that affects mineral stability, magma evolution, and ore-forming processes (Sun et al., 2015). Usually expressed relative to a particular oxygen buffer which refers to an assemblage of minerals or compounds that constrains temperature and pressure function. The most common oxygen buffers: fayalite–magnetite–quartz (FMQ), Co–CoO, hematite–magnetite (HM) (Chou 1978), Ni–NiO (NNO), and MnO–Mn$_3$O$_4$ (Huebner and Sato, 1970). The HLE zircon has a wide range of oxygen fugacity, ranging from -7.49 to -16.37 (Av. -11.89) (**Appendix 11**) (**Fig. 6.10-D**) which indicates that the HLE zircon is related to oxide magma.
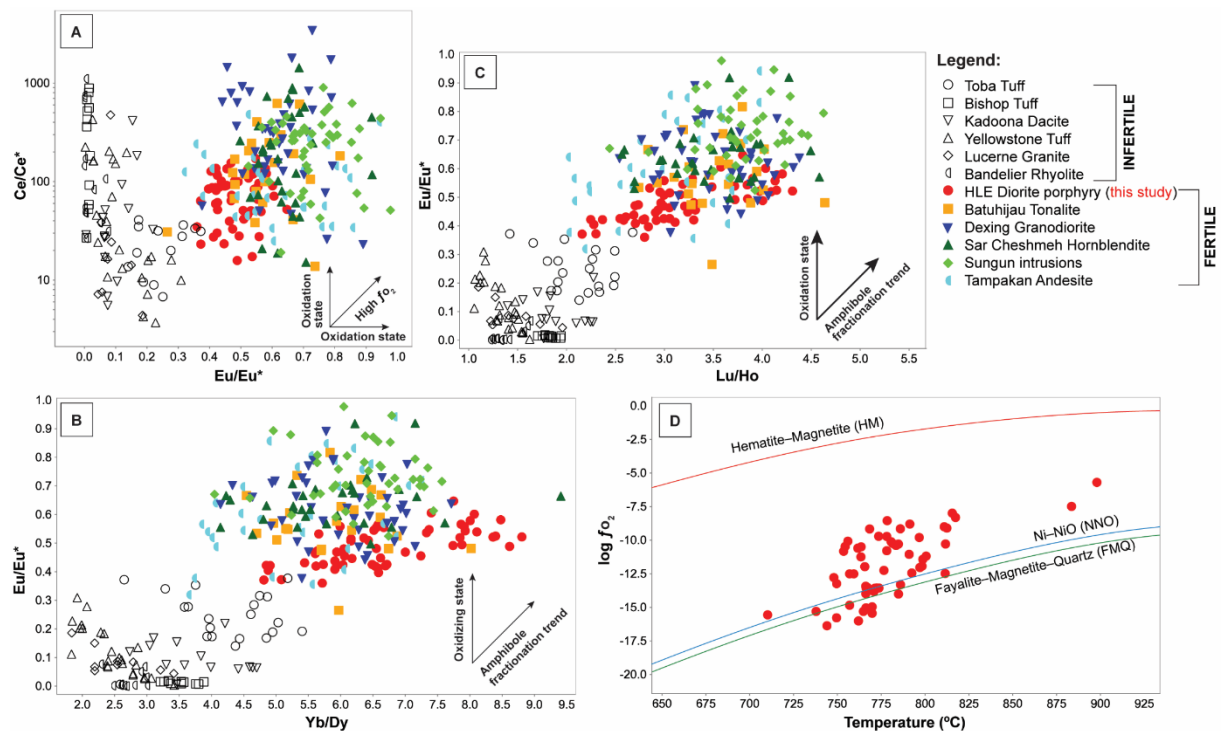
Figure 6. 10 Comparison of zircon compositions from fertile and infertile samples. (**A; B**) Ce/Ce* vs. Eu/Eu* and Eu/Eu* vs. Yb/Dy diagram after Ngoniri et al. (2021) and (**C**) Eu/Eu* vs. Lu/Ho diagram. (**D**) Oxygen fugacity (fO_2) vs. temperature diagram overlying mineral buffer: FMQ, HM Chou (1978), and Ni–NiO (NNO) Huebner & Sato (1970). The temperature is calculated using Geo-fO_2 software Li et al. (2019) based on the titanium (Ti) in zircon thermobarometer from Ferry & Watson (2007).

Furthermore, the presence of the Fe-oxide (magnetite?) and exsolution lamellae texture of magnetite-ilmenite as zircon-hosted inclusions (**Fig. 6.3**) also indicates that the zircon from the HLE prospect related to the oxide magma (Wones, 1989; Rene, 2008. Furthermore, oxidized magmas are important to extract and transport metals and sulfur from magma sources to upper crustal levels (Richards, 2011; Hattori, 2018).

In general, the average of the FMQ values of zircon from fertile samples, including the HLE zircon, is above FMQ +2.0, while the infertile samples are mostly below FMQ +1.5 (Supplementary 1; **Fig. 6.11**). High fO_2 values (oxidized magma) above FMQ +2 have a high S solubility as SO_4^{2-}, while the low fO_2 values below FMQ +2 (reduced magma) have a low S solubility of S as S^{2-} (Jugo et al., 2005) (**Fig. 6.11**).
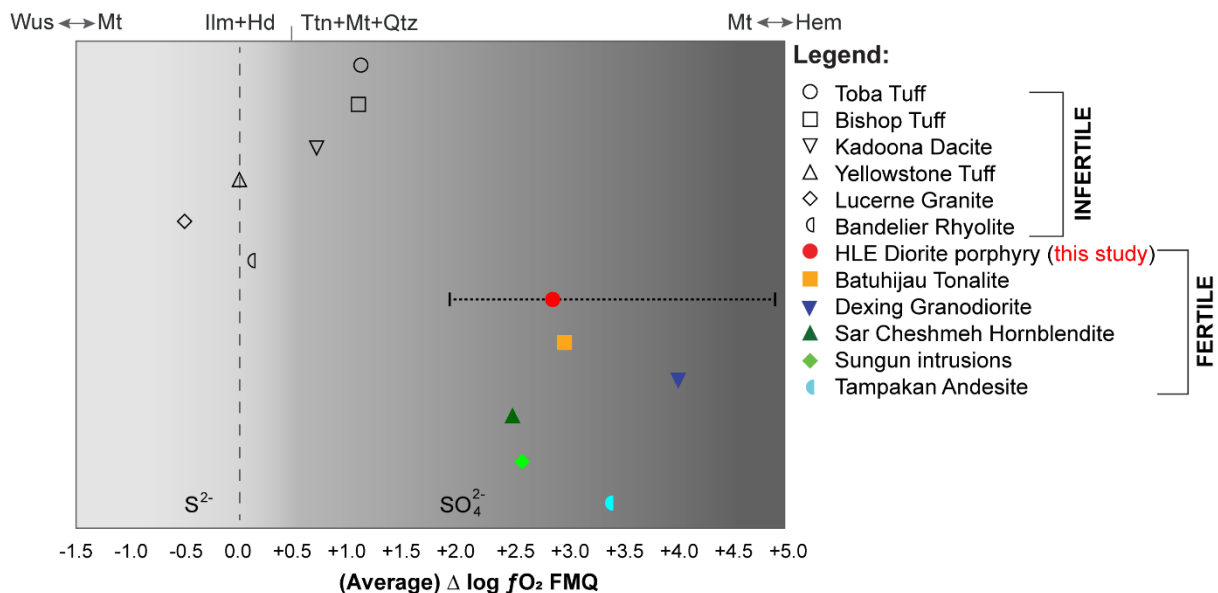
Figure 6. 11 Oxidation conditions of various as infertile and fertile samples, modified from Jugo et al. (2005); Hattori (2018). Note that magmas associated with porphyry Cu deposits mostly show $fO2$ above FMQ + 2. Abbreviation: Wus=Wustite, Mt=Magnetite, Ilm=Ilmenite, Hd=Hedenbergite, Ttn=Titanite, Qtz=Quartz, Hem=Hematite

By applying fertility indicators from our result to detrital zircons minerals, exploration for porphyry Cu-Au prospect in a greenfield or covered terrains can be improved in reconnaissance-stage exploration along the Sunda arc, especially in the eastern Sunda arc. Furthermore, detrital zircons analyzed following their compositions can be used to discriminate whether an area with a lack of geological information has un-prospective intrusions or prospective intrusions, thus indicating the potential exploration targets.

6.4 CONCLUSIONS

1. Geochemistry of zircon indicates that the zircon was a product of magmatism with an average crystallization temperature of 780 °C.

2. The U-Pb zircon dating yielded ages of 1.2 to 1.0 Ma (middle Pleistocene).

3. The presence of magnetite-ilmenite inclusions in zircon indicates that the zircon from the HLE prospect formed in an oxidized magma. Trace element analysis indicates Eu/Eu* > 0.4, and Ce/Ce* > 50, and average ΔFMQ +2.9 ± 1.9.

4. Ratios of the trace elements, Yb/Dy >0.4 and Lu/Ho >2.0 indicate amphibole fractionation in early stage, and the presence of amphibole implies magma had high water content (H_2O > 4 wt.%).

5. The geochemistry of zircon: Eu/Eu*, Ce/Ce*, Yb/Dy, and Lu/Ho is applicable for magma fertility assessment.

REFERENCES

Aldan, A.F., Idrus, A., Takahashi, R., Kaneko, G., 2022. High-Sulfidation Epithermal – Porphyry Transition in the Kumbokarno Prospect, Trenggalek District , East Java, Indonesia: Constraints from Mineralogy, Fluid Inclusion, and Sulfur Isotope Studies. Resource Geology 72: 1-25. https://doi.org/10.1111/rge.12289

Arribas, A., Jr., Hedenquist, J.W., Itaya, T., Okada, T., Concepcion, R.A., and Garcia, J.S., Jr., 1995. Contemporaneous formation of adjacent porphyry and epithermal Cu-Au deposits over 300 Ka in northern Luzon, Philippines: Geology, v. 23, p. 337-340.

Asadi, S., Moore, F. & Fattahi, N., 2013. Fluid inclusion and stable isotope constraints on the genesis of the Jian copper deposit, Sanandaj–Sirjan metamorphic zone, Iran. Geofluids 13, 66–81.

Audley-Charles, M. G., 1975. The Sumba fracture: A major discontinuity between eastern and western Indonesia, *Tectonophysics, 26*, p.213–228. https://doi.org/10.1016/0040-1951(75)90091-8

Babcock, R.C., Jr., Ballantyne, G.H., Phillips, C.H., 1995. Summary of the geology of the Bingham District , Utah: in Pierce, F.W., and Bolm, J.G., eds., Porphyry Copper Deposits of the American Cordillera: Arizona Geological Society Digest, v. 20, p. 316-335.

Bakker, R.J. (2001). Fluids: new software package to handle microthermometric data to calculate isochores. DOI: 10.1111/j.1468-8123.2009.00240.x

Bakker, R. J., and Diamond, L.W. (2006). Estimation of volume fractions of liquid and vapor phases in fluid inclusions, and definition of inclusion shapes. Amer. Mineral., v.91, pp.635-657. https://pure.unileoben.ac.at/portal/files/935367

Ballard, J.R., Palin, M.J., Campbell, I.H., 2002. Relative oxidation states of magmas inferred from Ce(IV)/Ce(III) in zircon: application to porphyry copper deposits of northern Chile. *Contrib. Mineral. Petrol. 144 (3)*, p.347–364. https://doi.org/10.1007/s00410-002-0402-5

Blamey, N. J. F. (2012) Composition and evolution of crustal, geothermal and hydrothermal fluids interpreted using quantitative fluid inclusion gas analysis. Jour. Geochem. Explor., 116-117, 17-27.

Bodnar, R. J. and Vityk, M. O. (1994) Interpretation of microthermometric data for H_2O-NaCl fluid inclusions. *In:* B. De Vivo and M.L. Frezzotti (Eds.) Fluid Inclusions in Minerals: Methods and Application, Pontignsno-Siena, 117130.

Bodnar, R. J. (2003) Introduction to aqueous-electrolyte fluid inclusions. *In:* I. Samson, A. Anderson and D. Marshall (Eds.) Fluid Inclusions: Analysis and Interpretation. Mineralogical Association of Canada, Short Course, 32, 81-100.

Burrows, D. R., Rennison M., Burt D., and Davies R., 2020. The Onto Cu-Au discovery, Eastern Sumbawa, Indonesia: A Large, Middle Pleistocene Lithocap-Hosted High-Sulfidation Covellite-Pyrite Porphyry Deposit. *Economic Geology*, 115 (7), p.1385–1412. https://doi.org/10.5382/econgeo.4766

Calder, M. F., Chang, Z., Arribas, A., Gaibor, A., Dunkley, P., Pastoral, J., Kouzmanov, K., Spandler, K., Hedenquist, J. W., 2022. High-Grade Copper and Gold Deposited During Post potassic Chlorite-White Mica-Albite Stage in the Far Southeast Porphyry Deposit, Philippines. Economic Geology. 117 (7), 1573–1596. https://doi.org/10.5382/econgeo.4940

Caritat De. P., Hutcheon, I., Walshe, J. L., 1993. Chlorite Geothermometry: A Review. Clays and clay mineral journal, Vol. 41, No. 2, 219-239. DOI: 10.1346/CCMN.1993.0410210

Carlile, J.C., and Mitchell, A.H.G.,1994. Magmatic arcs and associated gold and copper mineralization in Indonesia. *Journal of Geochemical Exploration, 50*, p.91-142. https://doi.org/10.1016/0375-6742(94)90022-1

Cathelineau, M. (1988) Cation site occupancy in chlorites and illites as a function of temperature. Clay Miner., 23, 471–485. https://doi.org/10.1180/claymin.1988.023.4.13

Cathelineau, M. and Nieva, D. (1985) A chlorite solid solution geothermometer. The Los Azufres (Mexico) geothermal system. Contrib. Mineral. Petrol., 91, 235–244. https://doi.org/10.1007/BF00413350

Chiaradia, M., and Caricchi, L., 2017. Stochastic modelling of deep magmatic controls on porphyry copper deposit endowment. Sci. Rep. 7:44523. https://doi.org/10.1038/srep44523

Chou, I.M., 1978. Calibration of oxygen buffers at elevated P and T using the hydrogen fugacity sensor. *Am. Mineral. 63*, 690–703. http://www.minsocam.org/ammin/AM63/AM63_690.pdf

Clark G.H, 1990. Geology of the mineral deposits of Australia and Papua New Guinea: in Hughes, F.E., eds., Australasian Institute of Mining and Metallurgy, Monograph Series 14, v. 2, p. 1807-1816.

Cooke, D.R., Hollings, P. and Walshe, J.L., 2005. Giant deposits characteristics, distribution and tectonic controls: Economic Geology, v. 100, p. 801-818.

Corbett, G. (2008) Influence of Magmatic Arc Geothermal Systems on Porphyry Epithermal Au-Cu-Ag Exploration Models. *Terry Leach Symposium, Sydney, October 17th, 2008*. Australian Institute of Geoscientist, Bulletin 48.

Cox, D.P., Singer, D.A., 1982. Distribution of gold in porphyry copper deposits: U.S. Geological Survey Open-File Report 88-46, 22 p. https://doi.org/10.3133/ofr8846

Davidson, J., Turner, S., Handley, H., Macpherson, C., Dosseto, A., 2007. Amphibole "sponge" in arc crust? Geology 35 (9), p.787–790. https://doi.org/10.1130/g23637a.1

Deer, W.A., Howie, R.A. and Zussman, J. (2013) *Introduction to the Rock-Forming Minerals (3rd edition)*. London: The Mineralogical Society. 506p

Dilles, J.H., A.J.R. Kent, J.L. Wooden, R.M. Tosdal, A. Koleszar, R.G. Lee, and L.P. Farmer., 2015. Zircon compositional evidence for sulfur-degassing from ore-forming arc magmas. Economic Geology, 110, p.241–251. https://doi.org/10.2113/econgeo.110.1.241

Elburg, M.A., van Bergen, M.J., Foden, J.D., 2004. Subducted upper and lower continental crust contributes to magmatism in the collision sector of the Sunda–Banda arc, Indonesia. *Geology 32*, p.41–44. https://doi.org/10.1130/G19941.1

Evans, A.M., 1993. Ore geology and Industrial Minerals an introduction: Blackwell scientific publications, 390 p.

Fadlin, Shaban, G., and Wildan, N.H. (2018). Active Continental Margin (ACM) Origin of tholeiitic magmatism in northern and southern Serayu-Banyumas, Central Java. *Jurnal Geology dan Sumberdaya Mineral (JGSM), 19(1), p.*15-30.

Fadlin, Shaban, G., Ariyanti, N., Hamzah, W. N., and Aditama, M. R., 2021. Tholeiitic basalt in Banyumas Basin (Kebasen, Central Java): The evidence of sedimentary recycling input and the contribution of oceanic slab on fore-arc active continental margin (ACM) magmatism. *IJOG*, *8(2)*, p.233-253. DOI:10.17014/ijog.8.2.233-253

Fall, A., Tattitch, B. and Bodnar, R. (2011). Combined microthermometric and Raman spectroscopic technique to determine the salinity of H2O-CO2-NaCl fluid inclusions

based on clathrate melting. Geochim. Cosmochim. Acta., v.75, pp.951-964. https://www.researchgate.net/publication/229349086

Ferry JM and Watson EB., 2007. New thermodynamic models and revised calibrations for the Ti-in-zircon and Zr-in-rutile thermometers. *Contrib. Mineral Petrol 154*, p.429–437. https://doi.org/10.1007/s00410-007-0201-0

Fiedrich, A.M., Martin, L.H.J., Storck, J.C., 2018. The influence of water in silicate melt on aluminium excess in plagioclase as a potential hygrometer. Sci Rep 8, 12421 (2018). https://doi.org/10.1038/s41598-018-29178-z

Foden, J.D. and Varne, R., (1980) The petrology and tectonic setting of Quaternary-Recent volcanic centres of Lombok and Sumbawa, Sunda arc: Chemical Geology, 30, 201−226.

Gardner, M.F., Troll, V.R., Gamble, J.A., Gertisser, R., Hart, G.L., And Rob M. Ellam, R.M., Harris, C., And Wolff, J.A., 2013. Crustal Differentiation Processes at Krakatau Volcano, Indonesia. *Journal of Petrology, 54(1)*, p. 149-182. https://doi.org/10.1093/petrology/egs066

Garwin, S. L.,2002. The Geologic Setting of Intrusion-Related Hydrothermal Systems near the Batu Hijau Porphyry Copper-Gold Deposit, Sumbawa, Indonesia: Global Exploration 2002, Integrated Methods for Discovery, Colorado, USA. *Society of Economic Geologists, Special Publication 9*, p.333-366. https://doi.org/10.5382/SP.09.15

Gertisser, R and Keller, J., 2003. Trace Element and Sr, Nd, Pb and O Isotope Variations in Medium-K and High-K Volcanic Rocks from Merapi Volcano, Central Java, Indonesia: Evidence for the Involvement of Subducted Sediments in Sunda Arc Magma Genesis. *Journal of Petrology, 44(3)*, p.457-489. https://doi.org/10.1093/petrology/44.3.457

Geshi, N., K. Nemeth, and T. Oikawa (2011), Growth of phreatomagmatic explosion craters: A model inferred from Suoana crater in Miyakejima Volcano, Japan, J. Volcanol. Geotherm. Res., 201, 30–38, doi:10.1016/j.jvolgeores.2010.11.012.

Grimes, C.B., John, B.E., Kelemen, P.B, Mazdab, F., Wooden, J.L., Cheadle, M.J., Hanghøj, K., Schwartz, J.J., 2007. The trace element chemistry of zircons from oceanic crust: a method for distinguishing detrital zircon provenance. *Geology vol. 3*, p.643–646. doi:10.1130/G23603A.1

Grimes, C.B., Wooden, J.L., Cheadle, M.J., John, B.E., 2015. "Fingerprinting" tectonomagmatic provenance using trace elements in igneous zircon. *Contrib. Mineral. Petrol. 170*, 46. https://doi.org/10.1007/s00410-015-1199-3

Guilbert, J.M., 1995. Geology, alteration, mineralisation, and genesis of the Bajo de la Alumbrera porphyry copper-gold deposit, Catamarca Province, Argentina: in Pierce, F.W., and Bolm, J.G., eds., Porphyry Copper Deposits of the American Cordillera, Arizona Geological Society Digest, v. 20, p. 646-656.

Hall, D. L., Sterner, S. M., & Bodnar, R. J., 1988. Freezing point depression of NaCl-KCl-H 2 O solutions. Economic Geology, 83, 197-202. DOI:10.2113/GSECONGEO.83.1.197

Hamilton, W. B., 1979. *Tectonics of the Indonesian Region*. US Geology Survey Professional Paper 1078, 345 p. https://doi.org/10.3133/pp1078

Hammarstrom, J.M., Bookstrom, A.A., Dicken, C.L., Drenth, B.J., Ludington, S., Robinson, G.R., Jr., Setiabudi, B.T., Sukserm, W., Sunuhadi, D.N., Wah, A.Y.S., and Zientek, M.L., with contributions from Cox, D.P., Jarnyaharn, P., Kopi, G., Ngoc, N.T.M., Otarawanna, P., Pei, C.S., Phany, U., Van Quy, Sakimoto, T., Saroa, D., Soares de Costa, N., Sotham, S., Sim, I.M., Trung, N.N., Wongsomasak, S., Yokarti, B., and Zaw, K., 2013. Porphyry copper assessment of Southeast Asia and Melanesia. *US Geological Survey Scientific Investigations Report 2010–5090–D*, 332 p. http://pubs.usgs.gov/sir/2010/5090/d/

Harrison, R.L., Maryono, A., Norris, M., Rohrlach, D., Cooke, D.R., Thompson, J.M., Creaser, J.A. and Thiede, D. A., 2018. Geochronology of the Tumpangpitu porphyry Au-Cu-Mo and high-suldation epithermal Au-Ag-Cu deposit: Evidence for pre- and post-mineralization diatremes in the Tujuh Bukit district , Southeast Java, Indonesia. *Economic Geology*. 113, 163-192. https://doi.org/10.5382/econgeo.2018.4547

Hattori, K., 2018. Porphyry copper potential in Japan based on magmatic oxidation state. *Resource Geology., 68*, p.126–137. https://doi.org/10.1111/rge.12160

Hawkesworth, C.J., Turner, S.P., McDermott, F., Peate, D.W., and Calsteren, P.van. (1997) U-Th Isotopes in Arc Magmas: Implications for Element Transfer from the Subducted Crust. *Science*, 276 (5312), 551−555.

Heinrich, CA., Driesner, T., Stefánsson, A., Seward, T. M.,2004. Magmatic vapor contraction and the transport of gold from the porphyry environment to epithermal ore deposits. Geology, 32 (9), 761 - 764. https://doi.org/10.1130/G20629.1

Heinrich, C. A., Candela, P. A., 2014. Fluids and ore formation in the earth's crust. In Holland, H. D. & Turekian, K. K. (eds.) Treatise on Geochemistry (2nd Edition), vol. 13, 1-28. https://doi.org/10.1016/B978-0-08-095975-7.01101-3

Holness, M. B. & Sawyer, E. 2008. On the pseudomorphing of melt-filled pores during the crystallization of magmatites. Journal of Petrology, 49, 1343.1363. https://citeseerx.ist.psu.edu/viewdoc/download

Hoskin P. W. O., 2005. Trace-element composition of hydrothermal zircon and the alteration of Hadean zircon from the Jack Hills, Australia.Geochim Cosmochim Acta 69, p.637–648. https://doi.org/10.1016/j.gca.2004.07.006

Huang, R., Audétat, A., 2012. The titanium-in-quartz (TitaniQ) thermobarometer: a critical examination and re-calibration. Geochim. Cosmochim. Acta, 84, 75–89. https://doi.org/10.1016/j.gca.2012.01.009

Huebner, J.S. and Sato, M.,1970. The oxygen fugacity–temperature relationships of manganese oxide and nickel oxide buffers. *Am. Mineral. 55*, p.934–952. http://www.minsocam.org/ammin/AM55/AM55_934.pdf

Idrus, A., Kolb, J., Meyer, F.M., Arif, J., Setyandhaka, D., Kepli, S. (2009a) A Preliminary Study on Skarn-Related Calc-Silicate Rocks Associated with the Batu Hijau Porphyry Copper-Gold Deposit, Sumbawa Island, Indonesia. Resource Geology, 59 (3), 295-306.

Idrus, A., Kolb J. and Meyer F.M. (2009b) Mineralogy, Lithogeochemistry and Elemental Mass Balance of the Hydrothermal Alteration Associated with the Gold-rich Batu Hijau Porphyry Copper Deposit, Sumbawa Island, Indonesia. *Resource Geology,* 59 (3), 215–230.

Idrus, A., and Kolb, J. and Meyer, F.M. (2007). Chemical composition of rock-forming minerals in copper-gold-bearing tonalite porphyry intrusions at the Batu Hijau deposit, Sumbawa Island, Indonesia: Implications for crystallisation conditions and fluorine-chlorine fugacity. *Resource Geology*. 57, 102-113. https://doi.org/10.1111/j.1751-3928.2007.00010.x

Imai, A and Ohno, S. (2005) Primary Ore Mineral Assemblage and Fluid Inclusion Study of the Batu Hijau Porphyry Cu-Au Deposit, Sumbawa, Indonesia. *Resource Geology,* 55 (3), 239−248.

Imai, A., Shinomiya J., Soe M.T, Setijadji L.D., Watanabe K. and Warmada I.W. (2007) Porphyry-Type Mineralization at Selogiri Area, Wonogiri Regency, Central Java, Indonesia. *Resource Geology,* 57 (2), 230−240.

Irvine, T.N. and Baragar W.R.A. (1971) A Guide to the chemical classification of the common volcanic rocks, *Canadian Journal of Earth Sciences, 8,* 523−548.

Jowett, E. C. (1991) Fitting iron and magnesium into the hydrothermal chlorite geothermometer. GAC/MAC/SEG Joint Annual Meeting (Toronto) Abstract, A62. https://www.researchgate.net/publication/298508601

Katili, J. A., 1975. Volcanism and plate tectonics in the Indonesian island arcs. Tectonophysics. 26, 3-4, p.165-188. https://doi.org/10.1016/0040-1951(75)90088-8

Klinkhammer, G. P., Elderfield, H., Edmond, J. M. and Mitra, A., (1995) Geochemical implications of rare earth element patterns in hydrothermal fluids from mid-ocean ridges. *Geochimica et Cosmochimica Acta,* 58 (23), 5105−5113.

Large, R.R., Gemmell, J.B. and Paulick, H. (2001) The Alteration Box Plot: A Simple Approach to Understanding the Relationship between Alteration Mineralogy and Lithogeochemistry Associated with Volcanic-Hosted Massive Sulfide Deposits. *Economic Geology,* 96, 957−971.

Lee, R.G., Dilles, J.H., Tosdal, R.M., Wooden, J.L., Mazdab, F.K., 2017. Magmatic evolution of granodiorite intrusions at the El Salvador Porphyry copper deposit, Chile, based on trace element composition and U/Pb age of zircons. Econ. Geol. 112 (2), p.245–273. https://doi.org/10.2113/econgeo.112.2.245

Levashova, E.V.; Skublov, S.G.; Popov, V.A., 2021. Distribution of Trace Elements Controlled by Sector and Growth Zonings in Zircon from Feldspathic Pegmatites (Ilmen Mountains, the Southern Urals). Geosciences, 11, 7. https://doi. org/10.3390/geosciences11010007

Li, N., Carranza, E.J.M., Ni, Z.Y. & Guo, D.S., 2012. The CO2-rich magmatic-hydrothermal fluid of the Qiyugou breccia pipe, Henan Province, China: implication for breccia genesis and gold mineralization. Geochemistry: Exploration, Environment, Analysis 12, 147–160. https://doi.org/10.1144/1467-7873/10-MINDEP-057

Li, W., Cheng, Y., & Yang, Z., 2019. Geo-fO2: Integrated software for analysis of magmatic oxygen fugacity. Geochemistry, Geophysics, Geosystems, 20 (5). p.2542-2555. https://doi.org/10.1029/2019GC008273

Li, Y and Audetat, A., 2013. Gold solubility and partitioning between sulfide liquid, monosulfide solid solution and hydrous mantle melts: Implications for the formation of Au-rich magmas and crust–mantle differentiation. Geochimica et Cosmochimica Acta, 118, p. 247-262, https://doi.org/10.1016/j.gca.2013.05.014

Lowenstern, J.B., 2001. Carbon dioxide in magmas and implications for hydrothermal systems. Mineralium Deposita 36, 490–502. https://doi.org/10.1007/s001260100185

Lu, Y.J., Loucks, R.R., Fiorentini, M., McCuaig, T.C., Evans, N.J., Yang, Z.M., Hou, Z.Q., Kirkland, C.L., Parra-Avila, L.A., Kobussen, A., 2016. Zircon compositions as a pathfinder for porphyry Cu ± Mo ± Au deposits. *Soc. Econ. Geol. Special Publ. 19*, p.329–347. https://doi.org/10.5382/SP.19.13

Ludwig, K. R., 2001, Isoplot/Ex, a geochronological toolkit for Microsoft Excel: Special publication: *Berkeley Geochronological Centre, Berkeley, California, v.1a-43*

Lowers, H. A., Rusk, B. G. & Koenig, A. 2007. Application of the TitaniQ geothermometer to hydrothermal quartz. Geological Society of America, Abstracts with Programs, 39(6), 607.

Lowenstern, J.B. (2001) Carbon dioxide in magmas and implications for hydrothermal systems. *Min Dep*, 36, 490−502.

MacDonald G.D, Arnold L.C, 1994. Geological and geochemical zoning of the Grasberg Igneous Complex, Irian Jaya, Indonesia: Journal of Geochemical Exploration, v. 50 p. 143-178. https://doi.org/10.1016/0375-6742(94)90023-X

Manalo, P.C., Subang, L.L., Imai, A., ...Takahashi, R., Blamey, N.J.F. (2020) Geochemistry and Fluid Inclusions Analysis of Vein Quartz in the Multiple Hydrothermal Systems of Mankayan Mineral District, Philippines. Resource Geology, 70, 1–27.

Maryono, Adi., Harrison, R. L., Cooke, D. R., Rompo, I., Hoschke, T. G., 2018. Tectonics and Geology of Porphyry Cu-Au Deposits along the Eastern Sunda Magmatic Arc, Indonesia. *Economic Geology, 113,* p.7-38. https://doi.org/10.5382/econgeo.2018.4542

Martins, H.C.B., Simoes, P.P., and Abreu, J., 2014. Zircon crystal morphology and internal structures as a tool for constraining magma sources: Examples from northern Portugal Variscan biotite-rich granite plutons. *C. R. Geoscience, 346*, p.233-243. https://doi.org/10.1016/j.crte.2014.07.004

Mernagh, T. P., Mavrogenes, J., 2019. Significance of high temperature fluids and melts in the Grasberg porphyry copper-gold deposit. Chemical Geology. Volume 508, Pages 210-224. https://doi.org/10.1016/j.chemgeo.2018.09.04

Mernagh, T. P., Leys, C., Henley, R. W., 2020. Fluid inclusion systematics in porphyry copper deposits: The super-giant Grasberg deposit, Indonesia, as a case study, Ore Geology Reviews, Vol. 123, pp13-68. https://doi.org/10.1016/j.oregeorev.2020.103570

Middlemost, E.A.K. (1994) Naming materials in magma/igneous rock system. *Earth Science Review,* 37 (3−4), 215−224.

Myaing, Y.Y., Idrus, A. and Titisari, A.D. (2018) Fluid Inclusion Study of The Tumpangpitu High Sulfidation Epithermal Gold Deposit in Banyuwangi District, East Java, Indonesia. *Journal of Geoscience, Engineering, Environment, and Technology,* 3 (1), 8−14.

Nevolko, P.A., Svetlitskaya, T.V., Savichev, A.A., Vesnin, V.S., and Fominykh, P.A., 2021. Uranium-Pb zircon ages, whole-rock and zircon mineral geochemistry as indicators for magmatic fertility and porphyry Cu-Mo-Au mineralization at the Bystrinsky and Shakhtama deposits, Eastern Transbaikalia, Russia. *Ore Geology Reviews, 139,* Part B. https://doi.org/10.1016/j.oregeorev.2021.104532

Ngoniri, A.H., Djomo, H.D., Ngnotue, T., Kenne, P.A., Mbianya, G.N., Ganno, S. and Nzenti, J.P., 2021. Zircon Trace Element Geochemistry and Ti-in-Zircon Thermometry of the Ngazi-Tina Pan-African Post-Collisional Granitoids, Adamawa Cameroon. International Journal of Geosciences, 12, p.307-328. https://doi.org/10.4236/ijg.2021.124017

Ohmoto, H., Lasaga, A. C., 1982. Kinetics of reactions between aqueous sulfates and sulfides in hydrothermal systems, Geochimica et Cosmochimica Acta, Volume 46, Issue 10, Pages 1727-1745. https://doi.org/10.1016/0016-7037(82)90113-2

Ohmoto, H., and Rye, R.O., 1979, Isotopes of sulphur and carbon, in Barnes, H.L., ed., Geochemistry of hydrothermal ore deposits, second edition: New York, John Wiley and Sons, Inc., p. 509-567.

Palaclos, C.M., Hein, U.F. and Dulskx, P. (1986) Behavior of rare earth elements during hydrothermal alteration at the Buena Esperanza copper-silver deposit, northern Chile. *Earth and Planetary Science Letters,* 80, 208−216.

Park, JW., Campbell, I.H., Chiaradia, M.,2021. Crustal magmatic controls on the formation of porphyry copper deposits. Nat Rev Earth Environ 2, 542–557. https://doi.org/10.1038/s43017-021-00182-8

Pearce, J.A. (1983) Role of the Sub-Continental Lithosphere in Magma Genesis at Active Continental Margins. In: Hawkesworth, C.J. and Norry, M.J., Eds., *Continental Basalts and Mantle Xenoliths*, Shiva Cheshire, UK, 230-249.

Pearce, J.A. (1996) A User's Guide to Basalt Discrimination Diagrams. In: Wyman, D.A., Ed., Trace Element Geochemistry of Volcanic Rocks: Applications for Massive Sulphide Exploration, *Geological Association of Canada*, 12, 79−113.

Pearce, J.A. (2008) Geochemical fingerprinting of oceanic basalts with applications to ophiolite classification and the search for Archean oceanic crust. *Lithos,* 100, 14−48.

Perk ins, C., McDougall, I., Claoué-Long, J., 1990. 40Ar/39Ar and U-Pb geochronology of the Goonumbla porphyry Cu-Au deposits, New South Wales, Australia: Economic Geology, v. 85,   p. 1808-1824.

Peterman, E. M. & Grove, M. 2010. Growth conditions of Synthetic muscovite + quartz: implications for quantifying retrograde metamorphism in exhumed magmatic arcs. Geology, 38, 1071.1074. https://doi.org/10.1130/G31449.1

Potter, R. W. (1977) Pressure corrections for fluid-inclusion homogenization temperatures based on the volumetric properties of the system $NaCl-H_2O$. Jour. Research U.S. Geol. Survey, 5, 603-607.

Proffett, J.M., 2003. Geology of the Bajo de la Alumbrera porphyry copper-gold deposit, Argentina: Economic Geology, v. 98, p. 1535-1574. https://www.segweb.org/pdf/brian-j-skinner-award/2003-proffett

Pupin, J.-P., 1980. Zircon and granite petrology. *Contrib. Mineral. Petrol. 110*, p.463–472. https://doi.org/10.1007/BF00381441

PT STM., 2018. Internal Exploration Report and Discussion *(unpublished)*

Randive, K. R., Hari, K. R., Dora, M. L., Malpe, D. B., and Bhondwe, A. A.,2014. Study of Fluid Inclusions: Methods, Techniques and Applications. Gond. Geol. Mag., V. 29 (1 and 2), pp.19-28. https://www.researchgate.net/publication/275337661

Richards, J. P., 2003. Tectono-magmatic precursors for porphyry Cu-(Mo-Au) deposit formation**:** Economic Geology, v. 98, p. 1515-1533.

Richards, J. P., 2011. High Sr/Y arc magmas and porphyry Cu ± Mo ± Au deposits: Just add water. Econ. Geol. 106 (7), p.1075–1081. https://doi.org/10.2113/econgeo.106.7.1075

Richards, J. P., 2015. The oxidation state, and sulfur and Cu contents of arc magmas: Implications for metallogeny. *Lithos*, *233*, 27–45. https://doi.org/10.1016/j.lithos.2014.12.011

Roedder, E., 1971, Fluid inclusion studies on the porphyry-type ore deposits at Bingham, Utah, Butte, Montana, and Climax, Colorado: Economic Geology, v. 66, p. 98-118.

Roedder, E. (1979). Fluid inclusions as samples of ore fluids. In: H.L. Barnes (Ed.), Geochemistry of hydrothermal ore deposits. 2nd ed. Wiley- New York, pp.684-737.

Roedder, E., 1984. Fluid inclusions: Mineralogical Society of America reviews in mineralogy 12, 644 p.

Reubi, O., Nicholls, A. I., and Kamenetsky, V. S., 2002. Early mixing and mingling in the evolution of basaltic magmas: evidence from phenocryst assemblages, Slamet Volcano, Java, Indonesia. *Journal of Volcanology and Geothermal Research*, 119(1-4), p.255-274. https://doi.org/10.1016/S0377-0273(02)00357-8

Ross, P.S and Bedard, J.H. (2009) Magmatic affinity of modern and ancient sub alkaline volcanic rocks determined from trace-element discriminant diagrams. *Canadian Journal of Earth Sciences,* 46, 823−839.

Rush, P.M., and Seegers, H.J., 1990. Ok Tedi copper-gold deposits: in Hughes, F.E., eds., Geology of the mineral deposits of Australia and Papua New Guinea: Australasian Institute of Mining and Metallurgy, Monograph Series 14, p. 1747-1754.

Rutter E. H., 1976. A Discussion on natural strain and geological structure - The kinetics of rock deformation by pressure solution. Royal Society of London. Series A, Mathematical and Physical Sciences 283: 203–219. http://doi.org/10.1098/rsta.1976.0079

Ryan, C.G., McInnes, B.M., Williams, P.J., Dong, G., Win, T.T. and Yeats, C.J. (2001) Imaging Fluid Inclusion Content using the New CSIRO-GEMOC Nuclear Microprobe. *Nuclear Instruments and Methods in Physics Research B*, 181, 570−577.

Rye, R.O., 2005. A review of the stable-isotope geochemistry of sulfate minerals in selected igneous environments and related hydrothermal systems. Chemical Geology, 215, pp. 5-36. https://doi.org/10.1016/j.chemgeo.2004.06.034

Sawkins, F.J., 1984. Metal deposits in relation to plate tectonics, Springer-Verlag, 325 p.

Seal, R.R.,2006. Sulfur Isotope Geochemistry of Sulfide Minerals. Reviews in Mineralogy and Geochemistry ; 61 (1): 633–677. https://doi.org/10.2138/rmg.2006.61.12

Seedorff E, Dilles JH, Proffett JM Jr., et al. (2005) Porphyry deposits – Characteristics and origin of hypogene features. Society of Economic Geologists, Economic Geology 100th Anniversary Volume, 1905–2005, 251–298. https://doi.org/10.5382/AV100.10

Setijadji, L.D., Kajino, S., Imai, A., and Watanabe, K., 2006. Cenozoic island arc magmatism in Java Island (Sunda arc, Indonesia): Clues on relationships between geodynamics of volcanic centers and ore mineralization. *Resource Geology, v. 56*, p.267–291. https://doi.org/10.1111/j.1751-3928.2006.tb00284.x

Setijadji, L.D., and Maryono, A., 2012. Geology and arc magmatism of the eastern Sunda arc, Indonesia: *Indonesian Society of Economic Geologists (MGEI) Annual Convention, Malang, Indonesia, November 26–27, 2012*, Proceedings, p.1–22

Seward, T. M., William-Jones, A. E., and Migdisov, A. A., 2014. The chemistry of metal transport and deposition by ore-forming hydrothermal fluids in Treatise on Geochemistry, 2nd Edn, eds H. Holland and K. Turekian (Amsterdam: Elsevier), 29–57. doi:10.1016/b978-0-08-095975-7.01102-5

Shannon, R.D., 1976. Revised effective ionic radii and systematic studies of interatomic in halide and chalcogenides. *Acta Crystallographica (Section A), 32.* p.751-765. https://doi.org/10.1107/S0567739476001551

Sheikh, L., Lutfi, W., Zhao, Z., and Awais, M., 2020. Geochronology, trace elements and Hf isotopic geochemistry of zircons from Swat orthogneisses, Northern Pakistan. *Open Geosciences, vol. 12, (1),* p. 148-162. https://doi.org/10.1515/geo-2020-0109

Shen, P., Hattori, K., Pan, H., Jackson, S., and Seitmuratova, E., 2015. Oxidation condition and metal fertility of granitic magmas: Zircon trace-element data from porphyry Cu deposits in the central Asian orogenic belt. *Econ. Geol., 110*, p.1861–1878. https://doi.org/10.2113/econgeo.110.7.1861

Shepherd, T. J. (1981). Temperature programmable heating-freezing stage for microthermometric analysis of fluid inclusions. Econ. Geol., v.76, pp.1244-1247.

Shu, Q., Chang, Z., Lai, Y., Hu, X., Wu, H., Zhang, Y., Wang, P., Zhai, D., and Zhang, C., 2019. Zircon trace elements and magma fertility: insights from porphyry (-skarn) Mo deposits in NE. China; *Mineralium Deposita, v. 54,* p.645–656. https://doi.org/10.1007/s00126-019-00867-7

Sillitoe, R.H. (2010). Porphyry Copper Systems. *Economic Geology*, *105(1)*, 3-41. https://doi.org/10.2113/gsecongeo.105.1.3

Sillitoe, R.H. (2012). Comments on the HLE Porphyry Copper-Gold Prospect and Hu'u Project Exploration, Sumbawa, Indonesia. *Internal report of Vale (unpublish)*.

Sillitoe, R.H., 1992. Gold-rich porphyry copper deposits: Geological model and exploration implications: Giant ore deposits workshop, Kingston Morrison, 38 p.

Sillitoe R.H.,1998. Major regional factors favoring large size, high hypogene grade, elevated gold content and supergene oxidation and enrichment of porphyry copper deposits, *in* Porter, T.M., ed., Conference of Porphyry and Hydrothermal Copper & Gold Deposits; a Global Perspective, Australian Mineral Foundation, Glenside, Proceedings, p. 21-34.

Sillitoe, R.H., 1979. Some thoughts on gold-rich porphyry copper deposits: Mineralium Deposita, v. 14, p. 161-174. https://doi.org/10.1007/BF00202933

Smythe, D.J., and Brenan, J.M., 2016. Magmatic oxygen fugacity estimated using zircon–melt partitioning of cerium. *Earth Planet. Sci. Lett. 453*, p.260–266. https://doi.org/10.1016/j.epsl.2016.08.013

Spear, F. S. & Wark, D. A. 2009. Cathodoluminescence imaging and titanium thermometry in metamorphic quartz. Journal of Metamorphic Geology, 27, 187.205. https://doi.org/10.1111/j.1525-1314.2009.00813.x

Sterner, S. M., Hall, D. L., Bodnar, R. J.,1988. Synthetic fluid inclusions. V. Solubility relations in the system NaCl-KCl-H2O under vapor saturated conditions, Geochimica et Cosmochimica Acta, Volume 52, Issue 5,Pages 989-1005, https://doi.org/10.1016/0016-7037(88)90254-2

Sudradjat, A., Andimangga, S. and Suwarna, N. (1998) Geological map of the Sumbawa quadrangle, Nusa Tenggara, Indonesia: Bandung, Indonesia, Geological Research and Development Centre.

Sundhoro, H., Bakrun, Sulaeman, B., T., Sumardi, E., Imnuel, M., Risdiato, D. and Liliek, R. (2005) Survei Panas Bumi Terpadu (Geologi, Geokimia dan Geofisika) Daerah Hu'u, Kabupaten Dompu, Provinsi Nusa Tenggara Barat. *Prosiding Kolokium Hasil Laporan Lapangan-DIM*, 38, 1−10.

Sun, W. D., Huang, R.F., Li, H., Hu, Y. B., Zhang, C. C., Sun, S. J., Zhang, L. P., Ding, X., Li, C. Y., and Zartman, R.E., 2015. Porphyry deposits and oxidized magmas. *Ore Geol. Rev., 65,* 97–131. https://doi.org/10.1016/j.oregeorev.2014.09.004

Sun, S. S., McDonough, W. F., 1989. Chemical and isotopic systematics of oceanic basalts: implications or mantle composition and processes, In Norry, M. J. (Ed.), Magmatism Basins. *Geo L. Soc. Spe Publ., 42,* 313–345. Doi: 10.1144/GSL.9.042.01.19

Sutarto, Idrus, A., Harijoko, A., Setijadji, L.D. and Meyer, F.M. (2015) Veins and Hydrothermal Breccias of The Randu Kuning Porphyry Cu-Au and Epithermal Au Deposits At Selogiri Area, Central Java Indonesia. *Journal of Applied Geology,* 7 (2), 80−99.

Takahashi, R., Tagiri, R., Blamey, N. J. F., Imai, A., Watanabe, Y. and Takeuchi, A. (2017) Characteristics and behavior of hydrothermal fluids for gold mineralization at the Hishikari deposits, Kyushu, Japan. Resource Geol., 67, 279–299.

Takenouchi and Kennedy (1965) The solubility of carbon dioxide in NaCl solutions at high temperatures and pressures. Amer. J. Sci., 263, 445–454.

Taylor, S.R. and McLennan, S.M. (1995) The geochemical evolution of The continental crust. *Reviews of Geophysics,* 33, 241−265.

Thomas, J. B., Watson, B. E., Spear, F. S., Shemella, P. T., Nayak, S.K., Lanzirotti, A., 2010. TitaniQ under pressure: the effect of pressure and temperature on the solubility of Ti in quartz. Contrib. Mineral. Petrol. 160, 743–759. https://link.springer.com/content/pdf/10.1007/s00410-010-0505-3

Titley, S.R., 1975. Geological characteristics and environment of some porphyry copper occurrences in the southwestern Pacific: Economic Geology, v. 70, p. 499-514.

Titley, S.R., Beane, R.E., 1981. Porphyry copper deposits; Part I, Geologic settings, petrology and tectogenesis, in Skinner, B.J., eds., Economic Geology 75th anniversary volume, p. 214-235.

Torres, A.I.S., Pandarinath, K., Surendra, P. and Dulski, V.P. (2010) Element Mobility Due to Hydrothermal Alteration in Los Azufres Geothermal Field, Mexico. *Proceedings World Geothermal Congress*. Bali, Indonesia, 25−29 April 2010

Trail, D., Watson, E.B., and Tailby, N.D., 2012, Ce and Eu anomalies in zircon as proxies for oxidation state of magmas: *Geochimica et Cosmochimica Acta, v. 97*, p.70–87. https://doi.org/10.1016/j.gca.2012.08.032

Van Leuwen, T (2018). Twenty-five more years of mineral exploration and discovery in Indonesia (1993 - 2017). 10th Anniversary special publication, Jakarta: Masyarakat Geologi Indonesia (MGEI). ISBN: 978-979-8126-34-5

Verdiansyah, O., Idrus, A., Setijadji, L. D., Sutopo, B., & Sukadana, I. G., 2022. Veins system and their mineralogical and microthermometric characteristics within the Humpa Leu East porphyry copper-gold mineralization at Hu'u district , Sumbawa island, Indonesia. Jurnal Teknologi, 84 (5), 35-49. https://doi.org/10.11113/jurnalteknologi.v84.17906

Wang, Q., Wei, Y. Yang, Y., and Peng, H., 2021. Zircon U–Pb Ages and Geochemistry of Granitoid in the Yuejinshan Copper-Gold Deposit, NE China: Constraints on Petrogenesis and Metallogenesis. *Minerals, 11,* 1206. https://doi.org/10.3390/min11111206

Wang, X., Griffin, W. L., and Chen, J., 2010. Hf contents and Zr/Hf ratios in granite zircons. *Geochemical Journal, Vol.44*, p.65-72. https://doi.org/10.2343/geochemj.1.0043

Wark, D.A., Hildreth, W., Spear, F.S., Cherniak, D.J., Watson, E.B., 2007. Pre-eruption recharge of the Bishop magma system. Geology35, 235–238. https://doi.org/10.1130/G23316A.1

Wark, D., Watson, E., 2006. TitaniQ: a titanium-in-quartz geothermometer. Contrib. Mineral. Petrol.152, 743–754. DOI:10.1007/S00410-006-0132-1

Watson, E. B., and Harrison, T. M., 2005. Zircon thermometer reveals minimum melting conditions on earliest. *Earth Planet Sci Lett 308*:841–844. Doi:10.1126/science.1110873

Watson, E. B., 1996. Surface enrichment and trace-element uptake during crystal growth. Geochem. Cosmochim. Acta, 60, 5013–5020. https://doi.org/10.1016/S0016-7037(96)00299-2

White, N.C., 1996. Hydrothermal alteration in porphyry copper systems: internal note for the Batu Hijau deposit, 14 p.

White, J., Ross, P.-S. (2011) Maar-diatreme volcanoes: a review. Journal of Volcanology and Geothermal Research, v. 201, p. 1-29. https://doi.org/10.1016/j.jvolgeores.2011.01.010.

Williams, J. A. E. and Heinrich, C. A. (2005) Vapor Transport of Metals and the Formation of Magmatic-Hydrothermal Ore Deposits. Economic Geology, 100, 1287-1312. https://doi.org/10.2113/gsecongeo.100.7.1287

Williamson, B., Herrington, R., Morris, A.,2016. Porphyry copper enrichment linked to excess aluminium in plagioclase. Nature Geosci 9, 237–241. https://doi.org/10.1038/ngeo2651

Yang, Y.F., Chen, Y.J., Li, N., Mi, M., Xu, Y.L., Li, F.L. & Wanc, S.Q., 2013. Fluid inclusion and isotope geochemistry of the Qian'echong giant porphyry Mo deposit, Dabie Shan, China: a case of NaCl-poor, CO2-rich fluid systems. Journal of Geochemical Exploration 124, 1–13. https://doi.org/10.1016/j.gexplo.2012.06.019

Zheng, Y., Zhang, C., Jia, F., Liu H., and Yan, Q., 2021. Apatite and Zircon Geochemistry in Yao' an Alkali-Rich Porphyry Gold Deposit, Southwest China: Implications for Petrogenesis and Mineralization. *Minerals 11, no. 11*: 1293. https://doi.org/10.3390/min11111293

Zhong, S. H., Feng, C. Y., Seltmann, R., Li, D., and Qu, H. Y., 2018. Can magmatic zircon be distinguished from hydrothermal zircon by trace element composition? The effect of mineral inclusions on zircon trace element composition. *Lithos 314–315*, p.646–657. https://doi.org/10.1016/j.lithos.2018.06.029

APPENDICES

Appendix 1. Whole-rock geochemical results of major, trace and rare earth elements for all phases of diorite and quartz diorite porphyry at the Humpa Leu East porphyry Cu-Au prospect.

Sample	VHD 001-459	VHD 001-421.7	VHD 001-445.7	VHD 001-450.5	VHD 001R-715.4	VHD 001R-517	VHD 001R-661.3	VHD 001R-539.8	VHD 001R-503.8
Intrusion Phase	Early phase	Early phase	Early phase	Early phase	Late phase	Late phase	Late phase	Late phase	Intermediate phase
SiO_2 (wt.%)	49.8	56.6	57.6	61.7	60.0	55.4	53.6	58.5	54.2
TiO_2	0.98	0.45	0.70	0.64	0.52	0.68	0.81	0.63	0.68
Al_2O_3	20.8	17.2	15.4	13.4	17.2	17.9	15.9	15.5	17.0
$Fe_2O_3(t)$	10.6	6.81	7.98	3.66	4.99	8.91	11.82	9.76	7.15
MnO	0.09	0.09	0.08	0.08	0.12	0.15	0.17	0.16	0.20
MgO	3.96	4.54	4.78	3.94	3.47	3.20	4.98	3.62	4.82
CaO	3.66	6.25	4.57	6.39	5.37	5.64	5.56	3.98	5.62
Na_2O	0.00	1.96	0.81	0.69	2.23	0.00	2.17	0.53	0.15
K_2O	2.52	0.75	2.85	2.66	1.38	1.92	0.58	2.01	1.96
P_2O_5	0.10	0.11	0.15	0.13	0.14	0.10	0.22	0.26	0.15
LOI	5.97	3.34	2.94	3.34	3.65	3.37	2.61	2.98	5.25
Total	98.5	98.2	97.9	96.6	99.0	97.2	98.4	98.0	97.2
Mn (ppm)	723	658	619	606	906	1,125	1,268	1,252	1,577
Cu	4,446	4,452	6,687	3,103	41.5	4,537	4,223	3,051	3,911
Au	0.10	0.28	0.31	0.20	0.07	0.13	0.38	0.18	0.14
Zn	415	156	383	154	118.	485.	280	492	267
Ga	41.4	31.8	68.0	56.4	43.5	32.8	30.8	55.1	44
Mo	27.5	15.1	15.6	15.0	12.9	14.9	4.73	10.8	11.1
Ag	0.84	1.48	2.00	0.79	0.89	0.45	0.85	0.76	0.61
Sb	0.21	0.20	0.42	0.18	1.19	0.16	0.13	0.24	0.22
Rb	65.4	12.9	80.1	72.1	42.0	43.4	16.6	46.5	46.7
Sr	162	309	252	379	398	228	377	283	266
Zr	55.9	63.2	57.2	55.6	84.3	88.2	59.7	75.0	91.8
Nb	1.76	0.92	2.09	1.96	1.48	5.06	2.76	2.29	2.92
Cs	2.87	2.13	3.36	2.13	2.07	1.91	2.26	2.25	3.63

Ba	357	257	975	834	425.	297	174	689	442
Hf	0.14	0.07	0.14	0.12	0.11	0.15	0.08	0.11	0.12
Ta	0.24	0.58	0.22	0.39	0.11	0.41	0.13	0.28	0.33
Pb	20.1	25.0	15.6	11.6	10.2	14.7	15.9	19.3	59.1
Th	1.98	1.04	4.77	1.73	1.50	5.36	2.39	5.68	8.41
U	0.60	0.20	0.39	0.42	0.32	0.75	0.25	0.71	0.81
La	10.6	6.52	9.82	11.1	8.81	22.4	10.1	14.1	15.0
Ce	21.0	14.4	20.3	22.0	19.5	47.6	21.4	29.9	27.0
Pr	2.59	1.88	2.44	2.66	2.52	5.58	2.58	3.45	2.92
Nd	11.5	8.50	10.7	11.2	11.1	22.3	11.0	14.3	12.0
Sm	3.05	2.04	2.39	2.54	2.59	4.18	2.47	3.19	2.73
Eu	1.61	0.78	1.07	1.38	1.10	1.17	0.86	1.53	0.88
Gd	3.41	2.15	2.52	2.61	2.76	3.74	2.46	3.34	2.92
Tb	0.55	0.33	0.37	0.39	0.44	0.50	0.37	0.49	0.43
Dy	3.23	1.88	2.18	2.27	2.62	2.69	2.05	2.70	2.48
Ho	0.65	0.37	0.43	0.45	0.53	0.53	0.41	0.52	0.49
Er	1.81	0.98	1.22	1.28	1.55	1.52	1.13	1.43	1.43
Tm	0.24	0.13	0.16	0.17	0.20	0.19	0.15	0.19	0.19
Yb	1.50	0.78	0.93	1.10	1.31	1.21	0.92	1.16	1.20
Lu	0.21	0.11	0.13	0.15	0.19	0.16	0.13	0.16	0.17
Y	15.7	9.44	10.7	10.8	13.1	12.8	9.94	12.8	12.6
V	295	125	177	118	107	122	206	164	158

Table 1 (cont.)

Sample	VHD 006-400.2	VHD 006-240.6	VHD 006-749.5	VHD 006-723	VHD 006-802.3	VHD 009A-354.8	VHD 009A-324.6	VHD 009A-669.6	VHD 009A-703.2
Intrusion Phase	Wall-rock (andesite)	Wall-rock (andesite)	Intermediate phase	Intermediate phase	Intermediate phase	Early phase	Early phase	Late phase	Late phase
SiO$_2$ (wt.%)	55.9	60.1	60.8	62.3	61.2	61.8	64.5	65.8	63.7
TiO$_2$	0.49	0.52	0.48	0.52	0.52	0.29	0.43	0.38	0.44

Al_2O_3	18.0	20.0	16.9	15.4	16.2	11.0	12.9	13.3	10.2
$Fe_2O_3(t)$	5.68	6.65	6.71	2.44	4.31	9.77	7.07	6.35	13.7
MnO	0.16	0.06	0.13	0.06	0.15	0.33	0.20	0.13	0.10
MgO	5.55	2.85	3.59	2.52	3.97	2.91	2.09	2.99	2.72
CaO	6.63	2.77	2.81	6.62	6.15	6.10	5.33	3.91	3.60
Na_2O	2.28	0.00	0.05	4.38	3.44	3.30	3.89	3.48	3.43
K_2O	0.35	2.47	2.31	1.04	0.31	0.47	0.44	0.74	0.36
P_2O_5	0.11	0.15	0.15	0.08	0.08	0.19	0.06	0.12	0.11
LOI	4.14	3.49	4.25	1.44	2.31	2.56	1.21	2.10	0.72
Total	99.3	99.0	98.1	96.9	98.6	98.7	98.1	99.3	99.1
Mn (ppm)	1,161	483	945	348	1,087	2,649	993	1,020	775
Cu	1,061	343	3,104	2,194	433	11,860	4,791	2,004	3,165
Au	0.09	0.07	0.11	0.13	0.13	4.24	0.13	0.21	0.58
Zn	547	819	188	114	226	582	460	131	151
Ga	30.5	180	50.8	32.7	30.3	24.3	29.3	36.8	30.0
Mo	3.23	141	14.1	76.1	7.16	8.93	11.6	5.02	2.85
Ag	0.36	0.14	13.2	0.55	0.20	3.35	0.74	0.42	0.69
Sb	0.14	0.45	13.9	1.11	0.45	1.51	0.34	0.42	0.66
Rb	8.31	65.8	52.7	20.7	10.5	4.66	38.0	12.3	5.13
Sr	383	155	267	508	543	310	299	385	323
Zr	69.7	82.1	66.6	75.2	88.9	43.0	65.5	70.7	47.7
Nb	1.80	2.04	2.58	1.44	1.93	0.55	3.01	1.65	0.98
Cs	2.80	4.77	2.83	1.19	1.04	0.13	2.06	0.79	0.35
Ba	228	2,272	589	343	216	159	267	328	226
Hf	0.16	0.19	0.12	0.11	0.31	0.35	0.97	0.20	0.25
Ta	1.90	1.20	2.47	0.19	0.83	0.28	0.68	0.89	0.07
Pb	17.1	11.0	28.3	21.5	30.8	62.1	24.6	10.5	8.02
Th	1.30	1.78	1.38	0.92	2.02	0.89	1.96	1.51	1.47
U	0.29	0.43	0.26	0.29	0.37	0.09	0.28	0.11	0.14

La	7.80	7.53	3.88	6.55	10.26	3.33	7.61	6.86	5.13
Ce	17.4	16.3	9.48	14.4	20.3	9.18	20.5	15.5	13.0
Pr	2.32	2.07	1.31	1.84	2.39	1.38	2.82	1.96	1.87
Nd	10.5	9.12	6.02	8.11	9.79	6.78	13.1	8.58	9.09
Sm	2.64	2.14	1.56	1.95	2.08	1.89	3.17	1.93	2.44
Eu	0.97	1.65	0.52	0.75	0.95	0.49	0.86	0.69	0.65
Gd	2.64	2.08	1.66	2.01	2.06	2.01	3.34	2.11	2.63
Tb	0.41	0.29	0.25	0.31	0.29	0.34	0.53	0.33	0.42
Dy	2.38	1.56	1.38	1.87	1.60	2.07	3.18	1.99	2.50
Ho	0.49	0.29	0.27	0.38	0.32	0.44	0.65	0.41	0.51
Er	1.39	0.80	0.74	1.11	0.94	1.26	1.88	1.24	1.44
Tm	0.19	0.11	0.10	0.15	0.12	0.18	0.26	0.18	0.21
Yb	1.26	0.67	0.62	0.93	0.86	1.28	1.74	1.23	1.35
Lu	0.18	0.10	0.09	0.13	0.12	0.20	0.26	0.18	0.20
Y	11.6	7.12	6.23	9.43	8.06	10.5	16.3	10.8	12.7
V	89.5	99.9	68.5	74.6	132	130	63.2	93.4	203

Appendix 2 EPMA result of pyrite chemistry, which is representative every vein/mineralization stage of the HLE prospect.

No	Sample ID	Vein type	Stages	Se (wt.%)	As (wt.%)	Fe (wt.%)	Ni (wt.%)	Au (wt.%)	Cu (wt.%)	Co (wt.%)	Zn (wt.%)	S (wt.%)	Sb (wt.%)	Ag (wt.%)	Pb (wt.%)	Total
1	013-1069	D vein	Late stage	0.00	0.03	46.4	0.03	0.00	0.00	0.08	0.00	53.2	0.00	0.00	0.00	99.7
2	013-1069	D vein	Late stage	0.04	0.05	46.0	0.02	0.00	0.00	0.08	0.01	52.7	0.00	0.00	0.00	98.9
3	013-1069	D vein	Late stage	0.00	0.01	45.9	0.00	0.00	0.00	0.08	0.00	52.5	0.00	0.00	0.00	98.5
4	013-1069	D vein	Late stage	0.08	0.04	46.2	0.00	0.00	0.01	0.07	0.00	52.6	0.00	0.00	0.00	99.0
5	013-1069	D vein	Late stage	0.00	0.03	45.7	0.00	0.00	0.00	0.07	0.00	52.8	0.00	0.00	0.00	98.7
6	013-1069	D vein	Late stage	0.00	0.02	46.0	0.01	0.00	0.00	0.08	0.00	52.9	0.00	0.00	0.00	99.0
7	013-1069	D vein	Late stage	0.00	0.05	46.5	0.00	0.00	0.00	0.08	0.00	53.1	0.00	0.00	0.00	99.7
8	013-1069	D vein	Late stage	0.03	0.01	46.2	0.01	0.00	0.00	0.07	0.00	52.7	0.00	0.00	0.00	99.1
9	013-1069	D vein	Late stage	0.02	0.11	46.1	0.00	0.00	0.00	0.08	0.00	52.4	0.00	0.00	0.00	98.7
10	013-1069	D vein	Late stage	0.01	0.09	46.2	0.00	0.00	0.01	0.08	0.00	52.8	0.00	0.00	0.00	99.2
11	013-1069	D vein	Late stage	0.04	0.00	46.0	0.00	0.00	0.00	0.07	0.02	53.3	0.00	0.00	0.00	99.4
12	013-1069	D vein	Late stage	0.07	0.03	46.1	0.00	0.00	0.00	0.08	0.00	52.5	0.00	0.00	0.00	98.8
13	013-1069	D vein	Late stage	0.02	0.02	46.4	0.00	0.00	0.02	0.08	0.00	52.9	0.00	0.00	0.00	99.4
14	013-1069	D vein	Late stage	0.03	0.04	46.2	0.00	0.00	0.01	0.08	0.00	53.4	0.00	0.00	0.00	99.8
15	013-1069	D vein	Late stage	0.04	0.03	46.1	0.00	0.00	0.00	0.09	0.00	52.7	0.00	0.00	0.00	99.0
16	013-1069	D vein	Late stage	0.07	0.00	46.3	0.02	0.00	0.01	0.08	0.00	53.0	0.00	0.00	0.00	99.5
17	013-1069	D vein	Late stage	0.09	0.03	46.3	0.02	0.00	0.00	0.08	0.00	53.1	0.00	0.00	0.00	99.6
18	013-1069	D vein	Late stage	0.07	0.02	46.3	0.01	0.00	0.01	0.09	0.00	52.7	0.00	0.00	0.00	99.3
19	013-1069	D vein	Late stage	0.00	0.05	46.1	0.00	0.00	0.01	0.08	0.00	52.9	0.00	0.00	0.00	99.1
20	013-1069	D vein	Late stage	0.03	0.02	46.2	0.00	0.00	0.01	0.08	0.00	52.9	0.00	0.00	0.00	99.2
21	013-1069	D vein	Late stage	0.01	0.00	46.2	0.00	0.00	0.01	0.08	0.00	53.6	0.00	0.00	0.00	99.9
22	013-1069	D vein	Late stage	0.00	0.01	46.4	0.04	0.00	0.01	0.08	0.00	53.7	0.00	0.00	0.00	100.2
23	013-1069	D vein	Late stage	0.00	0.01	46.1	0.01	0.00	0.02	0.07	0.00	54.2	0.00	0.00	0.00	100.4
24	013-1069	D vein	Late stage	0.00	0.04	46.3	0.00	0.00	0.00	0.07	0.00	53.5	0.00	0.00	0.00	100.0
25	013-1069	D vein	Late stage	0.09	0.00	46.2	0.00	0.00	0.01	0.07	0.01	52.4	0.00	0.00	0.00	98.8
26	013-1069	D vein	Late stage	0.05	0.01	45.9	0.00	0.00	0.01	0.07	0.00	52.4	0.00	0.00	0.00	98.4
27	013-1069	D vein	Late stage	0.08	0.03	46.2	0.00	0.00	0.01	0.07	0.00	52.9	0.00	0.00	0.00	99.4
28	013-1069	D vein	Late stage	0.03	0.01	46.4	0.00	0.00	0.00	0.08	0.00	53.2	0.00	0.00	0.00	99.7
29	013-1069	D vein	Late stage	0.03	0.03	46.0	0.00	0.00	0.01	0.09	0.05	52.4	0.00	0.00	0.00	98.6
30	013-1069	D vein	Late stage	0.00	0.00	45.6	0.00	0.00	0.00	0.08	0.01	51.5	0.00	0.00	0.00	97.2
31	013-1069	D vein	Late stage	0.03	0.02	45.8	0.02	0.00	0.00	0.08	0.00	51.9	0.00	0.00	0.00	97.9
32	013-1069	D vein	Late stage	0.07	0.00	45.9	0.00	0.00	0.00	0.08	0.00	52.0	0.00	0.00	0.00	98.1
33	013-1069	D vein	Late stage	0.05	0.02	45.7	0.01	0.00	0.00	0.08	0.00	51.8	0.00	0.00	0.00	97.6
34	013-1069	D vein	Late stage	0.00	0.00	45.8	0.00	0.00	0.00	0.08	0.01	51.4	0.00	0.00	0.00	97.3
35	013-1069	D vein	Late stage	0.00	0.00	46.2	0.00	0.00	0.00	0.06	0.00	52.1	0.00	0.00	0.00	98.4

1	009A-518	AB vein	Early stage	0.08	0.05	45.7	0.01	0.00	0.04	0.08	0.01	51.9	0.00	0.00	0.00	97.9
2	009A-518	AB vein	Early stage	0.04	0.00	45.9	0.04	0.00	0.05	0.08	0.00	52.3	0.00	0.00	0.00	98.4
3	009A-518	AB vein	Early stage	0.00	0.01	45.8	0.00	0.00	0.06	0.08	0.00	52.5	0.00	0.00	0.00	98.4
4	009A-518	AB vein	Early stage	0.04	0.14	45.9	0.00	0.00	0.07	0.11	0.00	52.4	0.00	0.00	0.00	98.7
5	009A-518	AB vein	Early stage	0.02	0.42	45.7	0.00	0.00	0.13	0.11	0.00	52.3	0.00	0.00	0.00	98.7
6	009A-518	AB vein	Early stage	0.09	0.03	46.1	0.01	0.00	0.05	0.09	0.00	53.1	0.00	0.00	0.00	99.5
7	009A-518	AB vein	Early stage	0.02	0.04	45.8	0.00	0.00	0.02	0.09	0.00	52.6	0.00	0.00	0.00	98.6
8	009A-518	AB vein	Early stage	0.03	0.03	46.0	0.00	0.00	0.03	0.07	0.02	53.4	0.00	0.00	0.00	99.6
9	009A-518	AB vein	Early stage	0.08	0.11	46.0	0.01	0.00	0.00	0.10	0.00	53.4	0.00	0.00	0.00	99.7
10	009A-518	AB vein	Early stage	0.07	0.11	45.6	0.01	0.00	0.01	0.08	0.01	53.2	0.00	0.00	0.00	99.0
11	009A-518	AB vein	Early stage	0.00	0.08	46.0	0.00	0.00	0.02	0.09	0.00	53.2	0.00	0.00	0.00	99.3
12	009A-518	AB vein	Early stage	0.00	0.26	45.4	0.00	0.00	0.88	0.12	0.00	52.7	0.00	0.00	0.00	99.4
13	009A-518	AB vein	Early stage	0.10	0.34	45.6	0.00	0.00	0.26	0.08	0.00	52.4	0.00	0.00	0.00	98.8
14	009A-518	AB vein	Early stage	0.00	0.05	45.8	0.00	0.00	0.00	0.08	0.00	52.7	0.00	0.00	0.00	98.6
15	009A-518	AB vein	Early stage	0.00	0.11	45.8	0.00	0.00	0.00	0.07	0.00	52.6	0.00	0.00	0.00	98.6
16	009A-518	AB vein	Early stage	0.03	0.20	46.1	0.00	0.00	0.00	0.07	0.01	52.5	0.00	0.00	0.00	98.9
17	009A-518	AB vein	Early stage	0.03	0.06	46.1	0.00	0.00	0.03	0.08	0.00	52.8	0.00	0.00	0.00	99.1
18	009A-518	AB vein	Early stage	0.01	0.05	46.1	0.00	0.00	0.01	0.07	0.00	52.7	0.00	0.00	0.00	99.0
19	009A-518	AB vein	Early stage	0.00	0.17	46.1	0.00	0.00	0.02	0.10	0.00	52.8	0.00	0.00	0.00	99.2
20	009A-518	AB vein	Early stage	0.00	0.16	46.3	0.01	0.00	0.02	0.15	0.01	52.3	0.00	0.00	0.00	99.0
21	009A-518	AB vein	Early stage	0.00	0.16	46.2	0.00	0.00	0.15	0.08	0.00	51.7	0.00	0.00	0.00	98.2
22	009A-518	AB vein	Early stage	0.04	0.13	46.1	0.00	0.00	0.01	0.08	0.00	52.8	0.00	0.00	0.00	99.1
23	009A-518	AB vein	Early stage	0.00	0.19	45.3	0.00	0.00	1.72	0.12	0.00	51.0	0.00	0.00	0.00	98.3
24	009A-518	AB vein	Early stage	0.08	0.46	46.1	0.00	0.00	0.02	0.12	0.00	52.3	0.00	0.00	0.00	99.1
25	009A-518	A-B vein	Early stage	0.00	0.22	46.2	0.00	0.00	0.27	0.37	0.01	52.4	0.00	0.00	0.00	99.5
26	009A-518	AB vein	Early stage	0.05	0.08	46.2	0.00	0.00	0.01	0.08	0.00	52.6	0.00	0.00	0.00	99.0
27	009A-518	AB vein	Early stage	0.02	0.04	46.2	0.01	0.00	0.07	0.09	0.00	52.4	0.00	0.00	0.00	98.8
28	009A-518	AB vein	Early stage	0.09	0.04	46.2	0.00	0.00	0.06	0.08	0.00	52.8	0.00	0.00	0.00	99.2
29	009A-518	AB vein	Early stage	0.05	0.02	46.3	0.00	0.00	0.05	0.09	0.01	52.5	0.00	0.00	0.00	99.0
30	009A-518	AB vein	Early stage	0.05	0.80	46.1	0.01	0.00	0.02	0.07	0.00	51.9	0.00	0.00	0.00	99.0
31	009A-518	AB vein	Early stage	0.10	0.25	46.2	0.00	0.00	0.02	0.08	0.00	52.0	0.00	0.00	0.00	98.6
32	009A-518	AB vein	Early stage	0.09	1.05	46.1	0.01	0.00	0.02	0.07	0.00	51.3	0.00	0.00	0.00	98.6
33	009A-518	AB vein	Early stage	0.03	0.58	45.9	0.00	0.00	0.04	0.09	0.00	51.6	0.00	0.00	0.00	98.3
34	009A-518	AB vein	Early stage	0.06	0.49	46.1	0.00	0.00	0.00	0.08	0.00	51.6	0.00	0.00	0.00	98.3
35	009A-518	AB vein	Early stage	0.02	0.40	46.0	0.00	0.00	0.02	0.08	0.00	51.7	0.00	0.00	0.00	98.2
36	009A-518	AB vein	Early stage	0.09	0.23	46.1	0.02	0.00	0.01	0.07	0.00	51.9	0.00	0.00	0.00	98.4
37	009A-518	AB vein	Early stage	0.04	0.52	45.8	0.03	0.00	0.01	0.08	0.00	51.6	0.00	0.00	0.00	98.0
38	009A-518	AB vein	Early stage	0.10	0.18	46.3	0.00	0.00	0.01	0.07	0.00	51.5	0.00	0.00	0.00	98.1

39	009A-518	AB vein	Early stage	0.07	0.19	46.4	0.00	0.00	0.01	0.07	0.01	51.5	0.00	0.00	0.00	98.3
40	009A-518	AB vein	Early stage	0.06	0.09	46.2	0.00	0.00	0.00	0.09	0.00	51.8	0.01	0.00	0.00	98.3
41	009A-518	AB vein	Early stage	0.03	0.14	46.3	0.00	0.00	0.02	0.08	0.00	52.0	0.00	0.00	0.00	98.6
42	009A-518	AB vein	Early stage	0.00	0.11	46.4	0.00	0.00	0.00	0.08	0.00	52.1	0.00	0.00	0.00	98.8
43	009A-518	AB vein	Early stage	0.00	0.05	46.4	0.01	0.00	0.01	0.10	0.00	52.3	0.00	0.00	0.00	98.8
44	009A-518	AB vein	Early stage	0.09	0.34	46.1	0.00	0.00	0.07	0.08	0.00	52.2	0.00	0.00	0.00	98.9
45	009A-518	AB vein	Early stage	0.06	0.00	45.8	0.00	0.00	0.08	0.15	0.00	52.0	0.00	0.00	0.00	98.1
1	009A-474.6	B vein	Inter. stage	0.00	0.01	45.6	0.01	0.00	0.03	0.15	0.00	51.7	0.00	0.00	0.00	97.5
2	009A-474.6	B vein	Inter. stage	0.02	0.02	46.1	0.02	0.00	0.02	0.09	0.00	52.1	0.00	0.00	0.00	98.4
3	009A-474.6	B vein	Inter. stage	0.05	0.01	45.8	0.00	0.00	0.02	0.09	0.00	51.1	0.00	0.00	0.00	97.1
4	009A-474.6	B vein	Inter. stage	0.07	0.13	45.9	0.00	0.00	0.07	0.08	0.00	52.6	0.00	0.00	0.00	98.9
5	009A-474.6	B vein	Inter. stage	0.14	0.01	45.7	0.00	0.00	0.02	0.07	0.00	51.9	0.00	0.00	0.00	97.8
6	009A-474.6	B vein	Inter. stage	0.08	0.00	45.8	0.00	0.00	0.02	0.08	0.00	51.9	0.00	0.00	0.00	97.9
7	009A-474.6	B vein	Inter. stage	0.12	0.00	45.9	0.01	0.00	0.02	0.10	0.00	51.9	0.00	0.00	0.00	98.1
8	009A-474.6	B vein	Inter. stage	0.00	0.00	45.8	0.00	0.00	0.03	0.12	0.01	51.5	0.00	0.00	0.00	97.5
9	009A-474.6	B vein	Inter. stage	0.02	0.00	45.5	0.00	0.00	0.02	0.59	0.00	52.2	0.00	0.00	0.00	98.3
10	009A-474.6	B vein	Inter. stage	0.10	0.01	45.8	0.03	0.00	0.02	0.16	0.00	52.1	0.00	0.00	0.00	98.2
11	009A-474.6	B vein	Inter. stage	0.00	0.01	46.2	0.00	0.00	0.02	0.13	0.00	52.1	0.00	0.00	0.00	98.5
12	009A-474.6	B vein	Inter. stage	0.00	0.03	46.1	0.00	0.00	0.01	0.09	0.01	52.3	0.00	0.00	0.00	98.5
13	009A-474.6	B vein	Inter. stage	0.00	0.00	46.0	0.00	0.00	0.01	0.08	0.00	52.1	0.00	0.00	0.00	98.2
14	009A-474.6	B vein	Inter. stage	0.08	0.00	46.0	0.00	0.00	0.02	0.09	0.00	52.9	0.00	0.00	0.00	99.1
15	009A-474.6	B vein	Inter. stage	0.01	0.17	45.2	0.01	0.00	0.15	0.08	0.00	52.1	0.00	0.00	0.00	97.8
16	009A-474.6	B vein	Inter. stage	0.09	0.08	46.1	0.00	0.00	0.10	0.09	0.01	52.5	0.00	0.00	0.00	99.0
17	009A-474.6	B vein	Inter. stage	0.04	0.73	45.8	0.00	0.00	0.02	0.12	0.00	51.4	0.00	0.00	0.00	98.1
18	009A-474.6	B vein	Inter. stage	0.00	0.00	45.8	0.01	0.00	0.02	0.10	0.00	51.8	0.00	0.00	0.00	97.7
19	009A-474.6	B vein	Inter. stage	0.00	0.03	45.9	0.00	0.00	0.01	0.09	0.78	51.9	0.00	0.00	0.00	98.7

Appendix 3 EPMA result of chalcopyrite chemistry, which is representative every vein/mineralization stage of the HLE prospect.

No.	Vein stage	Sample ID	As (wt.%)	Se (wt.%)	Zn (wt.%)	Pb (wt.%)	Cu (wt.%)	Fe (wt.%)	Au (wt.%)	Co (wt.%)	Ni (wt.%)	S (wt.%)	Ag (wt.%)	Sb (wt.%)	Cd (wt.%)	Bi (wt.%)	Total
1	B vein	009A-520	0.000	0.000	0.000	0.004	34.6	30.3	0.010	0.060	0.000	35.0	0.006	0.000	0.019	0.000	100.1
2	B vein	009A-520	0.024	0.000	0.060	0.051	34.7	30.3	0.016	0.049	0.000	34.2	0.014	0.000	0.000	0.000	99.5
3	B vein	009A-520	0.000	0.020	0.116	0.000	34.6	30.3	0.012	0.047	0.000	34.4	0.006	0.000	0.000	0.000	99.4
4	B vein	009A-520	0.000	0.000	0.061	0.034	34.6	30.5	0.002	0.057	0.000	34.5	0.001	0.000	0.006	0.000	99.8
5	B vein	009A-520	0.000	0.000	0.010	0.000	34.7	30.5	0.007	0.050	0.000	34.2	0.002	0.000	0.020	0.000	99.4
6	B vein	009A-520	0.000	0.000	0.081	0.031	34.7	30.4	0.010	0.043	0.000	34.3	0.001	0.000	0.013	0.002	99.6
7	B vein	009A-520	0.000	0.000	0.027	0.000	34.7	30.5	0.004	0.045	0.000	34.6	0.009	0.000	0.000	0.000	99.8
8	B vein	009A-520	0.037	0.000	0.022	0.039	34.7	30.4	0.018	0.043	0.000	34.5	0.007	0.000	0.035	0.013	99.7
9	B vein	009A-520	0.007	0.000	0.007	0.057	34.6	30.3	0.018	0.047	0.000	34.1	0.003	0.000	0.013	0.000	99.1
10	B vein	009A-520	0.011	0.003	0.000	0.049	34.6	30.2	0.007	0.047	0.000	33.8	0.007	0.000	0.018	0.005	98.8
11	B vein	009A-520	0.029	0.000	0.000	0.037	34.8	30.4	0.007	0.048	0.000	34.0	0.014	0.000	0.006	0.000	99.4
12	B vein	009A-520	0.035	0.000	0.000	0.062	34.5	30.3	0.009	0.053	0.000	33.6	0.009	0.000	0.009	0.005	98.5
13	B vein	009A-520	0.025	0.000	0.000	0.028	34.4	30.2	0.014	0.044	0.000	34.0	0.004	0.000	0.000	0.003	98.7
14	B vein	009A-520	0.000	0.000	0.000	0.013	34.6	30.3	0.022	0.055	0.000	33.9	0.014	0.000	0.010	0.000	98.9
15	B vein	009A-520	0.041	0.000	0.000	0.014	34.5	30.1	0.001	0.055	0.000	34.3	0.009	0.000	0.009	0.000	99.0
16	B vein	009A-520	0.000	0.000	0.015	0.058	34.5	30.2	0.034	0.039	0.000	33.7	0.004	0.000	0.002	0.000	98.6
1	AB vein	009A-518	0.000	0.000	0.000	0.000	33.6	30.1	0.002	0.047	0.000	34.4	0.006	0.000	0.005	0.000	98.1
2	AB vein	009A-518	0.000	0.000	0.066	0.000	33.7	30.6	0.000	0.051	0.000	34.3	0.006	0.002	0.010	0.000	98.6
3	AB vein	009A-518	0.000	0.000	0.052	0.000	33.7	30.4	0.000	0.047	0.000	34.2	0.005	0.000	0.000	0.000	98.3
4	AB vein	009A-518	0.000	0.000	0.105	0.000	33.6	30.2	0.000	0.050	0.000	34.1	0.004	0.000	0.005	0.000	98.1
5	AB vein	009A-518	0.000	0.000	0.000	0.000	33.6	30.4	0.000	0.048	0.000	34.3	0.009	0.000	0.005	0.000	98.3
6	AB vein	009A-518	0.000	0.000	0.122	0.000	33.6	30.3	0.000	0.046	0.000	34.2	0.003	0.013	0.005	0.000	98.3
7	AB vein	009A-518	0.000	0.000	0.005	0.000	33.6	30.3	0.000	0.051	0.000	34.1	0.004	0.000	0.000	0.000	98.0
8	AB vein	009A-518	0.000	0.000	0.000	0.000	33.7	30.3	0.013	0.053	0.000	34.1	0.000	0.000	0.006	0.000	98.2
9	AB vein	009A-518	0.008	0.000	0.033	0.000	33.8	30.3	0.000	0.051	0.000	34.2	0.005	0.000	0.007	0.000	98.4
10	AB vein	009A-518	0.019	0.000	0.000	0.000	33.8	30.3	0.000	0.047	0.000	34.2	0.005	0.000	0.017	0.000	98.3
11	AB vein	009A-518	0.000	0.000	0.000	0.000	33.8	30.2	0.000	0.048	0.000	34.1	0.001	0.000	0.000	0.000	98.2
12	AB vein	009A-518	0.000	0.000	0.035	0.000	33.6	30.2	0.008	0.055	0.000	34.1	0.007	0.004	0.036	0.000	98.1
13	AB vein	009A-518	0.000	0.000	0.000	0.000	33.6	30.3	0.000	0.049	0.000	34.0	0.000	0.003	0.000	0.000	97.9
14	AB vein	009A-518	0.000	0.000	0.118	0.000	33.8	30.5	0.000	0.048	0.000	34.2	0.000	0.000	0.000	0.000	98.6
15	AB vein	009A-518	0.017	0.000	0.034	0.000	33.8	30.4	0.000	0.050	0.000	34.2	0.000	0.000	0.006	0.000	98.5
16	AB vein	009A-518	0.000	0.000	0.000	0.000	33.7	30.4	0.000	0.059	0.000	34.2	0.000	0.000	0.010	0.000	98.4
17	AB vein	009A-518	0.011	0.000	0.000	0.000	33.7	30.2	0.000	0.047	0.000	34.2	0.005	0.000	0.004	0.000	98.2
18	AB vein	009A-518	0.000	0.000	0.000	0.000	33.8	30.5	0.000	0.048	0.000	34.2	0.002	0.000	0.000	0.000	98.6
19	AB vein	009A-518	0.011	0.000	0.000	0.000	33.8	30.6	0.000	0.038	0.000	34.2	0.006	0.000	0.001	0.000	98.6

116

20	AB vein	009A-518	0.016	0.000	0.035	0.000	34.0	30.6	0.000	0.051	0.000	34.2	0.010	0.003	0.005	0.000	98.9
21	AB vein	009A-518	0.000	0.000	0.000	0.006	34.7	30.4	0.000	0.044	0.000	34.4	0.012	0.000	0.008	0.004	99.6
22	AB vein	009A-518	0.000	0.000	0.000	0.024	34.6	30.4	0.000	0.049	0.000	34.4	0.004	0.000	0.002	0.000	99.5
23	AB vein	009A-518	0.030	0.000	0.084	0.034	34.8	30.4	0.000	0.045	0.000	34.2	0.014	0.002	0.000	0.000	99.6
24	AB vein	009A-518	0.013	0.000	0.088	0.055	34.6	30.4	0.000	0.040	0.000	34.2	0.001	0.000	0.009	0.000	99.4
25	AB vein	009A-518	0.004	0.000	0.000	0.016	34.8	30.5	0.000	0.050	0.000	34.2	0.005	0.000	0.003	0.000	99.6
26	AB vein	009A-518	0.020	0.000	0.018	0.048	34.7	30.6	0.000	0.042	0.000	34.2	0.010	0.000	0.004	0.000	99.5
27	AB vein	009A-518	0.000	0.000	0.090	0.000	34.6	30.4	0.000	0.046	0.000	34.2	0.013	0.000	0.008	0.000	99.5
28	AB vein	009A-518	0.000	0.000	0.058	0.000	34.9	30.6	0.000	0.051	0.000	34.1	0.010	0.000	0.009	0.000	99.7
29	AB vein	009A-518	0.000	0.000	0.000	0.000	34.8	30.5	0.000	0.047	0.000	34.2	0.001	0.002	0.010	0.000	99.5
30	AB vein	009A-518	0.031	0.000	0.026	0.013	34.3	30.2	0.000	0.040	0.000	33.8	0.005	0.000	0.012	0.000	98.5
31	AB vein	009A-518	0.000	0.000	0.102	0.053	34.8	30.5	0.000	0.041	0.000	34.3	0.006	0.000	0.000	0.000	99.8
32	AB vein	009A-518	0.028	0.000	0.000	0.035	34.8	30.7	0.000	0.049	0.000	34.1	0.000	0.000	0.001	0.000	99.7
33	AB vein	009A-518	0.017	0.000	0.064	0.002	34.8	30.6	0.000	0.059	0.000	34.2	0.008	0.000	0.000	0.000	99.8
34	AB vein	009A-518	0.009	0.000	0.038	0.046	34.9	30.5	0.000	0.053	0.000	34.2	0.003	0.000	0.000	0.000	99.8
35	AB vein	009A-518	0.000	0.000	0.000	0.008	34.7	30.6	0.000	0.047	0.000	34.3	0.008	0.000	0.002	0.000	99.6
36	AB vein	009A-518	0.000	0.000	0.024	0.010	34.7	30.5	0.000	0.041	0.000	34.2	0.011	0.000	0.001	0.000	99.5
37	AB vein	009A-518	0.024	0.011	0.011	0.036	34.8	30.5	0.000	0.062	0.000	34.1	0.010	0.000	0.003	0.000	99.5
38	AB vein	009A-518	0.034	0.000	0.034	0.034	34.9	30.5	0.000	0.040	0.000	34.1	0.005	0.000	0.009	0.000	99.6
39	AB vein	009A-518	0.022	0.000	0.000	0.044	34.8	30.5	0.000	0.042	0.000	34.1	0.000	0.000	0.011	0.000	99.5
40	AB vein	009A-518	0.002	0.000	0.012	0.000	34.8	30.3	0.000	0.049	0.000	34.1	0.003	0.000	0.004	0.006	99.3
1	C vein	009A-701	0.000	0.000	0.013	0.000	33.8	30.3	0.000	0.047	0.000	34.1	0.006	0.007	0.000	0.000	98.3
2	C vein	009A-701	0.023	0.000	0.010	0.000	33.8	30.5	0.000	0.052	0.000	34.1	0.002	0.000	0.000	0.000	98.5
3	C vein	009A-701	0.000	0.000	0.019	0.000	33.8	30.5	0.000	0.053	0.000	33.9	0.001	0.000	0.006	0.000	98.3
4	C vein	009A-701	0.000	0.000	0.065	0.000	33.8	30.3	0.000	0.048	0.000	34.1	0.004	0.000	0.008	0.000	98.4
5	C vein	009A-701	0.000	0.000	0.066	0.000	33.9	30.2	0.000	0.053	0.000	34.0	0.002	0.000	0.006	0.000	98.3
6	C vein	009A-701	0.004	0.000	0.054	0.000	33.9	30.2	0.000	0.059	0.000	34.0	0.000	0.000	0.009	0.000	98.3
7	C vein	009A-701	0.000	0.000	0.000	0.000	33.8	30.4	0.000	0.043	0.000	34.0	0.000	0.000	0.000	0.000	98.3
8	C vein	009A-701	0.000	0.000	0.016	0.000	33.8	30.6	0.000	0.050	0.000	34.1	0.000	0.000	0.003	0.000	98.6
9	C vein	009A-701	0.000	0.000	0.049	0.000	33.9	30.4	0.000	0.046	0.000	34.1	0.008	0.000	0.010	0.000	98.6
10	C vein	009A-701	0.017	0.000	0.009	0.000	33.8	30.5	0.000	0.051	0.000	33.9	0.002	0.000	0.015	0.000	98.3
11	C vein	009A-701	0.000	0.000	0.026	0.000	33.8	30.5	0.000	0.054	0.000	34.1	0.003	0.000	0.007	0.000	98.4
12	C vein	009A-701	0.000	0.000	0.005	0.000	33.9	30.5	0.000	0.044	0.000	34.0	0.000	0.000	0.016	0.000	98.5
13	C vein	009A-701	0.000	0.000	0.185	0.000	34.0	30.4	0.000	0.039	0.000	34.1	0.001	0.000	0.001	0.000	98.7
14	C vein	009A-701	0.030	0.000	0.044	0.000	33.7	30.4	0.000	0.052	0.000	33.9	0.002	0.000	0.007	0.000	98.1
15	C vein	009A-701	0.000	0.000	0.056	0.000	34.0	30.2	0.000	0.047	0.000	34.2	0.007	0.006	0.006	0.000	98.5
16	C vein	009A-701	0.024	0.000	0.038	0.000	33.9	30.3	0.000	0.046	0.000	34.1	0.005	0.000	0.000	0.000	98.4
17	C vein	009A-701	0.000	0.000	0.035	0.000	34.0	30.5	0.000	0.054	0.000	34.1	0.001	0.000	0.000	0.000	98.7

18	C vein	009A-701	0.000	0.000	0.000	0.000	34.0	30.4	0.000	0.048	0.000	33.9	0.000	0.000	0.012	0.000	98.4
19	C vein	009A-701	0.000	0.000	0.000	0.000	34.0	30.5	0.000	0.039	0.000	34.1	0.000	0.000	0.007	0.000	98.6
20	C vein	009A-701	0.000	0.000	0.065	0.000	33.7	30.8	0.000	0.046	0.000	34.0	0.009	0.000	0.000	0.000	98.6
1	C vein	009A-703	0.034	0.000	0.000	0.047	35.0	30.6	0.000	0.050	0.000	34.4	0.003	0.000	0.003	0.000	100.1
2	C vein	009A-703	0.012	0.000	0.000	0.046	34.9	30.6	0.000	0.053	0.000	34.1	0.004	0.000	0.001	0.000	99.7
3	C vein	009A-703	0.018	0.000	0.000	0.029	34.8	30.7	0.000	0.048	0.000	34.1	0.011	0.000	0.001	0.000	99.7
4	C vein	009A-703	0.008	0.000	0.000	0.045	34.9	30.6	0.000	0.041	0.000	34.2	0.004	0.000	0.004	0.000	99.9
5	C vein	009A-703	0.019	0.000	0.027	0.002	34.9	30.7	0.000	0.046	0.000	34.2	0.005	0.000	0.000	0.000	99.9
6	C vein	009A-703	0.019	0.000	0.000	0.000	34.9	30.8	0.000	0.056	0.000	34.2	0.000	0.000	0.006	0.000	100.0
7	C vein	009A-703	0.033	0.000	0.000	0.000	34.7	30.7	0.000	0.041	0.000	34.1	0.005	0.000	0.004	0.000	99.6
8	C vein	009A-703	0.000	0.000	0.000	0.029	35.0	30.7	0.000	0.058	0.000	34.2	0.004	0.000	0.004	0.000	100.0
9	C vein	009A-703	0.014	0.000	0.014	0.000	34.8	30.6	0.000	0.048	0.000	34.0	0.000	0.000	0.010	0.000	99.5
10	C vein	009A-703	0.001	0.000	0.036	0.014	34.8	30.5	0.000	0.043	0.000	33.9	0.014	0.000	0.004	0.000	99.3
11	C vein	009A-703	0.023	0.000	0.006	0.025	34.9	30.6	0.000	0.055	0.000	34.0	0.008	0.000	0.005	0.009	99.7
12	C vein	009A-703	0.000	0.000	0.000	0.003	34.9	30.8	0.000	0.058	0.000	33.9	0.010	0.000	0.000	0.000	99.6
13	C vein	009A-703	0.038	0.000	0.015	0.000	34.8	30.8	0.000	0.047	0.000	34.0	0.007	0.000	0.013	0.000	99.6
14	C vein	009A-703	0.000	0.000	0.074	0.028	34.8	30.6	0.000	0.050	0.000	33.9	0.010	0.000	0.000	0.010	99.5
15	C vein	009A-703	0.059	0.000	0.022	0.078	34.7	30.5	0.000	0.053	0.000	34.1	0.000	0.000	0.005	0.000	99.5
16	C vein	009A-703	0.000	0.000	0.000	0.000	34.9	30.6	0.000	0.048	0.000	34.0	0.002	0.000	0.000	0.001	99.5
17	C vein	009A-703	0.000	0.002	0.000	0.033	34.7	30.6	0.000	0.040	0.000	34.0	0.016	0.004	0.000	0.000	99.5
18	C vein	009A-703	0.030	0.000	0.000	0.038	34.8	30.6	0.000	0.043	0.000	34.3	0.002	0.000	0.001	0.000	99.8
19	C vein	009A-703	0.017	0.000	0.058	0.000	34.9	30.7	0.000	0.044	0.000	34.3	0.007	0.000	0.000	0.000	100.0
20	C vein	009A-703	0.003	0.008	0.000	0.000	34.9	30.7	0.000	0.048	0.000	34.2	0.003	0.000	0.007	0.000	99.8
1	A vein	009A-701	0.023	0.026	0.000	0.000	33.5	29.6	0.000	0.044	0.000	33.9	0.007	0.000	0.015	0.000	97.0
2	A vein	009A-701	0.039	0.000	0.027	0.000	33.4	29.6	0.000	0.046	0.000	34.0	0.001	0.000	0.004	0.000	97.1
3	A vein	009A-701	0.000	0.000	0.000	0.000	33.5	29.7	0.000	0.045	0.000	33.9	0.005	0.000	0.000	0.001	97.2
4	A vein	009A-701	0.033	0.000	0.030	0.040	33.5	29.6	0.000	0.043	0.000	33.9	0.005	0.000	0.003	0.000	97.1
5	A vein	009A-701	0.017	0.000	0.000	0.000	33.5	29.7	0.000	0.041	0.000	34.0	0.015	0.000	0.011	0.000	97.3
6	A vein	009A-701	0.000	0.000	0.042	0.001	33.5	29.7	0.000	0.051	0.000	33.9	0.012	0.000	0.000	0.000	97.2
7	A vein	009A-701	0.034	0.057	0.010	0.053	33.6	29.7	0.000	0.048	0.000	33.7	0.004	0.000	0.005	0.000	97.2
8	A vein	009A-701	0.000	0.000	0.000	0.025	33.7	29.8	0.000	0.043	0.000	33.6	0.021	0.000	0.000	0.000	97.2
9	A vein	009A-701	0.000	0.009	0.003	0.000	33.7	29.8	0.000	0.043	0.000	33.9	0.008	0.000	0.002	0.000	97.5
10	A vein	009A-701	0.000	0.000	0.000	0.070	33.7	29.6	0.003	0.050	0.000	33.9	0.008	0.000	0.009	0.000	97.3
11	A vein	009A-701	0.022	0.078	0.042	0.069	33.6	29.7	0.000	0.044	0.000	33.4	0.007	0.000	0.000	0.000	97.0
12	A vein	009A-701	0.007	0.000	0.000	0.000	33.8	29.8	0.000	0.051	0.000	33.6	0.001	0.000	0.003	0.013	97.3
13	A vein	009A-701	0.004	0.002	0.000	0.052	33.7	29.8	0.000	0.045	0.000	33.7	0.014	0.000	0.005	0.000	97.3
14	A vein	009A-701	0.000	0.012	0.044	0.078	33.7	29.8	0.000	0.044	0.000	33.8	0.009	0.000	0.012	0.000	97.4
15	A vein	009A-701	0.000	0.000	0.006	0.041	33.6	29.8	0.000	0.053	0.000	33.8	0.009	0.000	0.002	0.000	97.3

Appendix 4 EPMA result of bornite chemistry, which is representative every vein/mineralization stage of the HLE prospect.

No.	Vein stage	Sample ID	As (wt.%)	Se (wt.%)	Zn (wt.%)	Pb (wt.%)	Cu (wt.%)	Fe (wt.%)	Au (wt.%)	Co (wt.%)	Ni (wt.%)	S (wt.%)	Ag (wt.%)	Sb (wt.%)	Cd (wt.%)	Bi (wt.%)	Total
1	Disseminated	009A-416	0.000	0.000	0.099	0.000	61.9	11.1	0.000	0.020	0.000	24.8	0.016	0.000	0.000	0.000	97.9
2	Disseminated	009A-416	0.030	0.000	0.000	0.013	62.0	11.1	0.000	0.003	0.000	24.6	0.018	0.000	0.000	0.000	97.9
3	Disseminated	009A-416	0.000	0.000	0.161	0.040	62.1	11.2	0.011	0.022	0.000	24.8	0.022	0.000	0.006	0.012	98.5
4	Disseminated	009A-416	0.000	0.001	0.000	0.000	62.1	11.2	0.004	0.006	0.000	24.7	0.024	0.000	0.006	0.000	98.1
5	Disseminated	009A-416	0.013	0.000	0.033	0.058	61.8	11.1	0.004	0.021	0.000	25.0	0.019	0.000	0.003	0.000	98.1
6	Disseminated	009A-416	0.000	0.000	0.000	0.002	61.9	11.1	0.004	0.027	0.000	24.8	0.016	0.000	0.000	0.004	98.0
7	Disseminated	009A-416	0.001	0.000	0.033	0.023	61.8	11.2	0.004	0.019	0.000	24.7	0.011	0.000	0.008	0.000	97.9
8	Disseminated	009A-416	0.038	0.000	0.044	0.038	61.8	11.2	0.004	0.011	0.000	24.5	0.018	0.000	0.013	0.000	97.6
9	Disseminated	009A-416	0.003	0.047	0.135	0.022	62.0	11.3	0.004	0.009	0.000	24.7	0.015	0.000	0.000	0.000	98.1
10	Disseminated	009A-416	0.000	0.000	0.063	0.046	61.8	11.2	0.004	0.028	0.000	24.5	0.020	0.000	0.007	0.000	97.7
11	Disseminated	009A-416	0.000	0.000	0.023	0.029	62.0	11.2	0.004	0.019	0.000	24.9	0.023	0.000	0.002	0.000	98.2
12	Disseminated	009A-416	0.000	0.000	0.000	0.036	61.7	11.2	0.018	0.011	0.000	24.8	0.018	0.000	0.000	0.000	97.8
13	Disseminated	009A-416	0.000	0.000	0.000	0.004	61.5	11.1	0.003	0.015	0.000	24.6	0.024	0.000	0.002	0.000	97.2
14	Disseminated	009A-416	0.036	0.006	0.143	0.000	62.1	10.9	0.003	0.014	0.000	24.8	0.023	0.000	0.002	0.005	98.0
15	Disseminated	009A-416	0.033	0.000	0.000	0.044	62.7	11.3	0.003	0.030	0.000	24.5	0.018	0.000	0.002	0.000	98.7
16	Disseminated	009A-416	0.000	0.019	0.000	0.021	63.1	11.5	0.003	0.017	0.000	24.7	0.014	0.000	0.008	0.000	99.3
17	Disseminated	009A-416	0.000	0.000	0.000	0.000	63.1	11.5	0.003	0.015	0.000	24.7	0.017	0.000	0.000	0.000	99.3
18	Disseminated	009A-416	0.000	0.000	0.092	0.022	63.2	11.4	0.003	0.021	0.000	24.8	0.016	0.000	0.003	0.000	99.5
19	Disseminated	009A-416	0.000	0.000	0.082	0.000	62.9	11.4	0.003	0.016	0.000	24.8	0.017	0.000	0.000	0.000	99.1
20	Disseminated	009A-416	0.000	0.000	0.000	0.000	62.4	11.1	0.003	0.017	0.000	24.7	0.023	0.000	0.000	0.000	98.2
21	Disseminated	009A-416	0.000	0.000	0.000	0.030	61.9	11.1	0.003	0.010	0.000	24.7	0.026	0.002	0.000	0.000	97.9
22	Disseminated	009A-416	0.000	0.041	0.099	0.000	61.8	11.2	0.003	0.017	0.000	24.8	0.037	0.000	0.001	0.000	98.0
23	Disseminated	009A-416	0.000	0.003	0.079	0.037	62.0	11.1	0.003	0.016	0.000	24.7	0.030	0.000	0.000	0.000	97.9
24	Disseminated	009A-416	0.000	0.000	0.000	0.026	62.2	11.2	0.003	0.010	0.000	24.5	0.028	0.000	0.001	0.000	98.0
25	Disseminated	009A-416	0.000	0.020	0.083	0.000	62.2	11.1	0.003	0.010	0.000	24.5	0.025	0.000	0.000	0.000	98.0
26	Disseminated	009A-416	0.000	0.025	0.005	0.012	62.0	11.0	0.003	0.012	0.000	24.4	0.025	0.000	0.000	0.017	97.6
27	Disseminated	009A-416	0.000	0.052	0.000	0.000	62.0	11.1	0.003	0.023	0.000	24.4	0.026	0.000	0.000	0.000	97.7
28	Disseminated	009A-416	0.000	0.003	0.143	0.017	61.8	11.0	0.003	0.016	0.000	24.5	0.026	0.000	0.000	0.000	97.5
29	Disseminated	009A-416	0.000	0.000	0.165	0.000	61.9	11.1	0.003	0.023	0.000	24.6	0.032	0.000	0.000	0.000	97.8
30	Disseminated	009A-416	0.000	0.000	0.000	0.000	62.1	11.2	0.003	0.018	0.000	24.6	0.023	0.000	0.000	0.000	98.0
31	Disseminated	009A-416	0.000	0.000	0.045	0.000	62.1	11.1	0.003	0.018	0.000	24.7	0.031	0.000	0.010	0.000	98.0
32	Disseminated	009A-416	0.000	0.000	0.000	0.072	62.1	11.2	0.003	0.020	0.000	24.7	0.027	0.000	0.000	0.014	98.1
33	Disseminated	009A-416	0.041	0.000	0.031	0.000	61.6	11.0	0.003	0.018	0.000	24.8	0.035	0.000	0.000	0.000	97.5
34	Disseminated	009A-416	0.000	0.000	0.044	0.148	58.2	12.3	0.003	0.011	0.000	27.6	0.023	0.000	0.003	0.000	98.3
35	Disseminated	009A-416	0.000	0.011	0.128	0.040	58.2	12.5	0.003	0.019	0.000	27.7	0.027	0.000	0.000	0.003	98.6

119

36	Disseminated	009A-416	0.034	0.031	0.042	0.000	57.4	12.7	0.003	0.020	0.000	28.0	0.044	0.000	0.011	0.000	98.2
37	Disseminated	009A-416	0.000	0.038	0.000	0.018	57.7	12.5	0.003	0.028	0.000	27.6	0.027	0.000	0.013	0.016	97.9
38	Disseminated	009A-416	0.000	0.000	0.000	0.042	57.4	12.3	0.003	0.014	0.000	28.0	0.023	0.000	0.009	0.000	97.8
39	Disseminated	009A-416	0.000	0.000	0.034	0.051	60.6	13.2	0.003	0.017	0.000	25.3	0.027	0.000	0.004	0.000	99.3
40	Disseminated	009A-416	0.000	0.000	0.000	0.032	61.0	12.8	0.003	0.015	0.000	25.4	0.033	0.000	0.000	0.000	99.3
41	Disseminated	009A-416	0.003	0.000	0.040	0.058	61.1	12.2	0.003	0.013	0.000	25.1	0.027	0.000	0.006	0.000	98.4
42	Disseminated	009A-416	0.028	0.000	0.000	0.028	61.8	11.9	0.003	0.020	0.000	24.8	0.023	0.000	0.009	0.000	98.6
43	Disseminated	009A-416	0.000	0.013	0.000	0.000	61.7	11.9	0.003	0.020	0.000	25.0	0.021	0.000	0.006	0.000	98.7
44	Disseminated	009A-416	0.000	0.015	0.051	0.014	61.6	11.9	0.003	0.018	0.000	24.9	0.025	0.000	0.000	0.000	98.5
45	Disseminated	009A-416	0.000	0.000	0.038	0.078	61.5	12.0	0.003	0.015	0.000	25.1	0.024	0.000	0.000	0.000	98.7
46	Disseminated	009A-416	0.036	0.000	0.048	0.000	60.9	12.4	0.003	0.018	0.000	25.5	0.039	0.000	0.000	0.017	98.9
47	Disseminated	009A-416	0.000	0.001	0.014	0.058	61.4	11.8	0.003	0.022	0.000	25.4	0.034	0.000	0.010	0.000	98.7
48	Disseminated	009A-416	0.000	0.000	0.000	0.055	61.7	11.6	0.003	0.020	0.000	25.3	0.035	0.000	0.000	0.000	98.7
49	Disseminated	009A-416	0.000	0.000	0.134	0.000	62.0	11.5	0.003	0.008	0.000	25.0	0.031	0.000	0.000	0.000	98.7
50	Disseminated	009A-416	0.001	0.000	0.147	0.329	61.9	11.4	0.003	0.025	0.000	25.1	0.025	0.000	0.000	0.000	98.9
51	Disseminated	009A-416	0.019	0.000	0.000	0.025	61.8	11.4	0.003	0.020	0.000	25.0	0.027	0.000	0.008	0.000	98.2
52	Disseminated	009A-416	0.000	0.000	0.103	0.000	62.0	11.4	0.003	0.031	0.000	25.0	0.023	0.004	0.000	0.000	98.6
53	Disseminated	009A-416	0.058	0.011	0.079	0.032	61.6	11.6	0.003	0.010	0.000	25.0	0.027	0.000	0.000	0.000	98.3
54	Disseminated	009A-416	0.000	0.000	0.000	0.049	61.5	11.6	0.003	0.012	0.000	24.9	0.031	0.000	0.001	0.000	98.1
55	Disseminated	009A-416	0.000	0.000	0.000	0.000	61.3	11.7	0.003	0.022	0.000	25.0	0.024	0.000	0.000	0.000	98.0
56	Disseminated	009A-416	0.035	0.031	0.011	0.040	61.9	11.4	0.003	0.013	0.000	24.5	0.046	0.000	0.000	0.007	98.1
57	Disseminated	009A-416	0.000	0.071	0.000	0.000	62.1	11.3	0.003	0.020	0.000	24.8	0.054	0.000	0.000	0.000	98.3
58	Disseminated	009A-416	0.000	0.017	0.153	0.058	62.0	11.4	0.003	0.017	0.000	24.6	0.046	0.000	0.000	0.000	98.2
59	Disseminated	009A-416	0.008	0.010	0.000	0.014	62.0	11.3	0.003	0.010	0.000	24.6	0.054	0.000	0.000	0.017	98.0
60	Disseminated	009A-416	0.000	0.042	0.050	0.007	62.1	11.4	0.003	0.017	0.000	24.7	0.042	0.001	0.000	0.024	98.3
61	Disseminated	009A-416	0.000	0.000	0.000	0.012	62.2	11.4	0.003	0.021	0.000	24.8	0.039	0.000	0.000	0.004	98.4
62	Disseminated	009A-416	0.007	0.007	0.027	0.120	61.8	11.4	0.003	0.007	0.000	24.8	0.083	0.000	0.000	0.000	98.3
63	Disseminated	009A-416	0.000	0.000	0.000	0.024	61.9	11.3	0.003	0.014	0.000	24.9	0.049	0.000	0.000	0.012	98.2
64	Disseminated	009A-416	0.022	0.040	0.136	0.000	62.0	11.4	0.003	0.013	0.000	24.7	0.038	0.000	0.000	0.018	98.4
65	Disseminated	009A-416	0.000	0.016	0.030	0.042	62.0	11.3	0.003	0.014	0.000	24.8	0.048	0.000	0.000	0.000	98.3
66	Disseminated	009A-416	0.000	0.013	0.066	0.065	61.8	11.4	0.003	0.011	0.000	24.9	0.035	0.000	0.000	0.000	98.3
67	Disseminated	009A-416	0.000	0.000	0.000	0.120	62.0	11.3	0.003	0.014	0.000	24.8	0.045	0.000	0.001	0.000	98.3
68	Disseminated	009A-416	0.000	0.048	0.098	0.142	61.6	11.4	0.003	0.010	0.000	25.1	0.050	0.000	0.005	0.000	98.5
69	Disseminated	009A-416	0.000	0.000	0.000	0.092	62.0	11.4	0.003	0.010	0.000	24.8	0.050	0.000	0.000	0.015	98.4
70	Disseminated	009A-416	0.000	0.000	0.157	0.505	61.4	11.4	0.003	0.013	0.000	24.9	0.042	0.000	0.000	0.000	98.5
71	Disseminated	009A-416	0.034	0.021	0.061	0.026	61.8	11.5	0.013	0.012	0.000	25.0	0.036	0.000	0.014	0.005	98.5
72	Disseminated	009A-416	0.000	0.031	0.086	0.000	62.2	11.3	0.003	0.017	0.000	24.7	0.041	0.000	0.001	0.003	98.4
73	Disseminated	009A-416	0.015	0.002	0.102	0.066	62.3	11.4	0.003	0.017	0.000	24.9	0.048	0.000	0.000	0.000	98.8

74	Disseminated	009A-416	0.000	0.045	0.023	0.041	62.2	11.3	0.003	0.023	0.000	24.9	0.043	0.000	0.000	0.028	98.6
75	Disseminated	009A-416	0.000	0.029	0.047	0.000	62.2	11.5	0.003	0.027	0.000	25.0	0.041	0.000	0.000	0.000	98.8
76	Disseminated	009A-416	0.000	0.000	0.019	0.033	62.3	11.3	0.003	0.022	0.000	24.9	0.040	0.000	0.002	0.000	98.6
77	Disseminated	009A-416	0.051	0.000	0.000	0.000	62.2	11.4	0.003	0.012	0.000	25.0	0.048	0.000	0.000	0.001	98.7
78	Disseminated	009A-416	0.000	0.063	0.023	0.045	62.2	11.4	0.003	0.010	0.000	24.9	0.038	0.000	0.000	0.000	98.7
79	Disseminated	009A-416	0.000	0.029	0.116	0.011	61.9	11.5	0.005	0.018	0.000	24.7	0.047	0.000	0.005	0.000	98.3
80	Disseminated	009A-416	0.000	0.000	0.115	0.132	62.1	11.5	0.004	0.017	0.000	24.8	0.045	0.000	0.000	0.000	98.7
81	Disseminated	009A-416	0.000	0.027	0.025	0.049	62.0	11.4	0.001	0.019	0.000	24.8	0.041	0.000	0.000	0.000	98.4
82	Disseminated	009A-416	0.038	0.000	0.125	0.019	62.0	11.5	0.001	0.024	0.000	24.7	0.048	0.000	0.000	0.000	98.4
83	Disseminated	009A-416	0.000	0.000	0.045	0.000	62.2	11.4	0.001	0.015	0.000	25.0	0.048	0.000	0.005	0.000	98.7
84	Disseminated	009A-416	0.028	0.031	0.029	0.029	62.0	11.3	0.001	0.022	0.000	24.7	0.055	0.000	0.006	0.000	98.3
85	Disseminated	009A-416	0.000	0.030	0.000	0.232	62.1	11.4	0.001	0.020	0.000	24.8	0.042	0.000	0.000	0.000	98.5
86	Disseminated	009A-416	0.000	0.000	0.065	0.016	62.1	11.4	0.001	0.006	0.000	25.1	0.041	0.000	0.000	0.000	98.8
87	Disseminated	009A-416	0.000	0.015	0.000	0.011	62.1	11.5	0.001	0.016	0.000	25.0	0.046	0.000	0.000	0.000	98.6
88	Disseminated	009A-416	0.000	0.025	0.018	0.108	62.1	11.3	0.001	0.026	0.000	24.9	0.042	0.000	0.002	0.000	98.6

Appendix 5 EPMA result of chlorite chemistry, which is representative every alteration zone of the HLE prospect.

No	Sample ID	Alteration zone	SiO$_2$	TiO$_2$	Al$_2$O$_3$	FeO	MnO	MgO	CaO	Na$_2$O	K$_2$O	CuO	CoO	ZnO
1	VHD 009A-324.6	Sericite	28.5	0.04	17.0	21.8	1.56	18.34	0.26	0.03	0.03	0.02	0.03	0.25
2	VHD 009A-324.6	Sericite	28.3	0.04	17.2	22.2	1.45	17.88	0.18	0.04	0.05	0.01	0.04	0.23
3	VHD 009A-324.6	Sericite	28.2	0.04	17.7	22.7	1.40	17.36	0.28	0.01	0.02	0.01	0.02	0.24
4	VHD 009A-324.6	Sericite	28.0	0.03	17.8	23.0	1.46	17.01	0.31	0.01	0.02	0.01	0.03	0.22
5	VHD 009A-324.6	Sericite	27.8	0.04	17.5	23.3	1.22	17.47	0.22	0.01	0.02	0.02	0.06	0.21
6	VHD 009A-324.6	Sericite	28.4	0.06	17.1	22.0	1.46	18.40	0.20	0.01	0.01	0.01	0.04	0.25
7	VHD 009A-324.6	Sericite	27.8	0.05	17.1	22.5	1.32	17.42	0.22	0.02	0.03	0.01	0.04	0.22
8	VHD 009A-324.6	Sericite	27.8	0.03	17.1	23.1	1.51	16.73	0.28	0.02	0.01	0.00	0.03	0.22
9	VHD 009A-324.6	Sericite	28.0	0.00	17.1	22.9	1.76	17.06	0.26	0.02	0.02	0.03	0.03	0.24
10	VHD 009A-324.6	Sericite	27.4	0.10	16.2	22.7	1.35	17.28	0.20	0.01	0.01	0.01	0.05	0.26
11	VHD 009A-324.6	Sericite	28.3	0.06	17.7	23.9	1.50	16.84	0.29	0.03	0.01	0.00	0.04	0.23
12	VHD 009A-324.6	Sericite	28.2	0.10	17.2	23.0	1.62	17.10	0.29	0.03	0.02	0.00	0.02	0.27
13	VHD 009A-324.6	Sericite	27.8	0.04	16.7	23.3	1.31	16.96	0.32	0.04	0.01	0.01	0.03	0.24
14	VHD 009A-324.6	Sericite	28.2	0.04	18.3	23.1	1.25	16.77	0.27	0.03	0.06	0.00	0.04	0.20
15	VHD 009A-324.6	Sericite	28.2	0.04	17.7	23.2	1.30	17.12	0.27	0.04	0.04	0.02	0.05	0.22
16	VHD 009A-324.6	Sericite	28.9	0.05	17.3	21.3	1.48	18.89	0.21	0.02	0.02	0.02	0.03	0.27
17	VHD 009A-324.6	Sericite	29.1	0.08	16.4	21.1	1.34	19.72	0.19	0.03	0.01	0.01	0.04	0.20
18	VHD 009A-342.6	Sericite	27.5	0.02	16.8	21.8	2.03	17.69	0.20	0.02	0.03	0.16	0.06	0.30
19	VHD 009A-342.6	Sericite	27.6	0.02	17.1	21.7	2.47	17.41	0.23	0.03	0.04	0.14	0.04	0.30
20	VHD 009A-342.6	Sericite	27.7	0.01	16.6	21.8	1.32	18.06	0.28	0.02	0.02	0.11	0.04	0.33
21	VHD 009A-342.6	Sericite	27.3	0.02	17.0	21.9	2.57	17.27	0.25	0.02	0.03	0.15	0.03	0.30
22	VHD 009A-342.6	Sericite	27.3	0.03	17.3	22.4	1.89	17.10	0.23	0.02	0.03	0.09	0.05	0.29
23	VHD 009A-342.6	Sericite	28.3	0.00	17.3	22.2	1.05	18.12	0.22	0.03	0.03	0.05	0.04	0.32
24	VHD 009A-342.6	Sericite	28.1	0.01	17.0	22.2	1.09	17.86	0.25	0.04	0.02	0.05	0.03	0.30
25	VHD 009A-342.6	Sericite	27.2	0.02	17.0	23.2	2.22	16.62	0.18	0.02	0.04	0.05	0.02	0.26
26	VHD 009A-342.6	Sericite	26.8	0.00	16.7	22.8	2.54	16.26	0.21	0.05	0.03	0.07	0.05	0.28
27	VHD 009A-342.6	Sericite	27.1	0.02	17.1	21.6	2.17	17.32	0.16	0.07	0.05	0.39	0.04	0.35
28	VHD 009A-342.6	Sericite	27.3	0.01	17.4	22.6	2.16	16.96	0.22	0.04	0.03	0.32	0.06	0.35
29	VHD 009A-342.6	Sericite	27.5	0.04	16.9	22.4	2.47	17.02	0.19	0.02	0.03	0.07	0.05	0.39

30	VHD 009A-342.6	Sericite	27.2	0.02	17.2	22.9	2.20	16.88	0.18	0.03	0.02	0.15	0.04	0.38
31	VHD 009A-342.6	Sericite	26.8	0.02	16.4	22.0	2.07	16.87	0.19	0.02	0.03	0.16	0.06	0.28
32	VHD 009A-342.6	Sericite	27.3	0.03	16.8	22.0	2.54	16.70	0.23	0.04	0.02	0.22	0.06	0.33
33	VHD 009A-342.6	Sericite	27.2	0.03	16.8	21.9	2.28	16.83	0.21	0.03	0.05	0.14	0.05	0.30
34	VHD 009A-342.6	Sericite	27.4	0.02	17.1	21.5	2.24	17.37	0.24	0.05	0.03	0.18	0.04	0.31
35	VHD 009A-342.6	Sericite	27.5	0.04	16.9	22.2	2.11	17.35	0.22	0.05	0.03	0.19	0.04	0.33
36	VHD 009A-342.6	Sericite	26.7	0.01	17.2	24.2	1.55	15.74	0.20	0.04	0.02	0.13	0.05	0.42
37	VHD 009A-342.6	Sericite	27.3	0.01	16.9	21.3	2.27	17.36	0.18	0.04	0.03	0.07	0.05	0.51
38	VHD 009A-342.6	Sericite	27.6	0.02	16.9	21.7	1.54	17.62	0.21	0.02	0.04	0.09	0.04	0.50
39	VHD 009A-342.6	Sericite	27.8	0.03	16.9	21.1	1.73	17.81	0.20	0.04	0.05	0.08	0.05	0.49
40	VHD 009A-342.6	Sericite	27.4	0.01	16.6	21.3	1.45	17.66	0.19	0.04	0.05	0.09	0.05	0.51
1	VHD 009A-354.8	Chlorite-Sericite	25.2	0.03	14.5	16.2	2.26	16.22	0.19	0.05	0.02	0.01	0.04	0.34
2	VHD 009A-354.8	Chlorite-Sericite	25.0	0.01	15.3	15.9	2.00	17.44	0.14	0.05	0.02	0.01	0.02	0.28
3	VHD 009A-354.8	Chlorite-Sericite	25.6	0.00	15.5	15.5	1.83	17.44	0.10	0.07	0.02	0.01	0.04	0.35
4	VHD 009A-354.8	Chlorite-Sericite	25.9	0.01	15.6	14.6	1.13	18.38	0.21	0.06	0.02	0.00	0.04	0.34
5	VHD 009A-354.8	Chlorite-Sericite	25.6	0.03	14.6	15.7	2.18	16.83	0.25	0.06	0.02	0.01	0.04	0.32
6	VHD 009A-354.8	Chlorite-Sericite	26.4	0.00	14.9	15.6	2.00	17.36	0.26	0.05	0.03	0.00	0.04	0.36
7	VHD 009A-354.8	Chlorite-Sericite	26.7	0.00	15.0	15.9	1.81	17.56	0.22	0.04	0.02	0.00	0.02	0.32
8	VHD 009A-354.8	Chlorite-Sericite	26.3	0.00	14.5	16.4	2.13	16.95	0.26	0.06	0.02	0.00	0.01	0.35
9	VHD 009A-354.8	Chlorite-Sericite	25.5	0.00	15.3	16.7	2.05	17.07	0.09	0.05	0.02	0.02	0.02	0.36
10	VHD 009A-354.8	Chlorite-Sericite	25.9	0.01	15.7	16.7	2.27	16.78	0.15	0.05	0.02	0.01	0.04	0.34
11	VHD 009A-354.8	Chlorite-Sericite	26.7	0.00	14.7	15.5	2.09	17.19	0.28	0.07	0.01	0.01	0.02	0.36
12	VHD 009A-354.8	Chlorite-Sericite	26.1	0.02	16.4	16.1	2.07	17.23	0.19	0.06	0.01	0.00	0.01	0.34
13	VHD 009A-354.8	Chlorite-Sericite	28.0	0.01	15.3	12.0	0.34	18.29	0.49	0.04	0.02	0.01	0.04	0.18
14	VHD 009A-354.8	Chlorite-Sericite	26.6	0.00	15.7	15.5	1.42	17.23	0.28	0.07	0.03	0.02	0.03	0.30
15	VHD 009A-354.8	Chlorite-Sericite	29.1	0.00	16.7	15.1	0.80	19.06	0.34	0.05	0.04	0.02	0.04	0.26
16	VHD 009A-354.8	Chlorite-Sericite	27.0	0.01	15.9	14.5	1.31	17.63	0.23	0.07	0.02	0.02	0.04	0.27
17	VHD 009A-354.8	Chlorite-Sericite	27.7	0.03	15.7	15.3	0.86	16.93	0.34	0.04	0.03	0.01	0.04	0.22
18	VHD 009A-356.4	Chlorite-Sericite	28.5	0.01	18.9	21.6	2.28	16.07	0.15	0.03	0.21	0.03	0.04	0.35
19	VHD 009A-356.4	Chlorite-Sericite	28.0	0.00	18.6	22.3	2.50	16.29	0.15	0.02	0.18	0.00	0.05	0.40

20	VHD 009A-356.4	Chlorite-Sericite	28.0	0.04	18.3	22.4	2.73	16.70	0.20	0.03	0.04	0.00	0.04	0.39
21	VHD 009A-356.4	Chlorite-Sericite	27.9	0.00	18.1	22.0	2.65	16.70	0.23	0.02	0.05	0.02	0.05	0.39
22	VHD 009A-356.4	Chlorite-Sericite	29.7	0.03	19.3	19.9	2.16	15.00	0.17	0.03	0.74	0.03	0.03	0.32
23	VHD 009A-356.4	Chlorite-Sericite	28.6	0.04	18.8	22.0	2.46	16.39	0.22	0.03	0.22	0.00	0.05	0.33
24	VHD 009A-356.4	Chlorite-Sericite	27.3	0.01	18.0	22.3	2.71	15.82	0.18	0.01	0.08	0.00	0.04	0.35
25	VHD 009A-356.4	Chlorite-Sericite	28.6	0.04	19.0	22.0	2.14	16.44	0.15	0.04	0.20	0.02	0.06	0.35
26	VHD 009A-356.4	Chlorite-Sericite	27.6	0.01	18.0	22.4	2.88	16.41	0.19	0.05	0.05	0.02	0.04	0.42
27	VHD 009A-356.4	Chlorite-Sericite	27.8	0.00	18.1	22.5	2.75	15.94	0.16	0.04	0.09	0.00	0.05	0.45
28	VHD 009A-356.4	Chlorite-Sericite	27.6	0.06	18.1	22.2	2.75	16.47	0.20	0.04	0.05	0.02	0.06	0.43
29	VHD 009A-356.4	Chlorite-Sericite	29.4	0.05	19.9	21.0	2.09	15.61	0.27	0.02	0.42	0.07	0.05	0.28
30	VHD 009A-467.2	Chlorite-Sericite	26.5	0.03	19.3	27.7	0.89	13.18	0.15	0.00	0.15	0.06	0.04	0.16
31	VHD 009A-467.2	Chlorite-Sericite	26.0	0.05	18.4	27.5	0.73	13.77	0.11	0.02	0.05	0.05	0.06	0.16
32	VHD 009A-467.2	Chlorite-Sericite	29.8	0.10	19.1	21.0	0.98	15.21	0.13	0.02	0.67	0.04	0.04	0.20
33	VHD 009A-467.2	Chlorite-Sericite	29.9	0.01	19.7	23.1	0.83	13.45	0.11	0.02	0.74	0.05	0.03	0.11
34	VHD 009A-467.2	Chlorite-Sericite	30.0	0.02	19.4	21.4	1.33	14.29	0.11	0.05	0.79	0.04	0.06	0.13
35	VHD 009A-467.2	Chlorite-Sericite	26.8	0.06	17.8	26.4	1.01	14.99	0.09	0.01	0.04	0.04	0.06	0.10
36	VHD 009A-467.2	Chlorite-Sericite	28.8	0.15	18.9	22.8	1.53	14.68	0.10	0.03	0.30	0.03	0.03	0.22
37	VHD 009A-467.2	Chlorite-Sericite	32.0	0.33	19.5	19.4	1.03	14.14	0.14	0.04	0.62	0.04	0.03	0.21
38	VHD 009A-467.2	Chlorite-Sericite	29.1	0.14	18.9	22.1	1.13	14.92	0.10	0.03	0.34	0.02	0.04	0.13
39	VHD 009A-467.2	Chlorite-Sericite	28.2	0.07	18.1	22.9	1.14	15.63	0.10	0.00	0.32	0.04	0.03	0.13
40	VHD 009A-474.2	Chlorite-Sericite	26.9	0.01	18.6	21.3	1.10	15.84	0.26	0.03	0.03	0.00	0.06	0.22
41	VHD 009A-474.2	Chlorite-Sericite	27.8	0.03	19.1	18.5	0.98	14.48	0.20	0.04	0.37	0.00	0.02	0.18
42	VHD 009A-474.2	Chlorite-Sericite	27.7	0.03	19.1	21.0	1.05	16.45	0.23	0.01	0.03	0.00	0.02	0.16
43	VHD 009A-474.2	Chlorite-Sericite	27.6	0.02	19.1	21.1	1.06	15.53	0.25	0.01	0.02	0.01	0.05	0.16
44	VHD 009A-474.2	Chlorite-Sericite	28.1	0.03	19.2	20.6	1.02	15.51	0.27	0.02	0.06	0.00	0.03	0.21
45	VHD 009A-474.2	Chlorite-Sericite	25.9	0.03	18.0	19.7	1.05	14.34	0.26	0.01	0.04	0.01	0.04	0.23
46	VHD 009A-474.2	Chlorite-Sericite	26.8	0.01	18.6	21.4	1.06	15.51	0.23	0.03	0.02	0.05	0.01	0.20
47	VHD 009A-474.2	Chlorite-Sericite	27.0	0.01	18.6	19.8	0.96	16.97	0.15	0.02	0.12	0.01	0.04	0.18
48	VHD 009A-474.2	Chlorite-Sericite	30.1	0.02	20.6	17.8	0.87	15.83	0.22	0.43	0.59	0.00	0.02	0.22
49	VHD 009A-474.2	Chlorite-Sericite	26.5	0.03	18.4	19.9	1.00	16.41	0.20	0.02	0.03	0.02	0.04	0.16

50	VHD 009A-474.2	Chlorite-Sericite	28.0	0.02	19.6	19.3	1.01	17.95	0.14	0.00	0.06	0.00	0.03	0.16
1	VHD 009A-669.6	Potassic	28.5	0.03	17.1	20.1	0.77	19.78	0.21	0.01	0.02	0.00	0.04	0.08
2	VHD 009A-669.6	Potassic	27.8	0.04	17.7	21.6	0.82	17.75	0.24	0.01	0.02	0.03	0.05	0.10
3	VHD 009A-669.6	Potassic	28.2	0.03	17.6	19.1	0.61	20.01	0.19	0.00	0.01	0.02	0.02	0.12
4	VHD 009A-669.6	Potassic	27.9	0.05	18.4	20.4	0.69	18.98	0.22	0.03	0.01	0.02	0.02	0.10
5	VHD 009A-669.6	Potassic	27.6	0.02	18.3	21.6	0.78	18.17	0.22	0.01	0.03	0.13	0.03	0.09
6	VHD 009A-669.6	Potassic	28.0	0.08	17.7	20.7	0.71	19.22	0.21	0.02	0.02	0.08	0.03	0.05
7	VHD 009A-669.6	Potassic	27.6	0.07	18.4	21.7	0.81	18.18	0.22	0.02	0.03	0.13	0.04	0.09
8	VHD 009A-669.6	Potassic	28.5	0.08	17.7	20.4	0.74	18.71	0.29	0.02	0.05	0.07	0.03	0.11
9	VHD 009A-669.6	Potassic	27.7	0.02	18.8	21.8	0.81	17.93	0.25	0.02	0.04	0.11	0.04	0.08
10	VHD 009A-669.6	Potassic	27.8	0.05	18.3	19.8	0.69	18.74	0.22	0.01	0.06	0.13	0.01	0.10
11	VHD 009A-669.6	Potassic	28.2	0.02	19.0	20.1	0.69	18.86	0.25	0.01	0.04	0.07	0.03	0.09
12	VHD 009A-669.6	Potassic	27.4	0.00	19.0	20.3	0.67	18.42	0.22	0.01	0.05	0.04	0.03	0.13
13	VHD 009A-669.6	Potassic	27.8	0.05	18.7	20.1	0.67	18.54	0.26	0.01	0.04	0.06	0.03	0.13
14	VHD 009A-669.6	Potassic	28.7	0.11	17.4	19.8	0.68	19.71	0.22	0.02	0.02	0.10	0.04	0.10
15	VHD 009A-669.6	Potassic	28.6	0.03	18.1	20.5	0.73	19.20	0.22	0.03	0.02	0.05	0.02	0.09
16	VHD 009A-669.6	Potassic	28.7	0.10	17.7	18.8	0.58	21.00	0.16	0.00	0.04	0.03	0.04	0.07
17	VHD 009A-669.6	Potassic	27.7	0.01	18.3	19.7	0.64	18.39	0.25	0.02	0.07	0.03	0.04	0.15
18	VHD 009A-669.6	Potassic	26.9	0.03	17.5	19.6	0.69	18.11	0.22	0.04	0.06	0.02	0.04	0.15
19	VHD 009A-669.6	Potassic	27.8	0.05	17.3	20.3	0.75	19.12	0.16	0.03	0.03	0.02	0.04	0.05
20	VHD 009A-669.6	Potassic	27.8	0.04	17.9	19.5	0.65	19.03	0.23	0.07	0.09	0.02	0.03	0.11
21	VHD 009A-703.8	Potassic	28.8	0.01	17.0	19.5	0.63	20.97	0.27	0.01	0.03	0.02	0.05	0.08
22	VHD 009A-703.8	Potassic	29.0	0.00	17.1	19.9	0.61	20.90	0.30	0.07	0.09	0.05	0.05	0.09
23	VHD 009A-703.8	Potassic	28.3	0.04	16.8	18.7	0.58	20.71	0.29	0.03	0.03	0.07	0.02	0.12
24	VHD 009A-703.8	Potassic	28.7	0.00	17.8	19.5	0.64	21.51	0.20	0.01	0.03	0.03	0.04	0.09
25	VHD 009A-703.8	Potassic	27.5	0.01	16.7	19.6	0.66	19.67	0.30	0.12	0.10	0.07	0.02	0.07
26	VHD 009A-703.8	Potassic	28.5	0.01	17.2	18.7	0.64	21.34	0.23	0.01	0.01	0.05	0.05	0.14
27	VHD 009A-703.8	Potassic	27.8	0.03	17.6	19.5	0.67	21.00	0.10	0.01	0.03	0.21	0.03	0.08
28	VHD 009A-703.8	Potassic	28.8	0.03	17.2	18.2	0.67	21.33	0.34	0.02	0.03	0.00	0.05	0.14
29	VHD 009A-703.8	Potassic	29.4	0.04	17.1	18.6	0.69	21.35	0.36	0.03	0.05	0.04	0.01	0.18

30	VHD 009A-703.8	Potassic	28.5	0.00	17.1	17.8	0.77	21.57	0.21	0.01	0.02	0.01	0.04	0.15
31	VHD 009A-703.8	Potassic	28.0	0.04	17.0	20.0	0.46	20.99	0.15	0.02	0.02	0.02	0.04	0.06
32	VHD 009A-703.8	Potassic	28.4	0.02	17.2	18.5	0.50	21.79	0.15	0.02	0.01	0.00	0.04	0.15
33	VHD 009A-703.8	Potassic	28.2	0.01	16.4	18.0	0.62	21.48	0.25	0.02	0.04	0.01	0.03	0.16
34	VHD 009A-703.8	Potassic	28.1	0.02	16.8	19.0	0.65	21.02	0.23	0.01	0.04	0.01	0.04	0.10
35	VHD 009A-703.8	Potassic	29.1	0.01	16.9	18.6	0.64	21.98	0.25	0.03	0.04	0.11	0.04	0.22
36	VHD 009A-703.8	Potassic	27.3	0.00	17.0	19.2	0.69	20.49	0.14	0.02	0.02	0.22	0.04	0.08
37	VHD 009A-703.8	Potassic	28.5	0.02	16.9	19.7	0.51	21.11	0.15	0.01	0.02	0.51	0.02	0.07
38	VHD 009A-703.8	Potassic	27.8	0.01	16.6	18.9	0.58	20.59	0.21	0.02	0.02	0.36	0.05	0.05
39	VHD 009A-703.8	Potassic	28.7	0.02	16.3	17.7	0.57	21.87	0.27	0.04	0.03	0.01	0.03	0.17
40	VHD 009A-703.8	Potassic	28.5	0.03	17.1	18.0	0.66	22.07	0.22	0.02	0.02	0.02	0.05	0.17
41	VHD 009A-703.8	Potassic	28.0	0.01	17.0	20.8	0.80	19.53	0.29	0.02	0.02	0.01	0.05	0.12
42	VHD 009A-703.8	Potassic	28.7	0.02	17.0	19.4	0.73	20.21	0.28	0.01	0.03	0.01	0.03	0.11

Appendix 6 EPMA result of quartz chemistry, which is representative every alteration zone of the HLE prospect.

No.	Samples ID	Vein type	Stages	SiO2 (wt.%)	Al2O3 (wt.%)	Na2O (wt.%)	K2O (wt.%)	TiO2 (wt.%)	FeO (wt.%)	MnO (wt.%)	Total (wt.%)	XQtz_Ti
1	009A/704	A vein	Early stage	100.2	0.000	0.000	0.002	0.022	0.007	0.001	100.3	132
2	009A/704	A vein	Early stage	100.3	0.000	0.000	0.000	0.015	0.000	0.001	100.3	90
3	009A/704	A vein	Early stage	100.1	0.000	0.000	0.000	0.024	0.011	0.000	100.2	144
4	009A/704	A vein	Early stage	99.9	0.000	0.000	0.002	0.027	0.005	0.001	100.0	162
5	009A/704	A vein	Early stage	99.6	0.008	0.000	0.000	0.036	0.010	0.000	99.6	216
6	009A/704	A vein	Early stage	100.4	0.000	0.000	0.000	0.018	0.007	0.001	100.4	108
7	009A/704	A vein	Early stage	99.6	0.000	0.000	0.002	0.024	0.007	0.000	99.6	144
8	009A/704	A vein	Early stage	100.7	0.000	0.000	0.000	0.028	0.011	0.000	100.7	168
9	009A/704	A vein	Early stage	100.3	0.029	0.000	0.010	0.033	0.007	0.000	100.4	198
10	009A/704	A vein	Early stage	97.4	0.015	0.000	0.000	0.036	0.016	0.002	97.5	216
11	009A/704	A vein	Early stage	99.6	0.000	0.000	0.000	0.022	0.005	0.001	99.6	132
12	009A/704	A vein	Early stage	100.4	0.000	0.000	0.000	0.029	0.004	0.000	100.5	174
13	009A/704	A vein	Early stage	99.6	0.005	0.000	0.001	0.026	0.005	0.000	99.6	156
14	009A/704	A vein	Early stage	99.8	0.000	0.000	0.001	0.024	0.007	0.000	99.9	144
15	009A/704	A vein	Early stage	100.0	0.000	0.000	0.000	0.029	0.010	0.000	100.1	174
16	009A/704	A vein	Early stage	100.2	0.021	0.000	0.009	0.017	0.008	0.000	100.3	102
17	009A/704	A vein	Early stage	100.7	0.000	0.000	0.000	0.019	0.006	0.000	100.8	114
18	009A/704	A vein	Early stage	99.6	0.000	0.000	0.002	0.020	0.006	0.001	99.7	120
19	009A/704	A vein	Early stage	99.7	0.010	0.000	0.002	0.024	0.012	0.001	99.8	144
20	009A/704	A vein	Early stage	99.3	0.000	0.000	0.000	0.032	0.006	0.000	99.4	192
21	009A/520	A vein	Early stage	100.4	0.000	0.000	0.006	0.026	0.005	0.000	100.5	156
22	009A/520	A vein	Early stage	99.1	0.041	0.049	0.043	0.030	0.016	0.000	99.3	180
23	009A/520	A vein	Early stage	100.6	0.007	0.001	0.014	0.033	0.004	0.000	100.7	198
24	009A/520	A vein	Early stage	101.9	0.021	0.001	0.024	0.052	0.011	0.000	102.1	312
25	009A/520	A vein	Early stage	101.0	0.000	0.010	0.013	0.022	0.008	0.000	101.0	132
26	009A/520	A vein	Early stage	99.9	0.004	0.003	0.015	0.032	0.005	0.000	100.0	192
27	009A/520	A vein	Early stage	100.5	0.011	0.000	0.009	0.030	0.006	0.000	100.6	180
28	009A/520	A vein	Early stage	100.3	0.001	0.001	0.017	0.028	0.009	0.000	100.4	168
29	009A/520	A vein	Early stage	100.4	0.004	0.000	0.008	0.025	0.014	0.000	100.5	150
30	009A/520	A vein	Early stage	99.9	0.023	0.001	0.017	0.027	0.014	0.000	100.0	162
31	009A/520	A vein	Early stage	100.8	0.004	0.000	0.011	0.030	0.009	0.000	100.8	180
32	009A/520	A vein	Early stage	100.7	0.000	0.000	0.008	0.030	0.002	0.000	100.8	180
33	009A/520	A vein	Early stage	100.5	0.000	0.000	0.008	0.029	0.008	0.000	100.6	174
34	009A/520	A vein	Early stage	99.6	0.029	0.001	0.013	0.027	0.011	0.000	99.7	162
35	009A/520	A vein	Early stage	100.6	0.002	0.000	0.006	0.027	0.005	0.000	100.6	162

36	009A/520	A vein	Early stage	100.6	0.000	0.000	0.006	0.027	0.003	0.000	100.6	162
37	009A/520	A vein	Early stage	100.6	0.000	0.000	0.007	0.028	0.007	0.000	100.6	168
38	009A/520	A vein	Early stage	100.9	0.013	0.001	0.015	0.031	0.019	0.000	100.9	186
39	009A/520	A vein	Early stage	100.2	0.001	0.002	0.010	0.028	0.017	0.002	100.3	168
40	009A/520	A vein	Early stage	100.3	0.015	0.000	0.011	0.030	0.014	0.002	100.3	180
1	009A/518.2	AB vein	Early stage	100.3	0.041	0.000	0.014	0.024	0.013	0.000	100.4	144
2	009A/518.2	AB vein	Early stage	99.4	0.013	0.000	0.003	0.029	0.015	0.000	99.5	174
3	009A/518.2	AB vein	Early stage	101.0	0.015	0.000	0.002	0.014	0.014	0.000	101.1	83.9
4	009A/518.2	AB vein	Early stage	100.2	0.038	0.000	0.018	0.012	0.012	0.000	100.2	71.9
5	009A/518.2	AB vein	Early stage	100.5	0.001	0.000	0.003	0.013	0.002	0.001	100.5	77.9
6	009A/518.2	AB vein	Early stage	100.0	0.000	0.000	0.001	0.019	0.010	0.000	100.1	114
7	009A/518.2	AB vein	Early stage	100.1	0.061	0.000	0.027	0.023	0.007	0.000	100.3	138
8	009A/518.2	AB vein	Early stage	100.4	0.000	0.000	0.000	0.016	0.006	0.000	100.4	95.9
9	009A/518.2	AB vein	Early stage	100.7	0.000	0.000	0.001	0.016	0.007	0.000	100.7	95.9
10	009A/518.2	AB vein	Early stage	100.2	0.000	0.000	0.001	0.015	0.008	0.000	100.2	89.9
11	009A/518.2	AB vein	Early stage	100.1	0.000	0.000	0.001	0.013	0.006	0.007	100.1	77.9
12	009A/518.2	AB vein	Early stage	99.9	0.007	0.000	0.003	0.012	0.008	0.000	99.9	71.9
13	009A/518.2	AB vein	Early stage	100.8	0.000	0.000	0.000	0.014	0.012	0.000	100.8	83.9
14	009A/518.2	AB vein	Early stage	100.7	0.002	0.000	0.001	0.023	0.010	0.000	100.7	138
15	009A/518.2	AB vein	Early stage	100.3	0.005	0.000	0.002	0.022	0.014	0.000	100.4	132
16	009A/518.2	AB vein	Early stage	100.5	0.000	0.000	0.000	0.014	0.006	0.002	100.5	83.9
17	009A/518.2	AB vein	Early stage	100.4	0.000	0.000	0.003	0.012	0.012	0.000	100.5	71.9
18	009A/518.2	AB vein	Early stage	99.5	0.055	0.000	0.017	0.028	0.009	0.000	99.6	168
19	009A/518.2	AB vein	Early stage	99.6	0.018	0.000	0.008	0.008	0.020	0.000	99.7	47.9
20	009A/518.2	AB vein	Early stage	100.2	0.038	0.000	0.015	0.027	0.007	0.001	100.3	162
1	009A/520	AB vein	Early stage	101.3	0.000	0.000	0.004	0.019	0.006	0.000	101.3	114
2	009A/520	AB vein	Early stage	100.4	0.000	0.000	0.006	0.019	0.008	0.000	100.4	114
3	009A/520	AB vein	Early stage	99.6	0.041	0.000	0.024	0.032	0.009	0.000	99.7	192
4	009A/520	AB vein	Early stage	101.0	0.009	0.000	0.004	0.017	0.002	0.000	101.0	102
5	009A/520	AB vein	Early stage	98.5	0.036	0.002	0.017	0.006	0.013	0.000	98.6	36.0
6	009A/520	AB vein	Early stage	99.3	0.010	0.001	0.010	0.008	0.014	0.000	99.3	47.9
7	009A/520	AB vein	Early stage	100.3	0.012	0.000	0.007	0.011	0.011	0.000	100.4	65.9
8	009A/520	AB vein	Early stage	100.9	0.038	0.000	0.020	0.020	0.007	0.002	101.0	120
9	009A/520	AB vein	Early stage	100.7	0.064	0.000	0.035	0.024	0.007	0.000	100.9	144
10	009A/520	AB vein	Early stage	101.1	0.000	0.000	0.004	0.014	0.011	0.000	101.1	83.9
11	009A/520	AB vein	Early stage	100.9	0.000	0.000	0.002	0.014	0.007	0.000	100.9	83.9
12	009A/520	AB vein	Early stage	101.1	0.004	0.000	0.003	0.021	0.012	0.000	101.2	126
13	009A/520	AB vein	Early stage	100.0	0.333	0.026	0.132	0.019	0.057	0.000	100.6	114

14	009A/520	AB vein	Early stage	100.9	0.002	0.001	0.005	0.028	0.013	0.001	100.9	168
15	009A/520	AB vein	Early stage	101.3	0.054	0.000	0.028	0.043	0.005	0.000	101.4	258
16	009A/520	AB vein	Early stage	101.2	0.025	0.000	0.014	0.012	0.006	0.001	101.2	71.9
17	009A/520	AB vein	Early stage	99.8	0.014	0.005	0.013	0.012	0.016	0.000	99.8	71.9
18	009A/520	AB vein	Early stage	101.1	0.000	0.000	0.007	0.019	0.003	0.000	101.1	114
19	009A/520	AB vein	Early stage	100.9	0.000	0.000	0.005	0.024	0.008	0.000	100.9	144
20	009A/520	AB vein	Early stage	100.7	0.015	0.002	0.019	0.047	0.010	0.000	100.8	282
1	009A/518.2	B vein	Intermediate stage	100.0	0.023	0.000	0.011	0.011	0.019	0.000	100.1	46.1
2	009A/518.2	B vein	Intermediate stage	100.0	0.048	0.000	0.020	0.014	0.006	0.000	100.1	58.7
3	009A/518.2	B vein	Intermediate stage	100.3	0.000	0.000	0.008	0.013	0.001	0.002	100.4	54.5
4	009A/518.2	B vein	Intermediate stage	101.0	0.000	0.000	0.003	0.011	0.003	0.001	101.0	46.1
5	009A/518.2	B vein	Intermediate stage	100.1	0.025	0.000	0.011	0.010	0.010	0.000	100.2	42.0
6	009A/518.2	B vein	Intermediate stage	99.4	0.135	0.000	0.066	0.018	0.025	0.000	99.6	75.5
7	009A/518.2	B vein	Intermediate stage	100.6	0.025	0.000	0.012	0.024	0.010	0.001	100.7	101
8	009A/518.2	B vein	Intermediate stage	100.8	0.018	0.000	0.006	0.016	0.005	0.000	100.8	67.1
9	009A/518.2	B vein	Intermediate stage	99.2	0.025	0.000	0.002	0.015	0.000	0.000	99.2	62.9
10	009A/518.2	B vein	Intermediate stage	98.8	0.010	0.000	0.013	0.016	0.017	0.000	98.9	67.1
11	009A/518.2	B vein	Intermediate stage	100.5	0.000	0.000	0.005	0.019	0.008	0.000	100.5	79.7
12	009A/518.2	B vein	Intermediate stage	100.2	0.119	0.000	0.044	0.027	0.019	0.000	100.4	113
13	009A/518.2	B vein	Intermediate stage	100.8	0.005	0.000	0.011	0.039	0.004	0.000	100.9	164
14	009A/518.2	B vein	Intermediate stage	99.6	0.007	0.000	0.002	0.019	0.009	0.000	99.6	79.7
15	009A/518.2	B vein	Intermediate stage	100.6	0.000	0.000	0.005	0.019	0.007	0.000	100.7	79.7
16	009A/518.2	B vein	Intermediate stage	101.1	0.136	0.000	0.044	0.034	0.018	0.003	101.4	143
17	009A/518.2	B vein	Intermediate stage	100.8	0.000	0.000	0.003	0.014	0.007	0.000	100.8	58.7
18	009A/518.2	B vein	Intermediate stage	100.3	0.000	0.000	0.000	0.018	0.007	0.000	100.3	75.5
19	009A/518.2	B vein	Intermediate stage	100.6	0.000	0.000	0.001	0.018	0.005	0.002	100.6	75.5
1	013/1069	D vein	Late stage	100.5	0.323	0.000	0.001	0.004	0.014	0.000	100.8	16.8
2	013/1069	D vein	Late stage	100.3	0.191	0.000	0.010	0.001	0.023	0.000	100.5	4.20
3	013/1069	D vein	Late stage	100.9	0.000	0.000	0.001	0.001	0.010	0.000	100.9	4.20
4	013/1069	D vein	Late stage	100.5	0.069	0.000	0.001	0.001	0.023	0.000	100.6	4.20
5	013/1069	D vein	Late stage	100.4	0.321	0.000	0.003	0.000	0.026	0.000	100.8	0.00
6	013/1069	D vein	Late stage	100.7	0.006	0.000	0.001	0.022	0.014	0.000	100.8	92.3
7	013/1069	D vein	Late stage	100.8	0.080	0.000	0.005	0.000	0.018	0.003	100.9	0.00
8	013/1069	D vein	Late stage	100.0	0.363	0.000	0.000	0.000	0.057	0.003	100.4	0.00
9	013/1069	D vein	Late stage	100.4	0.217	0.000	0.005	0.005	0.003	0.000	100.6	21.0
10	013/1069	D vein	Late stage	100.9	0.038	0.000	0.000	0.002	0.002	0.000	100.9	8.39
11	013/1069	D vein	Late stage	100.6	0.061	0.002	0.014	0.000	0.001	0.000	100.6	0.00
12	013/1069	D vein	Late stage	100.2	0.200	0.000	0.004	0.001	0.004	0.001	100.4	4.20

13	013/1069	D vein	Late stage	100.5	0.038	0.000	0.000	0.001	0.000	0.000	100.5	4.20
14	013/1069	D vein	Late stage	100.5	0.010	0.000	0.001	0.001	0.006	0.004	100.5	4.20
15	013/1069	D vein	Late stage	100.6	0.030	0.000	0.001	0.004	0.006	0.001	100.7	16.8
16	013/1069	D vein	Late stage	100.6	0.000	0.000	0.003	0.000	0.007	0.003	100.6	0.00
17	013/1069	D vein	Late stage	100.6	0.000	0.000	0.002	0.003	0.003	0.001	100.6	12.6
18	013/1069	D vein	Late stage	100.5	0.010	0.000	0.000	0.000	0.000	0.000	100.5	0.00

Appendix 7 Representative mineral chemistry data of plagioclase in diorite and quartz diorite porphyry based on EPMA analysis.

Sample	VHD 009A-416	VHD 009A-416	VHD 009A-416	VHD 009A-416	VHD 009A-416	VHD 009A-416	VHD 009A-416
	Early phase	Early phase	Early phase	Early phase	Early phase	Early phase	Early phase
SiO_2 (wt.%)	54.6	53.2	54.2	54.1	53.8	53.0	54.1
TiO_2	0.00	0.00	0.00	0.00	0.00	0.00	0.00
Al_2O_3	27.5	28.5	27.9	27.6	27.8	28.6	27.8
FeO	0.13	0.14	0.14	0.13	0.12	0.10	0.13
MnO	0.01	0.01	0.00	0.00	0.00	0.00	0.00
MgO	0.01	0.01	0.01	0.00	0.01	0.00	0.01
CaO	10.2	11.6	10.8	10.5	10.6	11.4	10.4
Na_2O	5.60	4.76	5.17	5.47	5.41	4.97	5.40
K_2O	0.24	0.19	0.22	0.24	0.23	0.17	0.21
SrO	0.51	0.54	0.59	0.58	0.58	0.58	0.60
Total	98.8	99.0	99.0	98.7	98.6	99.0	98.8
Si (apfu)	2.50	2.44	2.48	2.49	2.47	2.43	2.48
Al	1.49	1.54	1.51	1.50	1.51	1.55	1.50
Ti	0.00	0.00	0.00	0.000	0.00	0.00	0.00
Fe	0.01	0.01	0.01	0.01	0.01	0.004	0.01
Mn	0.00	0.00	0.00	0.00	0.00	0.00	0.00
Mg	0.00	0.001	0.001	0.00	0.00	0.00	0.00
Ca	0.50	0.57	0.53	0.52	0.52	0.56	0.51
Na	0.50	0.42	0.46	0.49	0.48	0.44	0.48
K	0.014	0.011	0.013	0.012	0.013	0.010	0.012
Sr	0.01	0.01	0.01	0.01	0.01	0.01	0.01
An (mol. %)	49.4	56.7	52.8	50.8	51.3	55.5	51.1
Ab	49.1	42.2	45.9	47.9	47.4	43.6	47.7
Or	1.41	1.09	1.27	1.36	1.31	0.97	1.20

Table 3 (cont.)

Sample	VHD 006-723	VHD 006-723	VHD 006-723	VHD 006-723	VHD 006-723	VHD 006-723	VHD 006-723
Intrusion phase	Intermediate porphyry	Intermediate porphyry	Intermediate porphyry	Intermediate porphyry	Intermediate porphyry	Intermediate porphyry	Intermediate porphyry
SiO_2 (wt.%)	55.3	54.9	55.6	54.7	55.1	55.2	54.8
TiO_2	0.00	0.00	0.01	0.00	0.00	0.00	0.00
Al_2O_3	27.6	26.9	26.6	27.6	27.1	27.1	27.2
FeO	0.13	0.10	0.08	0.13	0.11	0.12	0.11
MnO	0.01	0.00	0.00	0.00	0.00	0.00	0.00
MgO	0.00	0.01	0.00	0.00	0.04	0.00	0.00
CaO	9.89	9.10	8.68	9.95	10.3	10.4	10.5
Na_2O	5.73	6.04	6.36	5.50	5.31	5.32	5.22
K_2O	0.14	0.21	0.25	0.19	0.20	0.170	0.16
SrO	0.61	0.66	0.66	0.68	0.62	0.65	0.58
Total	99.4	98.0	98.3	98.8	98.8	99.0	98.6
Si (apfu)	2.51	2.53	2.55	2.50	2.52	2.52	2.51
Al	1.48	1.46	1.44	1.49	1.46	1.46	1.47
Ti	0.00	0.00	0.00	0.00	0.00	0.00	0.00
Fe	0.004	0.003	0.003	0.003	0.003	0.003	0.003
Mn	0.00	0.00	0.00	0.00	0.00	0.00	0.00
Mg	0.00	0.00	0.00	0.00	0.00	0.00	0.00
Ca	0.48	0.44	0.43	0.49	0.51	0.51	0.51
Na	0.51	0.540	0.57	0.49	0.47	0.47	0.46
K	0.02	0.02	0.02	0.02	0.02	0.02	0.02
Sr	0.01	0.01	0.01	0.01	0.01	0.01	0.01
An (mol. %)	48.4	44.9	42.4	49.4	51.2	51.5	52.1
Ab	50.7	53.9	56.2	49.1	47.6	47.5	47.0
Or	0.81	1.21	1.45	1.15	1.16	1.00	0.93

Table 3 (cont.)

Sample	VHD 009A-703.8	VHD 009A-703.8	VHD 009A-703.8	VHD 009A-703.8	VHD 009A-703.8	VHD 009A-703.8	VHD 009A-703.8
Intrusion phase	Late phase	Late phase	Late phase	Late phase	Late phase	Late phase	Late phase
SiO_2 (wt.%)	56.2	55.0	54.3	54.6	54.9	54.6	54.8
TiO_2	0.00	0.0	0.0	0.0	0.0	0.0	0.0
Al_2O_3	25.6	26.8	27.5	26.9	27.2	27.0	27.2
FeO	0.10	0.09	0.09	0.07	0.07	0.08	0.08
MnO	0.01	0.00	0.00	0.00	0.00	0.00	0.00
MgO	0.01	0.00	0.05	0.00	0.00	0.00	0.00
CaO	8.47	9.67	10.4	9.89	10.1	9.98	10.3
Na_2O	6.63	5.97	5.53	5.76	5.78	5.74	5.46
K_2O	0.39	0.29	0.26	0.27	0.26	0.29	0.30
SrO	0.67	0.65	0.62	0.63	0.66	0.61	0.62
Total	98.0	98.4	98.7	98.1	99.0	98.3	98.8
Si (apfu)	2.59	2.53	2.49	2.52	2.51	2.52	2.51
Al	1.39	1.45	1.49	1.46	1.47	1.47	1.47
Ti	0.00	0.00	0.00	0.00	0.00	0.00	0.00
Fe	0.01	0.004	0.003	0.01	0.004	0.01	0.004
Mn	0.00	0.00	0.00	0.00	0.00	0.00	0.00
Mg	0.00	0.001	0.00	0.00	0.003	0.00	0.00
Ca	0.41	0.48	0.51	0.49	0.49	0.49	0.51
Na	0.59	0.53	0.49	0.52	0.51	0.51	0.49
K	0.01	0.01	0.02	0.01	0.01	0.01	0.01
Sr	0.01	0.01	0.01	0.01	0.01	0.01	0.01
An (mol. %)	40.2	46.4	50.3	47.9	48.3	48.2	50.2
Ab	57.6	52.0	48.2	50.5	50.2	50.1	48.1
Or	2.23	1.64	1.49	1.55	1.50	1.68	1.71

Abbreviations: apfu= atoms per formula unit, An= anorthite, Ab= albite, and Or= orthoclase

133

Appendix 8 Result of microthermetry analysis of fluid inclusion from late stage vein of HLE prospect.

No	Samples	Stage	FI phase	Shape	Size (μm)	Measured temp. (°C)	True temp. (°C)	Measured temp. (°C)	True temp. (°C)	Salinity (Wt. % NaCl equiv.)
1	VHD 013/1069	late stage (D vein)	Biphase (L+V)	oval-irregullar	25	252	242	-4.3	-3.7	6.0
2	VHD 013/1069	late stage (D vein)	Biphase (L+V)	oval	10	263	253	-4.8	-4.1	6.7
3	VHD 013/1070	late stage (D vein)	Biphase (L+V)	long oval	20	260	250	-5.4	-4.6	7.6
4	VHD 013/1071	late stage (D vein)	Biphase (L+V)	long oval	10	260	250	-4.5	-3.8	6.3
5	VHD 013/1072	late stage (D vein)	Biphase (L+V)	oval	10	270	260	-5.4	-4.6	7.6
6	VHD 013/1073	late stage (D vein)	Biphase (L+V)	long oval	20	275	265	-5.7	-4.9	8.0
7	VHD 013/1074	late stage (D vein)	Biphase (L+V)	oval-irregullar	15	242	231	-4.2	-3.6	5.9
8	VHD 013/1075	late stage (D vein)	Biphase (L+V)	long oval	20	272	262	-5.4	-4.6	7.6
9	VHD 013/1076	late stage (D vein)	Biphase (L+V)	long oval	15	282	273	-6.2	-5.3	8.7
10	VHD 013/1077	late stage (D vein)	Biphase (L+V)	oval	15	251	241	-4.2	-3.6	5.9
11	VHD 013/1078	late stage (D vein)	Biphase (L+V)	oval	15	251	241	-4.3	-3.7	6.0
12	VHD 013/1079	late stage (D vein)	Biphase (L+V)	oval	10	258	248	-4.5	-3.8	6.3
13	VHD 013/1080	late stage (D vein)	Biphase (L+V)	oval	10	240	229	-4.0	-3.4	5.6
14	VHD 013/1081	late stage (D vein)	Biphase (L+V)	long oval	15	283	274	-6.7	-5.8	9.4
15	VHD 013/1082	late stage (D vein)	Biphase (L+V)	oval	10	250	240	-4.0	-3.4	5.6
16	VHD 013/1083	late stage (D vein)	Biphase (L+V)	long oval	20	280	271	-6.1	-5.2	8.5
17	VHD 013/1084	late stage (D vein)	Biphase (L+V)	oval	10	241	230	-4.1	-3.5	5.6
18	VHD 013/1085	late stage (D vein)	Biphase (L+V)	oval	10	244	234	-4.3	-3.7	5.9
19	VHD 013/1086	late stage (D vein)	Biphase (L+V)	long oval	15	288	279	-6.5	-5.6	8.5
20	VHD 013/1087	late stage (D vein)	Biphase (L+V)	oval-irregullar	15	302	294	-7.2	-6.2	9.2
21	VHD 013/1088	late stage (D vein)	Biphase (L+V)	oval-irregullar	20	272	262	-5.4	-4.6	7.2
22	VHD 013/1089	late stage (D vein)	Biphase (L+V)	irregullar	15	280	271	-5.8	-5.0	7.7
23	VHD 013/1090	late stage (D vein)	Biphase (L+V)	irregullar	20	264	254	-4.7	-4.0	6.4
24	VHD 013/1091	late stage (D vein)	Biphase (L+V)	irregullar	10	265	255	-4.8	-4.1	6.5
25	VHD 013/1092	late stage (D vein)	Biphase (L+V)	irregullar	10	261	251	-4.8	-4.1	6.5
26	VHD 013/1093	late stage (D vein)	Biphase (L+V)	oval	10	266	256	-5.1	-4.4	6.9
27	VHD 013/1094	late stage (D vein)	Biphase (L+V)	long oval	15	265	255	-5	-4.3	6.7

28	VHD 013/1095	late stage (D vein)	Biphase (L+V)	irregullar	20	260	250	-4.2	-3.6	5.8
29	VHD 013/1096	late stage (D vein)	Biphase (L+V)	irregullar	15	267	257	-5.3	-4.5	7.1
30	VHD 013/1097	late stage (D vein)	Biphase (L+V)	irregullar	20	270	260	-5.5	-4.7	7.3

Appendix 9 Result of microthermetry analysis of fluid inclusion from intermediate stage vein of HLE prospect.

No	Samples	Stage	FI phase	Shape	Size (μm)	Measured temp. (℃)	True temp. (℃)	Measured temp. (℃)	True temp. (℃)	Salinity (Wt. % NaCl equiv.)
1	VHD 009A/474.2	Intermediate (B vein)	Biphase (L+V)	oval	10	246	236	-10.8	-9.5	12.4
2	VHD 009A/474.2	Intermediate (B vein)	Biphase (L+V)	long oval	25	325	318	-12.6	-11.2	13.6
3	VHD 009A/474.3	Intermediate (B vein)	Biphase (L+V)	oval	15	280	271	-11	-9.7	12.6
4	VHD 009A/474.4	Intermediate (B vein)	Biphase (L+V)	spherical	10	251	241	-10.7	-9.4	12.4
5	VHD 009A/474.5	Intermediate (B vein)	Biphase (L+V)	oval	10	265	255	-8.7	-7.6	10.7
6	VHD 009A/474.6	Intermediate (B vein)	Biphase (L+V)	long oval	20	296	287	-12.7	-11.3	13.7
7	VHD 009A/474.7	Intermediate (B vein)	Biphase (L+V)	long oval	15	276	266	-10.7	-9.4	12.4
8	VHD 009A/474.8	Intermediate (B vein)	Biphase (L+V)	long oval	15	281	272	-11.9	-10.5	13.2
9	VHD 009A/474.9	Intermediate (B vein)	Biphase (L+V)	long oval	15	283	274	-12.1	-10.7	13.3
10	VHD 009A/474.10	Intermediate (B vein)	Biphase (L+V)	oval	10	292	283	-12.3	-10.9	13.4
11	VHD 009A/474.11	Intermediate (B vein)	Biphase (L+V)	long oval	15	284	275	-11.7	-10.4	13.1
12	VHD 009A/474.2	Intermediate (B vein)	Biphase (L+V)	long oval	20	330	324	-14.3	-12.8	14.4

Appendix 10 Result of microthermetry analysis of fluid inclusion from early stage vein of HLE prospect.

No	Sample	Stage	FI phase	Size (µm)	Measured temp. (°C)	True temp. (°C)	Measured temp. (°C) of Halite	True temp. (°C) of Halite	Salinity (Wt. % NaCl equiv.)
1	VHD 009A/520	Early stage (A vein)	Biphase (L+V)	7	723	694	-	-	
2	VHD 009A/520	Early stage (A vein)	Biphase (L+V)	7	800	768	-	-	
3	VHD 009A/520	Early stage (A vein)	Biphase (L+V)	5	1053	1011	-	-	
4	VHD 009A/520	Early stage (A vein)	Biphase (L+V)	5	1046	1004	-	-	
5	VHD 009A/520	Early stage (A vein)	multiphase (V+S+L)	15	1222	1173	376	368	44
6	VHD 009A/520	Early stage (A vein)	multiphase (V+S+L)	10	1222	1173	380	372	45
7	VHD 009A/520	Early stage (A vein)	multiphase (V+S+L)	10	1220	1171	380	372	45
8	VHD 009A/520	Early stage (A vein)	multiphase (V+S+L)	10	1228	1179	384	376	45
9	VHD 009A/520	Early stage (A vein)	multiphase (V+S+L)	15	1226	1177	385	377	45
10	VHD 009A/520	Early stage (A vein)	multiphase (V+S+L)	15	1226	1177	385	377	45
11	VHD 009A/520	Early stage (A vein)	multiphase (V+S+L)	20	1270	1219	380	372	45
12	VHD 009A/520	Early stage (A vein)	multiphase (V+S+L)	15	1230	1180	380	372	45
13	VHD 009A/520	Early stage (A vein)	multiphase (V+S+L)	10	1260	1209	385	377	45
14	VHD 009A/520	Early stage (A vein)	multiphase (V+S+L)	10	1224	1175	379	371	44
15	VHD 009A/520	Early stage (A vein)	multiphase (V+S+L)	10	1275	1224	390	382	46
16	VHD 009A/520	Early stage (A vein)	multiphase (V+S+L)	10	1269	1218	385	377	45
17	VHD 009A/520	Early stage (A vein)	multiphase (V+S+L)	30	1264	1213	385	377	45
18	VHD 009A/520	Early stage (A vein)	multiphase (V+S+L)	25	1275	1224	392	384	46
19	VHD 009A/520	Early stage (A vein)	multiphase (V+S+L)	20	1297	1245	402	394	47
20	VHD 009A/520	Early stage (A vein)	multiphase (V+S+L)	25	1295	1243	391	383	46
21	VHD 009A/520	Early stage (A vein)	multiphase (V+S+L)	15	1295	1243	405	397	47
22	VHD 009A/520	Early stage (A vein)	multiphase (V+S+L)	15	1295	1243	445	436	52
23	VHD 009A/520	Early stage (A vein)	multiphase (V+S+L)	25	1294	1242	450	441	52
24	VHD 009A/520	Early stage (A vein)	multiphase (V+S+L)	20	1299	1247	385	377	45
25	VHD 009A/520	Early stage (A vein)	multiphase (V+S+L)	10	1290	1238	389	381	45
26	VHD 009A/520	Early stage (A vein)	multiphase (V+S+L)	8	1268	1217	365	357	43
27	VHD 009A/520	Early stage (A vein)	multiphase (V+S+L)	10	1264	1213	368	360	43
28	VHD 009A/520	Early stage (A vein)	multiphase (V+S+L)	10	1223	1174	350	343	42
29	VHD 009A/520	Early stage (A vein)	multiphase (V+S+L)	5	1262	1211	362	354	43
30	VHD 009A/520	Early stage (A vein)	multiphase (V+S+L)	5	1260	1209	361	353	43
31	VHD 009A/520	Early stage (A vein)	multiphase (V+S+L)	5	1260	1209	362	354	43

Appendix 11 LA-ICP-MS result of zircon grain from HLE prospect which representative early, intermediate and late stage of intrusion phase.

Sample ID	Description	Nb (ppm)	Ta (ppm)	La (ppm)	Ce (ppm)	Pr (ppm)	Nd (ppm)	Sm (ppm)	Eu (ppm)	Gd (ppm)	Tb (ppm)	Dy (ppm)
VHD006/500-502 (07)	HLE, Hu'u district	1.92	0.38	0.01	3.90	0.07	1.29	2.28	0.90	10.2	3.41	44.4
VHD006/500-502 (10)	HLE, Hu'u district	1.99	0.41	0.01	3.75	0.01	0.26	0.83	0.29	5.61	2.20	30.6
VHD006/500-502 (12)	HLE, Hu'u district	1.99	0.41	0.00	3.87	0.03	0.66	1.67	0.59	9.29	3.30	44.4
VHD006/500-502 (15)	HLE, Hu'u district	2.00	0.43	0.02	3.85	0.02	0.35	0.83	0.34	4.74	1.78	24.5
VHD006/500-502 (17)	HLE, Hu'u district	1.97	0.40	0.02	4.94	0.05	1.09	2.55	0.91	13.6	4.60	60.4
VHD006/500-502 (20)	HLE, Hu'u district	2.02	0.39	0.00	3.32	0.02	0.37	0.97	0.40	5.60	2.05	29.0
VHD006/500-502 (22)	HLE, Hu'u district	2.32	0.53	0.05	7.12	0.05	0.85	2.28	0.69	14.8	5.52	78.3
VHD006/500-502 (26)	HLE, Hu'u district	2.01	0.44	0.03	4.09	0.04	0.63	1.30	0.49	7.10	2.55	35.7
VHD006/500-502 (29)	HLE, Hu'u district	1.95	0.46	0.01	5.54	0.09	1.76	3.59	1.19	16.8	5.62	73.6
VHD006/500-502 (30)	HLE, Hu'u district	1.94	0.41	0.01	3.80	0.02	0.42	1.26	0.45	8.40	3.15	43.5
VHD006/500-502 (33)	HLE, Hu'u district	1.97	0.43	0.00	5.90	0.06	1.20	2.73	0.86	13.5	4.57	60.9
VHD006/500-502 (42)	HLE, Hu'u district	1.97	0.42	0.00	4.20	0.04	0.86	2.06	0.75	11.1	3.86	50.9
VHD009A/250-252 (01)	HLE, Hu'u district	2.56	0.63	0.00	5.04	0.06	1.19	2.69	0.85	12.6	4.40	58.0
VHD009A/250-252 (02)	HLE, Hu'u district	2.84	0.64	0.01	5.93	0.05	1.01	2.45	0.79	13.5	5.08	69.1
VHD009A/250-252 (03)	HLE, Hu'u district	2.37	0.54	0.00	3.06	0.02	0.36	0.91	0.37	5.19	1.95	27.0
VHD009A/250-252 (08)	HLE, Hu'u district	2.70	0.57	0.00	4.76	0.03	0.55	1.38	0.59	8.04	3.12	46.4
VHD009A/250-252 (11)	HLE, Hu'u district	2.60	0.59	0.05	5.10	0.06	0.92	2.13	0.73	11.5	4.16	56.4
VHD009A/250-252 (13)	HLE, Hu'u district	2.36	0.54	0.00	5.27	0.04	0.98	2.75	0.89	15.1	5.22	66.3
VHD009A/250-252 (14)	HLE, Hu'u district	2.79	0.63	0.00	6.28	0.06	1.19	2.85	1.00	17.2	6.35	87.1
VHD009A/250-252 (16)	HLE, Hu'u district	2.57	0.62	0.00	4.82	0.05	0.83	1.70	0.69	8.77	3.20	43.2
VHD009A/250-252 (21)	HLE, Hu'u district	2.65	0.61	0.11	5.26	0.06	0.70	1.43	0.54	7.84	2.95	43.4
VHD009A/250-252 (22)	HLE, Hu'u district	2.78	0.66	0.01	6.50	0.07	1.37	3.11	1.04	17.7	6.51	89.5
VHD009A/250-252 (23)	HLE, Hu'u district	2.38	0.55	0.00	3.86	0.04	0.71	1.58	0.59	8.41	3.09	42.5
VHD009A/250-252 (24)	HLE, Hu'u district	2.46	0.54	0.08	5.08	0.07	1.01	1.90	0.77	10.1	3.59	48.9
VHD009A/250-252 (28)	HLE, Hu'u district	2.32	0.51	0.00	4.25	0.02	0.54	1.50	0.53	9.46	3.53	49.1
VHD009A/250-252 (29)	HLE, Hu'u district	2.66	0.60	0.05	6.10	0.06	0.87	2.13	0.72	13.3	5.01	71.4
VHD009A/250-252 (31)	HLE, Hu'u district	2.18	0.57	0.00	5.80	0.04	0.97	2.51	0.77	12.5	4.26	55.6
VHD009A/250-252 (32)	HLE, Hu'u district	2.21	0.46	0.04	3.75	0.02	0.44	1.30	0.46	8.46	3.17	44.1
VHD009A/250-252 (33)	HLE, Hu'u district	2.23	0.49	0.00	4.77	0.06	1.18	2.61	0.96	14.7	5.21	69.6
VHD009A/250-252 (34)	HLE, Hu'u district	2.02	0.44	0.00	3.11	0.02	0.34	0.73	0.33	4.58	1.62	22.8
VHD009A/250-252 (38)	HLE, Hu'u district	2.09	0.48	0.01	4.58	0.07	1.36	2.70	0.95	11.9	3.98	51.1
VHD009A/250-252 (43)	HLE, Hu'u district	2.12	0.44	0.00	3.34	0.03	0.49	1.01	0.48	5.78	2.03	28.3

138

VHD009A/250-252 (44)	HLE, Hu'u district	2.23	0.47	0.01	3.93	0.03	0.55	1.23	0.48	6.49	2.28	32.1
VHD009A/250-252 (45)	HLE, Hu'u district	2.46	0.53	0.00	6.26	0.06	1.29	3.05	1.03	18.3	6.62	91.0
VHD009A/250-252 (49)	HLE, Hu'u district	2.96	0.59	0.04	10.1	0.07	1.28	2.89	1.28	19.5	7.74	114.3
VHD009A/250-252 (51)	HLE, Hu'u district	2.19	0.46	0.05	4.25	0.04	0.61	1.52	0.47	9.56	3.55	49.8
VHD009A/250-252 (53)	HLE, Hu'u district	2.12	0.46	0.01	4.66	0.09	1.53	2.82	1.01	13.1	4.34	57.8
VHD009A/250-252 (54)	HLE, Hu'u district	2.34	0.51	0.02	4.89	0.03	0.64	1.81	0.63	11.1	4.12	58.1
VHD009A/250-252 (55)	HLE, Hu'u district	1.99	0.41	0.01	4.39	0.04	0.89	2.18	0.86	11.2	3.72	47.6
VHD009A/250-252 (58)	HLE, Hu'u district	1.99	0.43	0.01	4.15	0.06	1.11	2.44	0.85	12.9	4.29	56.9
VHD001R/600-602 (05)	HLE, Hu'u district	1.75	0.35	0.00	2.80	0.01	0.28	0.68	0.31	3.89	1.43	19.6
VHD001R/600-602 (09)	HLE, Hu'u district	1.70	0.35	0.00	3.50	0.05	0.99	1.94	0.79	9.66	3.27	44.1
VHD001R/600-602 (15)	HLE, Hu'u district	1.81	0.36	0.01	4.19	0.08	1.51	2.72	0.99	12.5	4.18	54.6
VHD001R/600-602 (19)	HLE, Hu'u district	1.74	0.37	0.00	4.15	0.03	0.67	1.54	0.54	7.57	2.64	35.0
VHD001R/600-602 (22)	HLE, Hu'u district	1.69	0.34	0.02	4.24	0.08	1.47	2.92	1.13	13.0	4.17	53.2
VHD001R/600-602 (27)	HLE, Hu'u district	2.03	0.43	0.00	4.82	0.03	0.66	1.75	0.63	10.1	3.68	52.2
VHD001R/600-602 (28)	HLE, Hu'u district	1.71	0.33	0.00	2.89	0.01	0.32	0.80	0.35	4.55	1.66	21.9
VHD001R/600-602 (29)	HLE, Hu'u district	1.76	0.35	0.00	3.05	0.01	0.33	0.82	0.36	4.86	1.77	24.1
VHD001R/600-602 (34)	HLE, Hu'u district	1.82	0.37	4.34	13.1	1.31	6.30	2.07	0.58	6.96	2.33	32.3
VHD001R/600-602 (36)	HLE, Hu'u district	1.92	0.40	0.01	6.34	0.09	1.66	3.62	1.22	21.3	7.42	97.2
VHD001R/600-602 (43)	HLE, Hu'u district	1.69	0.33	0.00	3.01	0.03	0.53	1.11	0.48	5.73	1.97	26.5
VHD001R/600-602 (44)	HLE, Hu'u district	1.71	0.33	0.00	4.17	0.07	1.29	2.59	0.99	11.8	3.86	49.9
VHD001R/600-602 (46)	HLE, Hu'u district	1.76	0.37	0.00	5.47	0.04	0.98	2.73	0.85	15.1	5.16	66.6
VHD001R/600-602 (56)	HLE, Hu'u district	2.63	0.55	0.02	9.67	0.05	1.02	2.78	0.91	17.5	6.70	97.6
VHD001R/600-602 (64)	HLE, Hu'u district	1.72	0.34	0.00	3.86	0.04	0.82	1.76	0.71	8.72	2.96	39.1
VHD001R/600-602 (65)	HLE, Hu'u district	1.70	0.33	0.01	3.47	0.05	0.92	1.66	0.78	8.09	2.79	38.0
VHD001R/600-602 (66)	HLE, Hu'u district	1.99	0.39	0.00	5.10	0.03	0.53	1.43	0.53	8.44	3.24	47.4
VHD001R/600-602 (68)	HLE, Hu'u district	2.40	0.46	2.08	11.6	0.63	3.50	2.43	0.96	11.7	4.50	67.3
VHD001R/600-602 (70)	HLE, Hu'u district	1.91	0.42	0.01	5.89	0.05	1.12	3.03	0.91	18.3	6.81	91.6
VHD001R/600-602 (71-1)	HLE, Hu'u district	1.65	0.31	1.69	6.43	0.48	2.37	1.23	0.43	5.25	1.78	24.7
VHD001R/600-602 (71-2)	HLE, Hu'u district	1.77	0.34	0.00	3.56	0.03	0.58	1.29	0.59	6.77	2.38	32.4

Appendix 11 (continued)

Sample ID	Description	Ho (ppm)	Er (ppm)	Tm (ppm)	Yb (ppm)	Lu (ppm)	Y (ppm)	Ti (ppm)	Zr (ppm)	Hf (ppm)	Pb (ppm)	Th (ppm)
VHD006/500-502 (07)	HLE, Hu'u district	17.7	96.6	25.2	292	58.0	600	7.71	526608	9143	0.04	28.1
VHD006/500-502 (10)	HLE, Hu'u district	12.6	67.7	16.9	181	34.0	410	8.40	532194	9979	0.14	13.6
VHD006/500-502 (12)	HLE, Hu'u district	17.7	95.7	24.2	269	51.9	585	8.25	530856	9633	0.03	18.6
VHD006/500-502 (15)	HLE, Hu'u district	10.4	60.8	16.5	193	42.6	371	7.60	543153	10328	0.57	31.5
VHD006/500-502 (17)	HLE, Hu'u district	23.8	127	31.3	341	65.0	789	7.79	519215	9633	0.03	33.9
VHD006/500-502 (20)	HLE, Hu'u district	12.7	73.4	20.2	242	50.4	440	8.00	534045	9341	0.03	15.4
VHD006/500-502 (22)	HLE, Hu'u district	32.8	182	43.5	448	91.9	1070	11.5	519923	9383	1.02	38.4
VHD006/500-502 (26)	HLE, Hu'u district	15.0	85.6	23.4	281	57.9	514	8.39	546592	10538	0.09	30.9
VHD006/500-502 (29)	HLE, Hu'u district	28.9	156	39.5	437	86.6	967	5.89	534233	11025	0.09	57.6
VHD006/500-502 (30)	HLE, Hu'u district	17.5	93.9	23.7	258	48.8	568	8.68	526633	9416	0.06	14.7
VHD006/500-502 (33)	HLE, Hu'u district	23.6	124	30.6	331	61.6	762	7.92	531339	10455	0.06	44.9
VHD006/500-502 (42)	HLE, Hu'u district	19.9	108	27.5	308	59.1	656	7.48	542336	10103	0.03	22.8
VHD009A/250-252 (01)	HLE, Hu'u district	23.3	129	33.4	384	75.5	787	5.51	529245	10926	0.05	42.2
VHD009A/250-252 (02)	HLE, Hu'u district	29.3	159	40.5	452	85.5	946	11.6	545393	9647	0.07	32.8
VHD009A/250-252 (03)	HLE, Hu'u district	11.6	67.1	18.7	227	47.9	398	6.52	513473	9608	0.03	17.5
VHD009A/250-252 (08)	HLE, Hu'u district	20.5	119	32.0	376	76.3	693	9.54	538119	9244	0.04	26.5
VHD009A/250-252 (11)	HLE, Hu'u district	22.9	124	31.5	348	66.7	759	10.4	539260	9807	0.07	26.3
VHD009A/250-252 (13)	HLE, Hu'u district	25.2	128	30.6	325	59.6	797	7.43	532019	10449	0.05	35.7
VHD009A/250-252 (14)	HLE, Hu'u district	35.6	192	47.4	515	95.7	1131	10.3	538816	9489	0.05	36.8
VHD009A/250-252 (16)	HLE, Hu'u district	18.2	104	28.2	343	69.9	612	6.15	540032	10690	0.07	46.2
VHD009A/250-252 (21)	HLE, Hu'u district	19.2	115	31.4	374	76.9	663	8.38	543079	10054	0.06	31.4
VHD009A/250-252 (22)	HLE, Hu'u district	36.7	194	47.6	513	93.5	1130	10.1	551366	10003	0.04	36.8
VHD009A/250-252 (23)	HLE, Hu'u district	17.8	103	27.9	329	66.4	604	6.92	536827	10222	0.03	22.8
VHD009A/250-252 (24)	HLE, Hu'u district	20.2	113	30.7	359	70.3	685	21.8	523085	9524	0.16	34.0
VHD009A/250-252 (28)	HLE, Hu'u district	20.4	112	28.5	319	60.9	666	8.84	523947	9355	0.06	17.8
VHD009A/250-252 (29)	HLE, Hu'u district	31.0	174	43.6	469	96.3	1027	24.6	529201	9378	0.22	27.4
VHD009A/250-252 (31)	HLE, Hu'u district	22.2	121	32.2	372	73.3	754	4.06	539374	12617	0.08	61.6
VHD009A/250-252 (32)	HLE, Hu'u district	17.7	94.8	24.1	266	49.5	573	8.95	545034	9753	0.08	14.8
VHD009A/250-252 (33)	HLE, Hu'u district	27.5	145	35.9	392	74.3	881	9.06	528967	9279	0.03	29.8
VHD009A/250-252 (34)	HLE, Hu'u district	9.4	54.3	15.1	181	38.7	325	6.58	525830	9865	0.03	16.1
VHD009A/250-252 (38)	HLE, Hu'u district	20.2	109	28.7	329	63.8	680	6.24	529927	10249	0.05	33.8
VHD009A/250-252 (43)	HLE, Hu'u district	11.9	68.7	18.9	229	47.8	415	7.22	548428	9944	0.03	18.7
VHD009A/250-252 (44)	HLE, Hu'u district	13.8	82.2	23.0	282	59.5	490	8.60	537595	9264	0.04	19.1

VHD009A/250-252 (45)	HLE, Hu'u district	36.7	196	47.9	511	94.8	1164	10.2	529231	9326	0.05	38.6
VHD009A/250-252 (49)	HLE, Hu'u district	48.8	269	66.8	727	144	1628	12.2	538071	9002	0.91	92.2
VHD009A/250-252 (51)	HLE, Hu'u district	19.9	103	24.5	253	45.8	617	9.51	537707	10080	0.02	15.0
VHD009A/250-252 (53)	HLE, Hu'u district	23.1	125	31.6	356	69.3	766	7.33	539938	9910	0.05	45.5
VHD009A/250-252 (54)	HLE, Hu'u district	24.5	138	35.1	390	74.9	811	11.7	531718	9192	0.04	19.5
VHD009A/250-252 (55)	HLE, Hu'u district	18.0	94.6	24.0	269	51.3	600	8.02	535087	10203	0.04	32.2
VHD009A/250-252 (58)	HLE, Hu'u district	22.7	123	29.9	319	69.1	770	11.6	529898	10285	0.23	29.5
VHD001R/600-602 (05)	HLE, Hu'u district	8.3	48.7	13.6	166	35.1	295	6.68	536179	9643	0.02	13.5
VHD001R/600-602 (09)	HLE, Hu'u district	17.6	96.2	25.1	289	57.5	592	6.75	517252	9360	0.04	24.2
VHD001R/600-602 (15)	HLE, Hu'u district	21.5	117	29.9	336	65.7	731	7.71	529456	9052	0.04	26.1
VHD001R/600-602 (19)	HLE, Hu'u district	14.1	76.7	20.2	229	46.4	474	6.25	519040	9945	0.06	32.1
VHD001R/600-602 (22)	HLE, Hu'u district	20.5	110	28.3	319	61.6	695	7.12	532027	9799	0.08	35.9
VHD001R/600-602 (27)	HLE, Hu'u district	22.4	128	33.4	378	74.2	760	10.1	528201	8901	0.04	19.8
VHD001R/600-602 (28)	HLE, Hu'u district	9.2	51.8	14.4	172	36.0	315	7.09	527802	9537	0.03	14.1
VHD001R/600-602 (29)	HLE, Hu'u district	9.9	56.1	15.1	178	36.3	336	7.23	539089	9786	0.03	14.5
VHD001R/600-602 (34)	HLE, Hu'u district	13.8	80.1	21.7	258	53.0	475	8.58	531366	9160	0.32	18.3
VHD001R/600-602 (36)	HLE, Hu'u district	37.9	192	45.4	471	85.2	1188	8.96	538621	9444	0.05	52.1
VHD001R/600-602 (43)	HLE, Hu'u district	10.9	62.5	17.3	212	45.2	378	6.75	536652	9546	0.03	17.5
VHD001R/600-602 (44)	HLE, Hu'u district	20.1	110	28.6	325	64.1	677	7.44	536248	9317	0.04	25.7
VHD001R/600-602 (46)	HLE, Hu'u district	25.8	130	31.2	325	58.7	811	7.83	532111	10108	0.04	36.2
VHD001R/600-602 (56)	HLE, Hu'u district	42.7	239	60.1	643	121	1373	12.0	530517	9148	0.64	55.2
VHD001R/600-602 (64)	HLE, Hu'u district	15.7	85.2	22.5	261	51.6	524	7.43	538808	9867	0.04	26.9
VHD001R/600-602 (65)	HLE, Hu'u district	15.8	89.1	24.3	294	60.0	540	7.45	549258	9579	0.07	24.9
VHD001R/600-602 (66)	HLE, Hu'u district	20.2	114	29.4	332	64.8	680	9.06	535287	9308	0.03	27.8
VHD001R/600-602 (68)	HLE, Hu'u district	31.1	188	51.6	605	123	1091	11.8	564611	9250	0.11	54.2
VHD001R/600-602 (70)	HLE, Hu'u district	35.9	184	42.9	441	77.5	1108	9.65	538947	9874	0.04	31.2
VHD001R/600-602 (71-1)	HLE, Hu'u district	10.5	63	17.4	214	46.4	369	7.03	519133	9452	0.06	17.5
VHD001R/600-602 (71-2)	HLE, Hu'u district	13.5	75.8	20.5	240	48.4	451	7.38	536987	9948	0.03	15.1

Appendix 11 (continued)

Sample ID	Description	U (ppm)	Ce/Ce*	Ce/Nd	Eu/Eu*	logfO2	ΔFMQ	T(ºC)
VHD006/500-502 (07)	HLE, Hu'u district	52.7	24.1	3.02	0.57	-15.0	0.02	770
VHD006/500-502 (10)	HLE, Hu'u district	31.9	119	14.4	0.41	-8.5	6.24	778
VHD006/500-502 (12)	HLE, Hu'u district	39.6	45.6	5.86	0.46	-12.2	2.58	777
VHD006/500-502 (15)	HLE, Hu'u district	58.4	115	11.1	0.52	-9.2	5.85	768
VHD006/500-502 (17)	HLE, Hu'u district	55.9	32.2	4.52	0.48	-13.8	1.14	771
VHD006/500-502 (20)	HLE, Hu'u district	38.9	92.9	8.88	0.52	-9.7	5.18	774
VHD006/500-502 (22)	HLE, Hu'u district	74.3	71.1	8.36	0.36	-9.0	5.07	811
VHD006/500-502 (26)	HLE, Hu'u district	68.8	65.9	6.49	0.50	-10.8	4.01	778
VHD006/500-502 (29)	HLE, Hu'u district	101	23.2	3.15	0.47	-16.4	-0.79	744
VHD006/500-502 (30)	HLE, Hu'u district	32.6	72.8	9.01	0.42	-10.2	4.46	782
VHD006/500-502 (33)	HLE, Hu'u district	68.2	33.8	4.93	0.43	-13.6	1.36	772
VHD006/500-502 (42)	HLE, Hu'u district	46.8	36.9	4.87	0.48	-13.5	1.54	767
VHD009A/250-252 (01)	HLE, Hu'u district	83.1	33.5	4.22	0.45	-15.3	0.44	738
VHD009A/250-252 (02)	HLE, Hu'u district	70.9	50.1	5.84	0.42	-10.3	3.77	812
VHD009A/250-252 (03)	HLE, Hu'u district	44.6	89.4	8.51	0.53	-10.8	4.53	754
VHD009A/250-252 (08)	HLE, Hu'u district	64.7	95.0	8.63	0.54	-8.8	5.70	791
VHD009A/250-252 (11)	HLE, Hu'u district	53.1	45.0	5.56	0.45	-11.2	3.11	801
VHD009A/250-252 (13)	HLE, Hu'u district	52.8	32.7	5.36	0.42	-14.0	1.08	766
VHD009A/250-252 (14)	HLE, Hu'u district	74.8	43.1	5.29	0.44	-11.4	2.91	799
VHD009A/250-252 (16)	HLE, Hu'u district	112	57.2	5.80	0.54	-12.8	2.71	748
VHD009A/250-252 (21)	HLE, Hu'u district	83.2	87.4	7.54	0.49	-9.72	5.07	778
VHD009A/250-252 (22)	HLE, Hu'u district	72.3	37.5	4.74	0.43	-12.0	2.34	797
VHD009A/250-252 (23)	HLE, Hu'u district	58.7	52.9	5.41	0.49	-12.5	2.71	759
VHD009A/250-252 (24)	HLE, Hu'u district	74.0	47.7	5.04	0.54	-7.49	5.14	884
VHD009A/250-252 (28)	HLE, Hu'u district	44.6	68.4	7.90	0.43	-10.4	4.27	783
VHD009A/250-252 (29)	HLE, Hu'u district	69.6	66.3	6.99	0.41	-5.69	6.67	898
VHD009A/250-252 (31)	HLE, Hu'u district	118	45.9	5.97	0.42	-15.6	0.87	710
VHD009A/250-252 (32)	HLE, Hu'u district	36.0	69.2	8.51	0.43	-10.3	4.35	785
VHD009A/250-252 (33)	HLE, Hu'u district	57.1	30.5	4.03	0.47	-13.3	1.30	786
VHD009A/250-252 (34)	HLE, Hu'u district	37.6	97.2	9.27	0.56	-10.5	4.87	754
VHD009A/250-252 (38)	HLE, Hu'u district	65.2	25.2	3.36	0.51	-15.8	-0.33	750
VHD009A/250-252 (43)	HLE, Hu'u district	44.6	70.3	6.79	0.60	-11.2	3.88	763
VHD009A/250-252 (44)	HLE, Hu'u district	55.0	76.2	7.17	0.52	-10.1	4.61	781

VHD009A/250-252 (45)	HLE, Hu'u district	74.1	37.9	4.84	0.42	-11.9	2.41	798
VHD009A/250-252 (49)	HLE, Hu'u district	138	79.2	7.91	0.52	-8.31	5.62	817
VHD009A/250-252 (51)	HLE, Hu'u district	32.9	52.3	7.01	0.37	-11.1	3.45	791
VHD009A/250-252 (53)	HLE, Hu'u district	79.0	23.5	3.04	0.51	-15.3	-0.21	765
VHD009A/250-252 (54)	HLE, Hu'u district	52.4	68.0	7.66	0.43	-9.10	4.94	812
VHD009A/250-252 (55)	HLE, Hu'u district	48.8	33.3	4.96	0.53	-13.6	1.33	774
VHD009A/250-252 (58)	HLE, Hu'u district	51.5	28.0	3.75	0.46	-12.5	1.58	811
VHD001R/600-602 (05)	HLE, Hu'u district	35.3	106	10.1	0.58	-10.1	5.22	756
VHD001R/600-602 (09)	HLE, Hu'u district	50.5	29.3	3.55	0.56	-14.8	0.43	757
VHD001R/600-602 (15)	HLE, Hu'u district	50.2	21.2	2.77	0.52	-15.4	-0.46	770
VHD001R/600-602 (19)	HLE, Hu'u district	54.2	49.6	6.17	0.48	-13.2	2.22	750
VHD001R/600-602 (22)	HLE, Hu'u district	59.6	20.1	2.89	0.56	-16.0	-0.85	762
VHD001R/600-602 (27)	HLE, Hu'u district	55.7	68.1	7.30	0.46	-9.8	4.58	797
VHD001R/600-602 (28)	HLE, Hu'u district	34.0	85.5	8.96	0.57	-10.6	4.57	762
VHD001R/600-602 (29)	HLE, Hu'u district	34.7	85.7	9.13	0.55	-10.5	4.63	764
VHD001R/600-602 (34)	HLE, Hu'u district	45.2	27.4	2.08	0.47	-14.0	0.76	780
VHD001R/600-602 (36)	HLE, Hu'u district	71.3	25.7	3.82	0.42	-14.0	0.63	785
VHD001R/600-602 (43)	HLE, Hu'u district	39.8	54.7	5.68	0.58	-12.5	2.77	757
VHD001R/600-602 (44)	HLE, Hu'u district	51.1	24.7	3.24	0.55	-15.0	0.02	766
VHD001R/600-602 (46)	HLE, Hu'u district	54.1	34.1	5.55	0.41	-13.6	1.37	771
VHD001R/600-602 (56)	HLE, Hu'u district	110	88.3	9.48	0.40	-8.0	5.99	816
VHD001R/600-602 (64)	HLE, Hu'u district	53.1	37.9	4.70	0.56	-13.4	1.63	766
VHD001R/600-602 (65)	HLE, Hu'u district	54.3	36.2	3.79	0.65	-13.6	1.47	766
VHD001R/600-602 (66)	HLE, Hu'u district	60.1	92.3	9.63	0.47	-9.15	5.46	786
VHD001R/600-602 (68)	HLE, Hu'u district	133	50.5	3.33	0.55	-10.2	3.85	814
VHD001R/600-602 (70)	HLE, Hu'u district	56.4	35.5	5.26	0.37	-12.4	2.02	792
VHD001R/600-602 (71-1)	HLE, Hu'u district	44.3	36.9	2.71	0.52	-13.8	1.40	761
VHD001R/600-602 (71-2)	HLE, Hu'u district	38.1	56.3	6.16	0.61	-12.0	3.10	766

Appendix 12 LA-ICP-MS result of zircon U-Pb dating from HLE prospect which representative early, intermediate and late stage of intrusion phase.

No	Sample	Intrusion phase	^{206}Pb (ppm)	^{232}Th (ppm)	^{238}U (ppm)	^{232}Th/^{238}U (ppm)	^{238}U/^{206}Pb Age (Ma)	^{238}U/^{206}Pb Age (Ma) Error
1	VHD006/500-502 (07)	Early phase	0.04	28.1	52.7	0.53	1.32	0.10
2	VHD006/500-502 (12)	Early phase	0.03	18.6	39.6	0.47	1.17	0.07
3	VHD006/500-502 (17)	Early phase	0.03	33.9	55.9	0.61	1.01	0.12
4	VHD006/500-502 (20)	Early phase	0.03	15.4	38.9	0.40	1.47	0.08
5	VHD006/500-502 (26)	Early phase	0.09	30.9	68.8	0.45	1.23	0.06
6	VHD006/500-502 (29)	Early phase	0.09	57.6	101	0.57	1.51	0.11
7	VHD006/500-502 (33)	Early phase	0.06	44.9	68.2	0.66	1.54	0.12
8	VHD006/500-502 (42)	Early phase	0.03	22.8	46.8	0.49	1.14	0.06
9	VHD009A/250-252 (01)	Intermediate phase	0.05	42.2	83.1	0.51	0.99	0.05
10	VHD009A/250-252 (03)	Intermediate phase	0.03	17.5	44.6	0.39	1.22	0.07
11	VHD009A/250-252 (08)	Intermediate phase	0.04	26.5	64.7	0.41	1.05	0.06
12	VHD009A/250-252 (13)	Intermediate phase	0.05	35.7	52.8	0.68	1.55	0.21
13	VHD009A/250-252 (14)	Intermediate phase	0.05	36.8	74.8	0.49	1.20	0.07
14	VHD009A/250-252 (16)	Intermediate phase	0.08	46.2	112	0.41	1.17	0.08
15	VHD009A/250-252 (21)	Intermediate phase	0.06	31.4	83.2	0.38	1.18	0.32
16	VHD009A/250-252 (22)	Intermediate phase	0.04	36.8	72.3	0.51	1.04	0.13
17	VHD009A/250-252 (23)	Intermediate phase	0.03	22.8	58.7	0.39	0.98	0.05
18	VHD009A/250-252 (31)	Intermediate phase	0.08	61.6	118	0.52	1.12	0.05
19	VHD009A/250-252 (33)	Intermediate phase	0.03	29.8	57.1	0.52	1.01	0.05
20	VHD009A/250-252 (34)	Intermediate phase	0.03	16.1	37.6	0.43	1.41	0.52
21	VHD009A/250-252 (38)	Intermediate phase	0.05	33.8	65.2	0.52	1.36	0.10
22	VHD009A/250-252 (43)	Intermediate phase	0.03	18.7	44.6	0.42	1.20	0.08
23	VHD009A/250-252 (44)	Intermediate phase	0.04	19.1	55.0	0.35	1.12	0.07
24	VHD009A/250-252 (45)	Intermediate phase	0.05	38.6	74.1	0.52	1.20	0.14

25	VHD009A/250-252 (51)	Intermediate phase	0.02	15.0	32.9	0.46	1.00	0.07
26	VHD009A/250-252 (53)	Intermediate phase	0.05	45.5	79.0	0.58	0.97	0.19
27	VHD009A/250-252 (54)	Intermediate phase	0.04	19.5	52.4	0.37	1.30	0.14
28	VHD009A/250-252 (55)	Intermediate phase	0.04	32.2	48.8	0.66	1.31	0.15
29	VHD001R/600-602 (05)	Late phase	0.02	13.5	35.3	0.38	1.11	0.07
30	VHD001R/600-602 (09)	Late phase	0.04	24.2	50.5	0.48	1.30	0.07
31	VHD001R/600-602 (15)	Late phase	0.04	26.1	50.2	0.52	1.26	0.24
32	VHD001R/600-602 (27)	Late phase	0.04	19.8	55.7	0.36	1.20	0.06
33	VHD001R/600-602 (29)	Late phase	0.03	14.5	34.7	0.42	1.46	0.09
34	VHD001R/600-602 (36)	Late phase	0.05	52.1	71.3	0.73	1.21	0.06
35	VHD001R/600-602 (43)	Late phase	0.03	17.6	39.8	0.44	1.26	0.07
36	VHD001R/600-602 (44)	Late phase	0.04	25.7	51.1	0.50	1.34	0.07
37	VHD001R/600-602 (46)	Late phase	0.04	36.2	54.1	0.67	1.36	0.15
38	VHD001R/600-602 (48)	Late phase	0.64	55.2	110	0.50	1.51	0.28
39	VHD001R/600-602 (64)	Late phase	0.04	26.9	53.1	0.51	1.21	0.11
40	VHD001R/600-602 (66)	Late phase	0.03	27.8	60.1	0.46	0.90	0.07
41	VHD001R/600-602 (68)	Late phase	0.11	54.2	133	0.41	1.45	0.10
42	VHD001R/600-602 (70)	Late phase	0.04	31.2	56.4	0.55	1.21	0.08
43	VHD001R/600-602 (71-1)	Late phase	0.06	17.5	44.3	0.40	1.48	0.08